Mechanical and Hydraulic Properties of Opalinus Clay: Influence of Compositional Heterogeneity and Thermodynamic Boundary Conditions

---

Valerian Schuster

Kumulative Univ.-Diss.
zur Erlangung des akademischen Grades
“doctor rerum naturalium” (Dr. rer. nat.)
in der Wissenschaftsdisziplin Geologie

eingereicht an der
Mathematisch-Naturwissenschaftlichen Fakultät
Institut für Geowissenschaften der Universität Potsdam

Ort und Datum der Disputation: Potsdam, 10.10.2022

Hauptbetreuer:	Prof. Dr. Georg Dresen
Betreuerin:	Dr. habil. Anja M. Schleicher
Externer Gutachter:	Prof. Dr. Florian Amann

Published online on the
Publication Server of the University of Potsdam:
https://doi.org/10.25932/publishup-56678
https://nbn-resolving.org/urn:nbn:de:kobv:517-opus4-566786

Eidesstattliche Erklärung

Hiermit versichere ich an Eides statt, dass

- die eingereichte Arbeit oder wesentliche Teile derselben in keinem anderen Verfahren zur Erlangung eines akademischen Grades vorgelegt worden sind;
- bei der Anfertigung der Dissertation die Grundsätze zur Sicherung guter wissenschaftlicher Praxis der DFG eingehalten wurden, die Dissertation selbständig und ohne fremde Hilfe verfasst wurde, andere als die von mir angegebenen Quellen und Hilfsmittel nicht benutzt worden sind und die den benutzten Werken wörtlich oder sinngemäß entnommenen Stellen als solche kenntlich gemacht wurden.

Potsdam, 15.06.2022

_____

Valerian Schuster

Abstract

Deep geological repositories represent a promising solution for the final disposal of nuclear waste. Due to its low permeability, high sorption capacity and self-sealing potential, Opalinus Clay (OPA) is considered a suitable host rock formation for the long-term storage of nuclear waste in Switzerland and Germany. However, the clay formation is characterized by compositional and structural variabilities including the occurrence of carbonate- and quartz-rich layers, pronounced bedding planes as well as tectonic elements such as pre-existing fault zones and fractures, suggesting heterogeneous rock mass properties.

Characterizing the heterogeneity of host rock properties is therefore essential for safety predictions of future repositories. This includes a detailed understanding of the mechanical and hydraulic properties, deformation behavior and the underlying deformation processes for an improved assessment of the sealing integrity and long-term safety of a deep repository in OPA. Against this background, this thesis presents the results of deformation experiments performed on intact and artificially fractured specimens of the quartz-rich, sandy and clay-rich, shaly facies of OPA. The experiments focus on the influence of mineralogical composition on the deformation behavior as well as the reactivation and sealing properties of pre-existing faults and fractures at different boundary conditions (e.g., pressure, temperature, strain rate).

The anisotropic mechanical properties of the sandy facies of OPA are presented in the first section, which were determined from triaxial deformation experiments using dried and resaturated samples loaded at 0°, 45° and 90° to the bedding plane orientation. A Paterson-type deformation apparatus was used that allowed to investigate how the deformation behavior is influenced by the variation of confining pressure (50 – 100 MPa), temperature (25 – 200 °C), and strain rate ($1 \times 10^{-3} – 5 \times 10^{-6}$ s^{-1}). Constant strain rate experiments revealed brittle to semi-brittle deformation behavior of the sandy facies at the applied conditions. Deformation behavior showed a strong dependence on confining pressure, degree of water saturation as well as bedding orientation, whereas the variation of temperature and strain rate had no significant effect on deformation. Furthermore, the sandy facies displays higher strength and stiffness compared to the clay-rich shaly facies deformed at similar conditions by Nüesch (1991). From the obtained results it can be concluded that cataclastic mechanisms dominate the short-term deformation behavior of dried samples from both facies up to elevated pressure (<200 MPa) and temperature (<200 °C) conditions.

The second part presents triaxial deformation tests that were performed to investigate how structural discontinuities affect the deformation behavior of OPA and how the reactivation of pre-existing faults is influenced by mineral composition and confining pressure. To this end, dried cylindrical samples of the sandy and shaly facies of OPA were used, which contained a saw-cut fracture oriented at 30° to the long axis. After hydrostatic pre-compaction at 50 MPa, constant

strain rate deformation tests were performed at confining pressures of 5, 20 or 35 MPa. With increasing confinement, a gradual transition from brittle, highly localized fault slip including a stress drop at fault reactivation to semi-brittle deformation behavior, characterized by increasing delocalization and non-linear strain hardening without dynamic fault reactivation, can be observed. Brittle localization was limited by the confining pressure at which the fault strength exceeded the matrix yield strength, above which strain partitioning between localized fault slip and distributed matrix deformation occurred. The sandy facies displayed a slightly higher friction coefficient ($\approx$0.48) compared to the shaly facies ($\approx$0.4). In addition, slide-hold-slide tests were conducted, revealing negative or negligible frictional strengthening, which suggests stable creep and long-term weakness of faults in both facies of OPA. The conducted experiments demonstrate that dilatant brittle fault reactivation in OPA may be favored at high overconsolidation ratios and shallow depths, increasing the risk of seismic hazard and the creation of fluid pathways.

The final section illustrates how the sealing capacity of fractures in OPA is affected by mineral composition. Triaxial flow-through experiments using Argon-gas were performed with dried samples from the sandy and shaly facies of OPA containing a roughened, artificial fracture. Slate, graywacke, quartzite, natural fault gouge, and granite samples were also tested to highlight the influence of normal stress, mineralogy and diagenesis on the sustainability of fracture transmissivity. With increasing normal stress, a non-linear decrease of fracture transmissivity can be observed that resulted in a permanent reduction of transmissivity after stress release. The transmissivity of rocks with a high portion of strong minerals (e.g., quartz) and high unconfined compressive strength was less sensitive to stress changes. In accordance with this, the sandy facies of OPA displayed a higher initial transmissivity that was less sensitive to stress changes compared to the shaly facies. However, transmissivity of rigid slate was less sensitive to stress changes than the sandy facies of OPA, although the slate is characterized by a higher phyllosilicate content. This demonstrates that in addition to mineral composition, other factors such as the degree of metamorphism, cementation and consolidation have to be considered when evaluating the sealing capacity of phyllosilicate-rich rocks.

The results of this thesis highlighted the role of confining pressure on the failure behavior of intact and artificially fractured OPA. Although the quartz-rich sandy facies may be considered as being more favorable for underground constructions due to its higher shear strength and stiffness than the shaly facies, the results indicate that when fractures develop in the sandy facies, they are more conductive and remain more permeable compared to fractures in the clay-dominated shaly facies at a given stress. The results may provide the basis for constitutive models to predict the integrity and evolution of a future repository. Clearly, the influence of composition and consolidation, e.g., by geological burial and uplift, on the mechanical sealing behavior of OPA highlights the need for a detailed site-specific material characterization for a future repository.

Zusammenfassung

Geologische Tiefenlager stellen eine vielversprechende Lösung für die Endlagerung von Atommüll dar. Aufgrund seiner geringen hydraulischen Durchlässigkeit, hohen Sorptionskapazität von Schadstoffen sowie seines Selbstabdichtungspotentials von Rissen gilt Opalinuston (OPA) als geeignetes Wirtsgestein für die Langzeitlagerung von Atommüll in der Schweiz und in Deutschland. Die Tonformation weist jedoch eine lithologische und strukturelle Variabilität auf, die durch das Auftreten von karbonat- und quarzreichen Lagen, einer ausgeprägten Schichtung sowie tektonischen Elementen wie Störungszonen und Brüchen gekennzeichnet ist, was auf heterogene Gebirgseigenschaften hindeutet.

Die Charakterisierung dieser Heterogenität im Hinblick auf die Eigenschaften des Wirtsgesteins ist für Sicherheitsvorhersagen zukünftiger Endlager von wesentlicher Bedeutung. Diese beinhaltet ein detailliertes Verständnis der mechanischen und hydraulischen Eigenschaften, des Deformationsverhaltens sowie der zugrunde liegenden Deformationsprozesse, die eine verbesserte Beurteilung des wirksamen Einschlusses sowie der Langzeitsicherheit eines Tiefenlagers in OPA ermöglichen. Vor diesem Hintergrund präsentiert diese Arbeit die Ergebnisse von triaxialen Verformungsexperimenten, die an intakten und künstlich gestörten Proben der quarzreichen, sandigen sowie tonigen Fazies von OPA durchgeführt worden sind. Ein besonderer Fokus ist hierbei auf den Einfluss der mineralogischen Zusammensetzung auf das Verformungsverhalten sowie die Reaktivierungs- und Abdichtungseigenschaften von bereits bestehenden Scherzonen und Rissen bei unterschiedlichen Randbedingungen (z. B. Druck, Temperatur, Dehnungsrate) gelegt worden.

Im ersten Abschnitt werden die anisotropen mechanischen Eigenschaften der sandigen Fazies von OPA vorgestellt. Hierfür sind triaxiale Verformungsexperimente an getrockneten und wassergesättigten Proben durchgeführt worden, die in einem Winkel von 0°, 45° und 90° zur relativ zur vorhandenen Schichtung belastet worden sind. Mittels einer Paterson Gasdruckapparatur ist der Einfluss von Mantelspannung (50 – 100 MPa), Temperatur (25 – 200 °C) und Verformungsrate ($1 \times 10^{-3} - 5 \times 10^{-6}$ s^{-1}) auf das Deformationsverhalten untersucht worden. Die Experimente zeigen ein sprödes bis halbsprödes Verformungsverhalten der sandigen Fazies, wobei ein deutlicher Einfluss von Manteldruck, Wassersättigung sowie Schichtungsorientierung festgestellt werden konnte. Im Gegensatz dazu zeigt die Änderung von Temperatur und Verformungsrate keinen signifikanten Einfluss auf das Deformationsverhalten und die Festigkeitseigenschaften der sandigen Fazies. Verglichen mit der tonigen Fazies (Nüesch 1991) weist die sandige Fazies des OPA eine höhere Festigkeit und Steifigkeit auf. Die Ergebnisse deuten darauf hin, dass das kurzfristige Verformungsverhalten getrockneter Proben beider Faziestypen bis zu erhöhten Druck- (<200 MPa) und Temperaturbedingungen (<200 °C) von kataklastischen Deformationsmechanismen dominiert

wird.

Im zweiten Teil werden die Ergebnisse von triaxialen Deformationsexperimenten beschrieben, die durchgeführt worden sind, um den Einfluss von bereits bestehenden Störungen auf das Verformungsverhalten von OPA zu untersuchen und wie die Reaktivierung von Scherflächen durch die Mineralzusammensetzung und den Manteldruck beeinflusst wird. Dazu sind getrocknete zylindrische Proben der sandigen und tonigen Fazies von OPA verwendet worden, die zuvor in einem Winkel von 30° zur Längsachse halbiert worden sind. Nach einer hydrostatischen Vorkonsolidierung bei 50 MPa Druck, sind die Proben bei einer konstanten axialen Verformungsrate und Mantelspannungen von 5, 20 und 35 MPa deformiert worden. Bei niedriger Mantelspannung wird die Reaktivierung der Scherfläche durch einen Spannungsabfall eingeleitet, wobei weitere Verformung durch stark lokalisierte Scherung aufgenommen wird. Mit zunehmender Mantelspannung kann ein Übergang zu halbsprödem Verformungsverhalten beobachtet werden, das durch einen zunehmenden Anteil von Matrixdeformation ohne dynamische Verwerfungsreaktivierung gekennzeichnet ist. Dabei weist die sandige Fazies einen höheren Reibungskoeffizienten ($\approx$0,48) als die tonige Fazies ($\approx$0,4) auf. Die Experimente zeigen, dass spröde Reaktivierung der Scherfläche bis zu einer Mantelspannung erfolgt, ab der die Scherfestigkeit der künstlichen Störung die Fließspannung der Matrix übersteigt. Entsprechend beginnt mit weiter ansteigender Mantelspannung die Partitionierung von Deformation in Scherung und Matrixverformung. Relaxations- und Wiederbelastungstests (Slide-Hold-Slide) zeigen negative bzw. vernachlässigbare Reibungsverheilung auf, was auf eine geringe Wiederverfestigung und folglich aseismisches Kriechen als Langzeitverhalten von Scherzonen in OPA hindeutet. Die Ergebnisse zeigen, dass die spröde Reaktivierung von Scherzonen in OPA durch eine starke Überkonsolidierung und in geringen Tiefen begünstigt werden kann, was das Risiko von Seismizität und die Bildung hydraulischer Fließwege erhöht.

Der letzte Abschnitt veranschaulicht, wie die Transmissivität von Rissen in OPA von der wirkenden Normalspannung und Mineralzusammensetzung beeinflusst wird. Hierfür sind triaxiale Durchströmungsexperimente an getrockneten Proben der sandigen und tonigen Fazies von OPA durchgeführt worden, die eine künstlich angeraute Rissfläche enthielten. Um den Einfluss von Normalspannung, Mineralogie und Diagenese auf die hydraulische Rissverschließung zu untersuchen, sind darüber hinaus auch Risse in Schiefer, Grauwacke, Quarzit, Proben aus natürlichen Störungszonen und Granit getestet worden. Mit zunehmender Normalspannung konnte eine nichtlineare Abnahme der Risstransmissivität beobachtet werden, die nach Entlastung zu einer irreversiblen Reduktion der Transmissivität führt. Die Transmissivität von Gesteinen, die durch einen hohen Anteil mechanisch fester Minerale (z.B. Quarz) sowie einer hohen einaxialen Druckfestigkeit charakterisiert werden, reagieren robuster auf Spannungsänderungen. Dementsprechend zeigt die sandige Fazies von OPA im Vergleich zur tonigen Fazies eine höhere initale Risstransmissivität, die weniger empfindlich auf Spannungsänderungen reagiert. Obwohl die sandige Fazies

im Vergleich zu der untersuchten Schieferprobe einen niedrigeren Schichtsilikatgehalt aufweist, reagiert die Risstransmissivität des Schiefers deutlich geringer auf Spannungsänderungen. Aus den Experimenten kann abgeleitet werden, dass für die Bewertung der hydraulischen Rissverschließung in schichtsilikatreichen Gesteinen neben der mineralischen Zusammensetzung weitere Faktoren, wie der Grad der Metamorphose sowie Zementierung und Konsolidierung, berücksichtigt werden müssen.

Die Ergebnisse dieser Arbeit verdeutlichten die Rolle der Mantelspannung auf das Deformationsverhalten von intaktem und künstlich gestörten OPA. Obwohl die quarzreiche sandige Fazies von OPA aufgrund ihrer höheren Scherfestigkeit und Steifigkeit als günstiger für die Konstruktion von Untertagebauwerken angesehen werden kann, weisen die präsentierten Ergebnisse darauf hin, dass diese vorteilhaften mechanischen Eigenschaften mit einer Verringerung der hydraulischen Abdichtungskapazität verbunden sind, d.h. wenn sich Risse in der sandigen Fazies entwickeln, sind diese hydraulisch leitfähiger und bleiben durchlässiger im Vergleich zu Rissen in der tonigen Fazies bei einer gegebenen Spannung. Die Ergebnisse können die Grundlage für die Entwicklung konstitutiver Modelle bilden, die zur Einschätzung der Integrität eines zukünftigen Endlagers herangezogen werden können. Der Einfluss der mineralogischen Zusammensetzung sowie der Konsolidierung auf die mechanischen und hydraulischen Eigenschaften von OPA zeigen die Notwendigkeit einer detaillierten, standortspezifischen Materialcharakterisierung für ein zukünftiges Endlager.

Statement of Contribution

This cumulative thesis consists of three peer-reviewed papers. Two of them have been published in scientific journals, while the third has been accepted for publication. The Ph.D. candidate is first author of two of these three papers, which constitute Chapters 2, 3 and 4 of the thesis. Additional content from a peer-reviewed reply to a discussion by Crisci et al. (2022), also published in a scientific journal and authored by the Ph.D. candidate as first author, which is not presented nor discussed in the original publication on which Chapter 2 is based on, is included in this chapter. Each of these chapters is organized according to its published structure, namely comprising abstract, introduction, methods, results, discussion, conclusions and acknowledgments. Additionally, a general introduction to the topic is given in Chapter 1, whereas a summary of the main conclusions and an outlook of future work are presented in Chapters 5 and 6, respectively. A combined reference list is presented at the end of the thesis.
The major results of this thesis are published or accepted for publication in:

Chapter 2: **Schuster**, **V**., Rybacki, E., Bonnelye, A., Herrmann, J., Schleicher, A. M., & Dresen, G. (2021). Experimental Deformation of Opalinus Clay at Elevated Temperature and Pressure Conditions: Mechanical Properties and the Influence of Rock Fabric, published in Rock Mechanics and Rock Engineering, 54(8), 4009-4039. https://doi.org/10.1007/s00603-021-02474-3. The paper was authored by the Ph.D. candidate. Revisions made by the co-authors helped improving the paper substantially.
Schuster, **V**., Rybacki, E., Bonnelye, A., & Dresen, G. (2022). Authors' Reply to the Discussion by Crisci et al. (2021) on "Experimental Deformation of Opalinus Clay at Elevated Temperature and Pressure Conditions Mechanical Properties and the Influence of Rock Fabric" published in Rock Mechanics and Rock Engineering, 55(1), 467-469. https://doi.org/10.1007/s00603- 021-02675-w. The paper was authored by the Ph.D. candidate. Revisions made by the co-authors helped improving the paper substantially.

Chapter 3: **Schuster**, **V**., Rybacki, E., Bonnelye, A., Kwiatek, G., Schleicher, A. M., & Dresen, G. (2022). Strain Partitioning and Frictional Behavior of Opalinus Clay during Fault Reactivation accepted in Rock Mechanics and Rock Engineering, https://doi.org/10.1007/s00603-022-03129-7. The paper was authored by the Ph.D. candidate. Revisions made by the co-authors helped improving the paper substantially.

Chapter 4: Herrmann, J., **Schuster**, **V**., Cheng, C., Milsch, H., & Rybacki, E. (2022). Fracture Transmissivity in Prospective Host Rocks for Enhanced Geothermal Systems (EGS) published in Geosciences, 12(5), 195. https://doi.org/10.3390/geosciences12050195. The Ph.D. candidate co-authored this paper.

Declaration

The work presented here was funded with the financial support from the Federal Ministry of Education and Research under the Project Number 02NUK053D, the Helmholtz Association under the Project Number SO-093 and the GFZ German Research Centre for Geosciences Potsdam for the iCross project as well as by the "Multidisciplinary and multi-context demonstration of Enhanced Geothermal Systems Exploration and Exploitation Techniques and potentials (MEET)" research project funded by the European Union's Horizon 2020 research and innovation programme under Grant Agreement Number 792037, which is gratefully acknowledged. Experimental work, data analysis and interpretations were carried out mainly by the Ph.D. candidate with contributions from the co-authors listed in each chapter separately. All experiments were conducted at the "DeutschesGeoForschungZentrum (GFZ)" in Potsdam, Germany under the supervision of Michael Naumann, who is greatly acknowledged. Samples were prepared at GFZ by the Ph. D. candidate and Stefan Gehrmann (GFZ). Electron microscopy (SEM) was performed by the Ph.D. candidate after training and support by Dr. V. Roddatis and A. Schreiber (both GFZ). X-ray diffraction measurements were carried out by Dr. habil. A. M. Schleicher (GFZ), who is thankfully acknowledged.

Acknowledgment

First and foremost, I would like to thank my main supervisor Prof. Dr. Georg Dresen for giving me the chance to finish this work in the section Geomechanics and Scientific Drilling at the GeoFoschungsZentrum (GFZ) Potsdam. The constructive discussions with him were always helpful and clearly supported me in my scientific development.

I would also like to thank Dr. habil. Anja M. Schleicher for her supervision of this work and her scientific support. Thanks for the fantastic road trip to Mont Terri.

My deepest gratitude goes to my mentor Dr. Erik Rybacki for his irreplaceable help in the conception and preparation of the manuscripts and this work. Thank you for the countless hours of support and for always having an open door for me, especially for all non-work-related discussions.

I would like to thank Michael Naumann for many funny conversations, but above all for his great technical support and knowledge, without which the experiments carried out would not have been possible.

I am grateful to Dr. Audrey Bonnelye for her scientific and technical assistance, as well as the countless, but of course always constructive, coffee breaks.

Furthermore, I thank Dr. Grzegorz Kwiatek for his essential help in evaluating the ultrasonic measurements. I would like to thank Stefan Gehrmann for the excellent preparation of all samples as well as Rita Hamlischer for all organizational assistance. Finally, I would like to thank all my colleagues and friends at GFZ, but especially Amandine, Chaojie, Aglaja, Lei, Simon, Sagar, Claudius, Vivi, Christopher, Io, Lea, Maria and Bernhard, who welcomed me openly and warmly. Thank you for the scientific, but above all the non-scientific exchange .

A special thanks goes to my colleagues Dr. Johannes Herrmann, Dr. Stephan Bentz and Dr. Livia Nardini for the fun time in and outside the office, but also for the support and help, especially at the beginning of my Ph.D.

Furthermore, I am very fortunate that I had so many close friends both in Göttingen (Marcel, Junyi, Lukas, Yannick, Maverick and Maja) as well as in Darmstadt (JMA, Henning, Johannes, Tyne, Chris and Babsi) who supported me on this journey and gave me the necessary distraction I needed from time to time.

My deepest gratitude goes to my parents and family, without whose unlimited support none of this would have been possible.

Swantje, thank you for the countless conversations about rocks, which for you were mostly boring. You are the enrichment in my life.

Contents

List of Figures

List of Tables

1 General Introduction

1.1 Background

In March 2022 the European Commission has approved the Complementary Climate Delegated Act (EC 2022) stating that, under specific conditions, economic activities related to nuclear energy are covered by the EU taxonomy (EP 2020). The Commission has therefore concluded that nuclear energy is a viable energy source in line with the objectives of the European Green Deal to achieve the EU's climate and energy goals (EC 2019). Nevertheless, several EU and Central European countries, including Switzerland and Germany have decided to phase out nuclear energy within this and the following decade. In 2020, the European Statistical Office (Eurostat) has estimated that about 25% of the total electricity production in the EU was generated by nuclear power plants (Eurostat 2022). Considering the almost 70-year history of nuclear power generation, the total share of current and future electricity production and the associated accumulation of spent fuel, it becomes clear that a key part of the challenge in the European energy transition towards renewable energy, energy efficiency and sustainable development is the long-term safe storage and isolation of nuclear waste. Against this background, this thesis focuses on characterizing mechanical and hydraulic properties of a potential host rock formation that may support safety assessment and performance for deep geological disposal of nuclear waste.

Internationally debated and approved by the scientific community, there is consensus that the disposal in deep geological formations provides the safest solution for the long-term management of high-level nuclear waste (OECD/NEA 2008). Since the disposal of nuclear waste is commonly of national matter, strategies may vary countrywise, but are generally based on a multi-barrier approach, i.e., the spent fuel is placed into corrosion-resistant containers made of copper and steel that are surrounded by an engineered buffer (e.g., salt grit, bentonite) and finally the geologic host rock formation (e.g., Kim et al. 2011; Ojovan et al. 2019; OECD/NEA 2020). In order to guarantee the long-term isolation of the waste from the biosphere and limit radionuclide release, there are several requirements that have to be fulfilled by the ultimate natural geological barrier (Ojovan et al. 2019): Effectiveness of inclusion (e.g., low matrix permeability), durability (e.g., thermo-hydro-mechanical-chemical-biological, THMCB, stability over geological time scales), and predictable, site-specific geological properties (e.g., vertical homogeneity, depth and lateral continuity of the rock formation as well as low risk for seismicity). Against this background, scientific investigations have been focused on crystalline rock (Sweden (SKB AB 2011), Finland (Posiva/Oy 2012)), dome and bedded rock salt (U.S.A. (Hansen and Leigh 2011), Germany (e.g., Bracke et al. 2013)), volcanic tuff and ignimbrite (U.S.A. (Ewing and Macfarlane 2002, Swift

and Bonano 2016)) as well as plastic, poorly indurated (e.g., Boom Clay or Ypresian clays in Belgium (ONDRAF/NIRAS 2001)) and indurated (e.g., Callovo-Oxfordian Clay in France (ANDRA 2005), Opalinus Clay formation (OPA) in Switzerland (NAGRA 2002) and Germany (Hoth et al. 2007)) clay, as these formations represent potential host rocks for the final disposal of nuclear waste worldwide (e.g., Kim et al. 2011; McCartin et al. 2020). Each type of host-rock formation offers some specific properties that are relevant for a future repository.

Clay formations are distinguished by some favorable barrier properties such as a low hydraulic conductivity that is resulting in predominantly diffusion-driven transport mechanisms (Shackelford and Moore 2013) as well as a high sorption capacity (Hartmann et al. 2008), which makes them particularly suitable for the retention of radionuclide migration. Argillaceous formations have a self-sealing capacity due to their compaction behavior (change of shape and volume reduction of voids by pore collapse due to loading). This includes the ability to reduce the transmissivity of natural and/or artificially induced fractures by several hydro-mechanical, hydro-chemical and hydro-bio-chemical processes (Van Geet et al. 2008; Bock et al. 2010), which is enhanced by the presence of clay minerals with a high swelling potential (e.g., montmorillonite, smectite). Since the long-term sealing integrity in all types of potential host rock formations is threatened by the creation of an excavation damaged and disturbed zone (EDZ, EdZ) during the construction of underground openings (Tsang et al. 2005), the aforementioned properties of clay formations are, among others, decisive factors for a deep repository in this type of rock (Delage et al. 2010; Sellin and Leupin 2013).

The complex coupled processes (Fig. 1.1) that result from the construction of a deep repository and the storage of heat-generating waste in an argillaceous formation (Delage et al. 2010; Tsang et al. 2012) require a detailed knowledge of the mechanical behavior and hydraulic transport properties of the designated host rock in order to evaluate and predict its long-term performance as a natural barrier. Mechanical and sealing properties of clays are complex as they are a function of the material's geologic history and therefore depend on the experienced burial depth and the accompanied diagenetic processes (e.g., Gutierrez et al. 1996; Bjørlykke and Høeg 1997; Nygård et al. 2004, 2006). The strength and elastic properties of clay-rich rocks depend on the acting confining pressure (e.g., Ibanez and Kronenberg 1993; Niandou et al. 1997), temperature (e.g., Zhang et al. 2007; Masri et al. 2014), strain rate (e.g., Kwon and Kronenberg 1994; Bonnelye et al. 2017a, b), mineral composition (e.g., Bourg 2015; Herrmann et al. 2018), consolidation state (e.g., Ingram and Urai 1999; Nygård et al. 2006) as well as on the water content (e.g., Chiarelli et al. 2000; Wild et al. 2015). The hydraulic conductivity and sealing performance of argillaceous formations also depend on the mineral composition, e.g., type and total content of clay minerals as well as the degree of induration by diagenesis, consolidation or metamorphism (Neuzil 1994; Fisher and Knipe 2001; Bock et al. 2010; Mazurek et al. 2011). Once excavation and construction work has started, the hydro-mechanical and transport properties of the host rock will be modified

due to stress redistribution and desaturation, leading to the creation of a hydraulic conductive fracture network (e.g., Bossart et al. 2004; Tsang et al. 2005, 2012; Thöny 2014, Wild 2016; Amann et al. 2018). Furthermore, the effective stress state may be changed by gas generation, e.g., due to the anaerobic corrosion of the emplaced steel canisters by microbial activity (Ortiz et al. 2002;

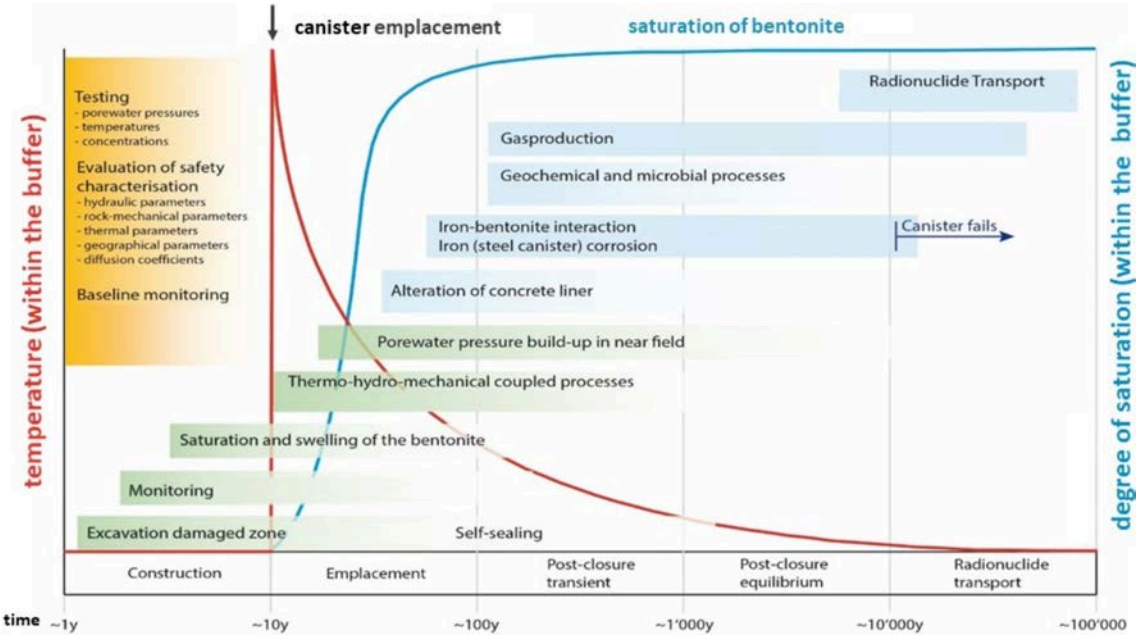

Figure 1.1: Key processes that are related to the construction and long-term evolution of a repository for the storage of nuclear waste (after Bossart et al. 2017a).

Marschall et al. 2005), and thermal pressurization due to the heat generated by the decay processes of the nuclear waste (e.g., Urpi et al. 2019). These processes may lead to mechanical destabilization, fault reactivation and thus to the creation of conductive flow paths. Finally, temperature driven clay mineral reactions and transformations (e.g., illitization) may alter the swelling and sorption capacity of the host rock (Bruno et al. 1992; Lee et al. 2010; Zheng et al. 2015; Sauer et al. 2020). Understanding the fundamental processes underlying the complex mechanical behavior and hydraulic properties of clays is essential in order to define the initial conditions of the repository site and its future development.

Due to its favorable barrier properties including a low matrix permeability, the capacity for self-sealing of fractures as well as the retardation and retention of radionuclides by sorption, the OPA formation is the envisaged host rock for the deep geological storage of nuclear waste in Switzerland (NAGRA 2002, 2019; Bossart and Milnes 2017; BFE 2018) and potentially in Germany (Hoth et al. 2007; Jobmann et al. 2017; BGE 2020). The site selection processes of both countries are very similar and guarantee a transparent procedure with the participation of national and public bodies (BFE 2021; StandAG 2017). Since Switzerland began evaluating potential sites for a repository in OPA in 2008, the selection has already been narrowed down to three potential re-

gions in 2018: Zürich Nordost, Nördlich Lägern and Jura Ost (NAGRA 2019). Germany restarted its site selection process in 2017 with the goal of a final site decision in 2031. In 2020 an interim report on sub-areas in Germany was presented in which the geological conditions are favorable for the safe disposal of radioactive waste in either clay, crystalline rock or salt (StandAG 2017, BGE 2020). Swiss OPA has been extensively studied in the laboratory and since 1996 at the Mont Terri Underground Research Laboratory (Canton Jura, Switzerland; Fig. 1.2a, b) with the focus on the characterization of the anisotropic hydro-mechanical behavior related to excavation, the determination of effective strength and stiffness parameters as well as coupled THMCB processes related to the construction and evolution of a repository (e.g., Nüesch 1991; Thury and Bossart 1999; Corkum and Martin 2007; Jahns 2007, 2010, 2013; Naumann et al. 2007; Popp and Salzer 2007; Schnier and Stürenberg 2006; Bossart and Thury 2008; Amann et al. 2011, 2012; Thöny 2014; Wild 2016; Bossart et al. 2017b; Bossart and Milnes 2017; Favero et al. 2018; Wild and Amann 2018; Minardi 2020; Winhausen et al. 2022). In addition, the Mont Terri Underground Research Laboratory (URL) is crossed by a reverse fault, also referred to as the "Main Fault", which enables to study hydro-mechanical, structural and petrophysical properties of a representative tectonic structure that could be potentially encountered in a repository in an argillaceous formation under in-situ conditions (e.g., Nussbaum et al. 2011, 2017; Laurich et al. 2014, 2017, 2018; Guglielmi et al. 2017; Jaeggi et al. 2017b; Wenning et al. 2021; Zappone et al. 2021; Hopp et al. 2022).

The Jurassic (Toarcian to Aalenian) OPA has been deposited in a shallow marine environment and reaches a thickness of 80 to 130 m in Switzerland and Germany (NAGRA 2002; Wetzel and Allia 2003; Hoth et al. 2007; BGE 2020). Although the OPA in Northern Switzerland displays an exceptional good lateral homogeneity (NAGRA 2002), in vertical direction (perpendicular to bedding plane orientation) some lithological variability was identified, mainly expressed by differing grain size, portion of main mineral components (clay minerals, quartz, carbonates), as well as color and porosity (Thury and Bossart 1999; Pearson et al. 2003; Wetzel and Allia 2003; Bossart and Thury 2008; Peters et al. 2011; Müller and Jaeggi 2012; Houben et al. 2014; Hostettler et al. 2017; Lauper et al. 2018, 2021; Kneuker and Furche 2021). Based on these criteria, OPA at the Mont Terri URL (Fig. 1.2b) was divided in three major sub-units: a shaly, sandy and carbonate-rich sandy facies (e.g., Hostettler et al. 2017; Lauper et al. 2018, 2021). Several studies focused on elaborating the influence and relation of the lithological variability on different rock properties including the distribution of mineral phases and porosity, grain size, hydraulic conductivity, cation exchange capacity, adsorption of radionuclides water retention capacity, as well as mechanical parameters including Young's modulus, strength and friction coefficient (e.g., Gräsle and Plischke 2010, 2011; Kaufhold et al. 2013; Houben et al. 2014; Siegesmund et al. 2014; Minardi et al. 2016; Philipp et al. 2017; Crisci 2019; Ferrari et al. 2020, Hennig et al. 2020; Kneuker et al. 2020; Zhang and Laurich 2019).

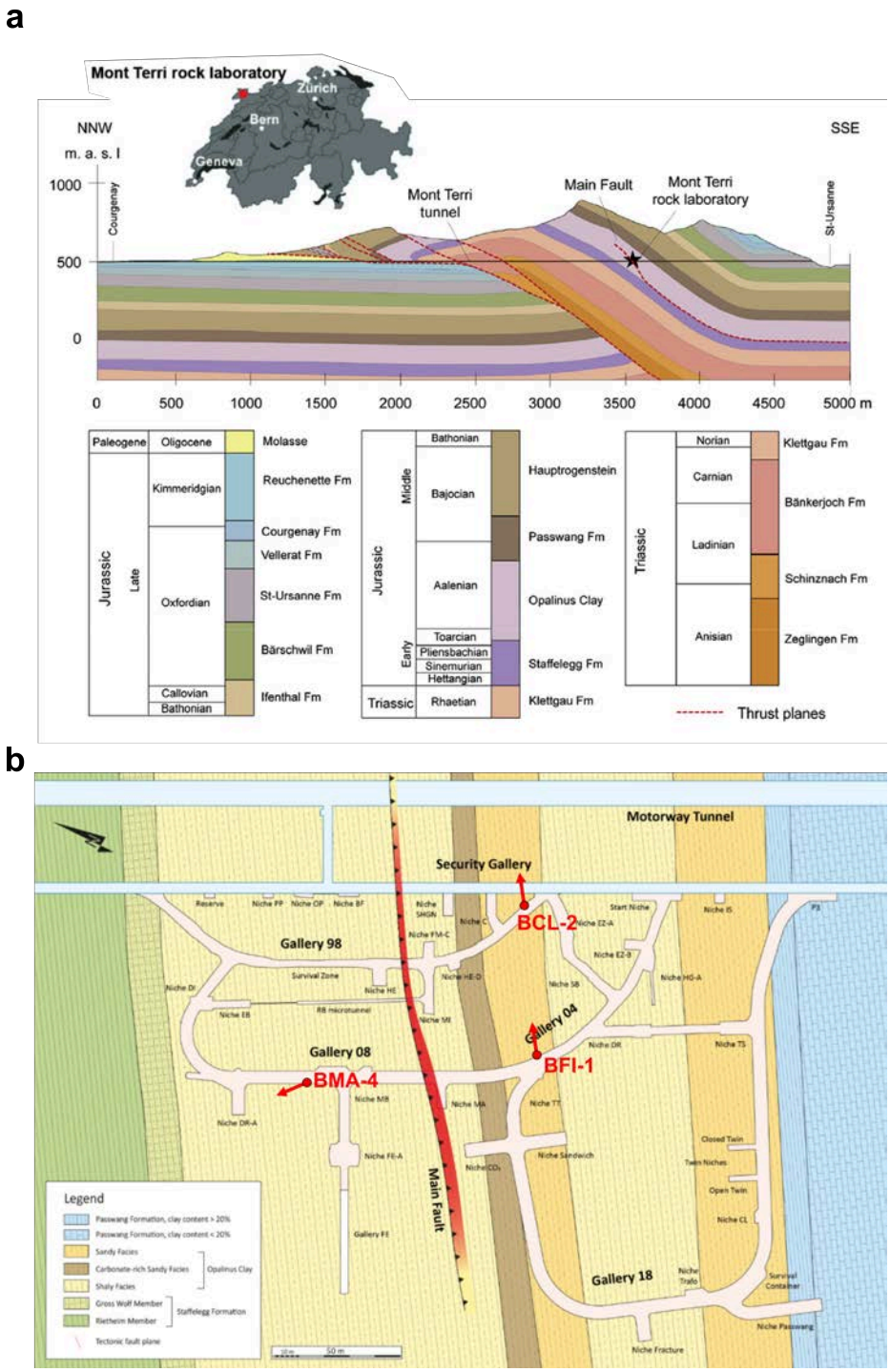

Figure 1.2: Map of Switzerland with the location of the Mont Terri Underground Research Laboratory (red star) as well as a cross-section of the Mont Terri anticline with the relevant stratigraphic units, location of the laboratory and the Main Fault (a). Schematic geological map of the URL with the drill core location of the investigated sample material in this thesis (b). Figures were modified after Bossart et al. 2017b and Mont Terri swisstopo (2022a, b).

1.2 Research Objective and Scientific Questions

The presence of tectonic discontinuities (e.g., fault zones), induced fractures due to excavation work (EDZ) and desaturation during the open drift stage or by heat generation, as well as lithological heterogeneities (different facies) should be minimized in a future repository site in OPA. However, the presence of faults, fractures and varying lithologies cannot be excluded, as is evident in the Mont Terri URL. The sandy facies of OPA is characterized by a higher quartz content and a higher shear strength and stiffness compared to the clay-rich shaly facies (cf., Popp and Salzer 2007; Gräsle and Plischke 2010, 2011; Siegesmund et al. 2014; Wild and Amann 2018; Favero et al. 2018; Giger et al. 2018; Crisci 2019; Zhang and Laurich 2019; Minardi et al. 2020). In the past, the majority of deformation experiments for the mechanical characterization of OPA has been carried out on the shaly facies (e.g., Nüesch 1991; Naumann et al. 2007; Amann et al. 2011, 2012; Favero et al 2018; Wild and Amann 2018; Minardi et al 2020; Winhausen et al. 2022). Therefore, little is known about the deformation behavior of the sandy facies. Despite its more desirable properties for underground excavation, the sandy facies displays a higher matrix permeability compared to the shaly facies, as well as a lower swelling capacity and thus a lower capability for self-sealing of fractures (e.g., Minardi et al. 2016; Philipp et al. 2017). Due to the higher quartz content, the deformation behavior of the sandy facies is more brittle with an increased leakage potential, as both are favored with decreasing clay mineral content (e.g., Gutierrez et al. 1996; Ingram and Urai 1999; Nygård et al. 2006; Bourg 2015). Because of its large size, it can be assumed that a future repository will cross different lithofacies types. Therefore, it is of great scientific interest to characterize the mechanical behavior and identify the differences due to lithological variability as well as the presence of discontinuities in order to assess the performance, long-term integrity and evolution of OPA as a natural geological barrier. The above motivates a number of scientific questions addressed in this thesis:

1. What are the micro-mechanical and physical processes leading to damage and failure in the sandy facies of OPA, how are they influenced by changing thermodynamic boundary conditions and rock fabric, and how does the behavior differ from the shaly facies?

2. How do pre-existing structural discontinuities influence the deformation behavior of the sandy and shaly facies of OPA and how is this affected by the acting stress field and different mineralogy?

3. What are the sealing mechanisms of the sandy facies and how much does the sealing capacity of fractures differ compared to the shaly facies of OPA?

1.3 Thesis Outline

This thesis comprises three articles mostly presenting laboratory deformation experiments performed on the sandy and shaly facies of OPA. In addition, a reply to a discussion by Crisci et al. (2022) on the paper from Chapter 2 is included. The obtained results aim to contribute to the general understanding of the deformation behavior of intact and faulted OPA related to compositional heterogeneity and sealing performance at different boundary conditions.

Following this Chapter, giving the introduction of this thesis, Chapter 2 provides a general characterization of the mechanical behavior of the sandy facies of OPA. To this end, constant strain rate, triaxial deformation experiments were performed on dry samples at various confining pressures (50 – 100 MPa), temperatures (25 – 200°C), and strain rates (1×10^{-3} – 5×10^{-6} s^{-1}). Samples were deformed at 0°, 45° and 90° to bedding plane orientation in order to investigate the anisotropy of strength, Young's modulus and deformation processes. In addition, the influence of water content on the deformation behavior was investigated at constant confining pressure (50 MPa) and temperature (100 °C) at strain rates of 5×10^{-4} and 5×10^{-6} s^{-1}. The results are compared to deformation tests of the shaly facies that were performed at similar conditions by Nüesch (1991).

Chapter 3 presents a study including triaxial deformation experiments performed on the sandy and shaly facies of OPA containing an artificial saw-cut fault plane inclined at 30° to loading direction. The dried samples were deformed perpendicular to bedding orientation with a constant displacement rate at confining pressures of 5, 20 and 35 MPa, with the aim of investigating the impact of mineralogy and confining pressure on fault reactivation in OPA.

Chapter 4 is dedicated to study the hydraulic properties of fractures within different rock types that are encountered in the framework of enhanced geothermal systems or nuclear waste disposal. In order to investigate the sustainability of fracture transmissivity as a function of normal stress, mineralogy and diagenesis, flow-through experiments were performed under triaxial conditions using samples of the shaly as well as sandy facies of OPA, slate, graywacke, quartzite, natural fault gouge, and granite.

Chapter 5 provides a general summary of the main results and conclusions with potential implications of the presented studies on the influence of compositional variation on the sealing performance of OPA.

Finally, Chapter 6 addresses suggestions and recommendations for potential future investigations and research perspectives based on the results of this dissertation.

2 Experimental Deformation of Opalinus Clay at Elevated Temperature and Pressure Conditions: Mechanical Properties and the Influence of Rock Fabric

Summary

The mechanical behavior of the sandy facies of Opalinus Clay (OPA) was investigated in 42 triaxial tests performed on dry samples at unconsolidated, undrained conditions at confining pressures (p_c) of 50 – 100 MPa, temperatures (T) between 25 – 200°C and strain rates ($\dot{\varepsilon}$) of 1×10^{-3} – 5×10^{-6} s^{-1}. Using a Paterson-type deformation apparatus, samples oriented at 0°, 45° and 90° to bedding were deformed up to about 15% axial strain. Additionally, the influence of water content, drainage condition and pre-consolidation was investigated at fixed p_c–T conditions, using dry and resaturated samples. Deformed samples display brittle to semi-brittle deformation behavior, characterized by cataclastic flow in quartz-rich sandy layers and granular flow in phyllosilicate-rich layers. Samples loaded parallel to bedding are less compliant compared to the other loading directions. With the exception of samples deformed 45° and 90° to bedding at p_c = 100 MPa, strain is localized in discrete shear zones. Compressive strength (σ_{max}) increases with increasing p_c, resulting in an internal friction coefficient of ≈ 0.31 for samples deformed at 45° and 90° to bedding, and ≈ 0.44 for samples deformed parallel to bedding. In contrast, pre-consolidation, drainage condition, T and $\dot{\varepsilon}$ do not significantly affect deformation behavior of dried samples. However, σ_{max} and Young's modulus (E) decrease substantially with increasing water saturation. Compared to the clay-rich shaly facies of OPA, sandy facies specimens display higher strength σ_{max} and Young's modulus E at similar deformation conditions. Strength and Young's modulus of samples deformed 90° and 45° to bedding are close to the iso-stress Reuss bound, suggesting a strong influence of weak clay-rich layers on the deformation behavior.

List of Symbols

σ_1	Maximum principal stress
θ	Angle between failure plane and samples axis
ρ	Density
φ	Porosity
$S_w\%$	Degree of water saturation
T	Temperature
p_c	Confining pressure
$\dot{\varepsilon}$	Strain rate
t_c	Consolidation time
L	Sample length
c	Isotropic consolidation coefficient
k	Hydraulic conductivity
K	Bulk modulus
γ_w	Unit weight of water
E_{oed}	Oedometer Young's modulus
ν	Poisson's ratio
E	Secant Young's modulus
B	Brittleness
σ_{max}	Peak (differential) strength
ε_{max}	Axial strain at peak strength
μ_y	Friction coefficient at yield stress
n, α	Constants
τ	Shear stress
τ_0	Cohesion
μ	Coefficient of internal friction at peak strength
σ_n	Normal stress
σ_{UCS}	Uniaxial compressive strength
φ	Friction angle
t_f	Required time to reach failure during drained shearing

2.1 Introduction

Argillaceous rocks, claystones or shales mainly consist of clay minerals typically with $\geq$50 volume percent (vol%) of particles sized $<$62.5 μm (e.g., Folk 1980). They account for roughly two-thirds of the sedimentary rock record (Milliken 2014), and are encountered in different natural settings such as sedimentary basins (Hornby et al. 1994) and accretionary wedges (Yamaguchi et al. 2011; Chester et al. 2013; Morley et al. 2017). Clay-rich sedimentary rocks play also a fundamental role in many engineering applications, including the extraction of hydrocarbons as well as the exploitation of geothermal energy from unconventional deep shale reservoirs (e.g., Blackwell et al. 2013; McGlade et al. 2013). Due to a low hydraulic conductivity, high self-sealing potential as well as sorption capacity, clay-rich shales constitute potential host rocks for the storage of nuclear waste (Madsen 1998; Delage et al. 2010; Sellin and Leubin 2013), and represent a suitable cap-rock sealing for the geological storage of carbon dioxide (Busch et al. 2008; Boosari et al. 2015; Bourg 2015).

Predicting the mechanical behavior and hydrological properties of clay-rocks across several spatial and temporal scales requires knowledge of the processes leading to damage and failure at the respective thermodynamic boundary conditions. However, physical and mechanical properties of shales depend on many factors caused by their complex sedimentary and tectonic history. These factors include diagenetic processes influenced by chemical reactions, mechanical loading and temperature variations (Gutierrez et al. 1996; Bjørlykke and Høek 1997; Nygård et al. 2004; Wenk et al. 2008; Ilgen et al. 2017; Morley et al. 2017). Additionally, shales display an increased crystallographic and shape-preferred orientation of phyllosilicates, resulting in a distinct anisotropy of physical and mechanical properties related to the depositional and diagenetic conditions, mineral composition and thermal maturity (e.g., Chiarelli et al. 2000; Wenk et al. 2008; Sone and Zoback 2013; Siegesmund et al. 2014; Liu et al. 2018). Previous experimental studies show that the strength and elastic properties of clay-rich rocks depend on applied confining pressure (e.g., Ibanez and Kronenberg 1993; Niandou et al. 1997; Petley 1999; Naumann et al. 2007; Herrmann et al. 2018), temperature (e.g., Zhang et al. 2007; Masri et al. 2014; Rybacki et al. 2015; Liu et al. 2019), strain rate (e.g., Swan et al. 1989; Chong and Boresi 1990; Kwon and Kronenberg 1994; Al-Bazali et al. 2008; Bonnelye et al. 2017a, b; Hou et al. 2019), and water content (e.g., Valès et al. 2004; Zhang et al. 2012; Wild et al. 2015; Zhang and Laurich 2019).

For the storage of nuclear waste, several European countries operate underground research laboratories (URL) to investigate the coupling of the different factors that control the response of the host rock during the construction and installation of a clay repository site (Delage et al. 2010; Tsang et al. 2012). The Opalinus Clay (OPA) formation is the envisaged host rock for geological disposal of radioactive waste in Switzerland (NAGRA 2002) and is also considered for a high-level nuclear waste repository in Germany (Jobmann et al. 2017). Under in-situ conditions,

OPA has been extensively studied at the Mont Terri Underground Research Laboratory (URL) (Switzerland) where three different main lithofacies types were identified within the formation: A shaly facies, a carbonate-rich sandy facies and a sandy facies (Thury and Bossart 1999; Pearson et al. 2003; Bossart and Milnes 2017; Lauper et al. 2018). For the safety assessment of OPA as a potential repository formation, prior laboratory deformation experiments have mainly focused on the characterization of the anisotropic and hydro-mechanically coupled behavior related to the excavation processes as well as the determination of effective strength and stiffness parameters of the homogeneous, clay-rich shaly facies (e.g., Corkum and Martin 2007; Naumann et al. 2007; Popp and Salzer 2007; Amann et al. 2011, 2012; Wild et al. 2015; Zhang et al. 2017; Favero et al. 2018; Giger et al. 2018; Orellana et al. 2018b, 2019; Wild and Amann 2018; Minardi et al. 2020). However, due to its higher elastic moduli the sandy facies has recently gained importance in research (Kaufhold et al. 2013, 2016; Siegesmund et al. 2014; Minardi et al. 2016; Jaeggi et al. 2017a; Zhang and Laurich 2019). The sandy facies of OPA displays a pronounced, fabric related heterogeneity that is characterized by an alternated bedding of quartz- and clay-rich layers (Peters et al. 2011; Kaufhold et al. 2013; Houben et al. 2014).

Detailed knowledge of rock mechanical behavior and elastic properties is necessary for modelling construction-related damage of a future repository site (e.g., Salager et al. 2013; Parisio et al. 2015). The development of constitutive models predicting long-term integrity and evolution of the host rock rests on micro-mechanical analysis to unravel the physical processes governing deformation (Bock et al. 2006). So far, little is known about deformation processes and micromechanics causing anisotropic rheological behavior of experimentally deformed OPA. Nüesch (1991) studied the mechanical behavior of shaly facies OPA at a range of confining pressures, temperatures and strain rates as well as the influence of water content on deformation perpendicular and parallel to bedding. Under the applied conditions, Nüesch concluded that deformation of OPA is largely governed by cataclastic flow. Previous studies were limited to macro- and mesoscale structures, due to difficult sample preparation of OPA (e.g., Klinkenberg et al. 2009; Amann et al. 2012; Kaufhold et al. 2013, 2016). More recent studies applied ion beam preparation tools like BIB/FIB (broad and focused ion beam) for the use of scanning electron microscopy (SEM) imaging, to resolve mineral and pore fabrics of shales and clays at the micro scale (Keller et al. 2011, 2013a, b; Loucks et al. 2012; Houben et al. 2014; Laurich et al. 2014, 2017, 2018; Desbois et al. 2017, 2018; Philipp et al. 2017; Schuck et al. 2020). Desbois et al. (2018) described the microstructures of deformed shaly OPA samples from triaxial experiments conducted by Amann et al. (2012), revealing localized deformation with dilatant microcracking and cataclastic fabrics, dominated by granular flow and bending of phyllosilicates outside of the shear zone. So far, physical and mechanical properties of sandy facies OPA have not yet been characterized at similar resolution as shaly OPA.

In an effort to investigate the anisotropic mechanical behavior of sandy facies OPA, we per-

formed a series of triaxial tests at varying confining pressures, temperatures and strain rates. Cylindrical samples were deformed either dry or re-saturated, and loaded in three different orientations of the sample with respect to bedding. Electron microscopy was performed on broad ion beam polished surfaces of deformed sample material to investigate the deformation microstructures formed in each sample orientation. A damage model is proposed that combines the observations from macro to micro scale with the failure behavior at test conditions. This study aims to contribute to the general understanding of anisotropic clay deformation related to compositional heterogeneity at different boundary conditions.

2.1.1 Geological Setting and Material Description

The investigated sample material belongs to the Opalinus Clay formation, an over-consolidated clay-rich shale that was collected from the Mont Terri URL (Switzerland). OPA has been deposited in a shallow marine environment during the late Toarcian to Aalenian about 180 Ma ago (Reisdorf et al. 2014). Maximum burial depth of OPA at the Mont Terri URL was estimated to be about 1350 m in late-Tertiary with a maximum temperature of 85 °C reached during the early Cretaceous (Mazurek et al. 2006). The present overburden ranges between 230 and 330 m (Thury and Bossart 1999). The sedimentary, compaction and burial history of OPA led to a sub-parallel arrangement of clay platelets with respect to macroscopic bedding (Wenk et al. 2008). Due to this and the heterogeneity of macro- and microfabric in OPA, hydrological, microstructural, mechanical and transport-related properties exhibit transverse isotropy (e.g., NAGRA 2002; Van Loon et al. 2004; Gräsle and Plischke 2010, 2011; Keller et al. 2011, 2013b; Siegesmund et al. 2014; Keller and Holzer 2018). Porosity estimates depend on resolution of the respective method, ranging between 4.9 and 19.1vol% with best porosity estimates of 18vol% and 11.1vol% for the shaly and sandy facies, respectively. The average pore size is estimated between 2 and 20 nm equivalent pore diameter for both facies types (Thury and Bossart 1999; Minon et al. 2010; Peters et al. 2011; Keller et al. 2013a; Houben et al. 2014; Jaeggi et al. 2014; Philipp et al. 2017; Seiphoori et al. 2017). Permeability of the sandy and the shaly facies of OPA ranges between 2×10^{-21} and 1×10^{-19} m^2 (NAGRA 2002; Bossart and Thury 2008; Philipp et al. 2017; Yu et al. 2017).

Samples used in this study were prepared from the sandy facies of OPA. At the URL, the sandy facies may be further separated into four sub types (cf., Müller and Jaeggi 2012), but can be generally described as a dark-grey silty to sandy claystone (Peters et al. 2011; Hostettler et al. 2017). The mineral composition of the sandy facies is dominated by clay minerals [6 – 70 weight percent (wt%)], quartz (16 – 52wt%), carbonates (7 – 66wt%; mainly calcite, dolomite/ankerite and siderite) and feldspars (5 – 15wt%). Clay minerals are mainly illite, kaolinite and chlorite (29 – 70wt%), as well as illite-smectite mixed layers (5 – 20wt%) (Thury and Bossart 1999; Pearson et al. 2003; Peters et al. 2011; Becker 2012; Zhang and Laurich 2019). Organic matter, rutile

and apatite occur in minor amounts. The rock displays a wavy lamination of light grey layers and lenses of fine-grained quartz sand alternating with black clay-rich layers (Peters et al. 2011; Müller and Jaeggi 2012; Reisdorf et al. 2014). Some carbonate-rich lenses and bioclasts are embedded in a weak, macroscopically visible laminated matrix forming mm- to dm-scale heterogeneous layers (Kaufhold et al. 2013, 2016; Houben et al. 2014; Jaeggi et al. 2014). Compared to the shaly facies, the sandy facies of OPA is typically rather heterogeneous and displays larger mineral clasts (silt to fine-sand fraction) as well as a higher content of quartz and carbonates with generally lower amounts of clay minerals (Thury and Bossart 1999; Pearson et al. 2003; Klinkenberg et al. 2009; Minon et al. 2010; Gräsle and Plischke 2011; Kaufhold et al. 2013; Minardi et al. 2016; Bossart and Milnes 2017).

2.2 Methods

2.2.1 Sample Preparation and Characterization

The sample material was provided by Swisstopo (Federal Office for Topography, Wabern, Switzerland) and originates from borehole BFI-1 (Fig. 1.2)located in Gallery 04 (Mont Terri URL). Drilling of 101 mm diameter cores was carried out parallel to the local bedding orientation under dry conditions using compressed air as a cooling fluid. To prevent desaturation after extraction, cores were subsequently stored in plastic liners wrapped in aluminum foil, and vacuum sealed. Samples obtained in this study were taken from a 25 cm long core section drilled about 8 m into the gallery wall. We prepared cylindrical specimens of 10 mm diameter and 20 mm length with parallel end faces for triaxial tests. Several samples were first dried at 110 °C until a constant weight was reached, resulting in an average water content of 4.2±0.6wt% for fresh core material. Samples were drilled at an angle of 0°, 45° and 90° to cylinder axis and bedding direction, further referred to as p-, z- and s-samples respectively (Fig. 2.9a, e, i). To prevent cracking, the majority of tested samples were carefully dried at 50 °C at a relative humidity (RH) of about 22±5% until constant weight was reached. Further drying of sub-samples at 110 °C for >48 h revealed a residual water content of about 0.4wt% on average for 'dry' samples.

To investigate the influence of water content on the mechanical behavior, one set of p-, z- and s-samples was stored in a desiccator at room temperature exposed to a relative humidity of 95±5% for up to 5 weeks. To achieve the desired humidity, we employed a vapor equilibrium technique using a supersaturated K_2SO_4-solution (e.g., Laloui et al. 2013). Bulk density of cylindrical samples was determined from the ratio of weight and volume. For dry samples, values range between 2.34 and 2.44 g/cm^3 (average: 2.37±0.02 g/cm^3) and for saturated samples densities were 2.44 – 2.47 g/cm^3 (average: 2.45±0.04 g/cm^3). We used a He-pycnometer (Micromeritics, AccuPyc 1340) to calculate the connected porosity of dried specimens via bulk and skeletal volume, re-

sulting in porosities between 7.7 and 13.5vol% (average: 12.3±1.2vol%). Obtained values for porosity, grain and bulk density are consistent with previous data for the sandy facies of OPA (Peters et al. 2011; Yu et al. 2017; Zhang and Laurich 2019). The degree of saturation was estimated from the ratio of volumetric water content and total porosity (cf., Amann et al. 2011), yielding values of 94.6 – 97.9% (average: 96.1±1.3%) after the saturation procedure.

Four sub-samples from the drilled core section containing all samples were used to determine the bulk mineral composition by X-ray diffraction analysis (XRD) (Table 2.1). Analysis was performed using a PANalytical Empyrean X-ray diffractometer, operating at 40 kV and 40 mA with Cu-Kα radiation and a step size of 0.013°2θ from 4.6 to 85°. The mineralogy was first determined with the software EVA (version 11.0.0.3) by Bruker. Rietveld refinement for quantitative analysis was performed using the program BGMN and the graphical user interface Profex (version 3.10.2, Döbelin and Kleberg 2015). The error is expected to be in the range of 3wt%.

Table 2.1: Petrophysical properties and bulk mineralogy of the investigated sample material obtained from sub-samples of the drilled core section.

Sample ID	ρ (g/cm)	φ (vol%)	Clay (wt%)	Quartz (wt%)	Carbonates (wt%)	Feldspar (wt%)	Pyrite (wt%)
101	2.39	12.9	17	54	20	10	<1
204	2.39	11.8	16	55	20	9	<1
205	2.37	12.7	28	50	13	9	<1
2011	2.37	12.4	53	37	5	6	<1

ρ density, φ porosity

Bulk mineralogy (Table 2.1) reveals quartz (samples 101-205) or clay-rich domains (sample 2011), consistent with the mineral composition described in literature and reflecting the spatial heterogeneity of sandy facies. We further quantified the mineralogy of individual black clay-rich and light grey sand-rich layers using sub-samples retrieved from the raw material, directly extracted from the core without further treatment as well as from deformed specimens tested at different temperatures (cf., chapter 2.3.1.3). The results reveal some compositional variability between both layer types, whereas sand layers display a higher quartz (47±3wt%) and carbonate (16±6wt%) content in average and clay-rich layers a comparable increased mean clay content of 45±10wt% (Table 2.2).

Deformed samples were embedded in epoxy resin and cut perpendicular to the macroscopically visible shear plane and parallel to the σ_1-direction using a low-speed microdiamond saw (Fig. 2.1). Subsequently, surfaces of half cut samples were hand-polished. Reflected light optical scans of the deformed samples were made using a Leica DM RX microscope. For each sample we measured the angle between failure plane and loading direction (θ). Based on macroscopic

inspection, rectangular shaped subsamples ($11 \times 8 \times 3$ mm^3) were cut for further broad ion beam polishing. Resulting sections were pre-polished under dry conditions with SiC grinding paper down to P4000 grade. BIB-polished surfaces were prepared using a JEOL IB-19520CCP polisher at low pressure (4×10^{-4} Pa) conditions. Polishing time was 2 hours at 8 kV 200 μA and 6 hours at 6 kV, 150 μA, which removed a layer of approximately 100 µm thickness. The sizes of resulting BIB cross-sections were about 2.5 mm^2, prepared parallel to loading direction (Fig. 2.1). Furthermore, several BIB cross sections of undeformed material were prepared using the same procedure. Microstructural observations on carbon-coated BIB cross sections were performed with a FEI Quanta 3D Dual Beam scanning electron microscope (SEM) at 20 kV acceleration voltage and 5 mm working distance. Semi-quantitative geochemical analysis was conducted with an attached EDAX energy dispersive X-ray analyzer (EDX).

Table 2.2: Mineral composition of sand- and clay-rich layers, extracted from samples tested at different temperature conditions (cf., chapter 2.3.1.3) as well as from raw material.

Sample ID	Layer type	T (°C)	Clay (wt%)	Quartz (wt%)	Carbonates (wt%)	Feldspar (wt%)	Pyrite (wt%)
Raw	Sand layer	25	26	48	19	8	<1
OT1B	Sand layer	50	37	50	8	6	<1
OT23	Sand layer	100	28	44	22	7	<1
OT13B	Sand layer	200	29	47	16	8	<1
Raw	Clay layer	25	42	40	10	8	<1
OT1B	Clay layer	50	41	38	9	13	<1
OT23	Clay layer	100	59	27	9	5	<1
OT13B	Clay layer	200	36	41	16	7	<1

T temperature

Depending on layer composition, the size of clastic minerals increases from <30 µm in clay dominated layers up to 80 µm in sand-rich layers and lenses (Fig. 2.2a, b). Sandy domains regularly display high amounts of blocky calcite or kaolinite cement, filling the space between detrital quartz (Fig. 2.2b). However, diagenetic cementation of the clay-rich matrix is weak (cf., Corkum et al. 2007; Seiphoori et al. 2017).

At SEM resolution, visible pores are mainly located in the clay matrix (Fig. 2.2a–c). Size and orientation of single pores depends on matrix compaction and orientation of single clay particles. In clay-rich layers, individual clay platelets are densely packed within the matrix and contain interparticle pores, both of which are aligned sub-parallel to the macroscopically visible bedding orientation. In contrast, the matrix as well as the kaolinite cement barely show compaction where clasts build a grain-supported framework (Fig. 2.2b, c). Here, clay particles show a random

orientation with larger interparticle pores compared to the matrix-supported domains (Fig. 2.2c).

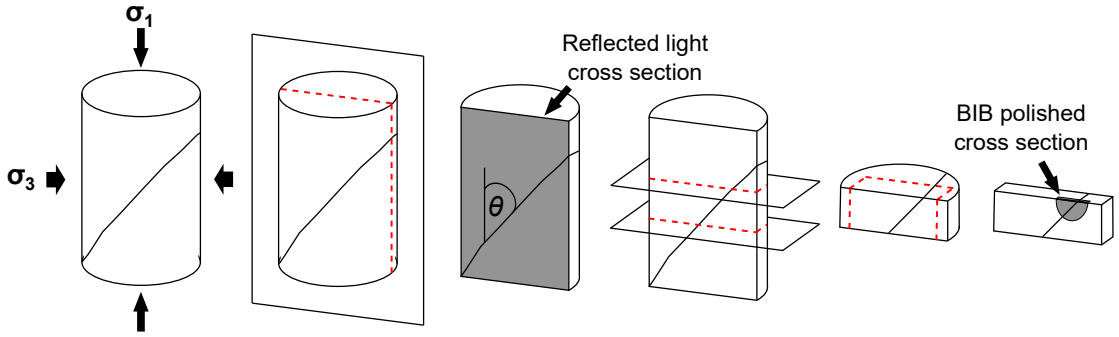

Figure 2.1: Overview of the preparation procedure (from left to right) for reflected light and BIB-SEM microstructural investigation of deformed samples. Dotted lines indicate cutting planes. θ is the angle between failure plane and loading direction. Figure is not to scale.

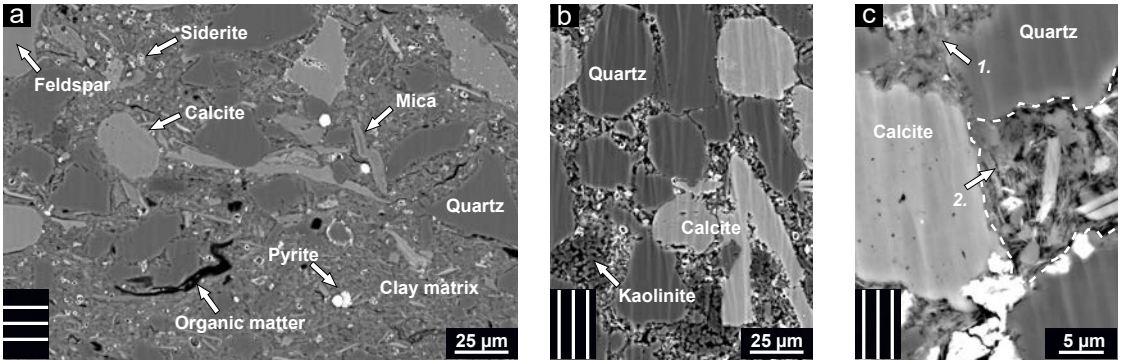

Figure 2.2: Backscattered electron images of undeformed Opalinus Clay of the sandy facies (**a**-**c**) with bedding orientation indicated in the black boxes at the bottom left of each picture. **a** Clay layer showing characteristic mineral phases surrounded by clay matrix, barely touching each other. **b** Sand layer showing quartz grains cemented by kaolinite and blocky calcite. **c** Differences in the orientation and compaction of clay particles in clay matrix (**1**) and in areas of grain supported framework (**2**).

2.2.2 Experimental Methods

Triaxial deformation experiments were performed over a wide range of temperatures (T = 25 – 200 °C) and confining pressures (p_c = 50 – 100 MPa) at constant strain rates ($\dot{\varepsilon}$) ranging from 1×10^{-3} to 5×10^{-6} s^{-1}, using a Paterson-type deformation apparatus (Paterson 1970). Specimens were contained in copper jackets with a thickness of 0.35 mm, which prevented intrusion of the confining pressure medium (argon gas). Specimens were heated at a rate of 20 °C/min using a three-zone oven installed inside the pressure vessel (Paterson,1970) after the confining pressure was applied. Axial stress was calculated from an internally recorded axial force, which was corrected for copper jacket strength, assuming constant volume deformation. Axial strain was determined from external linear-variable displacement transducer (LVDT) readings, corrected for system compliance.

Estimated uncertainties of resulting stress and strain values are <4% and <6%, respectively (cf., Rybacki et al. 2015; Herrmann et al. 2018).

Samples were tested at undrained conditions and were not pre-consolidated prior to testing. For this, impermeable aluminum oxide spacers were placed at both ends of the specimens. Furthermore, in order to estimate the influence of drainage conditions and pre-consolidation on strength of dried samples (that contain a small amount of ∼0.4wt% residual water), we used both permeable and impermeable spacers in the assembly and deformed three dried p-samples at p_c = 50 MPa, T = 100 °C and $\dot{\varepsilon} = 5 \times 10^{-4}$ s^{-1}. For drained conditions, we used permeable aluminum oxide spacers with a porosity of approximately 25vol%. Samples were consolidated at p_c = 50 MPa and T= 100 °C for ∼18 h. To check whether the applied consolidation time was sufficient, we estimated the theoretical minimum consolidation time (t_c) using the expression $t_c = 0.196 \times L^2 / c$ (Bishop and Henkel, 1962). L is sample length and c is the coefficient of isotropic consolidation. For s-samples t_c is about 11 h using an isotropic consolidation coefficient of $c \approx 0.002$ mm^{2}s^{-1}. The coefficient c was calculated following the procedure suggested by Head and Epps (2014) using the relation $c = (k \times K) / \gamma_w$, where K is the bulk modulus, k is the hydraulic conductivity and γ_w is the unit weight of water. The bulk modulus was estimated from the oedometer Young's modulus (E_{oed}) measured by Ferrari et al. (2016) in high-pressure oedometric compression tests on Opalinus Clay. Both quantities are related by $K / E_{oed} = (1 + \nu) / (3 \times (1 - \nu))$ assuming an isotropic material with linear elastic behavior. The drained Poisson's ratio is assumed to be $\nu = 0.25$ and the hydraulic conductivity $k = 1 \times 10^{-14}$ ms^{-1} (cf., Amann and Vogelhuber 2015).

The Young's modulus E was determined using the secant method. To this end, the slope of corrected axial strain-differential stress curves was determined between origin and strain at 50% peak stress. Due to the low stiffness of the Paterson apparatus, the accuracy of E estimated from calibration runs is <20% (Herrmann et al. 2018). The yield point was determined from stress-strain plots, where the differential stress graph deviates from linearity. In addition, we estimated brittleness B, which is commonly used in petroleum engineering to classify the mechanical behavior of reservoir rocks into brittle (1) and ductile (0) deformation (Holt et al. 2011). B was calculated from the ratio of elastic strain to strain at peak strength (Rybacki et al. 2016) and was used to characterize the pre-failure behavior of the tested samples. It should be mentioned that the brittleness index is an empirical parameter based on a variety of existing definitions related to rock composition, deformation behavior or elastic properties (Rybacki et al. 2016; Zhang et al. 2016). The estimated error of determined B is about 30% (cf., Rybacki et al. 2016).

2.3 Results

We performed 42 triaxial deformation experiments at varying confining pressure, temperature and strain rate. Tests were done on cylindrical samples of the sandy facies of dry OPA with three

different loading orientations (0°, 45° and 90°) with respect to bedding. In addition, we investigated the influence of water content, pre-consolidation and drainage condition on the deformation behavior at selected boundary conditions.

2.3.1 Mechanical Behavior Under Triaxial Conditions

2.3.1.1 Effect of Pre-consolidation and Drainage Condition

To examine the influence of drainage conditions on the deformation behavior, we deformed dried and saturated p-samples (0° towards bedding) at p_c = 50 MPa, T = 100°C and $\dot{\varepsilon}$ = 5 × 10^{-4} s^{-1} at both drained and undrained conditions. Independent of the applied drainage condition, dry samples exhibit almost identical deformation behavior (Fig. 2.3a, Table 2.3). In contrast, for saturated samples, strength σ_{max} and axial strain at peak strength ε_{max} are strongly reduced at drained compared undrained conditions. Also, the Young's modulus of saturated samples is slightly lower at drained compared to undrained conditions, whereas brittleness was not affected for dry and saturated samples at both applied conditions (Table 2.3).

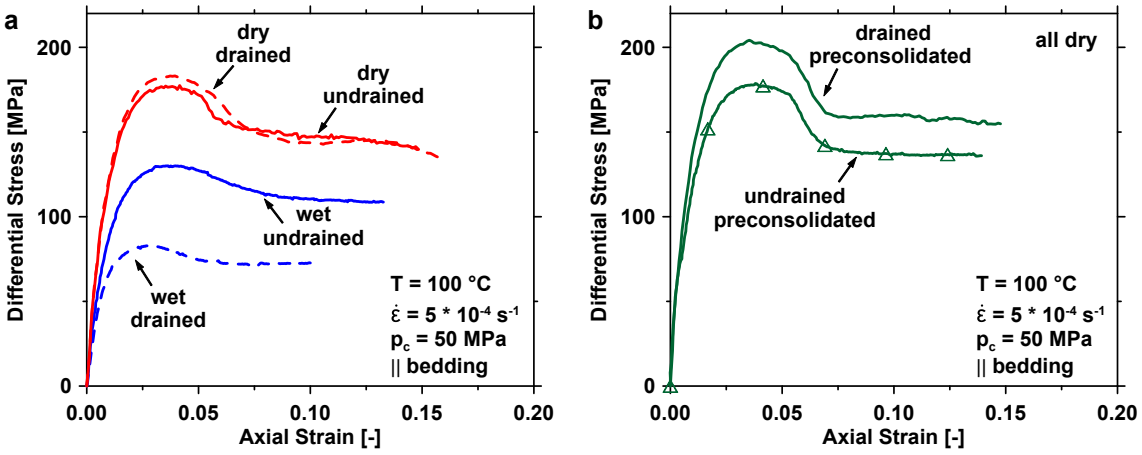

Figure 2.3: Influence of drainage condition on dry and saturated samples (**a**) as well as the effect of pre-consolidation on dried samples at different drainage conditions (**b**). Undrained and drained conditions refer to the use of low and high porous spacers. Deformation conditions and sample orientation are indicated.

To test the effect of pre-consolidation on deformation, p-samples were tested at similar deformation conditions using both permeable and impermeable spacers. No significant change of the mechanical behavior was observed if samples were pre-consolidated at undrained conditions (cp., Fig. 2.3a, b). On the other hand, the pre-consolidated sample tested at drained conditions displayed an increase of the peak strength by about 14% and about 20% of the Young's modulus (Fig. 2.3b). Again, brittleness was not affected.

Our results indicate a minor influence of drainage condition and pre-consolidation on the de-

formation behavior of dried samples. Therefore, most tests were conducted on dry samples at different pressure, temperature and strain rates at undrained conditions without pre-consolidation.

Table 2.3: Petrophysical parameters and mechanical data of samples deformed at p_c = 50 MPa, T = 100 °C, $\dot{\varepsilon} = 5 \times 10^{-4}$ s^{-1} with different saturation degree S_w as well as drainage condition and pre-consolidation.

Sample ID	Sample orientation	Sample condition	ρ (g/cm^3)	φ (vol%)	σ_{max} (MPa)	ε_{max} (%)	E (GPa)	B (-)	θ (°)
OT02	p	dry	2.36	12.1	177	3.45	15.2	0.34	33’
OT11	p	dry, drained	2.35	13.2	183	3.91	15.1	0.31	29’
OT04	p	S_w = 97.9%	2.46	13.8*	130	3.64	10.1	0.35	30’
OT21	p	S_w = 95.6%, drained	2.44	14.3*	83	2.87	9.2	0.32	33
OT06	p	dry, t_c = 17:40 h	2.36	12.4	179	3.78	13.8	0.34	28
OT12	p	dry, drained, t_c = 18:50 h	2.35	13.2	204	3.47	16.5	0.36	26’

ρ density, φ porosity, σ_{max} peak strength, ε_{max} strain at peak strength, E Young’s modulus, B brittleness, θ angle between failure plane and loading direction, ’ two failure planes, S_w% degree of saturation, t_c consolidation time. p (0°), z (45°) and s (90°) represent the sample orientation between the loading direction relative to the bedding plane. * determined from sub-samples after drying at 110°C. Drained refers to the use of high porous spacers

2.3.1.2 Effect of Confining Pressure and Bedding Orientation

To investigate the effect of pressure on the mechanical properties of OPA, we deformed dried samples in all three orientations at constant strain rate of $\dot{\varepsilon} = 5 \times 10^{-4}$ s^{-1} and temperature of T = 100 °C, applying confining pressures of p_c = 50, 75 and 100 MPa. Stress-strain curves of tested samples show that the mechanical behavior of OPA is strongly affected by confining pressure as well as sample orientation with respect to bedding (Figs. 2.4a–c, 2.5).

P-samples (Fig. 2.4a) show macroscopically brittle to semi-brittle deformation behavior with

low yield strain and extended non-linear strain hardening before peak stress (Evans and Kohlstedt 1995). Beyond failure, p-samples exhibit relatively distinct strain weakening down to a steady residual differential stress. In comparison, samples oriented at 45° (Fig. 2.4b) and perpendicular (Fig. 2.4c) to bedding showed more ductile behavior yielding at higher strain. These samples show minor post-peak weakening, in particular at elevated confining pressures ($p_c \geq$75 MPa).

In general and independent of the bedding orientation, the samples showed increasing peak strength σ_{max} (Fig. 2.4d) and axial strain at peak strength ε_{max} (Table 2.4) with increasing confining pressure. Strain at peak strength of z- and s-samples was most affected by confining pressure.

No systematic correlation was found between calculated static Young's modulus and applied confining pressure (Fig. 2.4e) for all sample orientations. In contrast, B of z- and s-samples decreased with increasing p_c (Fig. 2.4f). The brittleness index of p-samples remained almost constant with increasing confining pressure. It ranged between 0.29 and 0.34, indicating relatively ductile pre-failure deformation behavior of p-samples.

Table 2.4: Petrophysical parameters and mechanical data of samples deformed at $\dot{\varepsilon} = 5 \times 10^{-4}$ s^{-1}, T = 100 °C and different confining pressures p_c.

Sample ID	Sample orien-tation	ρ (g/cm^3)	φ (vol%)	p_c (MPa)	σ_{max} (MPa)	ε_{max} (%)	E (GPa)	B (-)	θ (°)
OT02	p	2.36	12.1	50	177	3.45	15.2	0.34	33'
OT01A	p	2.37	12.9	75	193	5.16	12.7	0.29	35
OT02A	p	2.40	10.1	100	246	5.50	14.3	0.31	30
OT05	z	2.36	13.3	50	142	4.17	7.6	0.45	47
OT03A	z	2.38	11.9	75	184	4.66	10.7	0.37	45
OT06A	z	2.36	12.8	100	185	6.13	8.6	0.35	-
OT01	s	2.37	12.3	50	167	4.65	7.4	0.49	33
OT04A	s	2.37	12.6	75	179	4.62	9.3	0.42	37
OT05A	s	2.38	12.7	100	209	7.43	8.6	0.33	-

ρ density, φ porosity, σ_{max} peak strength, ε_{max} strain at peak strength, E Young's modulus, B brittleness, θ angle between failure plane and loading direction, ' two failure planes. p (0°), z (45°) and s (90°) represent the sample orientation between the loading direction relative to the bedding plane

In Fig. 2.5 we compare the values of peak strength, Young's modulus and brittleness obtained at different confining pressures as a function of bedding orientation with respect to the loading

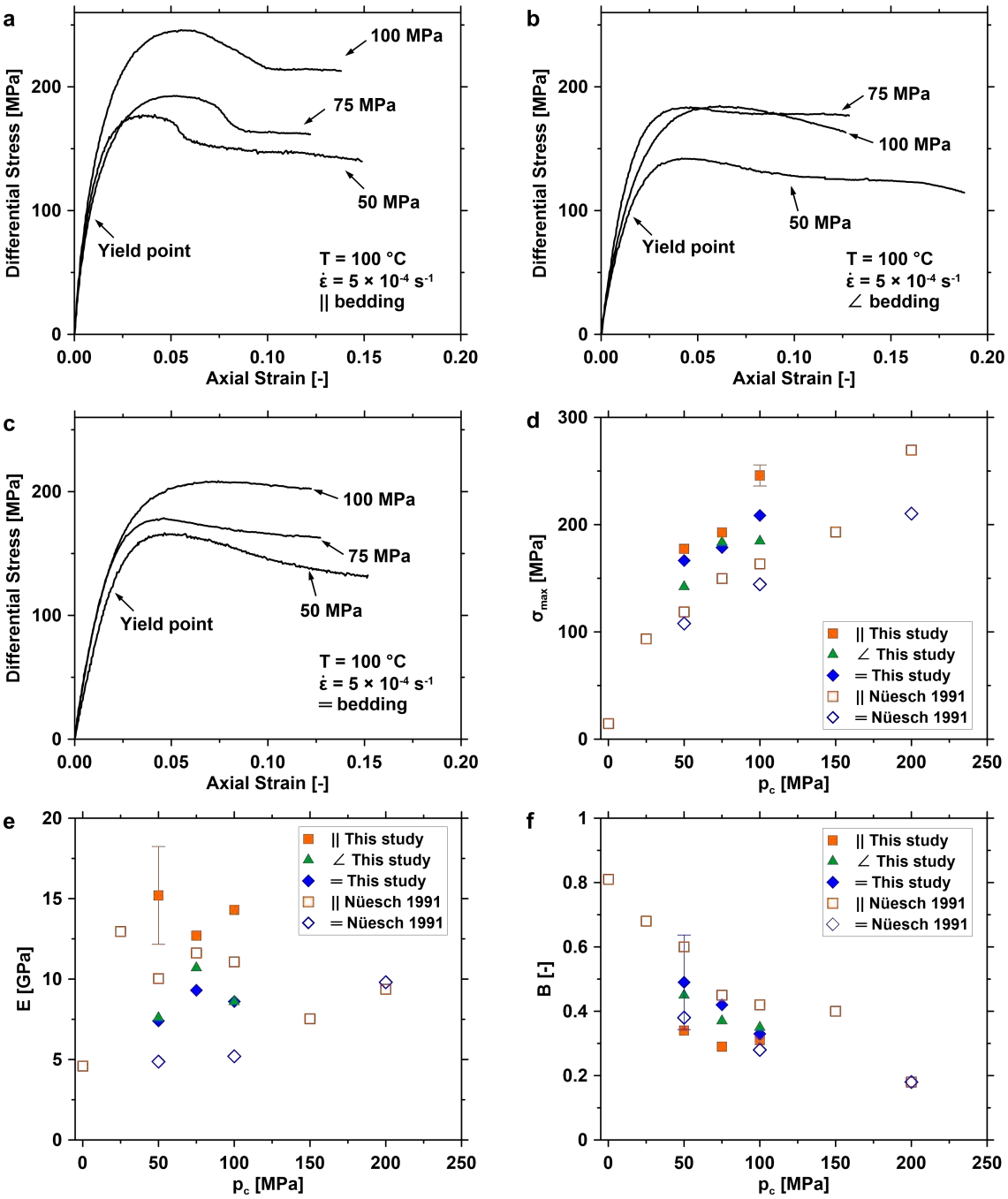

Figure 2.4: Stress-strain curves showing the influence of confining pressure p_c on deformation behavior of the sandy facies samples (this study, solid symbols) deformed parallel (**a**), 45° (**b**) and perpendicular (**c**) to bedding direction as well as the relation between confining pressure p_c and peak strength σ_{max} (**d**) Young's modulus E (**e**) and brittleness B (**f**) in comparison to the shaly facies deformed at T = 20 °C and $\dot{\varepsilon} = 10^{-4}$ s^{-1} (Nüesch 1991). Deformation conditions and sample orientation are indicated. Yield point in **a**–**c** is indicated for each sample orientation deformed at p_c = 50 MPa.

direction. For sandy facies OPA, highest peak strength is obtained in samples oriented parallel

to bedding. Minimum strength was found for samples oriented 45°, as commonly observed for transversely isotopic materials (e.g., Ibanez and Kronenberg 1993; Niandou et al. 1997; Naumann et al. 2007; Islam and Skalle 2013; Liskjak et al. 2014). However, strength anisotropy is small and ranges between $\sigma_{max\ p}$ / $\sigma_{max\ z,\ s}$ = 1.0 – 1.3. Young's modulus decreased continuously with increasing inclination of the bedding plane to loading orientation (Fig. 2.5b).

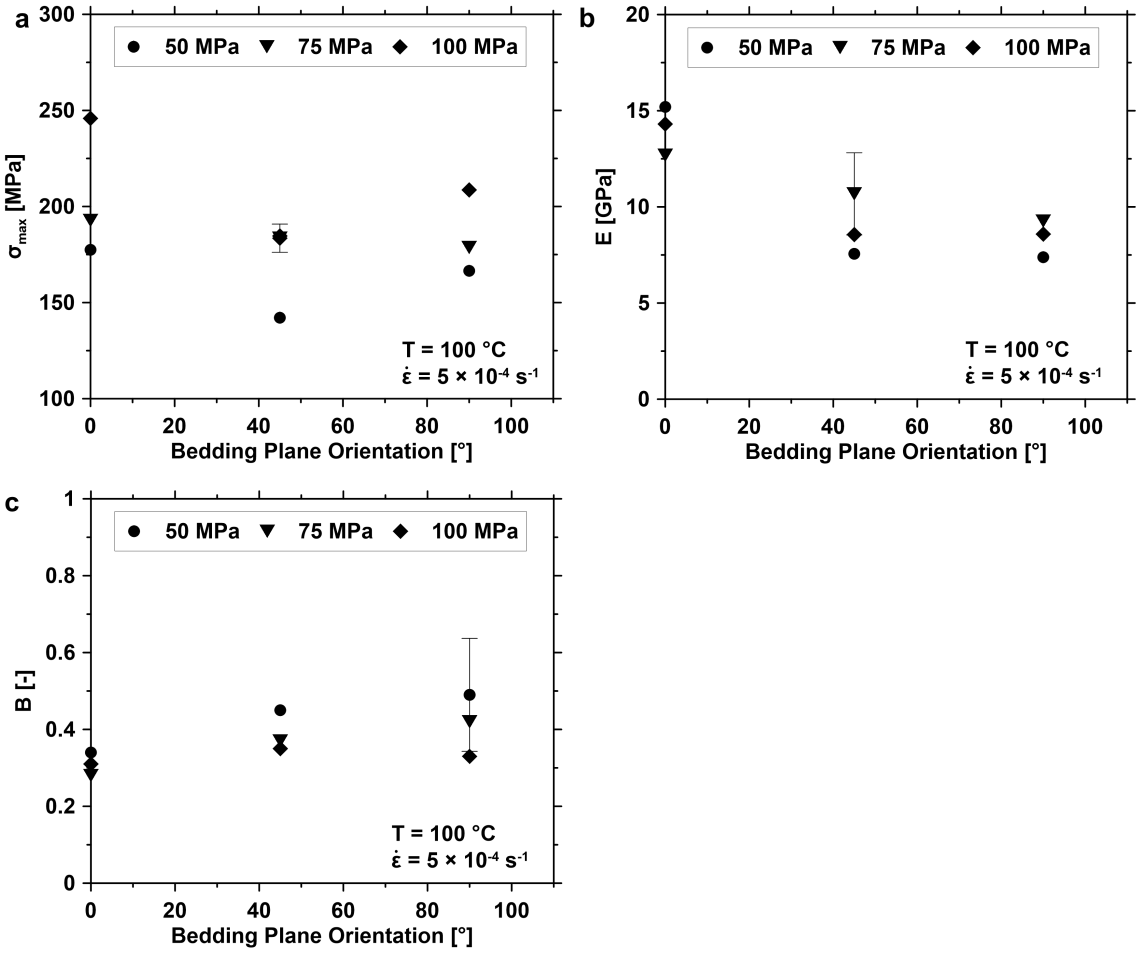

Figure 2.5: Variation of peak strength σ_{max} (**a**), Young's modulus E (**b**) and brittleness B (**c**) as a function of the orientation between bedding plane and loading direction. Deformation conditions are indicated.

The elastic anisotropy was found to be higher than the strength anisotropy (E_p / $E_{z,\ s}$ = 1.2 – 2.1). P-samples display highest Young's moduli (12.7 – 15.2 GPa), while Young's moduli of z- and s-samples are comparable and in the range of 7.4 – 10.7 GPa. Brittleness, as defined in this study, shows minor anisotropy at low confinement of 50 MPa (B_p / E_s = 0.7) and almost no influence of orientation at p_c = 100 MPa (Fig. 2.5c).

2.3.1.3 Effect of Temperature

To determine the effect of temperature (T = 25, 50, 100, 150 and 200 °C) on the mechanical properties of dried OPA samples, deformation experiments were performed at fixed confining pressure and constant strain rate conditions of p_c = 50 MPa and $\dot{\varepsilon} = 5 \times 10^{-4}$ s^{-1}, respectively. The results reveal that strength, elasticity and brittleness of the sandy facies were not significantly affected by varying temperatures up to 200 °C (Table 2.5, Fig. 2.6).

Table 2.5: Petrophysical parameters and mechanical data of samples deformed at $\dot{\varepsilon} = 5 \times 10^{-4}$ s^{-1}, p_c = 50 MPa and different temperatures T.

Sample ID	Sample orientation	ρ (g/cm^3)	φ (vol%)	T (°C)	σ_{max} (MPa)	ε_{max} (%)	E (GPa)	B (-)	θ (°)
OT08B	p	2.38	12.1	25	177	3.11	15.3	0.37	28
OT02B	p	2.37	11.1	50	175	3.63	14.4	0.34	35’
OT02	p	2.36	12.1	100	177	3.45	15.2	0.34	33’
OT07B	p	2.37	10.2	150	183	3.52	14.3	0.36	32
OT04B	p	2.44	7.7	150	215	1.95	25.3	0.44	25
OT09B	p	2.37	12.7	200	175	3.65	14.6	0.33	30’
OT11B	z	2.37	12.4	25	157	3.58	9.8	0.45	41
OT01B	z	2.36	12.7	50	155	3.91	9.5	0.42	30*
OT05	z	2.36	13.3	100	142	4.17	7.6	0.45	47
OT06B	z	2.39	11.2	150	140	3.65	9.3	0.42	32*
OT10B	z	2.37	11.8	200	152	2.98	10.8	0.47	33
OT03B	s	2.38	12.5	50	172	3.42	10.2	0.50	30
OT01	s	2.37	12.3	100	167	4.65	7.4	0.49	33
OT05B	s	2.38	13.2	150	157	4.40	8.5	0.42	41
OT12B	s	2.35	13.5	200	177	3.82	10.9	0.42	33
OT13B	s	2.39	12.3	200	173	4.02	10.2	0.42	39

ρ density, φ porosity, σ_{max} peak strength, ε_{max} strain at peak strength, E Young’s modulus, B brittleness, θ angle between failure plane and loading direction, ’ two failure planes. p (0°), z (45°) and s (90°) represent the sample orientation between the loading direction relative to the bedding plane

Stress-strain curves of all sample orientations were almost independent of temperatures and showed only minor differences (Fig. 2.6a–c), with the exception of one low porous p-sample deformed at 150 °C (OT04B), which was distinctly stronger and stiffer than the others (Fig. 2.6a). Z- and s-samples showed a slight gradual transition from brittle deformation at low temperature towards more ductile behavior with minor post-failure weakening at high T (Fig. 2.6b, c). Peak

strength of z- and s-samples displayed a small decrease with increasing temperatures up to 150 °C (Fig. 2.6d). Total strain at failure (Table 2.5), Young's moduli (Fig. 2.6e) and brittleness values (Fig. 2.6f) are independent of T.

2.3.1.4 Effect of Strain Rate

The effect of strain rate on the mechanical behavior of dried OPA was tested at strain rates between $\dot{\varepsilon} = 1 \times 10^{-3}$ and 5×10^{-6} s^{-1} at p_c = 50 MPa and T = 100 °C (Table 2.6). Stress-strain curves (Fig. 2.7a-c) showed only weak trends concerning the effect of strain rate on the deformation behavior of tested samples.

Table 2.6: Petrophysical parameters and mechanical data of samples deformed at p_c = 50 MPa, T = 100 °C and different strain rates $\dot{\varepsilon}$.

Sample ID	Sample orien-tation	ρ (g/cm^3)	φ (vol%)	$\dot{\varepsilon}$ (s^{-1})	σ_{max} (MPa)	ε_{max} (%)	E (GPa)	B (-)	θ (°)
OT13	p	2.35	13.1	1×10^{-3}	192	3.56	15.5	0.35	31'
OT02	p	2.36	12.1	5×10^{-4}	177	3.45	15.2	0.34	33'
OT16	p	2.39	10.3	1×10^{-4}	183	3.44	15.8	0.34	29
OT17	p	2.36	12.7	1×10^{-4}	165	3.58	13.4	0.34	32'
OT15	p	2.37	12.5	1×10^{-5}	165	4.03	12.8	0.32	31
OT07	p	2.34	13.4	5×10^{-6}	198	3.76	13.6	0.39	30
OT14	p	2.36	12.7	5×10^{-6}	160	3.99	11.8	0.34	31
OT19	z	2.36	12.9	1×10^{-3}	158	3.76	9.1	0.46	37
OT05	z	2.36	13.3	5×10^{-4}	142	4.17	7.6	0.45	47
OT18	z	2.36	13.0	1×10^{-4}	155	4.18	9.7	0.38	31*
OT10	z	2.36	13.2	5×10^{-6}	148	2.68	11.4	0.49	41
OT23	s	2.37	13.0	1×10^{-3}	154	4.39	8.9	0.39	43
OT01	s	2.37	12.3	5×10^{-4}	167	4.65	7.4	0.49	33
OT26	s	2.35	13.3	1×10^{-4}	176	3.95	10.9	0.41	35
OT22	s	2.41	11.2	5×10^{-6}	194	3.71	13.6	0.39	33

ρ density, φ porosity, $\dot{\varepsilon}$ strain rate, σ_{max} peak strength, ε_{max} strain at peak strength, E Young's modulus, B brittleness, θ angle between failure plane and loading direction, ' two failure planes, * z-samples with failure plane perpendicular to bedding. p (0°), z (45°) and s (90°) represent the sample orientation between the loading direction relative to the bedding plane

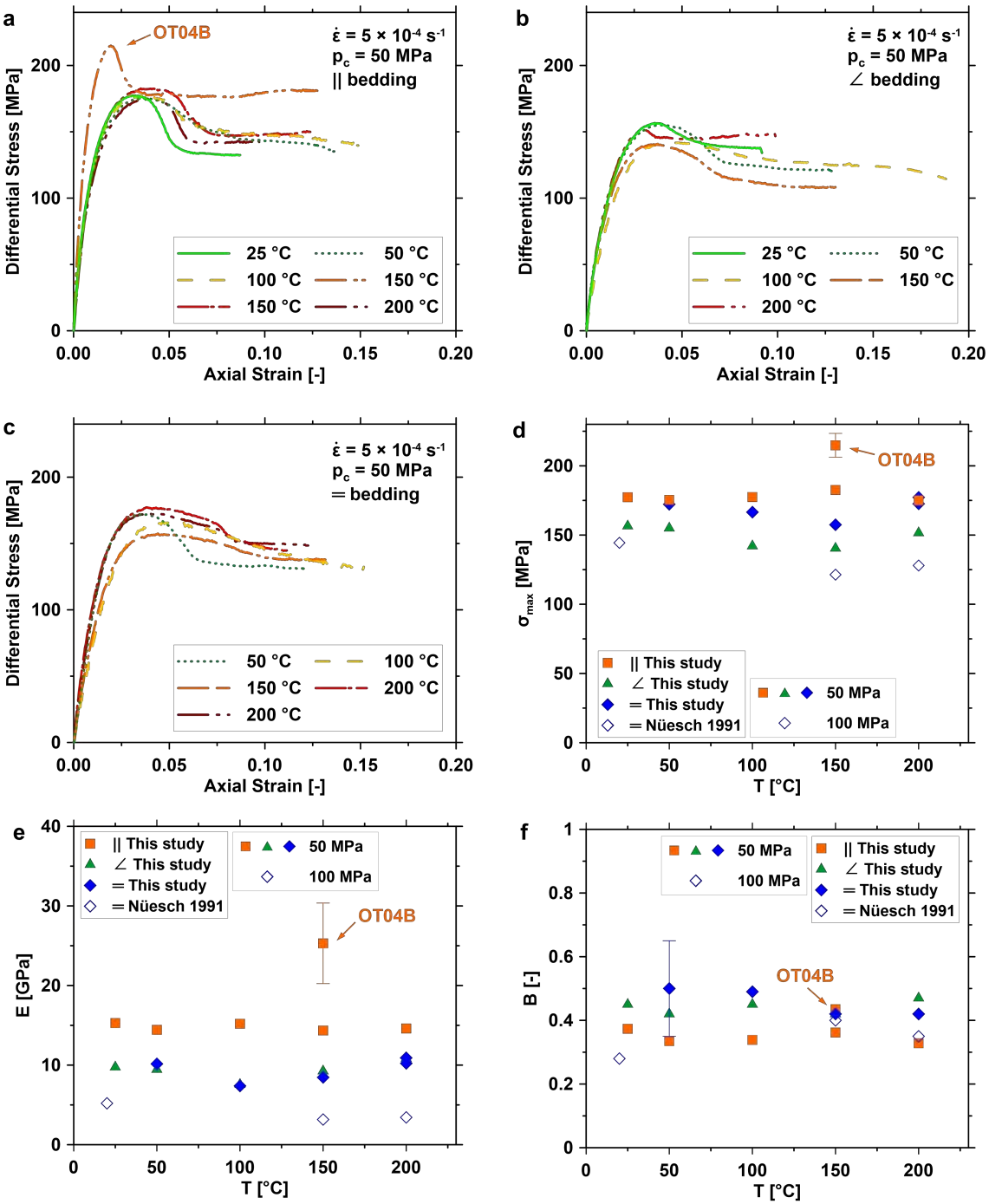

Figure 2.6: Influence of temperature T on stress-strain behavior of parallel (**a**), 45° (**b**) and perpendicular (**c**) oriented samples of the sandy facies. The relation between temperature T and peak strength σ_{max} (**d**), Young's modulus E (**e**) as well as brittleness B (**f**) of this study is compared to the results of the shaly facies, tested at p_c = 100 MPa and $\dot{\varepsilon} = 8.4 \times 10^{-5} - 8.8 \times 10^{-5}$ s^{-1} (Nüesch 1991) represented by open symbols. Deformation conditions and sample orientations are indicated.

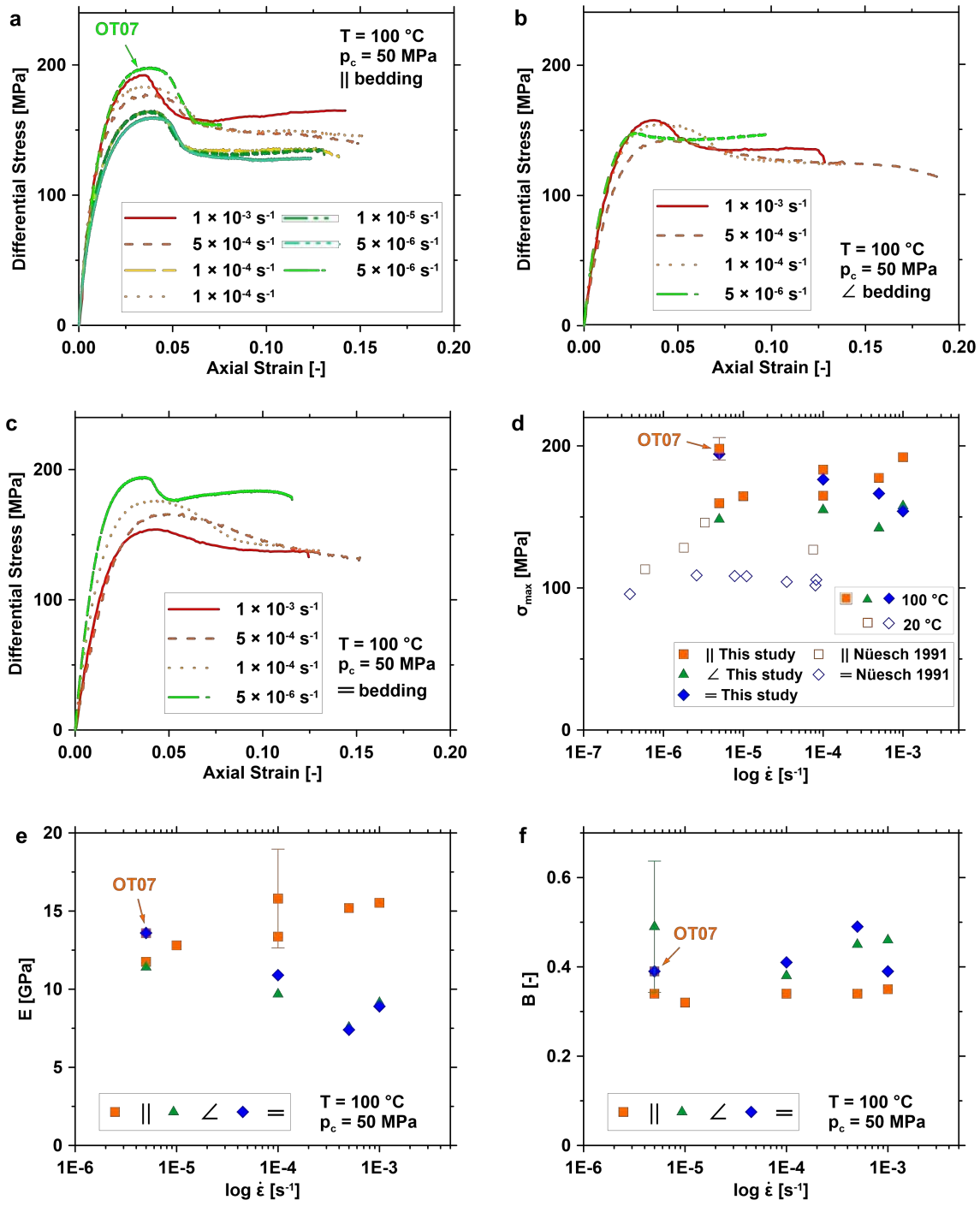

Figure 2.7: Effect of strain rate $\dot{\varepsilon}$ on the mechanical behavior of samples loaded parallel (**a**), 45° (**b**) and perpendicular (**c**) to bedding orientation. Influence of strain rate $\dot{\varepsilon}$ on the peak strength σ_{max} of the sandy facies (this study) in comparison to the results of the shaly facies (Nüesch 1991), represented by open symbols, both facies are tested at p_c = 50 MPa (**d**). Correlating strain rate$\dot{\varepsilon}$ vs. Young's modulus E (**e**) reveal opposite behavior of strength for p- and s-samples, whereas strength of z-samples shows no correlation with strain rate. A clear relation between strain rate $\dot{\varepsilon}$ and brittleness B was not found (**f**). Deformation conditions and sample orientations are indicated.

Irrespective of sample-to-sample variation, p-samples display a trend of decreasing peak strength with decreasing strain rate (Fig. 2.7d). One sample (OT07) tested at the lowest strain rate showed relatively high strength (Table 2.6). This sample was characterized by through-going sand layers. Z-samples showed no clear effect of strain rate on strength. In contrast, s-samples displayed an almost linear increase of peak strength with decreasing strain rate. In most cases, the shape of stress-strain curves, in particular post peak strain weakening, was not systematically affected by the applied strain rate. Notably, strain at peak strength and yield point of p-samples decreased slightly with increasing strain rate. For z- and s-samples, axial strain at peak and yield stress decreased with decreasing strain rate.

Young's moduli of p-samples decreased with decreasing strain rate, in contrast to s- and z-samples for which Young's modulus decreased with increasing strain rate (Fig. 2.7e). However, brittleness of all samples was not affected by applied strain rate (Fig. 2.7f).

2.3.1.5 Effect of Water Content

To investigate the influence of water content on the mechanical behavior of OPA, we deformed saturated samples (S_w = 96.1±1.3%) at p_c = 50 MPa, T = 100 °C and strain rates of $\dot{\varepsilon} = 5 \times 10^{-4}$ s^{-1} and 5×10^{-6} s^{-1} at undrained conditions (Table 2.7). Compared to dry samples, saturated samples

Table 2.7: Petrophysical parameters and mechanical data of samples deformed at p_c = 50 MPa, T = 100 °C and different strain rates $\dot{\varepsilon}$ as well as saturation degree S_w.

Sample ID	Sample orientation	S_w (%)	ρ (g/cm^3)	φ (vol%)	$\dot{\varepsilon}$ (s^{-1})	σ_{max} (MPa)	ε_{max} (%)	E (GPa)	B (-)	θ (°)
OT02	p	dry	2.36	12.1	5×10^{-4}	177	3.45	15.2	0.34	33'
OT04	p	97.9	2.46	13.8*	5×10^{-4}	130	3.64	10.1	0.35	30'
OT05	z	dry	2.36	13.3	5×10^{-4}	142	4.17	7.6	0.45	47
OT025	z	95.2	2.46	13.8*	5×10^{-4}	74	2.50	8.8	0.34	38
OT01	s	dry	2.37	12.3	5×10^{-4}	167	4.65	7.4	0.49	33
OT03	s	97.5	2.47	14.0*	5×10^{-4}	98	5.31	5.8	0.32	37
OT22	s	dry	2.41	11.2	5×10^{-6}	194	3.71	13.6	0.39	33
OT09	s	94.6	2.45	13.1*	5×10^{-6}	126	4.09	7.3	0.43	39

ρ density, φ porosity, σ_{max} peak strength, ε_{max} strain at peak strength, E Young's modulus, B brittleness, θ angle between failure plane and loading direction, ' two failure planes, S_w degree of saturation. p (0°), z (45°) and s (90°) represent the sample orientation between the loading direction relative to the bedding plane. * determined from sub-samples after drying at 110 °C

show strongly reduced strength, depending on sample orientation (Fig. 2.8). At high strain rate

($\dot{\varepsilon} = 5 \times 10^{-4}$ s^{-1}), peak strength of s- and z-samples is reduced by 41% and 48%, respectively, whereas the peak strength of parallel oriented p-samples is reduced by 27% (Table 2.7). Strain at peak strength is quite similar for dry and saturated p- and s-samples, whereas saturated z-samples show a reduction of about 40% compared to dry samples. The difference in strength between samples prepared with different bedding orientations is larger for saturated samples compared to dry specimens. S-samples were additionally deformed at a strain rate of $\dot{\varepsilon} = 5 \times 10^{-6}$ s^{-1} revealing a peak strength reduction for saturated samples of 35%. Interestingly, for both dry and saturated samples, peak strength was higher at $\dot{\varepsilon} = 5 \times 10^{-6}$ s^{-1} compared to $\dot{\varepsilon} = 5 \times 10^{-4}$ s^{-1} (Fig. 2.8c).

For p- and s-samples the Young's modulus decreased with increasing water saturation but remained constant within error bars for z-samples. In contrast, brittleness shows no clear correlation with sample saturation (Table 2.7).

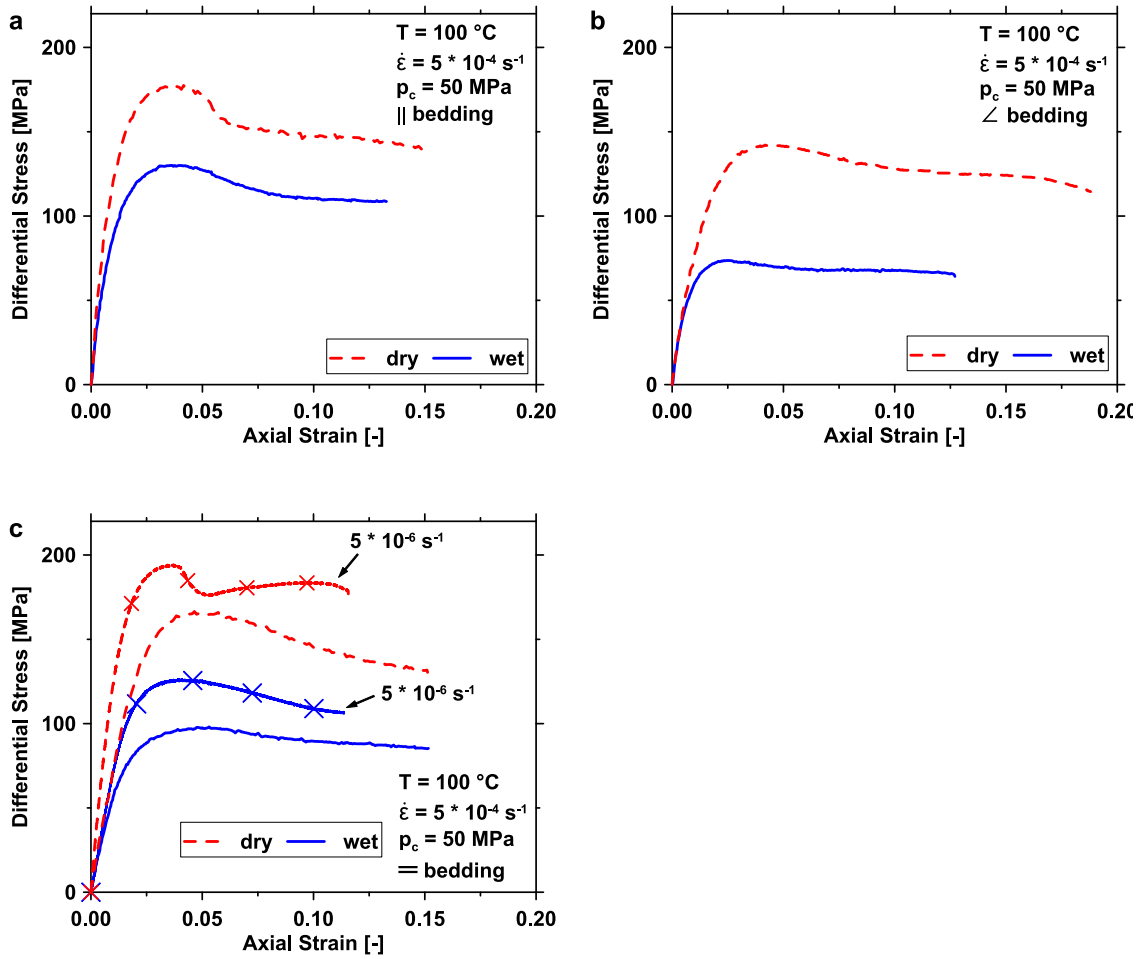

Figure 2.8: Effect of saturation on the mechanical response of parallel (**a**), 45° (**b**) and perpendicular (**c**) oriented samples at different strain rates. Deformation conditions and sample orientations are indicated.

2.3.2 Deformation Structures

2.3.2.1 Macrofabrics of Deformed Samples

Macroscopic observation of the deformed samples revealed localized, narrow (0.25 – 1 mm) shear zones and/or distributed deformation, depending on applied confining pressure conditions and loading direction with respect to bedding orientation (Figs. 2.9 and 2.10). Neither temperature nor strain rate affected strain localization, shear zone orientation and deformation regime. Shape, width and orientation of localized shear zones depend on compositional heterogeneity and anisotropy of the undeformed sample.

Cross sections prepared normal to the macroscopic shear plane show that p-samples exhibit formation of one or two shear fractures oriented 28° – 35° to the loading direction. Single shear fractures often occur in samples dominated by quartz-rich layers. These samples disintegrated along the shear plane after they were removed from the copper jacket. In some cases, shear plane orientation changes locally or is offset, reminiscent of kink bands (Figs. 2.9b, 2.10a white arrow). Some samples show kink bands leading to formation of two parallel fractures with increasing strain (Table 2.3–2.7, Figs. 2.9c, 2.10b). Within the kink-bands, clay-rich layers rotate between 50° and 80° relative to the original bedding orientation (Fig. 2.10a black arrow, Fig. 2.10b white arrow). Shear zone boundaries and discrete fractures in p-samples always develop sub-parallel to bedding direction and crosscut compositional layering. Single shear zones tend to widen, offset and branch in quartz-rich layers and are narrow in clay-rich zones (white half-arrows in Fig. 2.10a).

In z-samples, shear zones formed at 30° – 50° to the sample axis, which are predominantly localized in clay-rich layers (Fig. 2.9f–h). Shear zones formed mostly sub-parallel to bedding orientation, rarely perpendicular to bedding (Table 2.5, 2.6). For example, stress-strain curves of z-samples tested at 50 °C and 150 °C show pronounced post-peak strain weakening, associated with the formation of a macroscopic shear zone oriented perpendicular to bedding (Fig. 2.6). In general, the orientation of shear zones in z-samples changes depending on compositional layering

►**Figure 2.9:** Top row: Photographs of undeformed samples of the sandy facies Opalinus Clay prepared parallel (**a**), 45° (**e**) and perpendicular (**i**) to bedding. Below: Reflected light micrographs show deformation features of samples compressed parallel (**b–d**), 45° (**f–h**) and perpendicular (**j–l**) to bedding. At constant p_c = 50 MPa, T = 100 °C samples OT17 (1×10^{-4} s^{-1}) and OT22 (5×10^{-6} s^{-1}) were deformed at varied strain rates $\dot{\varepsilon}$. Samples OT09B (200 °C), OT11B (25 °C), OT10B (200 °C) and OT13B (200 °C) were deformed at different temperatures T but constant p_c = 50 MPa and $\dot{\varepsilon} = 5 \times 10^{-4}$ s^{-1}. OT04A and OT05A were deformed at p_c = 100 MPa, T = 100 °C and $\dot{\varepsilon} = 5 \times 10^{-4}$ s^{-1}. OT04 was saturated to S_w = 97.9% and deformed at p_c = 50 MPa, T = 100 °C and $\dot{\varepsilon} = 5 \times 10^{-4}$ s^{-1} Angular deviations along the shear surfaces are indicated by the asymmetrical plunge of black arrowheads, locating the traces of discrete and distributed (white) shear zones. The vertical crack in sample OT05A (**l**) is due to preparation. The areas marked by white frames are shown in detail in Fig. 2.10. See text for details, indicated by black and white arrows.

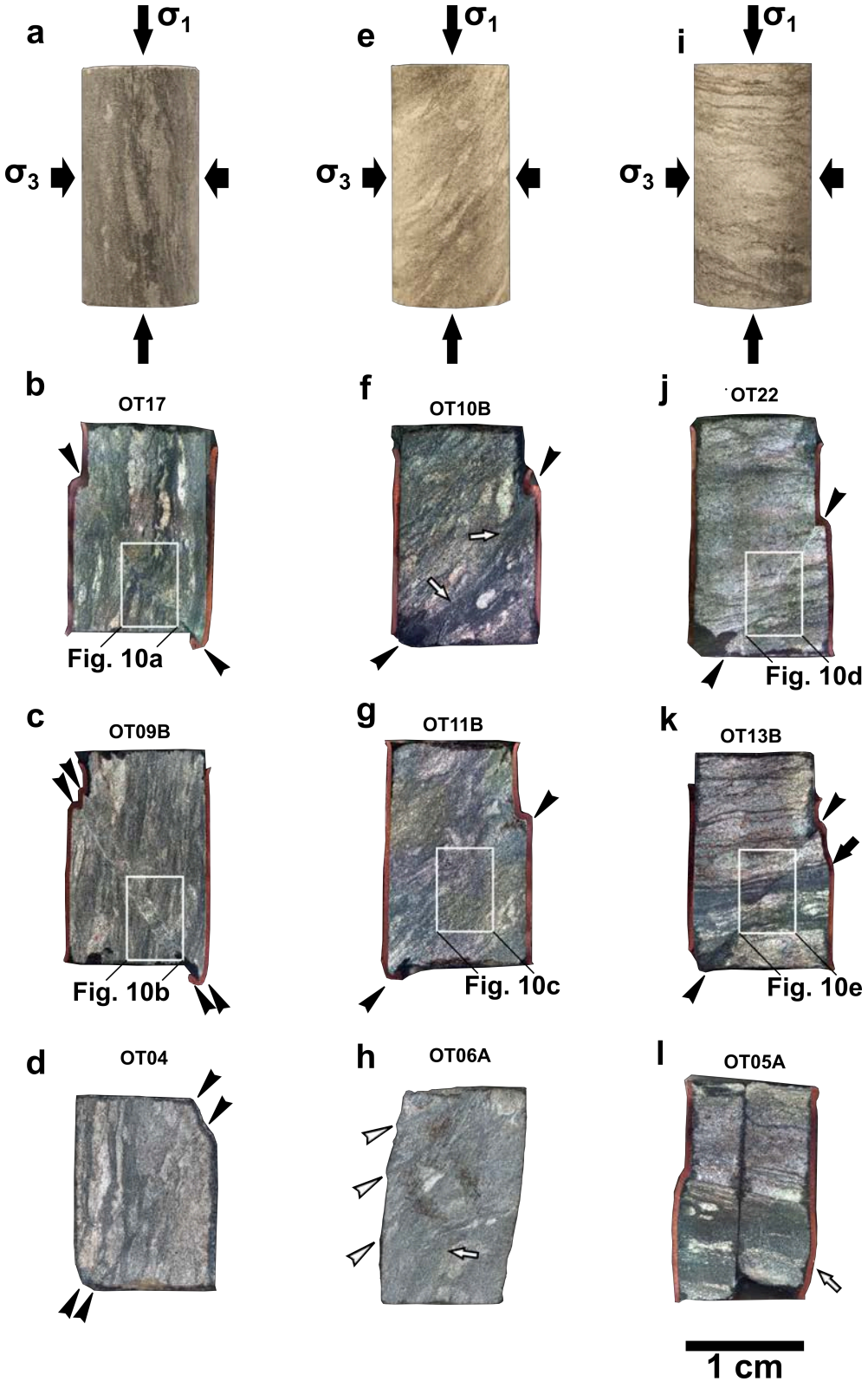
a
σ1
σ3
e
σ1
σ3
i
σ1
σ3
b
OT17
Fig. 10a
f
OT10B
j
OT22
Fig. 10d
c
OT09B
Fig. 10b
g
OT11B
Fig. 10c
k
OT13B
Fig. 10e
d
OT04
h
OT06A
l
OT05A
1 cm

(white arrows in Fig. 2.9f, h). Macroscopically, shear zones are thin (<0.75 mm) and often difficult to identify with highly localized shear displacement (Fig. 2.10c, white arrow). The width of shear zones increased at high pressure (p_c ≥75 MPa) and with increasing initial thickness of clay-rich layers in the undeformed sample. At 100 MPa confining pressure, z-samples exhibit almost homogeneous shortening with some minor shear zones (Fig. 2.9h, white arrowheads).

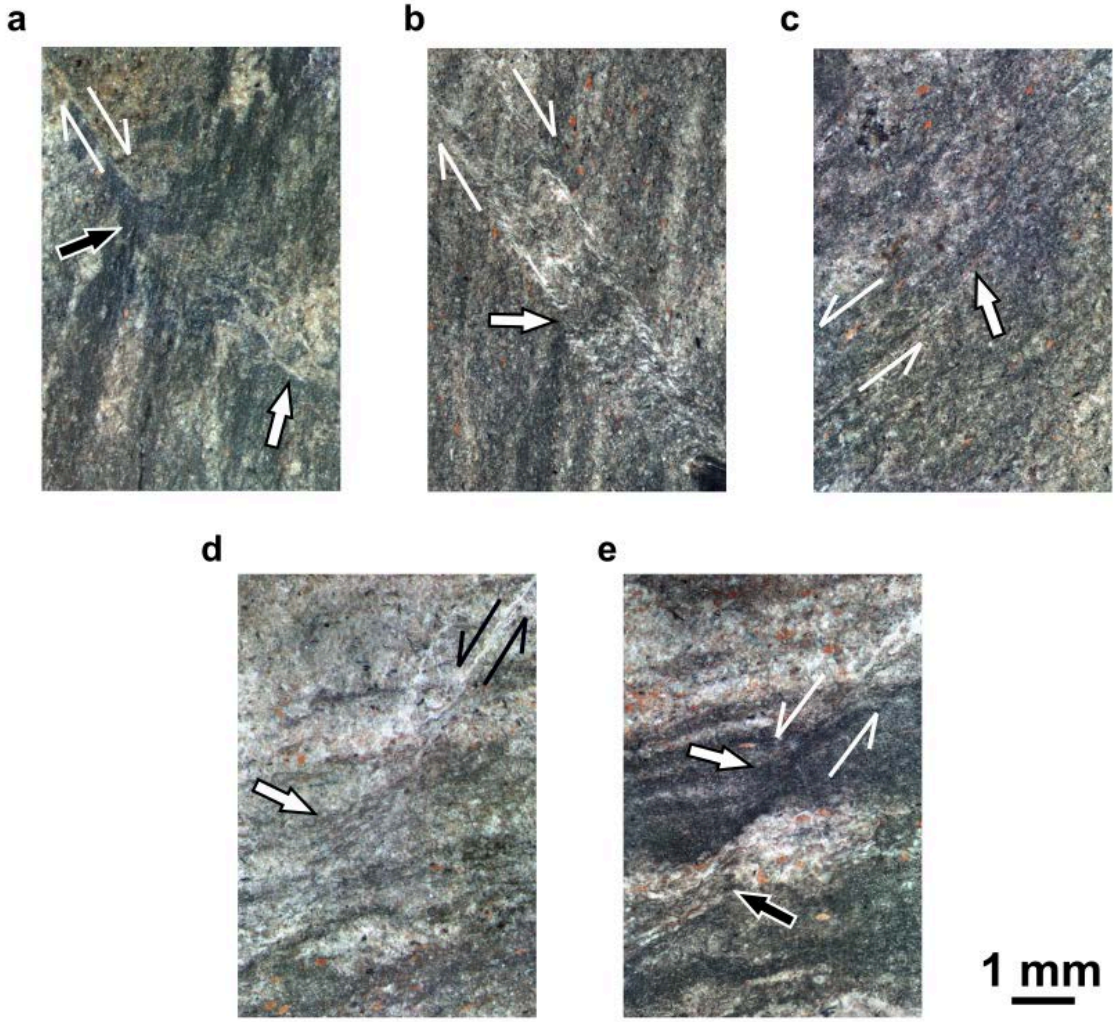

Figure 2.10: Reflected light micrographs showing details of deformation features in the sandy facies Opalinus Clay (cf. white frames in Fig. 2.9). White and black half-arrows indicate the width of the developed shear zones as well as the sense of shear. See text for details, indicated by black and white arrows.

Single shear bands that are aligned between 30° and 49° to the loading axis are developed in s-samples (Fig. 2.9j–l). The amount and spatial distribution of clay-rich layers affects strain localization and shear plane orientation. Samples that contain high amounts of large quartz-rich seams display narrow and steeply inclined (θ) shear zones (Fig. 2.9j). In contrast, shear zones are wider

in clay-rich parts (Fig. 2.10d, e white arrows). Additionally, specimens that contain individual clay-rich layers of several millimeter widths, display bulging (Fig. 2.9k, black arrow). Strain is localized in narrow shear zones showing changing inclination at compositional boundaries (Fig. 2.10e, black arrow). At a confining pressure of p_c = 100 MPa, deformation is distributed within clay-rich layers (Fig. 2.9l, white arrow).

Macroscopically, strain is localized in clay-rich layers in deformed s- and z-samples, whereas continuous quartz-rich layers remain unaffected (upper sample half in Fig. 2.9f, g and Fig. 2.9j–l).

Macroscopic deformation structures of saturated samples are similar to those of dry samples tested at similar conditions. However, saturated samples (Fig. 2.9d) display branching of shear zone networks and increasing shear zone width in s- and p-samples.

2.3.2.2 Microstructures of Deformed Samples

Deformation microstructures of selected samples containing shear zones were examined by SEM, using BIB-polished cross sections, prepared perpendicular to σ_1-direction. Two to three areas were polished per sample to image a macroscopic visible shear zone in which strain localized as well as sections several millimeters apart from the shear zone. Deformed samples show a combination of brittle (microfracturing, frictional sliding, grain rotation) and crystal plastic (bending and kinking of phyllosilicates) deformation processes at the tested experimental conditions (Fig. 2.11).

The shear zones observed in p- and s-samples are characterized by shape-preferred orientation of non-clay minerals and clay matrix. Clay minerals display a sigmoidal alignment in the sense of shear at an angle of about 40° and 60° to bedding for s- and p-samples, respectively (Fig. 2.11a, c). Shear zones may be recognized by rotation of fractured grains (Fig. 2.11c point 1) and bending of micas and clay minerals (dotted line Fig. 2.11a, c), indicating a gradual fabric transition between shear zone and wall rock (dotted line in Fig. 2.11a, c). Strain in the shear zone of p-samples is heterogeneously distributed (Fig. 2.11a). Clastic mineral grains are often fractured and aligned, showing different degrees of fragmentation ranging from single fractures and trails of comminuted quartz (Fig. 2.11a point 6 and 9) up to almost fully disintegrated calcite (Fig. 2.11a point 5) reworked within the shear zone. Within the damage zone, clastic grains are highly comminuted, with angular grain fragments and particle sizes less than 1 µm. Trails of crushed grains (e.g. former framboidal pyrite in Fig. 2.11a point 1, Fig. 2.11c point 5) formed oblique to the shear direction, indicating sigmoidal P-foliation (Rutter et al. 1986). In shear zones of s-samples we also find rotation of fractured grains (Fig. 2.11c point 2, 5 and 6) and organic matter (Fig. 2.11c point 3) aligning parallel to P-foliation as well as the development of an S-C fabric (Logan et al. 1979), as shown by the dash-dotted line in Fig. 2.11c. A network of lense-shaped clusters was found, which are separated

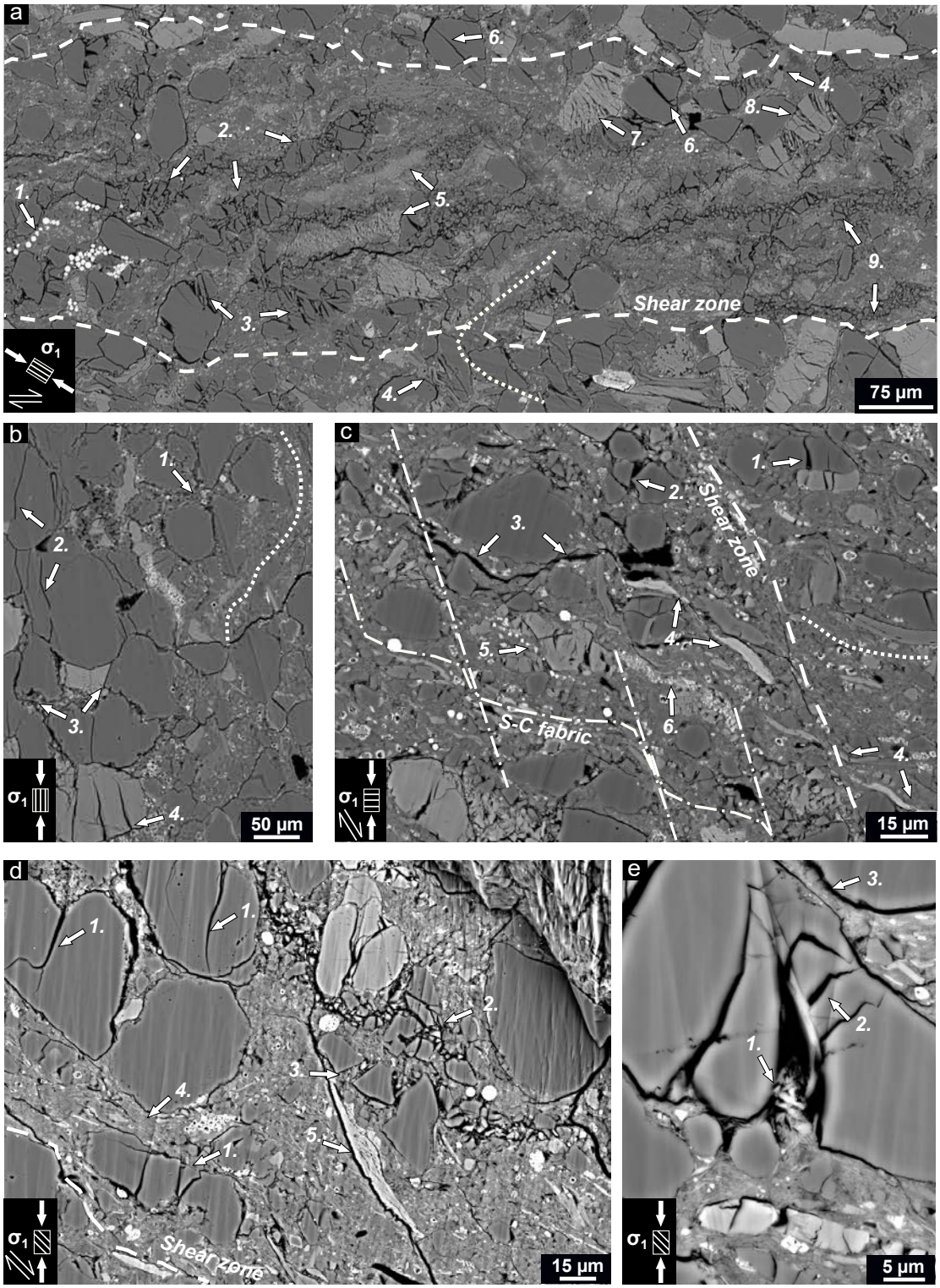
a
1.
2.
3.
4.
5.
6.
7.
8.
9.
Shear zone
σ1
75 µm
b
1.
2.
3.
4.
σ1
50 µm
c
1.
2.
3.
4.
5.
6.
Shear zone
S-C fabric
σ1
15 µm
d
1.
2.
3.
4.
5.
Shear zone
σ1
15 µm
e
1.
2.
3.
σ1
5 µm

◀**Figure 2.11:** Opalinus Clay of the sandy facies deformed at p_c = 50 MPa, $\dot{\varepsilon} = 5 \times 10^{-4}$ s^{-1} and T = 100 °C parallel (**a**–**b**), perpendicular (**c**) and 45° (**d**–**e**) to bedding direction. Shear and loading direction are indicated in the black boxes at the bottom left of each picture. Shear zone boundaries are indicated by dashed lines (**a**, **c**, **d**). Dotted lines represent shape-preferred orientation of clay particles around clastic grains outside the shear zone (**b**) or the gradual fabric transition between shear zone and wall rock (**a**, **c**). Further details labeled by numbers can be found in the text (chapter 2.3.2.2).

by anastomosing open fractures possibly due to unloading (Fig. 2.11d point 5). The clusters are of varying size, show almost no visible porosity, and display µm-thin sheared boundaries with individual nanometer-sized clay particles aligned parallel to the local shear direction, indicating clay particle sliding. Especially calcite (Fig. 2.11a point 7) and feldspar (Fig. 2.11a point 8) grains preferentially fracture along cleavages displaying mosaic fragmentation. In shear zones of s- and z-samples, grain fragments are offset indicating slip parallel to the shear direction. In samples oriented 45° to bedding, clay particles are strongly aligned parallel to the shear direction (Fig. 2.11d point 4). Clasts are rotated parallel to bedding and are surrounded by micro shear zones formed by the clay matrix that are also indicated by strong delamination and kinking of micas (Fig. 2.11d point 5). As observed macroscopically, strain localized at the boundary of sand layers and lenses in the clay matrix of s- and z-samples. Depending on the degree of comminution and reworking into the clay matrix, fractured quartz grains display increased interparticle porosity (Fig. 2.11a points 2 and 3). Domino-like boudins of fractured grains, cracks oriented sub-parallel to σ_1-direction with asymmetric apertures (Fig. 2.11d point 1), and intrusion of clay matrix into open fractures (Fig. 2.11d point 3, Fig. 2.11e point 1) indicate a process of episodic fracturing and rotation of non-clay minerals (Fig. 2.11d point 2, Fig. 11e point 2).

In sand lenses outside the shear zone, clastic minerals are frequently inter- and intragranular fractured without visible offsets and matching grain boundaries of single fragments (Fig. 2.11b point 2, 3 and 4). Impingement cracks are predominantly generated at the tip of single grains touching each other, suggesting stress concentration. Fractures are often open with apertures up to several micrometers sub-parallel to the maximum stress direction, indicating Mode I fracturing. Intergranular fractured calcite and quartz grains are highly abundant in sandy layers of samples oriented parallel to bedding (Fig. 2.11b point 3) but less prominent in s- and z-samples. The clay matrix, filling the space between grain-supported mineral clasts, shows almost no deformation (Fig. 2.11b point 1).

Isolated grains embedded in the clay matrix show a shape-preferred orientation along the bedding direction and seldom display cracks sub-parallel to the σ_1-direction. Particles of organic matter as well as framboidal pyrite are bent and elongated. Depending on their orientation relative to the loading direction, micas are locally delaminated along the (001) basal plane, and strongly bent and kinked (Fig. 2.11a point 4, Fig. 2.11c point 4). With increasing bulk strain, kinked mi-

cas become fractured or boudinaged, creating voids. Pore collapse within the matrix is indicated by highly compacted clay particles generally aligned parallel to bedding. However, clay platelets in the vicinity of mineral clasts strongly arrange around local grain boundaries by microfolding, kinking and bending (Fig. 2.11b dotted line). As observed in undeformed material, the clay matrix is heterogeneously compacted with high strain localization and the occurrence of nanometer-sized clay particles at bottlenecks between single non-clay mineral grains (Fig. 2.11e point 3).

Microstructures of water-saturated samples were similar to dry samples tested at similar conditions. However, shear zone boundaries in p- and s-samples as well as foliation within the shear zone are more pronounced at high saturation.

2.4 Discussion

The sandy facies of Opalinus Clay displays brittle to semi-brittle deformation characteristics (Evans and Kohlstedt 1995) at the applied experimental conditions of confining pressure, temperature, strain rate and water saturation. The samples were deformed by a combination of distributed brittle (microfracturing, particle sliding) and crystal plastic (bending, kinking) mechanisms. Stress-strain curves showed non-linear strain hardening until peak stress, followed by post-peak strain weakening turning into stable sliding at constant stress. Strength strongly increased with applied confining pressure. Measured strength and Young's modulus revealed minor temperature and strain rate sensitivity that is expected if crystal plastic deformation and/or stress corrosion are not the dominant deformation mechanisms. Sample strength was strongly affected by water content and the angle between loading direction and bedding plane orientation at all tested conditions, which is in good agreement with results reported for the shaly facies of Opalinus Clay (e.g., Nüesch 1991; Naumann et al. 2007; Popp and Salzer 2007; Jaeggi et al. 2014). Due to the strong heterogeneity of the sample material, the pre-existing fabric of individual samples also affected the deformation behavior. We observed increased brittle behavior and strength for extreme low porous samples (e.g., OT04B) and samples that are dominated by quartz-rich sand layers cross-cutting the entire specimen (e.g., OT07). In the following, we discuss the influence of loading conditions with respect to bedding orientation, rock composition and initial fabric conditions on the mechanical response.

2.4.1 Anisotropic Deformation Behavior

2.4.1.1 Deformation Mechanisms and Structural Development at Microscale

The distribution of clay- and quartz-rich layers in sandy facies OPA and the orientation of loading direction to bedding control the partitioning between different deformation processes accommodating sample deformation. These comprise cataclastic flow involving microcracking and particle

sliding of clastic grains, granular flow including frictional sliding of clay and non-clay particles, and crystal plasticity resulting in bent and kinked phyllosilicates presumably initiated by dislocation glide (e.g., Kronenberg et al. 1990; Ibanez and Kronenberg 1993). The micro-mechanisms control macroscopic deformation behavior and formation of shear zones. Independent of the deformation conditions and for all sample orientations, we observed brittle deformation processes like inter- and intragranular cracking, grain comminution, particle sliding and rotation at microscale, accommodating localized or distributed deformation by enhanced cataclastic or granular flow respectively (e.g., OT06A).

Young's moduli measured for samples loaded parallel to bedding are high compared to other orientations (Fig. 2.5b). This is likely due to a load-bearing framework formed by axially oriented quartz-rich layers (Sone and Zoback 2013). Various microcracks outside the shear zone (Fig. 2.11b) suggest progressive grain damage at the grain-grain contacts of the clastic minerals, leading to failure of the p-samples beyond the yield point. Brittleness values B of p-samples are low. At failure, p-samples display strong strain weakening (Fig. 2.4a), associated with cataclastic flow, rotation and comminution of clastic grain fragments and shear band formation (Fig. 2.11a).

In contrast, s-samples show lower Young's moduli compared to p-samples and minor strain hardening. This may be related to a preferred orientation of phyllosilicates, which are aligned sub-perpendicular to the loading direction. Strain accumulates in the more compliant clay matrix, resulting in lower Young's moduli than observed for p-samples. Axial propagation of microcracks is blunted at low stresses by the dense clay matrix. Finally, at elevated stresses, fracturing of quartz, calcite and feldspar grains occurs. After failure, granular flow with particle sliding of aligned clay aggregates and clastic particles controls strain weakening.

Comparable mechanisms as observed in s-samples are expected to act during the deformation of z-samples. For samples in this orientation we found the lowest peak strength (Fig. 2.5a). This may be explained by the high shear stress resolved on the basal planes (001) of phyllosilicates. These are mainly oriented at 45° to the loading direction, which enables deformation processes like delamination, basal slip and frictional sliding of phyllosilicates at lower stress than presumably needed for the fracturing of clastic grains (e.g., Kronenberg et al. 1990; Mares and Kronenberg 1993). The shear bands observed in z- and s- samples are in agreement with the observed microstructures, revealing preferred localization in clay-rich zones.

The deformation mechanisms observed in our samples are in agreement with the mechanisms observed in other laboratory studies conducted on Opalinus Clay. For the shaly facies, Nüesch (1991) concluded that strain localizes mainly by cataclastic flow accompanied by shearing and kinking of clay minerals, which is in agreement with the results obtained by Amann et al. (2012), Kaufhold et al. (2016), Desbois et al. (2018) and Orellana et al. (2018b) for the shaly and the sandy facies Opalinus Clay. This suggests that Opalinus Clay deforms by brittle cataclastic flow under ambient and elevated pressure conditions ($<$400 MPa). However, in deformed shaly facies

samples, micro-fracturing was rarely found to be intragranular and was dominant within shear zones. Matrix deformation was induced by pore compaction and granular flow. Microstructures inferred from experiments suggesting microcracking, intracrystalline plasticity of phyllosilicates and particle sliding are similar as observed in naturally deformed Opalinus Clay (Laurich et al. 2014, 2017, 2018). However, naturally generated gouge also shows evidence of pressure solution-precipitation and clay formation processes that are not captured under laboratory conditions, likely because these processes are too slow at experimental conditions (Laurich et al. 2014).

2.4.1.2 Damage Initiation, Failure and the Influence of Confining Pressure

The observed increase of strength with increasing confining pressure (Fig. 2.4d) is typical for dilatant brittle deformation. However, deformation of the sandy facies OPA is marked by non-linear strain hardening, which indicates that the initiation of damage and thus the accommodation of non-reversible strain is initiated before the peak stress is reached (e.g., Popp and Salzer 2007; Amann et al. 2012). We assume that the yield stress, determined at the onset of nonlinearity of stress-strain curves, is equal to the stress at which damage initiates (e.g., Dresen and Evans 1993). Within the range of 50 MPa $\leq p_c \leq$ 100 MPa the axial yield stress σ_y of our experiments performed on dry rocks, reveals an almost linear increase with increasing confining pressure p_c (Fig. 2.12a). We applied least square fitting to obtain the best fit slope constant n that relates σ_y and confining pressure p_c to calculate the friction coefficients at yield μ_y for each orientation with the expression $\mu_y = (n-1)/(2\sqrt{n})$ (Zoback 2007). Resulting values are between 0.16 and 0.26 (Table 2.8). Furthermore, peak strengths of the same samples were fitted to a linear Mohr-Coulomb failure criterion, expressed as $\tau = \tau_0 + \mu\sigma_n$ or $\sigma_1 = \sigma_{UCS} + np_c$, where τ is the shear stress, τ_0 is the cohesion and σ_n is the normal stress (Fig. 2.12a). Using the previously applied equation, we

Table 2.8: Comparison between friction coefficient at yield stress μ_y and coefficient of internal friction μ at peak stress with extrapolated unconfined compressive strength (σ_{UCS}). μ and σ_{UCS} were determined using a linear Mohr-Coulomb failure criterion.

Sample orientation	μ_y (-)	μ (-)	σ_{UCS} (MPa)
p	0.26±0.14	0.44±0.1	102±34
z	0.16±0.11	0.31±0.13	106±36
s	0.17±0.04	0.31±0.06	121±16

p (0°), z (45°) and s (90°) represent the sample orientation between the loading direction relative to the bedding plane

obtain the coefficient of internal friction μ at bulk failure that differs from μ_y, which is determined from the axial stress at damage initiation. Least square regression yields $\mu_p \approx 0.44\pm0.10$, $\mu_z \approx 0.31\pm0.13$, $\mu_s \approx 0.31 \pm0.06$ (Table 2.8) and friction angles ($\phi = tan^{-1}\mu$) of ϕ_p = 24°, ϕ_z = 17° and

ϕ_s = 17° for p-, z- and s-samples respectively (Fig. 2.12a). The resulting angles between shear zone and samples axis ($\theta = 45 - \phi/2$, Jaeger et al. 2007) are between 33° and 36°, and in good agreement with measured angles of 30° – 47° of sheared samples (Table 2.4).

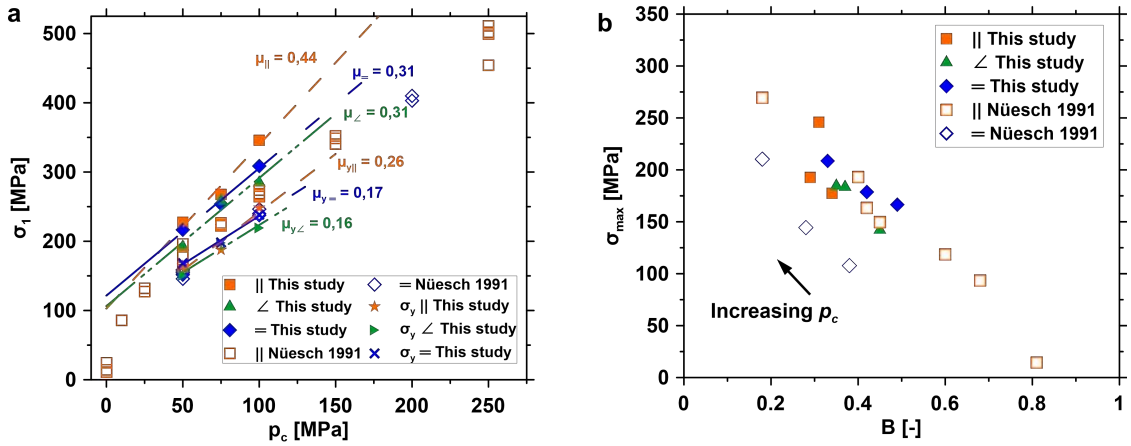

Figure 2.12: Influence of confining pressure p_c on axial peak strength and axial stress at the deviation from linearity (σ_y) (**a**) of the sandy facies of Opalinus Clay (this study) tested at T = 100 °C and $\dot{\varepsilon}$ = 5 × 10^{-4} s^{-1} (solid symbols) in comparison to the axial peak strength of the shaly facies obtained at T = 20 °C and $\dot{\varepsilon}$ = 1.3 × 10^{-7} – 8.4 × 10^{-5} s^{-1} (Nüesch 1991) represented by open symbols. Shown friction coefficients were estimated from axial peak stress (μ) and yield stress at onset of non-linearity (μ_y) of the sandy facies. (**b**) Correlation between the peak strength σ_{max} and brittleness B (**b**) of both facies determined at different confining pressures p_c (cf., **a**).

Compared to the shaly facies of Opalinus Clay, samples from the sandy facies in p- and s-orientation are significantly stronger (Fig. 2.4d, Fig. 2.12a), as they contain more quartz and other clastic minerals (e.g., Pearson et al. 2003). Nüesch (1991) performed undrained triaxial deformation experiments on the shaly facies of Opalinus clay at T = 20 °C, $\dot{\varepsilon}$ = 1.3 × 10^{-7} – 8.4 × 10^{-5} s^{-1} and p_c <400 MPa, using air-dried samples with 1.8wt% water content. He estimated internal friction coefficients of $\mu_p \approx 0.28$ (parallel) and $\mu_s \approx 0.26$ (perpendicular) to bedding that are lower than our estimates for the sandy facies. Our observation that samples taken from the sandy facies are stronger with higher elastic moduli (Figs. 2.4, 2.12) is consistent with previous studies (cf., Popp and Salzer 2007; Gräsle and Plischke 2010, 2011; Amann et al. 2011, 2012; Vöbel et al. 2014; Siegesmund et al. 2014; Wild and Amann 2018; Favero et al. 2018; Giger et al. 2018; Zhang and Laurich 2019; Minardi et al. 2020).

As for other clay rich rocks, previous and our observations indicate that strengths and elastic properties of Opalinus Clay samples depend significantly on mineralogical composition, in particular on the respective content of clay minerals, quartz, feldspar and carbonates (e.g., Lupini et al. 1981; Chiarelli et al. 2000; Ikari et al. 2007, 2009; Crawford et al. 2008; Kaufhold et al. 2013; Kohli and Zoback 2013; Rybacki et al. 2015; Fang et al. 2017; Herrmann et al. 2018). In addition, the fraction of coarse-grained mineral clasts (Nüesch 1991; Ferrari et al. 2020) and

varying burial depth and geological uplift (Ferrari et al. 2016; Favero et al. 2016; Crisci et al. 2019) were found to be important factors affecting strength. Compared to other clay-rich shales, coefficients of internal friction for Opalinus Clay are in the same range compared to published data on Posidonia shale ($\mu_s \approx 0.16 - 0.39$) and Upper Bowland Shale ($\mu_s \approx 0.39$) deformed at p_c <100 MPa (Rybacki et al. 2015; Herrmann et al. 2018), Wilcox Shale ($\mu_p \approx 0.48$, $\mu_z \approx 0.3$ and $\mu_s \approx 0.38$) at p_c <200 MPa (Ibanez and Kronenberg 1993), Tournemire Shale ($\mu_p \approx 0.23$, $\mu_z \approx 0.23$ and $\mu_s \approx 0.27$) at p_c <80 MPa (Bonnelye et al. 2017a) and Eagle Ford and Haynesville Shale ($\mu_{p,\ s} \approx 0.3 - 0.5$) deformed parallel and perpendicular to the bedding orientation at p_c <70 MPa (Sone and Zoback 2013).

Interestingly, friction values at yield (μ_y) are lower than bulk coefficients of internal friction μ (Table 2.8). The difference may be associated with different acting mechanisms (e.g., microcracking or particle sliding) related to the fabric of the sample (e.g., sample orientation, distribution of quartz- and clay-rich layers). Comparing our results to the friction coefficients of several phyllosilicates and simulated gouges made of quartz-clay mixtures (Saffer and Marone 2003; Tembe et al. 2010; Behnsen et al. 2012), we find μ_y values close to the friction coefficients of pure clay minerals or the clay-rich end-member of gouge mixtures ($\mu \approx 0.1 - 0.3$). On the other hand, the determined bulk friction μ corresponds better to friction coefficients of gouge mixtures with increased quartz content between 40 – 60wt% ($\mu \approx 0.3 - 0.6$) (Tembe et al. 2010). Furthermore, friction values at yield μ_y of the sandy facies samples are close to bulk coefficients of internal friction for shaly facies OPA ($\mu = 0.26 - 0.28$) determined by Nüesch (1991). For the deformation behavior of the sandy facies samples, this may suggest different prevailing deformation mechanisms acting at σ_y and σ_{max}. Damage initiation might be more influenced by clay minerals and granular flow, whereas bulk failure is more affected by microfracturing of clastic minerals (e.g., quartz, calcite).

Extrapolated unconfined compressive strengths (σ_{UCS}) of tested p- and s-samples (Table 2.8) are more than twice as high as reported previously (e.g., Jaeggi et al. 2014). This may be explained by the transition from dilatancy to increased sample compaction at elevated pressures, suggesting a non-linear relationship between shear strength and confining pressures as reported for shaly Opalinus Clay (e.g., Naumann et al. 2007; Amann et al. 2012; Wild and Amann 2018), Tournemire Shale (Niandou et al. 1997; Masri et al. 2014), Meuse-Haute/Marne Claystone (Hu et al. 2014) and Wilcox Shale (Ibanez and Kronenberg 1993).

Based on the definition of the used brittleness index, B values of the sandy as well as the shaly facies OPA (determined from the data obtained by Nüesch 1991) vary substantially with applied p_c. Therefore, B reveals a negative correlation with peak strength (Fig. 2.12b) illustrating the increased hardening behavior with increasing confining pressure (Fig. 2.4f). However, irrespective of the clay content, Young's moduli of Opalinus Clay show no clear correlation with increasing confining stress (Fig. 2.4e), peak strength or brittleness (Table 2.4).

2.4.2 Effect of Temperature and Strain Rate on Deformation Behavior

2.4.2.1 Temperature

Temperature variations up to T = 200 °C show little effect on the mechanical behavior of dry Opalinus Clay samples (Fig. 2.6). The peak strength of p-samples remains unaffected by temperature changes, whereas z- and s-samples reveal minor weakening with increasing temperatures up to 150 °C (Fig. 2.6d). The latter is in agreement with the temperature sensitivity of s-samples obtained from the shaly facies, as observed by Nüesch (1991) at p_c = 100 MPa (Fig. 2.6d). The weakening may be a consequence of the low residual water content (about 0.4wt%) remaining in the used dried samples. Because of the very low permeability of clay-rich rocks at undrained test conditions, increasing temperatures may lead to elevated pore pressure and, thus to a reduction of the effective mean stress (e.g., Monfared et al. 2011b; Mohajerani et al. 2012; Menaceur et al. 2016). In addition, thermally driven pressurization may facilitate interparticle motion of clay particles due to water adsorption (e.g., Ibanez and Kronenberg 1993), resulting in a reduction of the inherent cohesion and friction resistance of the material (e.g., Sammis et al. 2011; Zhang 2017). The latter effect is expected to be minor for p-samples with strong layers containing clastic minerals, which may explain the negligible influence of temperature on strength.

Interestingly, strength increases slightly for z- and s-samples at T = 200 °C. This may be caused by mobilization and removal of interlayer clay bound water, which can lead to mechanical strengthening by the reduction of interlayer spacing between individual clay particles and the collapse of nanopores. Therefore, frictional resistance between clay particles, and stiffness and strength may all increase (Moore and Lockner 2004; Reches and Lockner 2010; Sammis et al. 2011; Kubo and Katayama 2015; Zhang et al. 2017; Rassouli and Zoback 2018; Sharma et al. 2019). From X-ray diffraction-, infrared spectroscopy and thermogravimetric analyses, strengthening caused by inter- and intracrystalline clay mineral dehydration may be expected at temperatures T >150 °C (e.g., Mikhail and Guindy 1971; Bala et al. 2000; Schleicher et al. 2015; Schnetzer et al. 2016). However, X-ray diffraction patterns of samples tested at varying temperatures remain similar.

Temperature sensitivity of strength and elastic properties of samples were further related to an increased contribution of viscoplastic processes (e.g., dislocation glide in phyllosilicates) and/or thermally enhanced subcritical crack growth (stress corrosion) during deformation (e.g., Kranz et al. 1982; Atkinson 1984; Kronenberg et al. 1990; Ibanez and Kronenberg 1993; Mares and Kronenberg 1993; Heap et al. 2009a; Rybacki et al. 2015; Herrmann et al. 2018). However, since enhanced dislocation activity of clastic and clay minerals was not resolved at TEM scale, we cannot verify this by our microstructural analysis.

2.4.2.2 Strain Rate

The influence of strain rate on the peak strength, Young's modulus and brittleness of tested samples is weak and depends on orientation between loading direction and bedding (Fig. 2.7). Taking sample to sample reproducibility into account, peak strengths and Young's modulus of p-samples decrease slightly with decreasing strain rates (Table 2.6, Fig. 2.7d, e). This is in line with measurements on the shaly facies samples of Opalinus Clay from Nüesch (1991), also showing a weak reduction of peak strengths for p-samples (Fig. 2.7d). In contrast, for s-samples, strength and Young's modulus of sandy facies OPA appear to increase with decreasing strain rate, whereas strength of the shaly facies seems to be unaffected.

Macro- and microfabric analysis of deformed sandy facies samples show that semi-brittle deformation involves a combination of brittle (e.g., microfracturing, particle sliding) and crystal plastic (e.g., dislocation glide of phyllosilicates) deformation mechanisms. At low strain rates, strength of samples is expected to decrease due to the activation of rate-dependent plastic deformation mechanisms (e.g., Ibanez and Kronenberg 1993). This may indicate that potentially rate-dependent micro-mechanisms (e.g., dislocation glide and reorientation of minerals) are more important at low rates, but cracking and cataclastic flow is important at high rates (Chong et al. 1980; Chong and Boresi 1990; Bonnelye et al. 2017b). The decrease of strengths and Young's moduli with decreasing strain rate was also found for several other clay-rich rocks. Assuming dislocation glide within clay minerals, the relation between strain rate and strength was expressed by $\dot{\varepsilon} \propto \exp(\alpha \times \sigma_{max})$ (Chong et al. 1980; Chong and Boresi 1990; Ibanez and Kronenberg 1993; Kwon and Kronenberg 1994; Rybacki et al. 2015; Herrmann et al. 2018; Hou et al. 2019). For the empirical constant α, we obtain $\alpha_p = 0.53$ for the sandy facies and $\alpha_p = 0.6$ for the shaly facies measured by Nüesch (1991). These values are comparable to the results obtained by Ibanez and Kronenberg (1993) for Wilcox Shale ($\alpha_p = 0.3$, $\alpha_v = 0.5$ and $\alpha_s = 0.36$), Rybacki et al. (2015) for Posidonia (Dotternhausen and Wickensen location) Shale ($\alpha_s = 0.48$ and 0.27) as well as for Posidonia (Harderode location) and Bowland Shale ($\alpha_s = 0.16$ and 0.57) (Herrmann et al. 2018). At high strain rates energy dissipation by plastic processes is limited, but an increasing number of micro-cracks are expected to be activated (Chong and Boresi 1990; Hou et al. 2019). Cracking and dilatancy are expected to contribute to work hardening until sample failure occurs. In addition, the increase of strength at high strain rates might be explained by a strain rate-dependent fracture toughness as suggested for the deformation of shales (Bonnelye et al. 2017 a, b; Mahanta et al. 2017).

Interestingly, z- and s-samples responded differently to the variation of applied strain rate compared to p-samples (Fig. 2.7). Possibly, this may be related to compositional heterogeneity and sample to sample variation. For z- and s-samples we observed that localization and sample fracture patterns depend on the thickness of clay-rich layers. With increasing initial thickness, stress-

strain curves and macrofabric of deformed samples reveal less localized behavior and increased strain partitioning in clay-rich layers. Furthermore, time-dependent reorientation of clay particles and shear-induced compaction of clay-rich layers may also be responsible for the apparent rate-dependent strength observed for s-samples. However, strain rate dependency of the investigated samples is low and presumably overprinted by sample inhomogeneity.

2.4.3 The Effect of Water

Water saturation of samples shows a strong effect on the deformation behavior of sandy Opalinus Clay specimens. Peak strengths of saturated samples are reduced for all tested sample orientations (Figs. 2.8, 2.13). We found an inverse linear relationship between water content (wt%) and peak strength. The resulting weakening gradients due to increasing water content were -9 MPa/wt%, -15 MPa/wt% and -14 MPa/wt% H_2O for p-, z- and s-samples, respectively. For comparison, the reduction is about -19 MPa/wt% for s-samples of the shaly facies tested at T = 20 °C and p_c = 75 MPa (Nüesch 1991), which is in good agreement with our results (Fig. 2.13a). With increasing saturation, Young's modulus of p-samples decreased by about -1 GPa/wt% H_2O and by -0.3 GPa/wt% H_2O for s-samples, whereas there was no significant effect of water saturation on the Young's modulus of z-samples (Fig. 2.13b). A comparable weakening effect of increasing water saturation on peak strength was also found for Callovo-Oxfordian Clay -6 MPa/wt% (Chiarelli et al. 2000), Tournemire Shale -10 MPa/wt% (Valès et al. 2004), Wilcox Shale -45 MPa/wt% (Ibanez and Kronenberg 1993) and Alum Shale -16 MPa/wt% (Rybacki et al. 2015).

The decrease in strength and stiffness properties with increasing water content is commonly attributed to the increased thickness of adsorbed interlayer and interparticle bonded water of clay minerals (e.g., Nüesch 1991; Ibanez and Kronenberg 1993). As a result, the frictional movement of individual clay particles is facilitated due to decreasing solid-solid contacts (e.g., Sammis et al. 2011; Zhang 2017; Zhang and Laurich 2019). Furthermore, excess pore pressures may develop in saturated samples due to undrained boundary conditions at elevated pressures and temperatures as well as during differential loading, reducing the effective mean stress and frictional strength (Ibanez and Kronenberg 1993; Islam and Skalle 2013). In contrast, decreasing saturation can lead to an increase of capillary and osmotic suction inside the pores of clay aggregates, which increases the shear resistance between individual grains resulting in increased strength and elastic properties (e.g., Zhang et al. 2012; Wild et al. 2015; Minardi et al. 2016; Zhang 2017).

We observed stronger weakening for z- and s-samples due to increased water saturation compared to p-samples (Figs. 2.8, 2.13a). This may be explained by orientation-dependent excess pore pressure, possibly related to anisotropic permeability, and by the transversely isotropic elastic behavior of Opalinus Clay. The generation of excess pore pressure depends on the permeability of the deformed rock (Al-Bazali et al. 2008). Since the permeability of OPA is lower perpendic-

ular to bedding than parallel to it (e.g., NAGRA 2002; Keller et al. 2013a; Keller and Holzer 2018), pore pressure in parallel oriented samples may equilibrate faster during deformation than for the other two sample orientations. Furthermore, p- samples are stiffer and therefore generate less pore pressure from compaction compared to the more compliant z- and s-samples (e.g., Islam and Skalle 2013; Wild et al. 2015; Wild and Amann 2018). In addition, microstructures of deformed samples reveal substantial microcracking in p-samples as opposed to z- and s-samples. It is conceivable that dilatant microcracking increases the pore volume and reduces the pore pressure

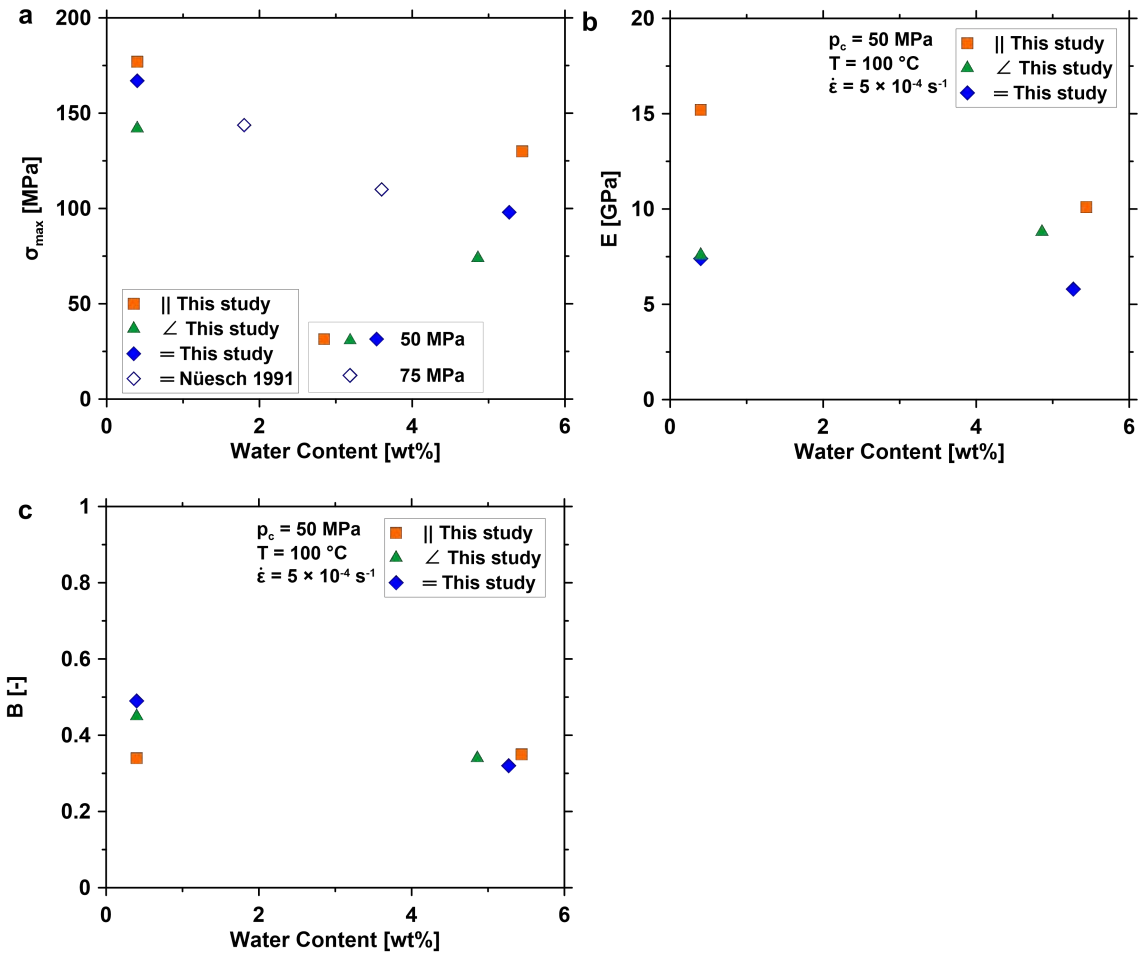

Figure 2.13: Influence of water content on the peak strength σ_{max} of the sandy facies (this study), tested at p_c = 50 MPa, T = 100 °C and $\dot{\varepsilon} = 5 \times 10^{-4}$ s^{-1} in comparison to the results of the shaly facies, tested at p_c = 75 MPa, T = 20 °C and $\dot{\varepsilon} = 3.0 \times 10^{-4}$ s^{-1} (Nüesch 1991), represented by open symbols (**a**). Correlation between water content as well as Young's modulus E (**b**) and brittleness B (**c**) of the sandy facies. Deformation conditions are indicated.

during deformation (e.g., Brace and Martin 1968; Islam and Skalle 2013; Wild and Amann 2018). The generation and dissipation of pore pressure in undrained experiments is therefore strongly controlled by dilatancy (Swan et al. 1989; Hu et al. 2014). In consequence, the generated pore

pressure in parallel samples would be lower and therefore the effective mean stress higher, which would result in higher strength.

Testing p-samples with porous spacers revealed that at drained conditions strength of the saturated sample was reduced by about 36% compared to undrained conditions, while dry samples were unaffected (Fig. 2.3a, Table 2.3). Expecting reduced mean effective stress at undrained conditions, the low strength of the saturated sample tested at drained conditions is counterintuitive. Pore pressure generation in low permeable samples highly depends on the applied strain rate and drainage condition, maybe explaining the strong effect for saturated samples (e.g., Swan et al. 1989; Al-Bazali et al. 2008; Monfared et al. 2011a; Belmokhtar et al. 2018; Minardi et al. 2020). To check if samples are drained at the applied strain rate, we estimated the time required during a drained shear experiment to dissipate 95% of the generated excess pore pressure until failure (t_f) using $t_{fd} = 1.667 \times L^2/c$ (Head and Epps 2014). This time is reduced to about $t_{fu} = 0.400 \times L^2/c$ under undrained conditions, where c is the consolidation coefficient, which can be determined from consolidation tests or from hydraulic conductivity and bulk modulus (e.g., Bishop and Henkel 1962; Ewy and Stankovich 2000). For our samples with L = 20 mm, we obtain t_{fd} = 3.3 × 10^5 s and t_{fu} = 8 × 10^4 s, which correspond to an average strain to failure of about 3.5% to critical strain rates of about 1 × 10^{-7} and 4.4 × 10^{-7} s^{-1}, respectively. This is one to the three orders of magnitude lower than the strain rates applied in this study. Hence, in our experiments most likely heterogeneous excess pore pressure was generated during deformation, which may explain the low strength obtained for the saturated sample tested with a porous spacer.

The effect of strain rate on the generation of pore pressure during differential loading of saturated samples is important. As revealed in a plethora of studies of clay-rich fault gouges, deformation transients may cause elevated local fluid pressures leading to crack formation. During fast loading of samples with low permeability, high pore pressures may build up locally and pore pressure may not equilibrate in samples, both in drained and undrained conditions. Locally varying effective pressure will affect deformation behavior in addition to confinement, porosity and permeability and rate-dependent deformation processes such as shear-enhanced compaction, dilatancy hardening, or pressure solution (e.g., Geng et al. 2018). We estimated that applied strain rates in our experiments were above the critical strain rates required for pore pressure equilibrium, so we expect that the deformation behavior of our samples probe the effect of local pore pressure transients.

The impact of strain rate on the mechanical behaviour of saturated samples was tested only for S-samples at 5 × 10^{-4} and 5 × 10^{-6} s^{-1}. The S-sample tested at a strain rate of at 5 × 10^{-6} s^{-1} displays ≈30% higher strength than the samples deformed at 5 × 10^{-4} s^{-1} (see Fig. 2.8c and section 2.3.1.5), because pore pressure in the slow test may have been better equilibrated, resulting in a lower mean pore pressure, which increases the effective pressure and thus strength.

However, it is important to note here that the estimated critical strain rate for pore pressure equi-

librium depends on several parameters and may be calculated with different approaches. As it was done above, consolidation theory can be used to predict the critical time, t_f, to maintain uniform pressure for poorly consolidated rocks during loading until failure.

Another approach to calculate the critical strain rate for the transition from undrained to (single-end) drained conditions maintaining equilibrium of pore pressure is given by the characteristic time scale of $t_c = L^2 \frac{\eta \beta_s}{k}$, where η is fluid viscosity, k is permeability, and β_s is storage capacity per unit volume, which might be approximated by $\beta_s \approx \beta\phi$ with β = compressibility of the pore fluid and ϕ = porosity (e.g., Fischer and Paterson 1989; Renner et al. 2000a). The term $k/(\eta\beta\phi)$ is the hydraulic diffusivity D. For our samples and experimental conditions $k \approx 10^{-20}$ m^2, $\phi \approx 0.13$, $\eta \approx 0.28 \times 10^{-3}$ Pas, and $\beta \approx 4.2 \times 10^{-10}$ Pa^{-1}, which yields $D \approx 6.5 \times 10^{-7}$ m^{2}s^{-1}, corresponding to $t_c \approx 6.1 \times 10^2$ s for our sample geometry. Therefore, the critical strain rate with respect to the approximate strain at failure (0.035) is of the order of $0.035/(6.1 \times 10^2 \text{ s}) = 5.7 \times 10^{-5}$ s^{-1}, which will be four times faster if both end surfaces are drained. This estimate is 2 orders of magnitude higher than that based on consolidation theory. Considering that significant volume changes associated with deformation, relevant for the hydraulic diffusivity, may occur up to a strain that is an order of magnitude lower than the failure strain (Duda and Renner 2012; Geng et al. 2018), the critical strain rate is also ten times slower ($\approx 5.7 \times 10^{-6}$ s^{-1}), which is still one order of magnitude higher than the approach based on the consolidation coefficient. The different approaches above illustrate the difficulty in correctly estimating conditions for pore pressure equilibration. We do not know which method is more reliable and all approaches rely on assumptions that we were not able to test, for example potential changes of hydraulic diffusivity or conductivity during deformation by the processes mentioned above (compaction weakening, dilatancy hardening, solution-precipitation). It should be pointed out that the estimation of a critical strain rate for pore pressure equilibrium should be regarded with caution.

2.4.4 Influence of Rock Fabric and Composition

In addition to experimental boundary conditions, heterogeneity of the macro- and microfabric of the specimens strongly affect the deformation behavior of Opalinus Clay of the sandy facies. Strength increases with increasing amount of interconnected quartz-rich layers and/or seems to increase with decreasing porosity (e.g., OT04B, OT16, OT22), whereas samples with more clay-rich layers display lower strength. Several studies show that sandy facies Opalinus Clay samples with higher quartz and carbonate (carbonate cement) content display higher stiffness and strength properties (e.g., Gräsle and Plischke 2010; Kaufhold et al. 2013), and are less sensitive to volumetric expansion due to increasing water content (Minardi et al. 2016). For shaly facies OPA, Crisci et al. (2019) found a positive correlation between clay mineral content and porosity, which both contribute to increasing compressibility. Becker (2012) observed a positive correlation be-

tween porosity and clay mineral content as well as a negative correlation between porosity and calcite content (Peters et al. 2011; Houben et al. 2014; Philipp et al. 2017). Furthermore, a combination of microcracking and plasticity was observed in laboratory deformation experiments of Callovo-Oxfordian Clay. It was shown that the material deformed more brittle with increasing calcite content and more ductile with increasing clay and/or water content (Chiarelli et al. 2000; Desbois et al. 2017). In an effort to describe the relationship between the influence of composition and rock fabric, Abou-Chakra Guéry et al. (2008) linked observed microstructural deformation mechanisms of individual compositional constituents to reproduce laboratory experiments of Callovo-Oxfordian Clay by applying a micromechanical elastoplastic damage model with a simplified three-phase medium composed of calcite and quartz distributed in a clay matrix.

In a simplified way, the combined influence of composition and bedding orientation on the mechanical behavior may be described by effective medium theories (e.g., Mavko et al. 2009). As commonly assumed for shales (e.g., Sone and Zoback 2013; Rybacki et al. 2015; Herrmann et al. 2018), we separate the composition of OPA into weak (clay minerals, total organic carbon and porosity) and strong (quartz, feldspar, carbonates, feldspar and pyrite) components and respective compositional end-members. For elastic properties, we used the strong (E_{strong} = 91 GPa) and weak (E_{weak} = 3 GPa) end-member Young's moduli determined by Herrmann et al. (2018). For the lower limit of the compressive strength, we used the strength of Boom Clay that is extrapolated to p_c = 50 MPa, resulting in $\sigma_{max\text{-}weak}$ = 35.5 MPa (Bouazza et al. 1996) and the peak strength of Novaculite $\sigma_{max\text{-}strong}$ = 699 MPa (Rybacki et al. 2015) for the respective strong end-member. Using the calculated strength and elastic end-member values, we plotted the Voigt (iso-strain), Reuss (iso-stress) and Voigt-Reuss-Hill (mean value of Voigt and Reuss bound) average against the volumetric content of weak components (Fig. 2.14a, b). For the sandy facies of OPA, we used the average composition of our mineralogical analysis (Table 2.1) and the average peak strength and Young's modulus determined at different strain rates and temperatures, which only show a minor effect on deformation behavior. For comparison, we included data of the shaly facies determined by Nüesch (1991) at similar confining pressure and strain rate conditions but at temperatures of T = 20 °C. Furthermore, experimental data of Upper Bowland (BOW), Alum (ALM) and Posidona (POS) Shale, measured by Rybacki et al. (2015) and Herrmann et al. (2018) at p_c = 50 MPa, $\dot{\varepsilon}$ = 5×10^{-6} s^{-1} and T = 100 °C were included for comparison. To further extend the range of material composition, mechanical data from the American, organic-rich gas shales Barnett (BAR), Haynesville (HAY) and Eagle Ford (EGF) obtained by Sone and Zoback (2013) were included. Strength and Young's modulus of these rocks were measured at $p_c \approx 10 - 60$ MPa, $\dot{\varepsilon} = 10^{-5}$ s^{-1} at room temperature after conducting several creep steps at different confining and differential pressures. We used the coefficients of internal friction determined by Sone and Zoback (2013) ($\mu_{p,\,s} \approx 0.3 - 0.8$) to extrapolate strength values to pressure conditions of p_c = 50 MPa. Due to the low strength anisotropy of the tested shales, p- and s-samples were treated equally by Sone and Zoback

(2013), resulting in one extrapolated strength value for both orientations. Used values of Young's modulus represent an average over the range of the applied experimental conditions.

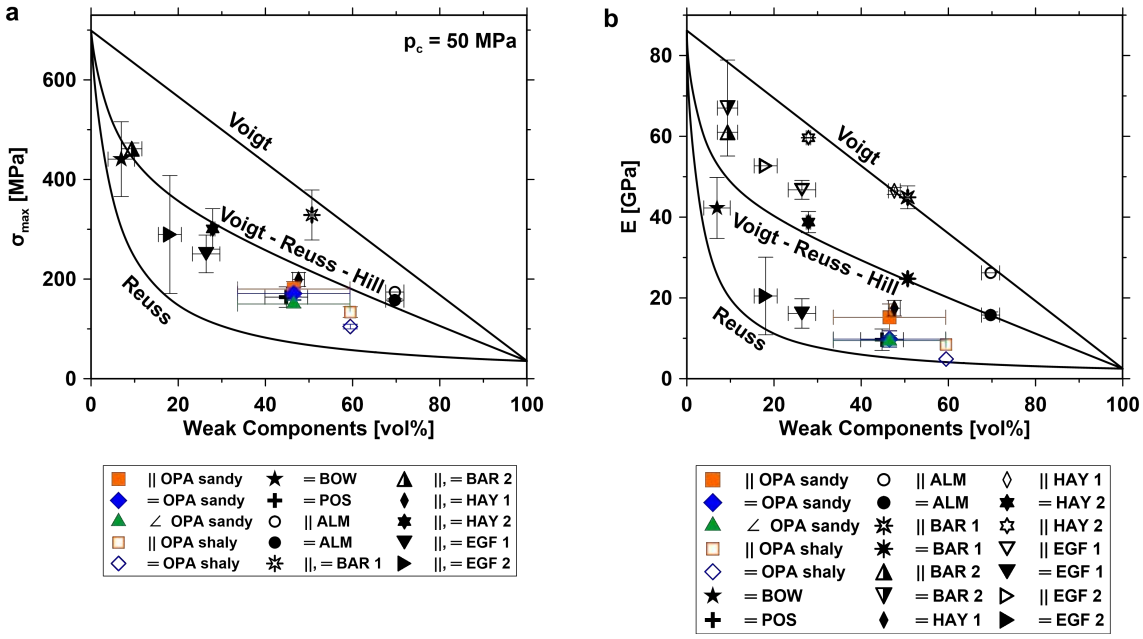

Figure 2.14: Peak strength σ_{max} (**a**) and Young's modulus E (**b**) of the sandy facies, obtained at p_c = 50 MPa, strain rates of $\dot{\varepsilon} = 1 \times 10^{-3} - 5 \times 10^{-6}$ s^{-1} and temperatures of T = 25 – 200 °C, as well as of the shaly facies measured by Nüesch (1991), tested at p_c = 50 MPa, T = 20 °C and $\dot{\varepsilon} = 8.4 \times 10^{-5} - 8.8 \times 10^{-5}$ s^{-1}, as a function of the volumetric fraction of weak components (clay minerals, total organic carbon and porosity). Experimental data are compared to mechanical results of black shales (BOW, POS, ALM) measured by Rybacki et al. (2015) and Herrmann et al. (2018) deformed at p_c = 50 MPa, $\dot{\varepsilon} = 5 \times 10^{-4}$ s^{-1} and T = 100 °C. Furthermore, mechanical data of American gas shales from Sone and Zoback (2013) are shown (BAR, HAY, EGF). Note here that the compressive strength for the latter shales was extrapolated to p_c = 50 MPa and the influence of confining pressure on Young's Modulus was neglected.

Young's moduli and peak strengths of OPA from both facies plot between the Voigt-Reuss-Hill and Reuss bounds (Fig. 2.14). Elastic properties of z- and s-samples, plot closer to the lower Reuss bound, suggesting stresses are similar between individual composite phases. This is in agreement with the common assumption that elastic deformation of z- and s-samples is governed by strain accumulation in compliant layers of weak phases. In contrast, p-samples show iso-strain of weak and rigid layers. The elastic anisotropy of OPA is low compared to the calculated bounds. The mechanical properties of the sandy facies samples show a small influence of compositional variations relative to the bounds. This is consistent with previous results showing increasing strength and Young's moduli with increasing content of strong phases once exceeding a threshold of about 70vol% (Crawford et al. 2008; Kohli and Zoback 2013; Bourg 2015; Herrmann et al. 2018). The increase may be explained by a compositional rock fabric transition in which deformation of interconnected weak phases changes to a structure in which deformation is supported by a load-bearing

framework of strong phase minerals such as quartz or feldspar. However, determined composition of the tested the sandy facies samples is still above the proposed threshold of 30vol% of weak phases.

Compared to samples from the shaly facies, the observed anisotropies of strength and elastic moduli are lower for samples of the sandy facies tested in our study. This might be associated with the higher quartz content of the sandy facies inhibiting the alignment of phyllosilicates during diagenesis (e.g., Wenk et al. 2008; Klinkenberg et al. 2009; Kaufhold et al. 2013; Siegesmund et al. 2014). Interestingly, compressive strength of p- and s-samples of OPA and deeply buried (>1.5 km) shales plot close to the Voigt-Reuss-Hill bound (Fig. 2.14a). On the other hand, these shales display a higher elastic anisotropy in comparison to Opalinus Clay with Young's moduli of p-samples closer to the upper Voigt (iso-strain) bound (Fig. 2.14b). For p- and s-samples this suggests that apart from the amount of weak components the rock fabric as well as the degree of diagenesis, cementation and consolidation have a stronger influence on the elastic anisotropy, failure mode and deformation behavior of shales in comparison to compressive strength anisotropy (e.g., Gutierrez et al. 1996; Bjørlykke and Høek 1997; Corkum and Martin 2007; Nygård et al. 2004; Loucks et al. 2012; Sone and Zoback 2013; Desbois et al. 2018; Crisci et al. 2019).

2.5 Conclusions

Triaxial deformation experiments were performed on the sandy facies of Opalinus Clay in order to investigate its anisotropic mechanical behavior as a function of the applied confining pressure, temperature, strain rate and water content as well as the response to varying drainage condition and pre-consolidation. Within the range of tested conditions, the sandy facies displays brittle to semi-brittle deformation behavior. The compressive strength as well as the Young's modulus and brittleness depend on the loading direction with respect to the bedding orientation. The highest strength values and Young's moduli are measured for parallel oriented samples.

The applied confining pressure as well as the degree of water saturation were found to have the most important effect on the deformation behavior. Both, the peak strength and Young's modulus decrease with increasing degree of saturation, whereas only the peak strength increases with increasing confining pressure. On the other hand, effects of pre-consolidation, drainage condition, temperature and strain rate are minor for samples with a reduced water content of about 0.4wt%. Apart from the influence of the applied deformation conditions on the mechanical behavior, the strong heterogeneity of the sandy facies characterized by alternating bedding of clay-rich and quartz-rich sandy layers also influences deformation. Samples with an increased amount of sand layers display higher peak strength and Young's modulus.

The deformation behavior of samples that are deformed parallel to the bedding plane is characterized by a distinct pre-failure strain hardening with an increased contribution of micro cracking.

Samples deformed at an angle of 45° and 90° to the bedding plane display minor hardening. Microstructures of deformed samples reveal evidence that the sandy facies fails by dominantly brittle mechanisms involving cataclastic and granular flow (microfractruring, frictional particle sliding) at the tested conditions. However, with increasing shear strain, grain size reduction and matrix intrusion in fractured grains, are leading to shear compaction and resealing of the damaged zone. Friction coefficients determined at yield stress are lower compared to internal coefficients of friction obtained at peak strength.

In comparison to the shaly facies, the sandy facies of Opalinus Clay displays higher strength and Young's modulus but lower anisotropy likely caused by the increased amount of strong phase minerals (e.g., quartz, carbonates). This observation is also in agreement with applied effective medium theories. For 45° and 90° oriented samples, determined peak strength and Young's modulus of both facies plot close to the iso-strain Reuss bound. Despite the lower amount of weak mineral phases, this suggests that the deformation behavior of the sandy facies is mainly influenced by the compliant phyllosilicate rich matrix in both sample orientations.

Acknowledgments

The authors acknowledge the financial support for the iCross project by the Federal Ministry of Education and Research (Project Number 02NUK053D), the Helmholtz Association (Project Number SO-093) and the GFZ German Research Centre for Geosciences Potsdam. Furthermore, Michael Naumann is highly appreciated for the support of triaxial deformation experiments. We thank Stefan Gehrmann for sample preparation as well as Vladimir Roddatis, Anja Schreiber and Ilona Schäpan for assistance at the SEM. Furthermore, we thank two anonymous reviewers, who helped to improve the manuscript with their constructive comments.

3 Strain Partitioning and Frictional Behavior of Opalinus Clay During Fault Reactivation

Summary

The Opalinus Clay (OPA) formation is considered a suitable host rock candidate for nuclear waste storage. However, the sealing integrity and long-term safety of OPA are potentially compromised by pre-existing natural or artificially induced faults. Therefore, characterizing the mechanical behavior and microscale deformation mechanisms of faults and the surrounding rock is relevant for predicting repository damage evolution. In this study, we performed triaxial tests using saw-cut samples of the shaly and sandy facies of OPA to investigate the influence of pressure and mineral composition on the deformation behavior during fault reactivation. Dried samples were hydrostatically pre-compacted at 50 MPa and then deformed at constant strain rate, drained conditions and confining pressures (p_c) of 5–35 MPa. Mechanical data from triaxial tests was complemented by local strain measurements to determine the relative contribution of bulk deformation and fault slip, as well as by acoustic emission (AE) monitoring, and elastic P-wave velocity measurements using ultrasonic transmissions. With increasing p_c, we observe a transition from brittle deformation behavior with highly localized fault slip to semi-brittle behavior characterized by non-linear strain hardening with increasing delocalization of deformation. We find that brittle localization behavior is limited by p_c at which fault strength exceeds matrix yield strength. AEs were only detected in tests performed on sandy facies samples, and activity decreased with increasing p_c. Microstructural analysis of deformed samples revealed a positive correlation between increasing p_c and gouge layer thickness. This goes along with a change from brittle fragmentation and frictional sliding to the development of shear zones with a higher contribution of cataclastic and granular flow. Friction coefficient at fault reactivation is only slightly higher for the sandy ($\mu \approx 0.48$) compared to the shaly facies ($\mu \approx 0.4$). Slide-hold-slide tests performed after ≈ 6 mm axial shortening suggest stable creeping and long-term weakness of faults at the applied conditions. Our results demonstrate that the mode of fault reactivation highly depends on the present stress field and burial history.

List of Symbols

μ	Amonton's friction coefficient	L	Sample length
θ	Angle between saw-cut plane and samples axis	S_q	Root mean square (RMS) roughness
ρ	Bulk density	φ	Porosity
p_c	Confining pressure	D_{tot}	Total axial shortening of the specimen
D_{LVDT}	Piston (LVDT) displacement	ε_{tot}	Total axial strain
ε_{ax}	Axial matrix strain	s_f	Slip along the saw-cut plane
ε_{vol}	Volumetric matrix strain	σ_1	Maximum principal stress
τ	Shear stress	σ_n	Normal stress
t_h	Hold period	$\Delta\mu_c$	Creep relaxation
$\Delta\mu_h$	Frictional strengthening	$\Delta\mu_w$	Frictional weakening
d_w	Slip weakening distance	σ_y	Yield stress bulk matrix
σ_f	Stress at onset of fault slip	ε_{rad}	Radial matrix strain
v_{sf}	Slip rate along the saw-cut plane	ε_{tf}	Transformed fault-parallel strain
σ_d^H	Differential stress at the start of Slide-Hold-Slide tests	β_c	Creep relaxation rate
β_h	Frictional healing rate	p	Mean effective pressure
ν	Specific volume	μ_f	Friction coefficient at onset of fault slip
k_m	Compliance of the testing machine	$\dot{\varepsilon}_s$	Specimen relaxation strain rate
σ_{ci}	Uniaxial compressive strength (UCS)	φ	Friction angle
c	Cohesion	m_i	Material-specific constant
σ_{matrix}	Matrix failure/flow strength	k_s	Specimen compliance
l_m	Conversion factor	$\dot{\varepsilon}_{creep}$	Creep strain rate
n	Power-law stress exponent	β	Exponential law stress gradient
$\frac{d\sigma}{dt}$	Stress rate	σ_d	Differential stress

3.1 Introduction

Characterized by a low hydraulic permeability (10^{-19} – 10^{-21} m^2), high self-sealing potential as well as sorption and retention capacity, the Opalinus Clay (OPA) formation has been selected as a suitable host rock for deep geological storage of nuclear waste in Switzerland (NAGRA 2002; Bossart and Milnes 2017). At any future repository site, the host rock is required to maintain integrity as a geological barrier over long time scales. However, the presence of pre-existing natural fractures and faults will alter the mechanical and hydraulic properties of the formation, thereby compromising its sealing capacity (Tsang et al. 2012). During the construction and lifetime of a repository, structural discontinuities can destabilize by changes in the effective stress field and may potentially trigger seismic hazard and damage to underground facilities. In the context of deep geological storage of nuclear waste, changes in the stress field may be induced by construction measures (e.g., tunneling activity) that can lead to the failure of the intact rock and/or to reactivation of bedding planes and faults (Lisjak et al. 2015; Amann et al. 2018; Rinaldi and Urpi 2020; Hopp et al. 2022). Furthermore, the alteration of in-situ pore pressure can change the effective stress state. After waste emplacement, nuclear decay processes will generate heat that can lead to the formation of excess pore pressure caused by the thermally induced expansion of the pore fluid in the low-permeable host rock (thermal pressurization; e.g., Gens et al. 2007; Ghabezloo and Sulem 2009; Urpi et al. 2019). Gas formation due to anaerobic microbial corrosion of emplaced steel canisters (Ortiz et al. 2002) as well as dynamic strains induced by natural distant earthquakes (Barbour 2015) can also locally change pore pressure. With increasing pore pressure, the effective normal stress acting on fault planes will decrease, which can lead to fault reactivation if the shear stress resolved on the fault plane exceeds the shear strength. Reactivation of faults may not only result in seismicity but can also lead to the creation of permeable fluid flow paths along faults and fractures. These may provide an opportunity for the release and migration of radioactive nuclides if they remain hydraulically conductive. Therefore, an important aspect of the long-term safety of future repository sites is the risk assessment for fault activation caused by stress perturbations.

Tectonic structures in OPA and other clay-rich host rocks may be detected by in-situ geophysical methods (e.g., Jaeggi et al. 2017b; Schuster et al. 2017). However, on a regional scale, a resolution is limited due to a low impedance contrast (e.g., Mazzoldi et al. 2012), as a composition of fault material and host rock may be similar, both being dominated by phyllosilicates. Analysis of microseismic activity following hydraulic stimulation in unconventional reservoirs has shown that induced inelastic damage is underestimated as clay-rich faults deform predominantly by aseismic slow slip (Zoback et al. 2012). Therefore, deformation of fault zones, induced damage and potential fluid migration pathways may remain undetected by seismicity measurements (Zoback and Gorelick 2012; Guglielmi et al. 2020, 2021). This increases uncertainties in hazard assessment

during the site characterization process in this type of host rock. To better assess the evolution of mechanical and hydraulic properties during site operations, a detailed knowledge of the deformation behavior of phyllosilicate-dominated faults intersecting clay-rich rock formations and the underlying deformation mechanisms is required.

OPA has been studied extensively under in-situ conditions at the Underground Rock Laboratory (URL) Mont Terri (Thury and Bossart 1999; Bossart and Milnes 2017). There, the "Main Fault" crossing the URL provides an opportunity to study the structural, petrophysical and hydro-mechanical properties of representative tectonic structures. The heterogeneous architecture of the up to 5 m thick fault zone constitutes scaly clay (Vannucchi et al. 2003), slickensides on fractures, mineralized veins, anastomosing networks of µm-thin shear zones and fault gouge (Nussbaum et al. 2011; Laurich et al. 2014, 2017, 2018; Jaeggi et al. 2017b), resulting in complex fault rupture behavior and modification of hydraulic properties when reactivated by gallery excavation and fluid injection (e.g., Guglielmi et al. 2017, 2020, 2021; Wenning et al. 2021; Hopp et al. 2022).

In several upper crustal fault zones located in different tectonic settings, the presence of clay minerals has been found to influence hydro-mechanical and frictional properties, fault weakness and strain accumulation by aseismic creep and slow slip (e.g., Faulkner et al. 2003; Fagereng and Sibson 2010; Schleicher et al. 2010; Collettini et al. 2019). Laboratory friction experiments have been performed on a variety of natural and synthetic fault gouges with varying proportions of different phyllosilicates showing that these minerals exhibit a low friction coefficient (μ = 0.03 – 0.5) relative to other rock types (e.g., granite, sandstone), whose friction coefficients are generally in the range of μ = 0.6 – 0.85 (Byerlee 1978). In addition, the frictional strength of the gouge decreases with increasing clay fraction (e.g., Logan and Rauenzahn 1987; Crawford et al. 2008; Tembe et al. 2010; Giorgetti et al. 2015; Ruggieri et al. 2021). In the framework of rate and state constitutive friction laws (e.g., Dieterich 1972; Ruina 1983; Marone 1998), the majority of clays revealed velocity-strengthening behavior at sliding velocities $<$1 cm/s as well as limited frictional healing, suggesting that these minerals have a stabilizing effect on faults, inhibiting earthquake nucleation and rupture propagation (Bos and Spiers 2000; Niemeijer and Spiers 2006; Tesei et al. 2012; Giorgetti et al. 2015; Carpenter et al. 2016; Ruggieri et al. 2021). However, the frictional behavior of clays is complex and depends on several factors such as crystal structure, presence and chemistry of fluids, stress, temperature and strain rate (e.g., Saffer and Marone 2003; Moore and Lockner 2004; Ikari et al. 2007, 2009; Behnsen and Faulkner 2012; den Hartog et al. 2012a, b). Due to their low permeability, water-saturated clay-rich rocks may be further weakened at seismic slip rates by thermal pressurization and/or fluid pressurization induced by shear-enhanced compaction, causing high fluid pressures (e.g., Faulkner et al. 2011; Behnsen and Faulkner 2012; Bullock et al. 2015). Clay minerals also influence the fabric of crustal faults (e.g., Faulkner et al. 2003; Vannucchi et al. 2003; Collettini et al. 2009b; Fagereng and Sibson 2010; see Collettini et al. 2019 and reference therein) and promote the development of interconnected, anastomosing

shear zones. Increasing fabric intensity further reduces frictional strength when compared to pulverized gouge produced from the same natural material, as was shown in laboratory tests (e.g., Collettini et al. 2009a; Niemeijer et al. 2010; Orellana et al. 2018a).

In accordance with previous laboratory friction experiments, wet gouge and scaly clay from OPA revealed low frictional strength (μ <0.5), a lack of re-strengthening and velocity-strengthening behavior (Orellana et al. 2018a, b, 2019), suggesting that faults in OPA could be easily reactivated and slip via aseismic creep. On the other hand, dry OPA gouge revealed velocity-weakening behavior and unstable sliding at shear velocities <10 µm/s (Orellana et al. 2019). Even though natural fault zones are barely dry, desaturation of the host-rock is expected during the open drift stage of the repository and due to heat-generation as a result of radioactive decay of the emplaced nuclear waste (Tsang et al. 2012).

The mechanical behavior of intact OPA is strongly dependent on water saturation, with strength and stiffness increasing as the degree of saturation decreases, favoring brittle deformation (e.g., Nuesch 1991; Wild et al. 2015; Zhang and Laurich 2019; Schuster et al. 2021). Embrittlement reduces the sealing capacity of clay-rich cap-rocks and increases the leakage along potential faults (Ingram and Urai 1999) as well as the risk for seismicity during fault reactivation (Rutqvist et al. 2016). Brittle deformation of clay-rich rocks is favored with decreasing clay mineral content and is further influenced by the present stress field and burial history (e.g., Gutierrez et al. 1996; Ingram and Urai 1999; Nygård et al. 2006; Bourg 2015). At the Mont Terri URL, several sub-units have been distinguished within the formation, which varies in grainsize, color as well as the proportions of the main mineral components: phyllosilicates, quartz and carbonates (Hostettler et al. 2017; Lauper et al. 2018, 2021; Kneuker and Furche 2021). Accordingly, OPA is generally subdivided into a carbonate-rich sandy, a shaly and a sandy lithofacies type at the URL (Thury and Bossart 1999; Pearson et al. 2003). The compositional variability is also reflected in the rock properties of the different facies. Hence, the quartz-rich sandy facies displays a higher shear strength and stiffness compared to the clay-rich shaly facies (Popp and Salzer 2007; Siegesmund et al. 2014; Schuster et al. 2021).

As shown in the Mont Terri URL, discontinuities and mineralogical heterogeneity are to be expected in a future repository in OPA. Consequently, a detailed knowledge of the mechanical and frictional behavior of faults or fractures and their interaction with the different surrounding lithofacies types is required to predict construction-related damage and long-term integrity. To date, few experimental studies have focused on host-rock heterogeneity and characterized the mechanical properties of the sandy facies of OPA (Zhang and Laurich 2019; Crisci et al. 2021; Schuster et al. 2021). In addition, most deformation experiments on OPA are limited to intact rock samples (e.g., Nuesch 1991; Amann et al. 2012; Wild and Amann 2018; Zhang and Laurich 2019; Schuster et al. 2021), resulting in a lack of laboratory studies characterizing the mechanical properties of faulted OPA taking compositional heterogeneities into account.

Here we performed a series of triaxial tests to investigate the impact of mineral composition and confining pressure on fault reactivation and deformation behavior of dry OPA, using cylindrical saw-cut samples from the shaly and sandy facies. Macroscopic observations, elastic P-wave velocity and AE measurements, and microscopic analysis using electron microscopy were combined to describe the deformation behavior, fault stability, gouge production, strain partitioning between localized fault slip and distributed off-fault matrix deformation as well as to study the prevailing micro-deformation mechanisms. After a fixed shear displacement, slidehold- slide tests were additionally performed to study fault healing and restrengthening.

3.2 Materials and Methods

3.2.1 Sample Characterization and Preparation

Samples from the shaly and sandy facies were obtained from the OPA formation collected at a depth of approximately 300 m in the Mont Terri URL (Thury and Bossart 1999; Hostettler et al. 2017). The Jurassic-aged OPA (Toarcian to Aalenian) was deposited in a shallow-marine environment and experienced a maximum burial depth of 1.35 km and a maximum temperature of 85 °C (Mazurek et al. 2006). Therefore, OPA exposed at the Mont Terri URL is over-consolidated. Core material of OPA was provided by Swisstopo (Federal Office for Topography, Wabern, Switzerland) and originates from borehole BMA-4 (shaly facies) and BCL-2 (sandy facies) at the Mont Terri URL (Fig. 1.2). Drill cores of 101 mm diameter were recovered under dry conditions using compressed air as a cooling agent. After extraction, the cores were stored in plastic liners and vacuum-sealed in aluminum foil preventing desaturation.

The shaly facies (Fig. 3.1b, d) is composed of rather homogeneous, dark-grey, laminated, argillaceous claystones mainly consisting of clay minerals (illite, illite-smectite kaolinite and chlorite) with silt to fine-sand sized bioclasts (e.g., fossil shells) and detrital quartz and feldspar grains dispersed throughout the clay-rich matrix (Kneuker and Furche 2021; Lauper et al. 2021). The OPA sandy facies (Fig. 3.1a, c) is a heterogeneous, siliceous-argillaceous claystone, characterized by an alternation of dark-grey, clay-rich layers and undulating lenses and layers of silt to sand-sized quartz and feldspar grains, cemented by carbonates (Lauper et al. 2018, 2021; Schuster et al. 2021). Well-pronounced bedding planes of OPA are caused by the preferential alignment of phyllosilicates, leading to a transverse isotropy of petrophysical, mechanical and hydraulic properties (e.g., NAGRA 2002; Wenk et al. 2008; Siegesmund et al. 2014; Favero et al. 2018; Schuster et al. 2021).

For each facies type, cylindrical samples with a final diameter of 50 mm were drilled perpendicular to the bedding. Cylindrical specimens were precision ground to 102 mm length and cut in half at an angle of $\theta = 30°$ oriented to the cylinder axis. Cutting and polishing of fault surfaces resulted

in a final sample length of $L = 101 \pm 1$ mm. Roughness of the saw-cut fault planes was produced by hand polishing using #180 grit silicon carbide abrasive grinding paper. To ensure a comparable initial roughness of the samples, roughened surfaces were scanned using a 3D optical profilometer. Average RMS (root mean square) roughness was $S_q = 7.9 \pm 2.0$ µm (cf., chapter 3.2.3). All preparation steps were performed under dry conditions, keeping exposure to the laboratory environment to a minimum.

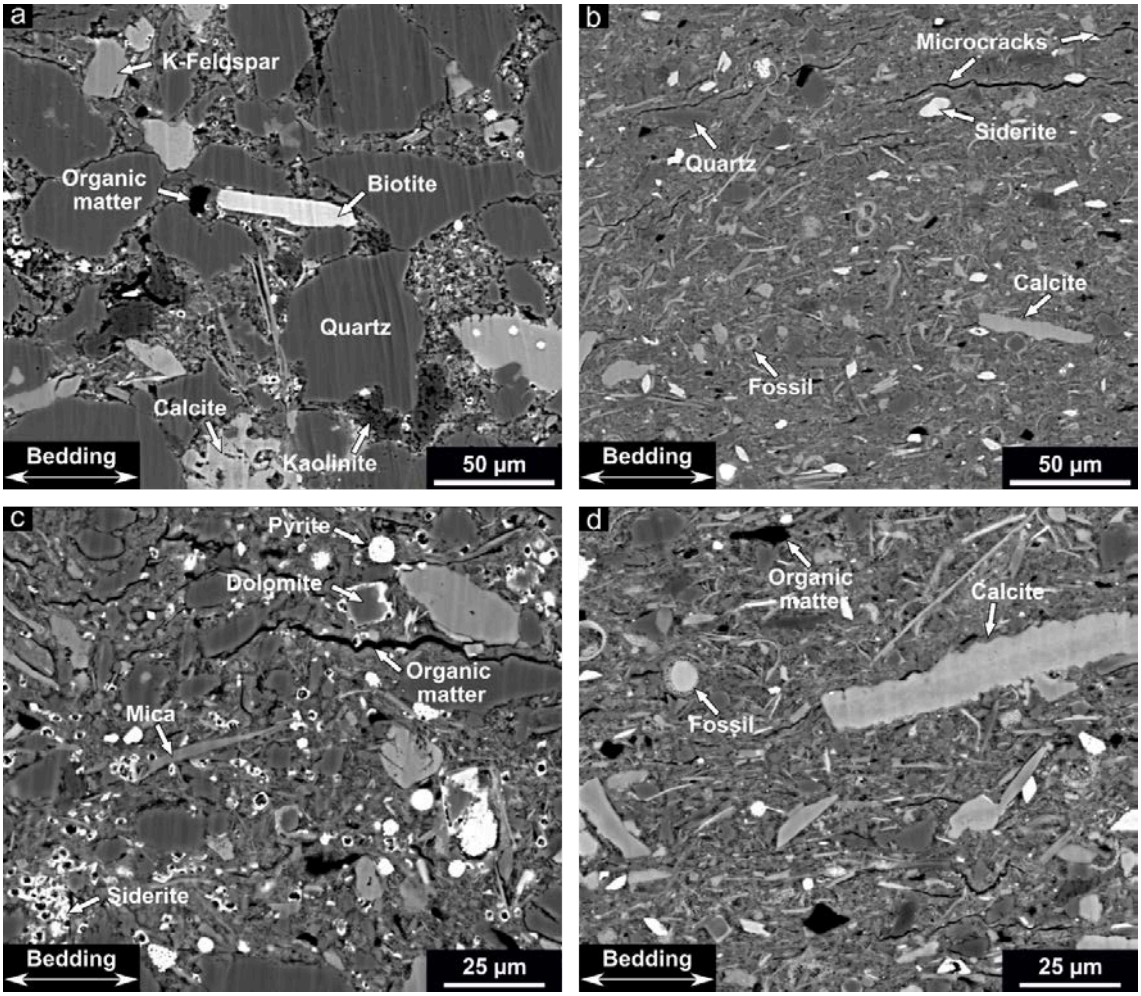

Figure 3.1: Backscattered electron microscope images of undeformed Opalinus Clay of the sandy (**a**, **c**) and shaly facies (**b**, **d**), showing microstructural differences in both facies' types as well as predominant mineral phases. **a** Sand layer of the sandy facies, characterized by a grain-supported framework of clastic mineral phases with barely compacted clay matrix filling the interparticle space. **b** The shaly facies is more homogeneous compared to the sandy facies with smaller grain sizes of clastic minerals. **c** Mineral grains in clay layers of the sandy facies display a smaller grain size compared to sand layers and are surrounded by clay matrix. Microstructures of clay layers of the sandy (**c**) and the shaly facies (**d**) appear similar. However, clay layers of the sandy facies display a higher content of quartz, whereas calcite is more abundant in the shaly facies.

After preparation, the specimens and several sub-samples, prepared from the remaining core material, were dried in an oven at a temperature of 50 °C with a relative humidity of 22±5% until a constant weight was reached. Residual water content was determined by drying sub-samples at 110 °C for >48 h. It is on average ≈1.0wt% for shaly and ≈0.4wt% for the sandy facies' samples, respectively. Sub-samples were used to estimate the connected porosity (φ) of samples from both facies' types, determined from skeletal and bulk density. Grain density was measured using a He-pycnometer (Micrometrics, AccuPyc 1340) and bulk density (ρ) was determined from the ratio of sample weight and volume. Bulk density is 2.30±0.02 g/cm^3 for the shaly facies and 2.37±0.01 g/cm^3 for the sandy facies with connected porosities φ of 15.7±1.3vol% and 11.1±1.1vol%, respectively. At the microscale, we observe several bedding-plane-parallel intergranular microcracks (Fig. 3.1b) in the undeformed samples, especially in shaly facies' samples, that potentially originate from stress relaxation during core drilling (e.g., Corkum and Martin 2007) and/or drying (e.g., Soe et al. 2009). These microcracks can account for up to 28vol% of porosity (Houben et al. 2013, 2014) and may be effectively closed under laboratory conditions at confining pressures ≥6 MPa (e.g., Winhausen et al. 2020).

Bulk mineralogy was determined using a PANalytical Empyrean X-ray diffractometer (XRD), operating at 40 kV and 40 mA with Cu-Kα radiation and a step size of 0.013°2θ from 4.6° to 85°. Major mineralogical phases were determined with the program EVA by Bruker (version 11.0.0.3) and quantified (±3wt%) by Rietveld refinement using BGMN software and Profex (version 3.10.2, Doebelin and Kleeberg 2015). Determined bulk mineralogical composition of both facies is listed in Table 3.1. Consistent with previous studies (e.g., Thury and Bossart 1999; Pearson et al. 2003; Bossart and Milnes 2017), the sandy facies reveals a higher content of quartz (42wt%) and feldspars (11wt%) with a lower proportion of clay minerals (36wt%) compared to the shaly facies of OPA.

Table 3.1: Bulk mineralogy of the sandy and shaly facies of Opalinus Clay obtained from sub-samples of used core sections.

Opalinus Clay	Clay (wt%)	Quartz (wt%)	Carbonates (wt%)	Feldspar (wt%)	Pyrite (wt%)
Sandy Facies	36	42	10	11	<1
Shaly Facies	74	9	11	5	<1

A pair of biaxial stacked rosette strain gauges was glued on the sample surface at the center of the upper and lower block of each specimen, which allowed the recording of the bulk vertical and radial matrix strain during axial deformation. Four additional single strain gauges were attached to the lower sample block at a distance of 3 mm to the saw-cut plane to monitor local strains parallel and perpendicular to the saw-cut fault plane (see Fig. A3.1a, b of the appendix to this chapter). To prevent intrusion of oil (confining medium), the saw-cut sample blocks were inserted

into a neoprene jacket of 2 mm thickness. Acoustic emissions (AE) and ultrasonic velocities were measured with 14 piezoelectric P-wave transducers (1 MHz resonant frequency) encapsulated into brass housings of 1 cm diameter that were glued on the sample surface at perforations of the neoprene jacket using epoxy (see Fig. A3.1). An additional pair of P-wave transducers was installed in the top and bottom steel plugs of the triaxial cell. This sensor setup ensured the recording of elastic P-wave velocities along different ray paths through the sample and AE localization.

3.2.2 Experimental Setup and Procedure

Triaxial deformation tests were performed at room temperature using a servo-hydraulic loading frame (Material Testing Systems, MTS; Stanchits et al. 2011). Prior to applying axial load, all tested saw-cut samples were hydrostatically pre-compacted at 50 MPa pressure for 18 h to ensure comparable initial asperity damage and matrix compaction for each sample. Subsequently, each saw-cut sample was unloaded to the respective target confining pressure (p_c = 5, 20 or 35 MPa) at a similar rate (1 MPa/min) as during loading. With the chosen confining pressure range, we intended to simulate the target depths of future repository sites (<1000 m depth). Triaxial tests were conducted at a constant axial piston displacement rate of 1 µm/s. The total axial shortening of the specimen (D_{tot}) was determined from the piston displacement (D_{LVDT}) measured externally by a linear-variable displacement transducer (LVDT). Experiments were terminated after D_{LVDT} $\approx$ 6.75 mm to prevent slip-induced jacket rupture and reduce geometry effects leading to stress and/or strain inhomogeneities. Piston displacement readings were corrected for both system compliance and stiffness of the loading frame ($\approx$0.67 – 0.7 MN/mm) resulting in a true sample axial deformation rate of $\approx$0.88 µm/s. Total axial strain ($\varepsilon_{tot} = D_{tot}/L \times 100\%$) was determined from the initial sample length (L) and corrected axial shortening of the specimen (D_{tot}). Axial strain was partitioned into matrix strain of the saw-cut blocks ε_{ax} measured with strain gauges and slip (s_f) along the saw-cut given by $s_f = (D_{tot} - \varepsilon_{ax} \times L)/cos\theta$ (see Fig. A3.1b). Strain partitioning (%) is expressed by the ratio of matrix strain ε_{ax} to a total axial strain of the sample ε_{tot}. Volumetric matrix strain was calculated by $\varepsilon_{vol} = \varepsilon_{ax} + 2 \times \varepsilon_{rad}$ from averaged axial and radial stain gauge readings of the saw-cut blocks. Axial stress (σ_1) was measured with a resolution of about $\pm$0.5 MPa by an external load cell corrected for sealing friction of the loading piston. Stiffness and friction were determined in calibration runs at relevant confining pressures using stainless steel cylinders. Shear (τ) and normal stress (σ_n) acting on the fault plane were derived from principal stresses $\tau = 1/2 \times (\sigma_1 - p_c) \times sin2\theta$ and $\sigma_n = 1/2 \times [(\sigma_1 + p_c) - (\sigma_1 - p_c) \times cos2\theta]$. Shear and normal stresses were corrected for the progressively reducing contact area along the inclined saw-cut during deformation (Tembe et al. 2010). Amonton's friction coefficient (μ) resolved on the saw-cut plane was determined by the ratio of shear to normal stress assuming no cohesion. Mechanical data were sampled at a rate of 10 Hz during axial deformation.

In an effort to evaluate creep relaxation and static frictional strengthening characteristics of artificially fractured OPA, we performed slide-hold-slide (SHS) tests (e.g., Dieterich 1972; Beeler et al. 1994; Marone 1998; Carpenter et al. 2016) for each sample. Axial displacement was first stopped after a piston displacement of $D_{LVDT} \approx 6$ mm for a holding period of $t_h = 60$ s. Subsequently, samples were re-sheared for $D_{LVDT} = 0.25$ mm at an axial displacement rate of $\approx$1 µm/s, followed by a second and third holding period of 600 and 6000 s, respectively. For the sample of the sandy facies that was deformed at $p_c = 5$ MPa, the piston was stopped at $D_{LVDT} \approx 7$ mm. Furthermore, for technical reasons, the experiment was interrupted during the third holding period, which is why only the first two periods were conducted. Following Karner et al. (1997) and Marone (1998), we determined from SHS tests (1) the reduction of friction ($\Delta\mu_c$) due to stress relaxation (difference between pre-hold friction coefficient and the value attained at the end of the hold period), (2) frictional strengthening ($\Delta\mu_h$) after reloading (difference between peak friction upon re-shear and the friction value prior to hold, corrected for strain hardening trends by linear trend lines connecting slide phases) and (3) frictional weakening $\Delta\mu_w$ and the respective weakening distance d_w (see Fig. A3.2a, b of the appendix to this chapter).

Full waveform AE signals as well as ultrasonic velocity signals were recorded at a sampling rate of 10 MHz and an amplitude resolution of 16 bits with a 16-channel transient recording system (DAXBox, Prökel). P-wave velocity measurements were performed using seven sensor pairs located on opposite sides of the sample surface and one pair on the top/bottom of the sample (see Fig. A3.1). Active ultrasonic transmission (UT) measurements were performed every 15 s throughout the whole experiment. P-wave travel times were picked using the Akaike information criterion (AIC) criterion and corrected for sample deformation and fault slip. UT measurements provided time-dependent quasi-anisotropic P-wave velocity model composed of five horizontal and one vertical layer that was further used to locate AE events (e.g., Stanchits et al. 2011; Goebel et al. 2014; Kwiatek et al. 2014). For AE localization, signals were first amplified by 40 dB and high-pass filtered at 100 kHz (Physical Acoustic Corporation). P-wave arrival times were automatically picked using AIC and convolutional neural network (e.g., Ross et al. 2018). To locate AE events, we used the Equivalent Differential Time method (e.g., Font et al. 2004), with the inverse problem solved using a combination of grid search followed by a simplex search technique. The average AE hypocenter location accuracy is $\pm$2 mm (Stanchits et al. 2011).

3.2.3 Microstructural Imaging

Top and bottom saw-cut fault surface topography of each sample was measured before and after deformation using a high resolution (0.1 µm) white light optical profilometer (Keyence VR3200) with a Z-axis measurement accuracy of $\pm$3 µm. Microtopography areas of 50 × 40 mm^2 (1062 × 850 px) were acquired at the same starting points to evaluate surface evolution.

Using a scanning electron microscope (FEI Quanta 3D Dual Beam), microstructural imaging was performed on samples that were selected from deformed specimens prepared parallel to shear displacement. The fault area of interest was first covered with epoxy resin to maintain microstructures (gouge and off-fault microstructures). Rectangular-shaped specimens (11 × 8 × 3 mm^3) were then cut and pre-polished by hand with SiC grinding paper down to P4000 grit for subsequent broad ion beam (BIB) polishing (JEOL IB-19520CCP). BIB polishing for 2 h at 8 kV, 200 µA and 6 h at 6 kV, 150 µA, removed a layer of approximately 100 µm thickness on an area of ≈2.5 mm^2. Additional samples of the (unpolished) fault surface were prepared to examine topography microstructures. Scanning electron microscopy (SEM) was performed on carbon-coated samples at an acceleration voltage of 20 kV and a working distance of 5 mm. Mineral phases were determined with an attached EDAX energy-dispersive X-ray analyzer (EDX).

3.3 Results

In total, we conducted six triaxial deformation tests on saw-cut samples of OPA. Samples from the sandy and shaly facies were deformed at confining pressures of p_c = 5, 20 and 35 MPa with axial deformation rates of ≈0.88 µm/s. Tests were performed at room temperature on cylindrical samples drilled perpendicular to bedding orientation and containing a saw-cut fault plane inclined at 30° to the loading direction. This set of experiments allows us to investigate the influence of sample composition and confining pressure on the localization behavior during reactivation of the fault plane, including AE activity as well as P-wave velocity evolution during deformation, and creep relaxation during hold periods.

3.3.1 Mechanical Data

3.3.1.1 Fault Reactivation and Frictional Behavior

The stress–strain behavior of samples from both facies types is strongly affected by the applied confining pressure. The differential stress ($\sigma_d = \sigma_1 - p_c$) of the assembly significantly increases with pressure and exhibits pronounced strain hardening at p_c = 20 and 35 MPa (Fig. 3.2a, b, Table 3.2). The initial phase of elastic loading up to the yield stress σ_y (marked with stars in Fig. 3.2a, b) persists up to a total axial strain between ε_{tot} = 0.14 – 1.2%. The yield stress indicates the onset of plastic deformation of sample blocks.

At 5 MPa confining pressure, axial matrix strain ε_{ax}, inferred from axial strain gauges glued to the saw-cut blocks, increases initially at a similar rate as total axial strain ε_{tot} (Fig. 3.2c, d), i.e. the fault is locked. At stress σ_f fault slip initiates, and axial shortening is progressively accommodated by fault slip (marked with dots in Fig. 3.2c, d). For the samples deformed at p_c = 5 MPa, σ_f closely corresponds to yield stress σ_y (Fig. 3.2). We observe a small stress drop of

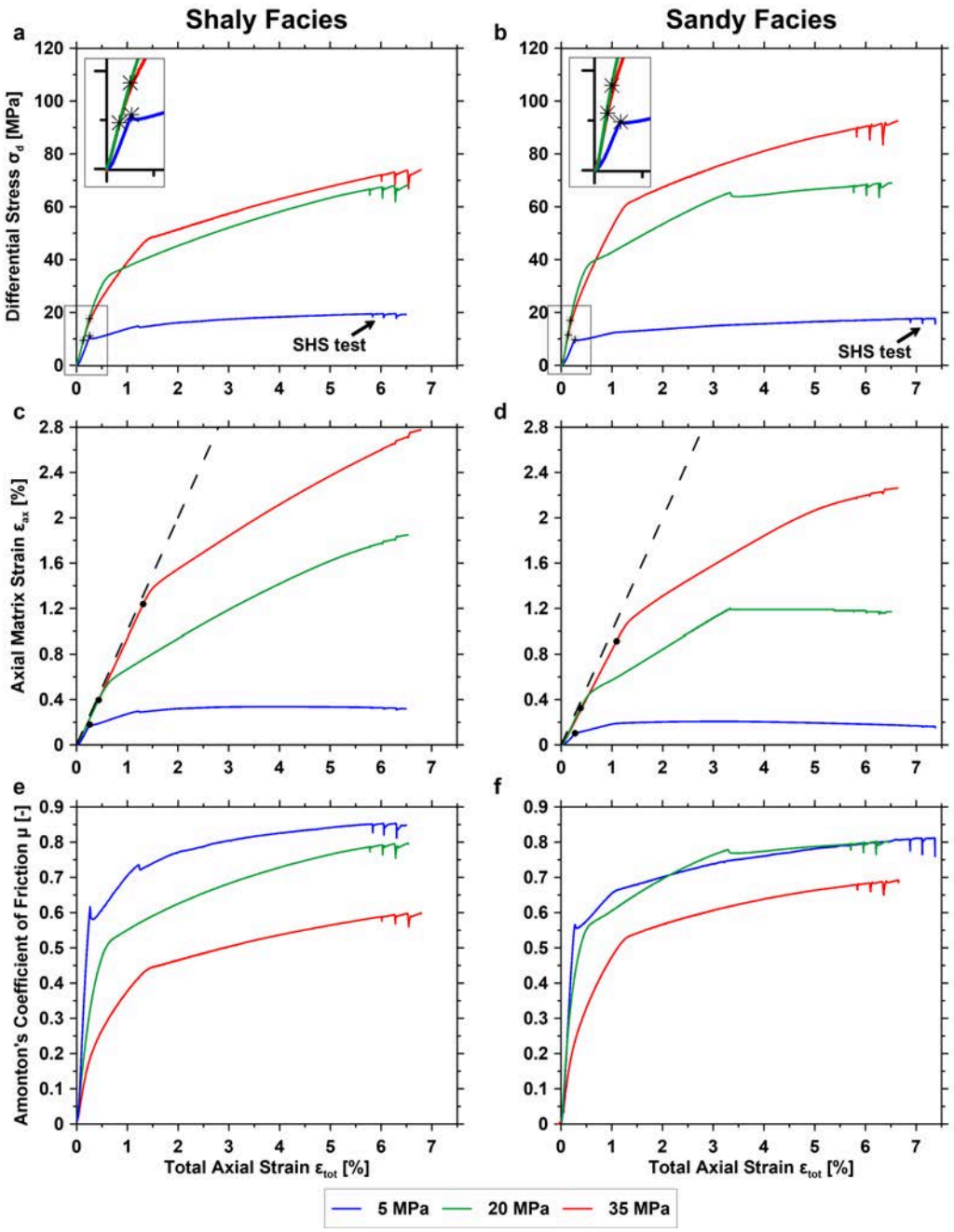

Figure 3.2: Mechanical data of fault reactivation experiments performed on the shaly (left column) and sandy facies (right column) of Opalinus Clay. Differential stress-total axial strain curves (**a**, **b**) showing the influence of confining pressure on deformation behavior. Yield stress σ_y is indicated by stars (enlarged section). Vertical matrix strain measured by strain gauges is plotted against total strain (**c**, **d**), indicating the degree of strain partitioning between fault slip and matrix compaction. Black dashed line represents a slope of 1, which corresponds to a fully locked fault. Black dots represent stress σ_f at onset of slip along saw-cut faults. Plots of Amonton's friction coefficient μ versus total axial strain (**e**, **f**) highlights the influence of facies type and confining pressure on strain hardening.

Table 3.2: Summary of experimental parameters and mechanical data.

Opalinus Clay	p_c (MPa)	σ_y (MPa)	σ_f (MPa)	Stress at ε_{tot} = 5% (MPa)	Total D_{tot} (mm)	Total s_f (mm)	Strain Partitioning (%)	Slip Events*	Stress Drop (MPa)	d_w (µm)	ν_{sf} (µm/s)
Sandy Facies	5	9.4	9.8	16.5	7.444	8.418	3	1. ε_{tot} = 0.28	0.3	4.9	1.2
Sandy Facies	20	17.0	32.2	66.7	6.599	6.256	18	1. ε_{tot} = 3.33	1.5	5.7	2.2
Sandy Facies	35	11.5	55.4	88.3	6.628	5.034	34	-	-	-	-
Shaly Facies	5	11.1	11.1	19.0	6.673	7.244	5	1. ε_{tot} = 0.27	1.0	6.9	2.2
								2. ε_{tot} = 1.23	0.5	5.8	2.1
Shaly Facies	20	17.6	27.8	63.3	6.783	5.451	28	-	-	-	-
Shaly Facies	35	9.4	46.5	67.7	6.548	4.468	41	-	-	-	-

p_c confining pressure, σ_y yield stress bulk matrix, σ_f stress at onset of fault slip, ε_{tot} total axial strain, D_{tot} LVDT displacement, s_f fault slip, * number of slip events at total axial strain ε_{tot} (%), d_w slip weakening distance, ν_{sf} slip rate

≈0.3 MPa and ≈1 MPa for sandy facies and shaly facies samples, respectively (Fig. 3.2a, b, Table 3.2). Subsequently, the shaly facies sample shows minor strain hardening until a second stress drop of ≈0.5 MPa occurs at $\varepsilon_{tot} \approx 1\%$, followed by a progressive decrease in hardening to an almost steady state stress level. The sandy facies sample also hardens up to $\varepsilon_{tot} \approx 1.1\%$, but without a stress drop. Subsequently, strain hardening is decreasing with increasing strain. Beyond $\varepsilon_{tot} \approx$ 1.1 – 1.2% matrix strain stops increasing and sample shortening is predominantly accommodated by fault slip (Fig. 3.2c, d). Friction coefficients at fault reactivation μ are ≈0.62 for shaly and 0.57 for sandy facies samples, respectively (Fig. 3.2e, f).

Samples that were deformed at confining pressures of 20 and 35 MPa display yielding (stars in Fig. 3.2a, b) followed by continuous strain hardening. Yield stress σ_y and stress level at onset of slip σ_f progressively deviate with increasing confining pressure with $\sigma_f > \sigma_y$. After fault slip starts at stress σ_f, vertical matrix strain increases at a progressively declining rate. Consequently, strain partitioning into matrix deformation of saw-cut blocks and fault slip evolves nonlinearly. No stress drops were observed except for the sandy facies sample deformed at p_c = 20 MPa. For this sample, the axial matrix strain stays constant after a stress drop of ≈1.5 MPa at $\varepsilon_{tot} \approx 3.3\%$, and sample shortening occurred by localized fault sliding only.

Up to stress σ_f at which sliding starts (dots in Fig. 3.2c, d), the fault remains almost completely locked and matrix strain increases at almost the same rate as the total axial strain. During this initial deformation ≈95% shortening is accommodated by the deformation of the sample blocks. With increasing confining pressure, the accumulated axial matrix strain and the stress at fault reactivation increase for samples from both facies. Partitioning of total sample strain into axial matrix strain increases (Fig. 3.2c, d). The ratio of shear stress to normal stress (friction coefficient μ) decreases with increasing confining pressure, in particular for shaly facies samples (Fig. 3.2e, f). The friction coefficients at fault reactivation of the sandy facies at p_c = 20 and 35 MPa are $\mu \approx$ 0.53 and 0.49 respectively, slightly higher compared to the shaly facies at similar pressures ($\mu \approx$ 0.45 and 0.43, respectively).

At 5 and 20 MPa confining pressure, we observed a few stick-slip events with small stress drops. Slip rates of events did not significantly exceed stable slip rates and ranged between 1.1 and 1.5 µm/s, corresponding to slip rates along the fault of v_{sf} = 1.3 – 1.7 µm/s. Stable slip rates along the fault range between 1.0 and 0.8 µm/s for the shaly facies and between 1.2 and 0.9 µm/s for the sandy facies saw-cuts, once slip is dominantly accommodating deformation, but depending on strain partitioning. In all samples, fault slip rates decrease with increasing confining pressure.

We used four single strain gauges attached to the lower sample block in order to measure localized deformation parallel (SGF1-3) and perpendicular (SGF4) to the fault at a distance of 3 mm (Fig. 3.3, see Fig. A3.1a). As observed for the axial strain gauges (Fig. 3.2a, c), strain along the fault increases linearly with total axial strain ε_{tot} at the beginning, independent of the applied confining pressure and in all facies, indicating a locked fault. At 5 MPa confining pressure, we observe

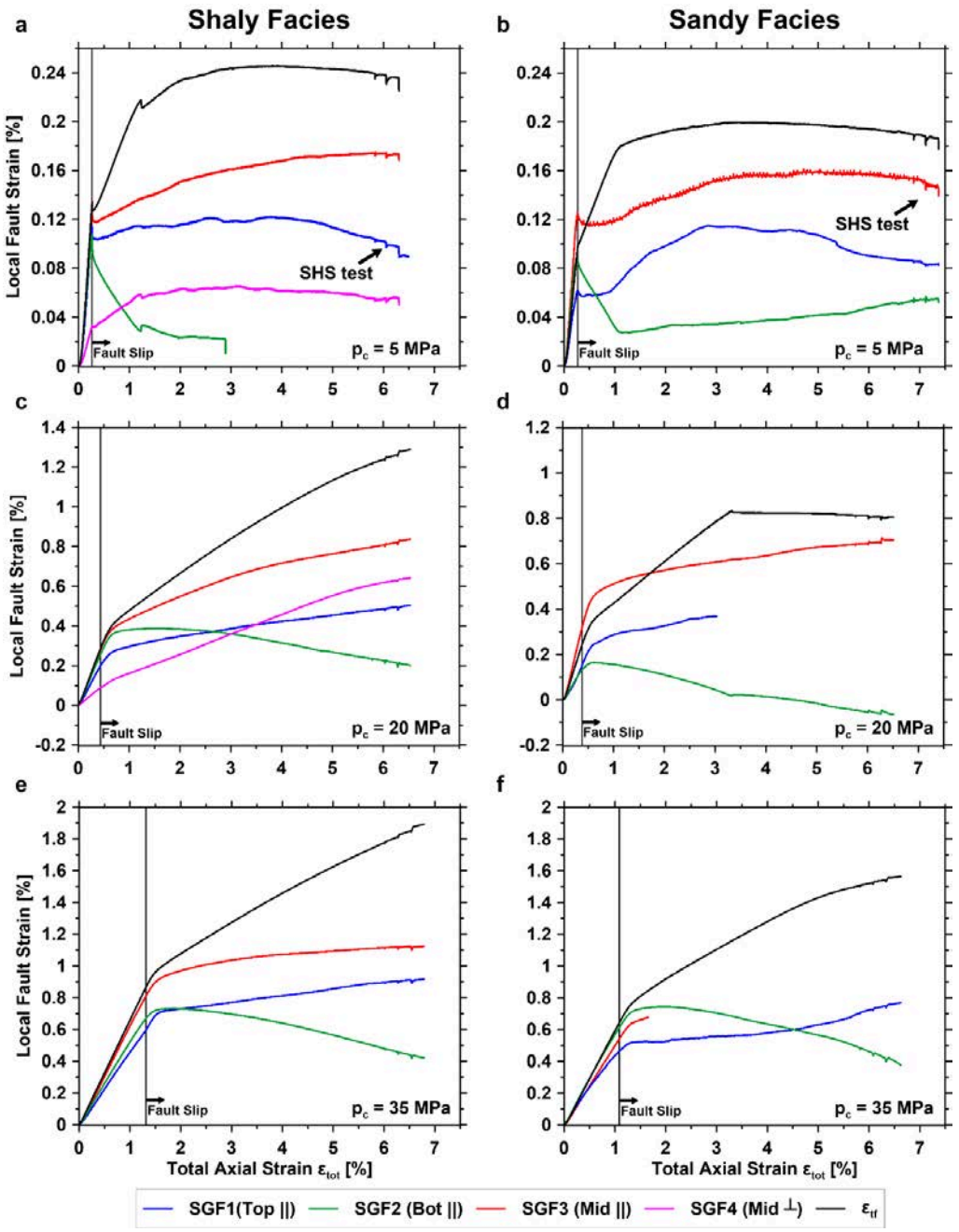

Figure 3.3: Local strain measured parallel (SGF1-SGF3) and perpendicular (SGF4) to the saw-cut fault plane as a function of total axial shortening ε_{tot} for the shaly (left column) and sandy (right column) facies of Opalinus Clay deformed at 5 (**a**, **b**), 20 (**c**, **d**) and 35 (**e**, **f**) MPa confining pressure. Strain gauges are attached along the lower sample block at a distance of 3 mm to the fault plane (see Fig. A3.1a of the appendix to this chapter). ε_{tf} shows the fault parallel strain transformed from axial and radial strain measured on the sample blocks. Note that some strain gauges are not shown or are only partially shown because they failed during the experiment. Vertical lines indicate the onset of fault slip determined from axial strain gauges (cf. dots in Fig. 3.2c, d).

an abrupt release of strain measured on all fault strain gauges for both facies at reactivation. On the other hand, at elevated pressure no dynamic strain release is observed as the fault starts sliding (Fig. 3.3c-f). Instead, measured fault strain starts to develop nonlinearly with increasing total axial strain when stress σ_f is reached. Generally, the onset of fault slip determined from axial strain readings (dots in Fig. 3.2c, d) agrees with the beginning of this non-linear increase in fault strain (Fig. 3.3 vertical lines).

Assuming homogeneous deformation of the sample blocks, we transformed the measured axial ε_{ax} and radial ε_{rad} strain to predict fault parallel strain using the expression $\varepsilon_{tf} = \varepsilon_{ax} \times cos2\theta + \varepsilon_{rad} \times cos2\theta$ (Jaeger et al., 2007). Before sliding is initiated, we find the transformed strain in good agreement with the strain measured by the parallel-oriented strain gauges, suggesting homogeneous strain distribution within the sample. After reactivation, we observe a uniform behavior of the strain gauges oriented parallel to the fault in all samples. With continuing total axial shortening after reactivation, fault parallel strain measured at the top and in the middle of the sample increases with a decreasing rate, while the strain gauges attached at the bottom of the fault show a release of strain. Furthermore, parallel strain transformed from axial and radial strain readings increasingly deviates after reactivation and with increasing confining pressure. The measurements suggest a heterogeneous strain and probably stress distribution along the saw-cut fault plane with non-uniform amounts of local slip being accommodate once slip is initiated. In addition, the deviation from transformed and measured parallel strain suggests higher strain relaxation close to the fault than in the sample blocks.

3.3.1.2 Slide-Hold-Slide Test

With the exception of the sandy facies sample deformed at 5 MPa confining pressure ($D_{LVDT} \approx 7$ mm), we performed slide-hold-slide (SHS) tests on each specimen after a total piston displacement of $D_{LVDT} \approx 6$ mm. Due to the applied confining pressure and different strain hardening behavior of the samples, differential stress reached at the start of SHS test (σ_d^H) varies. Hold times were 60, 600 and 6000 s and axial displacement after each hold period was 0.25 mm. During each period, the differential stress relaxed nonlinearly as elastic strain stored in the specimen and loading frame was released, resulting in sample creep (Fig. 3.4). Note, that in our experimental setup both the normal and shear stresses acting on the fault plane decreased during each hold period.

For samples from both facies types deformed at varying confining pressures, differential stresses decrease with increasing hold time, with increasing confining pressure and with larger initial σ_d^H (Fig. 3.4). After each hold period, elastic loading is terminated by a small stress drop once sliding on the saw-cut fault is activated (Table 3.3). Peak stresses achieved during loading increase with hold time, confining pressure and σ_d^H. However, at confining pressure of 35 MPa (Fig. 3.4e, f) initial peaks and stress drops become less prominent for the shaly facies sample.

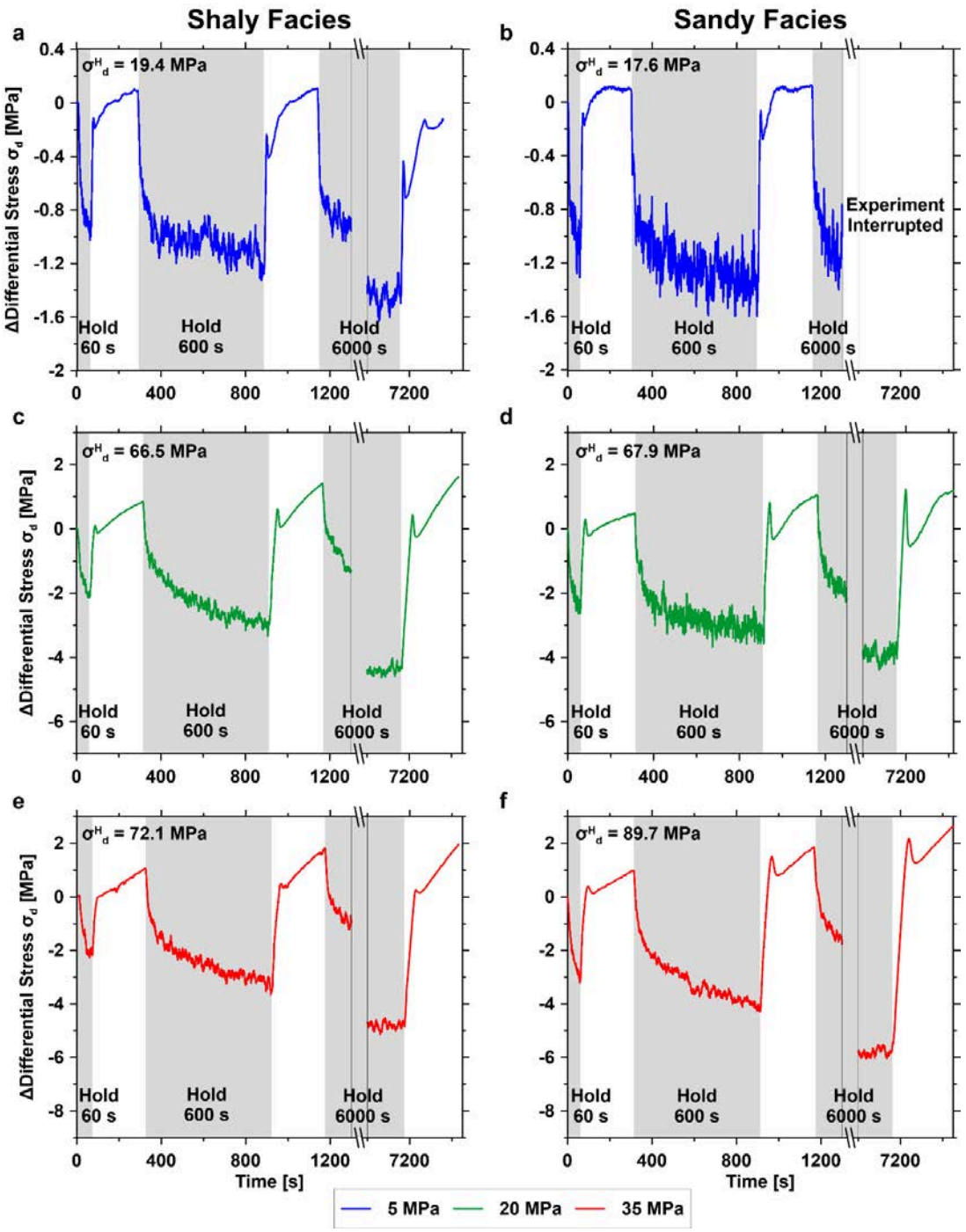

Figure 3.4: Slide-hold-slide tests performed on the shaly and sandy facies of Opalinus Clay deformed at confining pressures of p_c = 5, 20 and 35 MPa. During each hold period, ranging from 60 – 6000 s (indicated by grey areas and numbers), differential stress decreases as elastic strain stored in the sample and loading frame is relaxed. Note that differential stress $\Delta\sigma_d$ and time are all normalized to the start conditions of the first hold (60 s). Furthermore, note the broken time axis and different scales for $\Delta\sigma_d$ axis. Different initial differential stresses at the start of SHS tests (σ_d^H) are due to confining pressure and strain hardening behavior.

Stress relaxation was similar for all hold periods lasting different time intervals. Here, we focus on the effect of confining pressure on the hold period of 6000 s (Fig. 3.5) and measure axial and volumetric matrix strain and differential stress during the hold periods. Positive strain represents compaction and negative strain indicates dilatancy. The shaly facies sample deformed at 5 MPa confining pressure and the sandy facies samples deformed at 5 and 20 MPa confining pressure started dilating prior to SHS tests (Fig. 3.2). During stress relaxation, these specimens continue to dilate (Fig. 3.5a-d). This is in contrast to shaly facies samples deformed at 20 and 35 MPa confining pressure. During relaxation, axial and volumetric strain change from dilation to compaction within <1000 s. Similar behavior is observed for the sandy facies sample deformed at 35 MPa confining pressure.

Table 3.3: Summary of mechanical data from the observed stress drops that followed each hold period.

Opalinus Clay	p_c (MPa)	Hold Time Sequence (s)	Stress Drop (MPa)	d_w (µm)	v_{sf} (µm/s)
Sandy Facies	5	60	0.1	10.6	1.2
		600	0.2	15.3	1.5
		-	-	-	-
Sandy Facies	20	60	0.4	20.4	1.5
		600	1.0	31.9	2.3
		6000	1.6	37.0	3.7
Sandy Facies	35	60	0.3	28.0	1.0
		600	0.7	31.9	1.5
		6000	0.9	41.2	1.6
Shaly Facies	5	60	0.1	10.1	1.2
		600	0.2	13.1	1.5
		6000	0.3	18.6	1.5
Shaly Facies	20	60	0.2	16.2	1.3
		600	0.6	24.3	1.7
		6000	0.7	30.9	1.8
Shaly Facies	35	60	0.0	3.7	0.9
		600	0.1	16.2	1.1
		6000	0.1	20.3	1.1

p_c confining pressure, d_w slip weakening distance, v_{sf} slip rate

For sandy and shaly facies samples, we observed increasing creep relaxation $\Delta\mu_c$ with increasing hold time but smaller $\Delta\mu_c$ at higher confining pressures (Fig. 3.4, Fig. 3.6a, b). Samples from

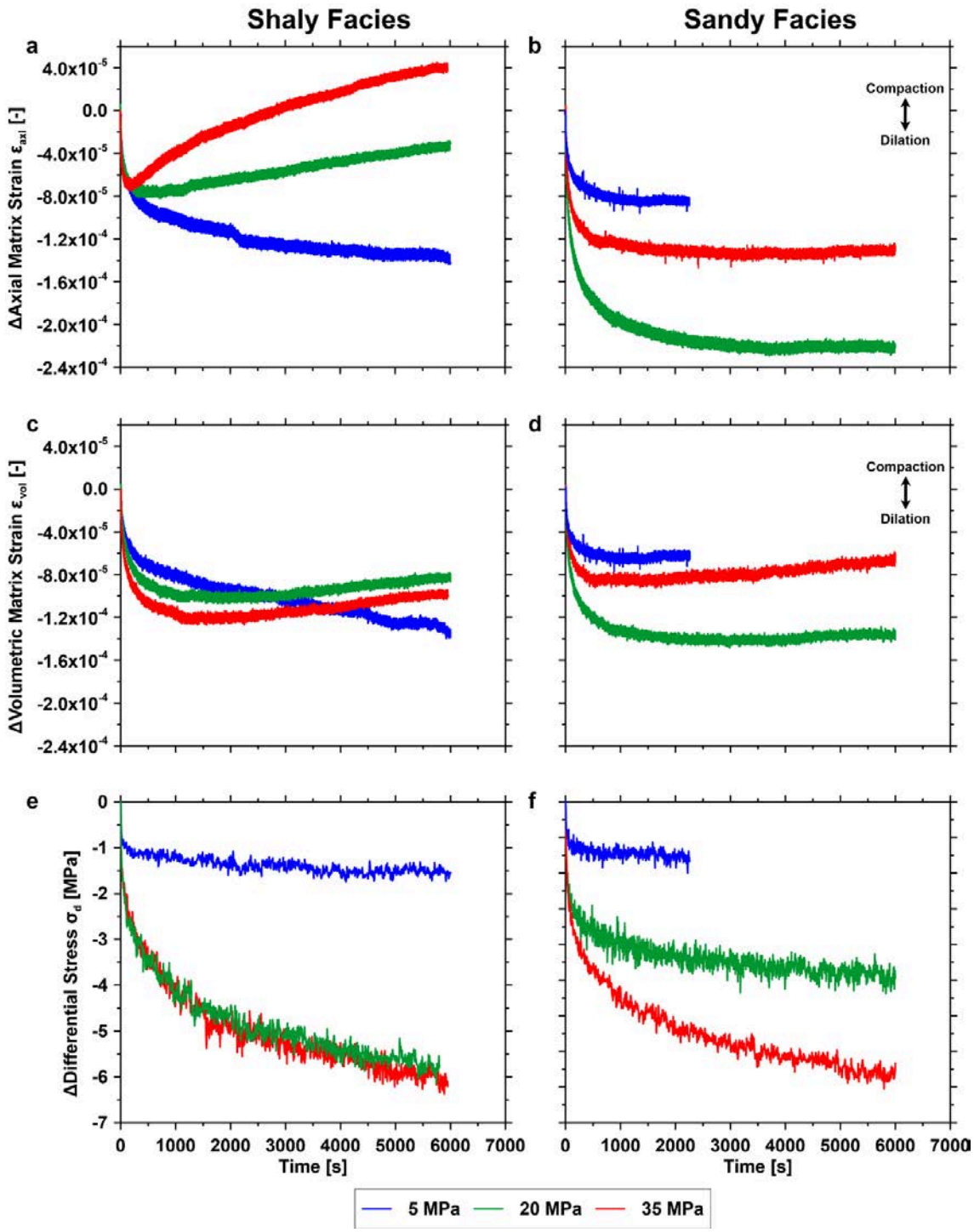

Figure 3.5: Normalized axial ε_{ax} (**a**, **b**) and volumetric ε_{vol} (**c**, **d**) strain as well as differential stress σ_d as a function of time during stress relaxation with a hold period of 6000 s of the shaly (left column) and sandy facies (right column) of Opalinus Clay. Note that the test of the sandy facies sample deformed at a confining pressure of 5 MPa was interrupted after ≈2000 s due to technical issues.

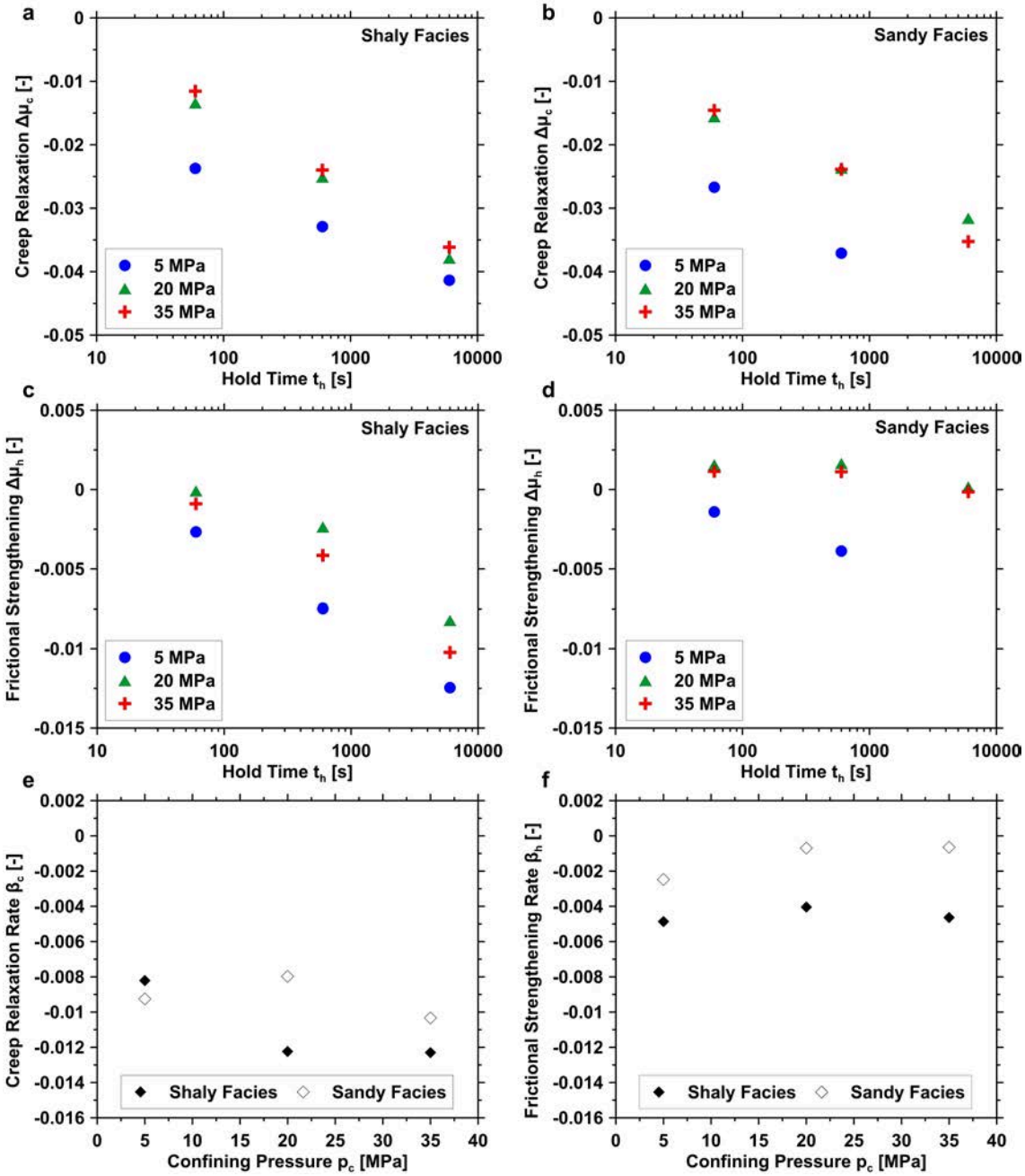

Figure 3.6: Hold time versus creep relaxation $\Delta\mu_c$ (**a**, **b**) and frictional strengthening $\Delta\mu_h$ (**c**, **d**) measured during SHS tests of the shaly and sandy facies of Opalinus Clay deformed at confining pressures between 5 and 35 MPa. Resulting creep relaxation β_c (**e**) and frictional strengthening β_h (**f**) rates of both facies are shown as a function of confining pressure p_c.

sandy and shaly facies behaved similar at comparable conditions unlike sample response to reloading that depended on OPA facies type. For the shaly facies of Opalinus Clay, strengthening $\Delta\mu_h$ is negative independent of hold time and confining pressure (Fig. 3.6c) and the total amount of

frictional strengthening decreases with increasing confining pressure but increases with increasing hold time. For the sandy facies frictional strengthening is negative at p_c = 5 MPa but close to zero at higher confinement at hold times of 60 and 600 s (Fig. 3.6d). At 6000 s, strengthening at p_c = 20 and 35 MPa is again slightly negative.

With the exception of the two experiments on sandy facies samples, creep relaxation and frictional strengthening follow a linear dependence with increasing hold time on semilogarithmic scale (Fig. 3.6). Following previous studies where SHS tests were performed on bare rock surfaces or natural and synthetic fault gouges of different compositions (e.g., Dieterich 1972; Marone 1998; Carpenter et al. 2016), creep relaxation rates (β_c) and frictional strengthening rates (β_h) may be expressed as $\beta_{c,h} = d(\Delta\mu_{c,h})/d(log_{10}(t_h))$. Both rates obtained are negative for the conducted experiments (Fig. 3.6e, f). Measured creep relaxation rates of the shaly facies are lower compared to those of the sandy facies at $p_c \geq$20 MPa and tend to decrease with increasing confining pressure, whereas β_c of the sandy facies is less affected by confining pressure (Fig. 3.6e). In contrast, frictional strengthening rates of both facies seem to increase slightly with increasing confining pressure (Fig. 3.6f), where β_h values of the sandy facies are higher compared to the shaly facies.

We observe a distinct peak in frictional strength upon reloading followed by a stress drop as fault slip starts. In general, the amount of frictional weakening $\Delta\mu_w$ and slip d_w are correlated as absolute values of both increases with increasing hold time (Fig. 3.7a, b). For all samples, weakening $\Delta\mu_w$ is less with increasing confining pressure and σ_d^H. For the sandy facies of OPA, slip weakening distance increases with increasing confining pressure, as for shaly facies samples deformed at p_c = 5 and 20 MPa. Furthermore, sandy facies samples displayed stronger frictional weakening $\Delta\mu_w$ and slip d_w at p_c = 20 and 35 MPa compared to the shaly facies.

To estimate the stability of the observed fault slips (during constant strain rate deformation and SHS tests), we have determined the unloading fault stiffness of OPA (k_f = -$\Delta\tau/\Delta s_f$) during each slip event, resulting in values between 4 and 34 MPa/mm. Instability may be promoted if the fault stiffness becomes greater than the system stiffness, i.e., a stiffness ratio $\kappa = k_s / k_f < 1$ (Rice 1983). To compare the given fault and system stiffness values, we projected k_f along the loading direction to obtain the equivalent axial stiffness of the fault, yielding values from 10 to 90 MPa/mm. For k_s, both the given machine stiffness ($k_m \approx$ 0.67 – 0.7 MN/ mm corresponding to $\approx$ 341 – 356 MPa/mm) and elastic rock matrix stiffness (k_r) have to be considered. Therefore, we determined Young's modulus E of each sample between the onset of deformation and yield stress. For the sandy and shaly facies, we obtain E = 11 – 14 GPa and 6 – 8 GPa, respectively, comparable to previous deformation experiments performed on OPA (e.g., Nüesch 1991; Schuster et al. 2021). Stiffness of the loading system is calculated via $k_s = 1/(1/k_r + 1/k_m)$, where rock matrix stiffness is estimated using the expression $k_r = E/L$. Depending on the facies type and confining pressure, loading system stiffness ranges between k_s = 52 – 100 MPa/mm. At none of the applied confining pressures the condition $\kappa = k_s/k_f < 1$ was met. We can therefore conclude that fault slip is stable

and accommodated by slow slip.

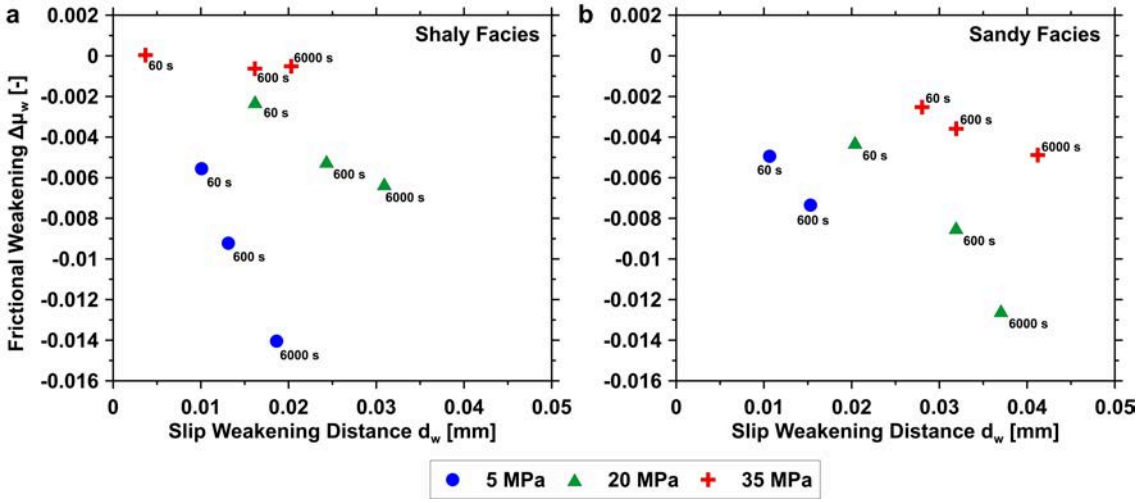

Figure 3.7: Frictional weakening $\Delta\mu_w$ versus slip weakening distance d_w of the shaly (**a**) and sandy facies (**b**) of Opalinus Clay measured at re-sliding after hold periods of 60, 600 and 6000 s (indicated by numbers).

3.3.2 Ultrasonic Velocities and Acoustic Emission Activity

We monitored elastic P-wave velocity evolution and AE activity during fault reactivation and present here three different velocity traces (see Fig. A3.1a, Fig. 3.8). P-wave velocity was measured parallel to the sample axis crossing the saw-cut plane, providing the velocity normal to bedding orientation $V_p(90°)$ (see Fig. A3.1a, sensor pairs: Z16-L15). P-wave velocity parallel to bedding orientation $V_p(0°)$ and perpendicular to the cylinder axis was measured at the top ((V_p^T) and bottom (V_p^B) part of the sample at an offset of ≈1.5 cm from the fault plane (see Fig. A3.1a, sensor pairs: I5-W7 and C11-R13).

P-wave velocity parallel to the bedding is higher than perpendicular to it (Fig. 3.8). Using the ratio of measured initial velocities parallel and perpendicular to foliation as a measure of anisotropy (V_p (0°) / V_p (90°)), the anisotropy of shaly facies samples (≈1.7 – 1.9) exceeds that of sandy facies samples (≈1.3 – 1.6). The differences between V_p (0°) and V_p (90°) decrease at elevated confining pressures and axial shortening. In comparison to previous axial deformation, sample relaxation and fault reactivation during SHS tests have no significant effect on P-wave velocities.

At 5 MPa confining pressure, bulk horizontal velocity $V_p^{B,T}$ (0°) of all samples ranges between 3.6 and 3.7 km/s and displays no significant change during axial deformation (Fig. 3.8a, b). In contrast, P-wave velocities measured parallel to the sample axis and normal to bedding V_p (90°) increase with increasing axial load. Initial velocity increase is about 180 m/s for the shaly and ≈75 m/s for the sandy facies' samples, respectively, up to fault reactivation and stress drop. Subsequently, with increasing axial shortening and fault slip the velocity changes increasingly less.

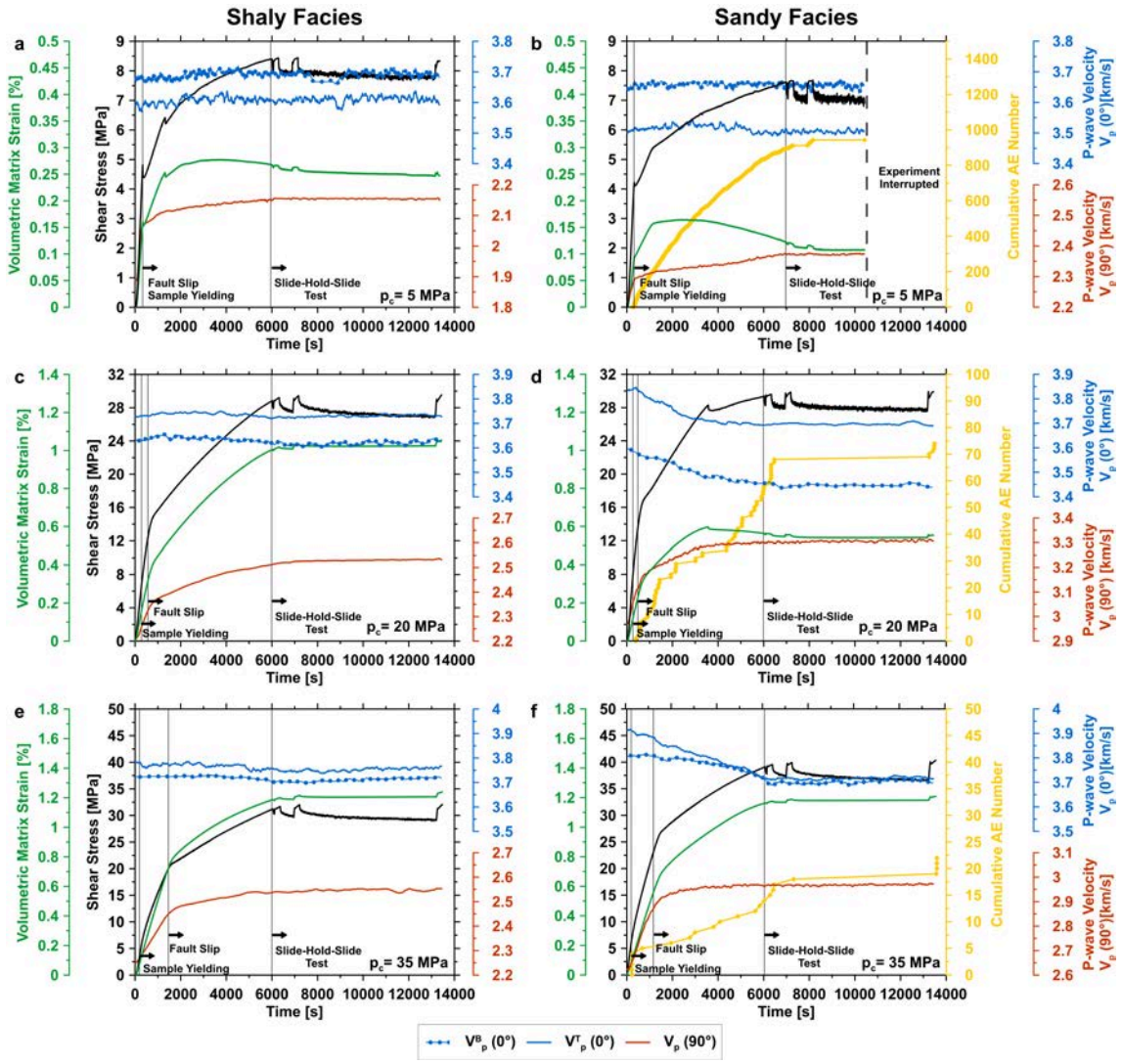

Figure 3.8: Temporal evolution of shear stress (black), volumetric strain (green), cumulative acoustic emission (AE) activity (yellow) as well as horizontal (0°, bulk) and vertical (90°, crossing the saw-cut) P-wave velocity (blue and red, respectively) for the shaly (left column) and sandy facies (right column) of Opalinus Clay deformed at a confining pressure of 5 MPa (**a**, **b**), 20 MPa (**c**, **d**) and 35 MPa (**e**, **f**). Note the different scales. Vertical lines indicate sample yielding, onset of fault slip and the start of the slide-hold-slide test protocol.

At 20 and 35 MPa confining pressure, initial horizontal velocity increased slightly by about 4 m/s/MPa for the shaly facies and ≈9 m/s/MPa for the sandy facies' samples. The increase is more pronounced for the vertical P-wave velocity (shaly facies ≈12 m/s/MPa, sandy facies ≈13 m/s/MPa in average). Interestingly, $V_p^{B,T}$ (0°) progressively decreases during deformation (Fig. 3.8c-f). The observed velocity decrease is distinctly stronger for the sandy facies (≈200 m/s) compared to the shaly facies (≈20 m/s). The evolution of V_p (90°) with ongoing deformation shows the same trend as described for the experiments performed at 5 MPa confining pressure. However, the dif-

ference between the initial velocity and the velocity at fault reactivation increases with increasing confining pressure and is higher for the sandy (≈200 m/s at p_c = 20 MPa and 280 m/s at p_c = 35 MPa) than for the shaly facies (150 and 200 m/s, respectively). Simultaneously, the accumulated volumetric strain prior to fault reactivation increases with increasing confining pressure. Increasing vertical velocity coincides with increasing stress and volumetric strain, except for the sandy facies at p_c = 20 MPa, where the volumetric strain decreases after the stress drop (Fig. 3.8d). This suggests that the vertical velocity increase is caused by sample bulk deformation and limited by the onset of shear displacement along the fault.

AEs were detected only during deformation tests performed on sandy facies samples. AE cumulative number increased with increasing load, depending on confining pressure and strain partitioning (Fig. 3.8b, d, f). At 5 MPa confining pressure, AE activity is correlated with fault sliding and starts at fault reactivation (Fig. 3.8b). With increasing deformation, AE activity decreased. During hold periods in SHS tests, no AEs were recorded for all specimens. However, as piston displacement resumed, AE activity simultaneously continued. With increasing confining pressure, the cumulative number of recorded AE decreased drastically (note different scales in Fig. 3.8). At p_c = 20 and 35 MPa, the onset of AE coincided with the yield stress. AE hypocenters from sandy facies samples are dominantly located along the saw-cut fault plane (see Fig. A3.3 of the appendix to this chapter), with the largest density of events surrounding the fault core of the sample deformed at 5 MPa confining pressure (≈10 mm).

3.3.3 Deformation Structures

After each experiment, the fault surface topography of deformed samples was measured using surface profilometry. Subsequent microstructural observation of the fault topography was performed using SEM imaging of cm-sized blocks cut from one sample block. In addition, BIB-polished cross sections oriented perpendicular to the shear direction were prepared to characterize deformation structures of the interface between the fault surface and the wall rock and associated gouge development.

3.3.3.1 Surface Topography

In general, fault structures of deformed samples depend on confining pressure and sample facies. The roughness of the sheared fault surfaces increased compared to the starting saw-cut. Sandy facies samples display sliding surfaces that are rougher compared to the shaly facies samples deformed at similar conditions (Fig. 3.9). Root mean square roughness S_q also increased with increasing confining pressure. Tiny groove patterns created during sample preparation of the fault (Fig. 3.9a, b) were overprinted by shear deformation.

Samples of the sandy and shaly facies deformed at 5 MPa confining pressure display mating

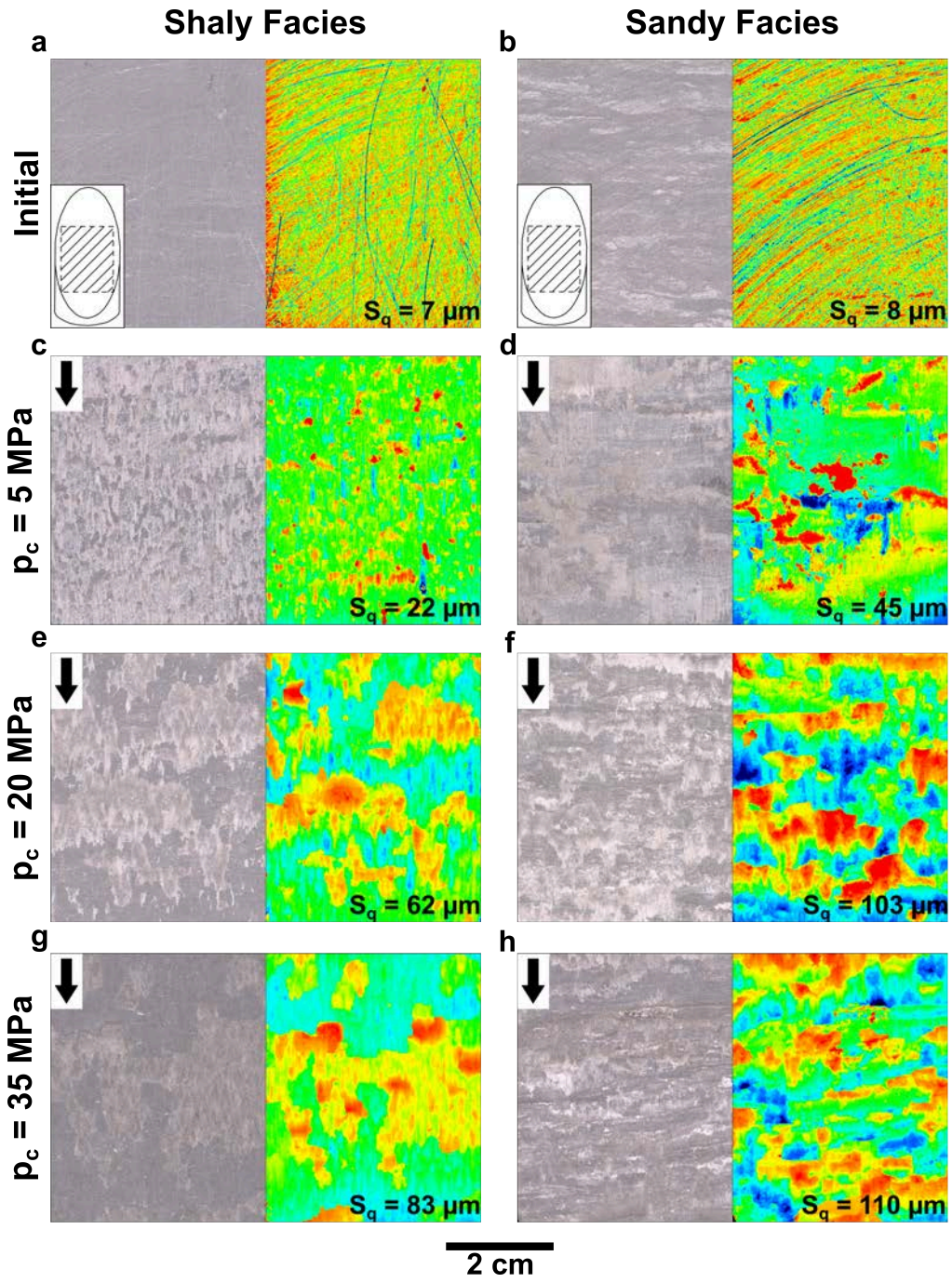

Figure 3.9: Optical image of fault surface structures (footwall sample) with respective microtopography map and average RMS surface roughness S_q (measured by 3D optical profilometry) before (**a**, **b**) and after triaxial tests on Opalinus Clay at confining pressures of p_c = 5, 20 and 35 MPa (top to bottom). Initial roughness was in average S_q = 7.9±2.0 µm. Deformed samples from the shaly facies (left column) reveal smoother surfaces than those of the sandy facies (right column). The color bar on the right shows the elevation of asperities on the fault surface. Arrows indicate movement of missing block. Microtopography maps were acquired on an area of 50 × 40 mm^2 located at the same position for each sample (see inset in **a** and **b**).

fault surfaces covered with finely pulverized wear particles (light grey colored in Fig. 3.9c, d). Gouge particles are distributed rather homogeneously on the surface, with several elongated topographic elevations formed by accumulated gouge. These asperities are smaller and flatter for the shaly facies, but larger and patchier for the sandy facies. Elongated heights on faults of sandy facies samples with their long axis oriented perpendicular to the displacement direction represent sheared sand layers of the wall rock. Topographic lows lack gouge particles and show evidence of striation characterized by grooves oriented in the sense of shear.

Gouge layers changed with increasing confining pressure depending on starting material. At confining pressures >5 MPa slickensides developed and pulverized wear particles on the surfaces decrease gradually. Samples of the shaly facies revealed cohesive, platy, fragmented gouge, that is shinier and less pulverized at higher confining pressure (Fig. 3.9d, g). Topographic lows are characterized by shiny, polished, uniformly flattened and striated slickenside surfaces. Fault surfaces from sandy facies samples show the development of a stepped topography of undulating, asymmetric asperities that are elongated perpendicular to the sliding direction (Fig. 3.9f, h). Roughness S_q of faults from sandy facies samples was larger compared to shaly facies faults.

It is important to note that the overall surface roughness of the samples deformed at confining pressures >5 MPa increases as larger asperities are formed by broken gouge. For these samples, we analyzed separately the topography that has been developed on the surfaces of the wall rock and gouge (Table 3.4). For both facies, RMS surface roughness of slickensides on the wall rock are lower than that of the gouge, and for the sandy facies the roughness of both surface types is distinctly lower compared to the complete analyzed fault surface (Fig. 3.9c-h). As for the whole surface (Fig. 3.9), the sandy facies has a higher roughness compared to the shaly facies for both types of surfaces.

Table 3.4: Root mean square (RMS) surface roughness S_q of wall rock and gouge surfaces of the shaly and sandy facies of Opalinus Clay deformed at 20 and 35 MPa confining pressure (p_c).

Opalinus Clay	p_c = 20 MPa		p_c = 35 MPa	
	S_q Wall Rock (µm)	S_q Gouge (µm)	S_q Wall Rock (µm)	S_q Gouge (µm)
Shaly Facies	12	36	11	38
Sandy Facies	26	64	26	50

p_c confining pressure

Microscopic observations of the developed surface topographies are consistent down to the SEM-scale (Fig. 3.10). Comminuted clastic and phyllosilicate minerals forming pulverized gouge layers show grain sizes in the submicron range (Fig. 3.10a, b). Smooth and polished slickenside surfaces with low topography reveal a homogeneous coating of highly aligned clay particles oriented parallel to the shear surface with striations (Fig. 3.10d, e). We also observed an increase in gouge layer width with increasing pressures. For the sandy facies of OPA deformed at 5 MPa

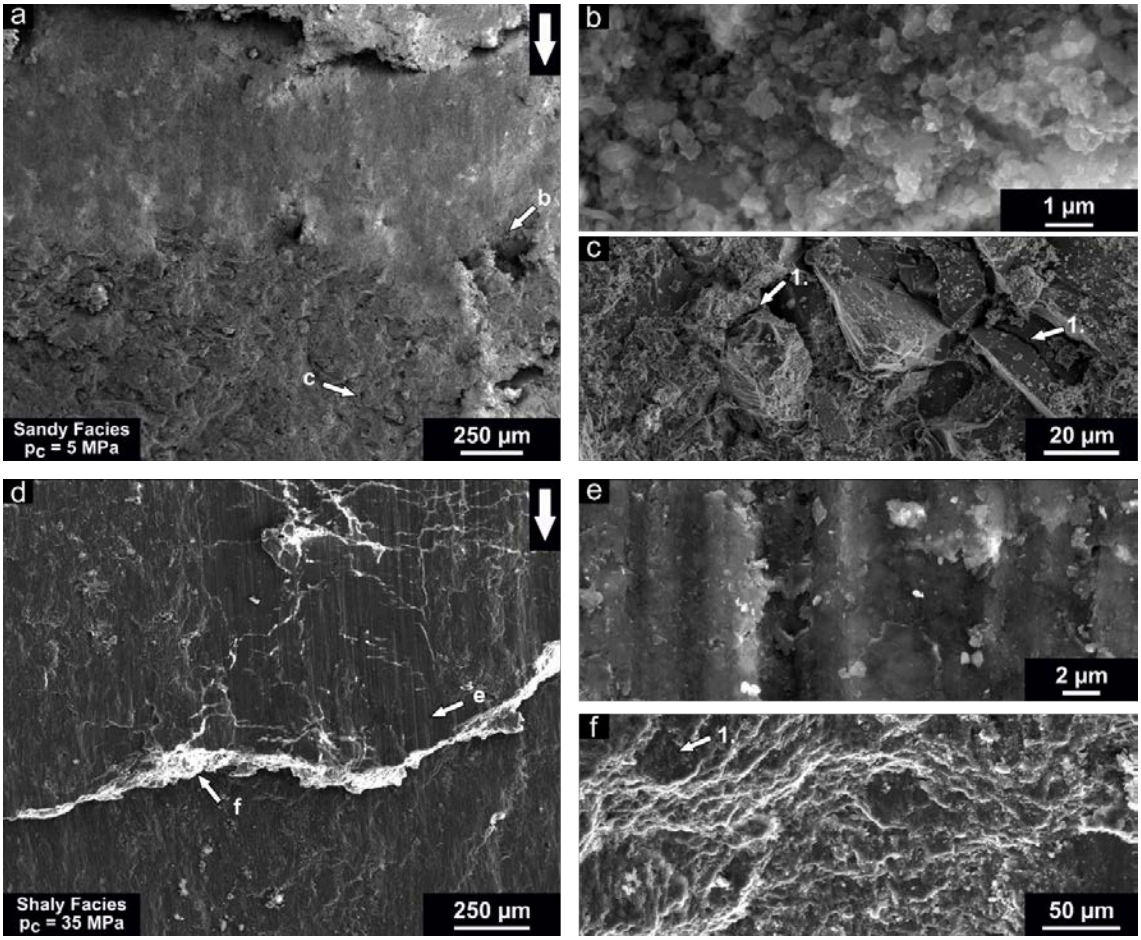

Figure 3.10: SEM image of representative fault surface structures of the sandy facies (**a**) deformed at 5 MPa confining pressure. As shown in **b** at high magnification (inset of **a**), matte, pulverized wear shows an accumulation of fragmented clastic and clay minerals with a lower fabric intensity compared to slickenside surfaces. In areas with little gouge covering (**c**), clastic grains display fractures and signs of rotation in the sense of shear (inset of **a**). Fault surface of the shaly facies sample deformed at 35 MPa confining pressure (**d**) showing the development of slickensides and striations on gouge surfaces and along the boundary between fault zone and wall rock. Polished surfaces are marked by highly laminated clay particles forming a connected smooth covering interrupted by grooves (**e**). At the edges where the cohesive gouge was broken apart after sample separation, several phyllosilicate minerals are aligned in parallel (**f**). Arrows in **a** and **d** indicate movement of the missing block.

confining pressure, in areas with little gouge several clastic grains in sand layers of the wall rock are visible showing microcracks and rotation in the direction of slip (Fig. 3.10c1). At high confining pressure no comparable structures were found in both facies types. Instead, the wall rock was covered homogeneously with slickensides formed by oriented clay particles. In addition, we observed a stepped topography of multiple layers of clay minerals stacked parallel to the slip direction at the edges where the cohesive gouge was broken up after the separation of the sample halves (Fig. 3.10d, f). Some of these "steps" with larger exposed surface areas also show slickensides

(Fig. 3.10f1). This suggests the development of several parallel-oriented shear planes within the fault gouge. Fault surfaces developed at 20 MPa confining pressure show transitional structures compared to samples deformed at 5 and 35 MPa.

Finally, we determined the mineralogical composition of produced gouge from all samples. To this end, a spatula was used to carefully remove the top layer of the sheared fault surface for subsequent XRD analysis (Table 3.5). Compared to the bulk composition of undeformed material (Table 3.1), gouge of the sandy facies displays a clear depletion of quartz (≈-21wt%) content, whereas we observe an enrichment of clay minerals (≈+30wt%). On the other hand, there is no significant compositional difference between the bulk and gouge composition of the shaly facies.

Table 3.5: Mineralogical composition of produced gouge after deformation of the shaly and sandy facies of Opalinus Clay at confining pressures p_c of 5 – 35 MPa.

Opalinus Clay	p_c (MPa)	Clay (wt%)	Quartz (wt%)	Carbonates (wt%)	Feldspar (wt%)	Pyrite (wt%)
Sandy Facies	5	65	24	5	6	<1
Sandy Facies	20	68	21	6	6	<1
Sandy Facies	35	66	20	4	10	<1
Shaly Facies	5	72	9	17	1	<1
Shaly Facies	20	76	8	12	3	<1
Shaly Facies	35	79	9	9	2	<1

p_c confining pressure

3.3.3.2 Microstructural Observations of Wall Rock and Fault Interface

The gouge and damage in the adjacent host rock after deformation was observed using BIB-polished cross-sections prepared parallel to the direction of slip and perpendicular to the fault plane. In reflected light microscopy, gouge appears darker compared to the wall rock, probably due to grain size reduction, with occasional light-colored gouge appearing in lenses. At SEM-scale, brightness difference of these gouge lenses can be attributed to an enrichment of fragmented calcite mineral grains identified by EDX. Note that epoxy resin intruded between the gouge and wall rock interface due to the preferred orientation of particles at shear. Furthermore, SEM analysis

of BIB-cross-sections reveals several microstructural elements that developed within the gouge. Following Logan et al. (1979) (see Fig. A3.4 of the appendix to this chapter) structures may be identified as Riedel, Y, P and boundary shear planes, which opened upon unloading but show signs of offset. We find deformation structures indicating cataclasis, frictional granular flow and intracrystalline plasticity of phyllosilicates as major acting mechanisms accommodating gouge deformation.

Structural fabric elements developed in the gouge of the two facies types are similar for each applied confining pressure (Fig. 3.11) with deformation microstructures generally characterized by grain size reduction of non-clay minerals, a higher fabric intensity compared to the wall rock as well as a strong shape-preferred orientation of clastic and clay minerals that distinctly differs from bedding plane orientation. The clay matrix anastomoses around clastic grains and exhibits a dominant foliation in P-orientation (sub-perpendicular to σ_1-direction), which is frequently interrupted by several R_1 and Y shears. The longest (<150 μm), continuous R_1 shear planes formed in samples deformed at p_c = 5 MPa (Fig. 3.11a, b). Largest clastic particles in the gouge mostly consist of quartz and display grain sizes <50 μm in the sandy and <15 μm in the shaly facies samples. The sub-rounded grains show low sphericity and align parallel to clay matrix foliation (P- and R_1-shear planes). Particles in the gouge indicate a wide grain size distribution ranging from sub-micron to several tens of microns. Gouge layer thickness is heterogenous and a function of confining pressure and facies type revealing layers between 60 – 70 μm for samples deformed at 5 MPa confining pressure up to 200 and 280 μm for samples from sandy facies and 100 and 150 μm for shaly facies samples deformed at p_c = 20 and 35 MPa, respectively.

In gouge layers of the shaly facies of OPA (Fig. 3.11a, c, e), clasts are fully matrix supported and display smaller grain sizes compared to the sandy facies (Fig. 3.11b, d, f). P- and Riedel shear planes may be identified by reopened fractures after unloading, revealing μm-thin shear zones with nanometer-sized clay minerals bent or aligned parallel to the local shear direction. Mineral clasts generally align with their longest axis parallel to gouge foliation. Shear zones anastomose around small clastic grains, resulting in a dense network of distributed shear planes. In both facies' types we find former framboidal pyrite (Fig. 3.11a3, Fig. 3.11f1) distributed along Riedel and P-shear planes as well as mica delaminated and bent in slip direction (Fig. 3.11f3). Active fragmentation by cataclasis inside the gouge is indicative for calcite grains forming trails of broken clasts and spalling (Fig. 3.11a4, Fig. 3.11c1, Fig. 3.11e1). Fossils, which are abundant in the undeformed material and wall rock of the shaly facies, are absent in the developed gouge and have probably completely disintegrated. Samples of the shaly facies that were deformed at confining pressures of 20 and 35 MPa, reveal several Y-shears that intersect with P- and R_1-shear planes forming an undulating array of lentoid microlithons of varying size with sigmoidal shaped shear boundaries (Fig. 3.11c2, Fig. 3.11e). Y-shears seem to be less abundant in gouge produced at 5 MPa confining pressure.

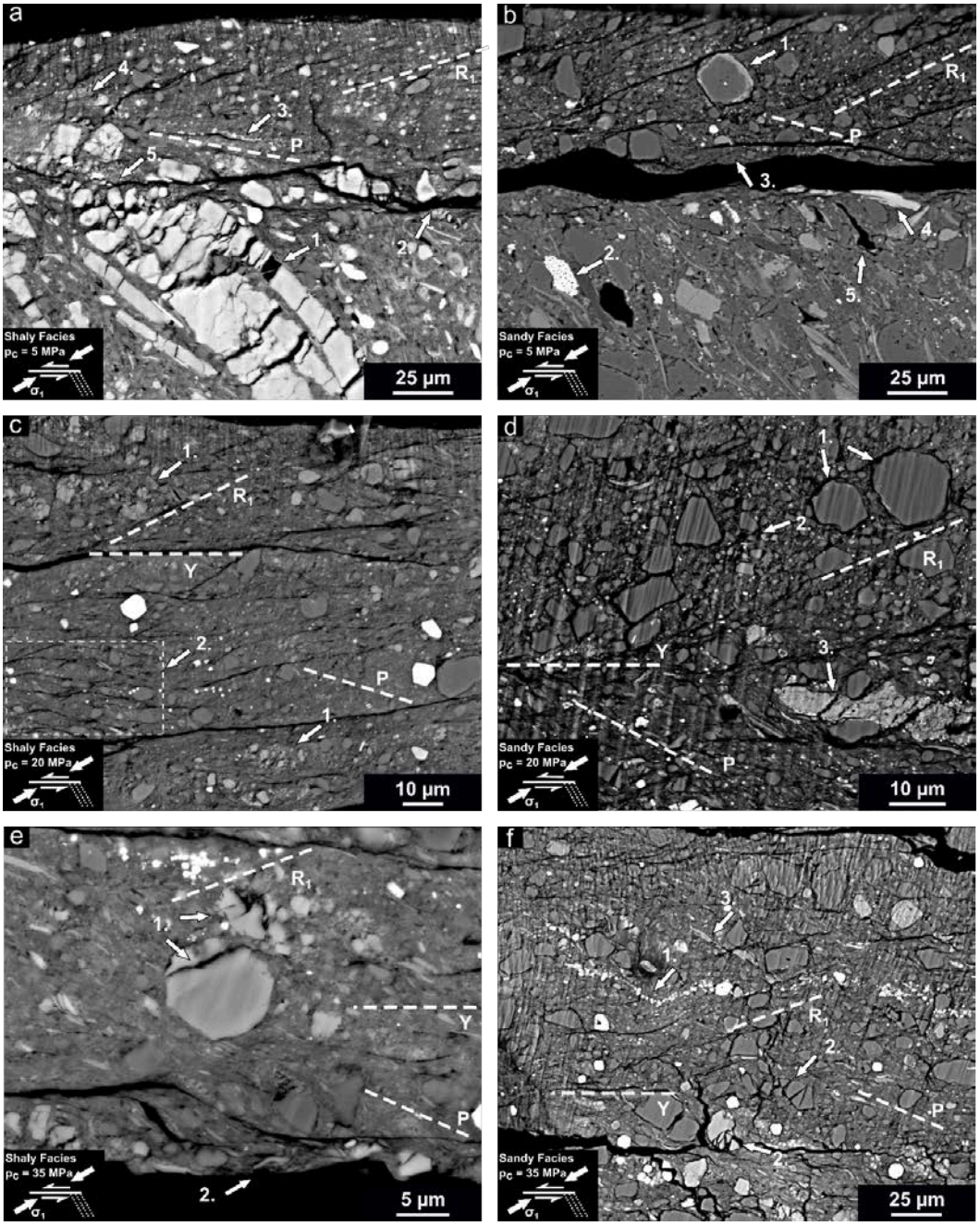

Figure 3.11: Micrographs of microstructures developed in gouge of the shaly (**a**, **c**, **e**) and sandy (**b**, **d**, **f**) facies of Opalinus Clay deformed at p_c = 5 – 35 MPa showing the development of several Riedel-, boundary- and Y-shear planes. Longest axis of phyllosilicate minerals preferentially aligns parallel to P-orientation. In comparison to the shaly facies, gouge development in the sandy facies is dominated by active cataclasis indicated by several broken clastic minerals and grain fragmentation. Instead, several distributed µm-thin shear zones accommodate strain in the gouge of the shaly facies with only minor cataclasis. Confining pressure, bedding plane orientation of the wall rock as well as shear and loading direction are indicated in the black boxes at the bottom left of each picture. Further details (also labeled by numbers) can be found in the text (chapter 3.3.3.2).

Gouge of sandy facies samples is characterized by a larger number of mineral clasts of different sizes, resulting in a broader grain size distribution, a more heterogeneous appearance as well as a higher porosity. Larger clasts coated with clay minerals often show particles rotated between adjacent R_1-shear planes (Fig. 3.11b1, Fig. 3.11d1). Furthermore, we find broken feldspar and quartz grains, which either display single fractures open subparallel to the σ_1-direction (Fig. 3.11d3, Fig. 3.11f2) or are highly comminuted (Fig. 3.11d2, Fig.19f) resulting in angular fragments <1 µm with large interparticle porosity. With progressive strain, clastic fragments may become more spherical and rounded as a result of abrasion and flaking, whereas interparticle pore space seems to decrease as clasts are reworked in the clay matrix. In sandy facies gouge, cataclasis increases with increasing confining pressure shown by an increasing amount of broken clastic grains with no or little offset as well as trails of fragmented grains. Slip also localized in R_2-shear planes in samples deformed at a confinement of 35 MPa (see Fig. A3.5c of the appendix to this chapter). Comparable to the shaly facies, the abundancy of Y-shears seems to be lowest at 5 MPa confining pressure. Furthermore, Y-shears seem to develop preferentially in areas of increased clay matrix content.

Increasing contribution of cataclasis, number of undulating shear networks as well gouge layer thickness indicates continuous delocalization of strain within the developed gouge with increasing confining pressure.

In the shaly facies but also in in clay-rich areas of the sandy facies, gouge is bordered by very discrete, thin boundary shears (<5 µm width) in which clay minerals align parallel to the fault surface (Fig. 3.11a2, Fig. 3.11b3, Fig. 3.11e2), creating a sharp contact to the bedding plane orientation of the wall rock (Fig. A3.5d1, Fig. A3.5e1). On the other hand, larger calcite grains in the shaly facies or clasts in grain-supported (sand layers) layers in the sandy facies frequently display inter- and intragranular fractures close to the gouge-wall rock boundary. The fractures are oriented sub-parallel to the σ_1-direction, indicating Mode I fracturing and stress concentration at grain contact surfaces (Fig. 3.11a1, Fig. A3.5a1, Fig. A3.5b1). Fractured grains often display matching grain boundaries without visible offset and apertures of several micrometers wide.

In general, and irrespective of confining pressure, the width of the damage zone adjacent to the saw-cut faults is very limited and does not exceed about 0.5 mm in sandy facies samples and is less than 0.2 mm wide in shaly facies samples. However, approaching the gouge-wall rock interface, a gradual fabric transition is sometimes indicated by fractured grains rotated towards the shear zone in sense of slip. This is shown by asymmetric opened apertures and bending and delamination of micas (Fig. 3.11b4, Fig. A3.5d1). Mineral clasts that are close to boundary shears are comminuted or flaked and dragged into the gouge (Fig. 3.11a5, Fig. A3.5a2). In the sandy facies, intergranular fractures are abundant in sand-layers, with almost undeformed clay-minerals filling the interparticle pore space (Fig. A3.5b3). Boundary shears pass through this porous, comminuted zone (Fig. A3.5b4) eroding the wall rock and supplying the gouge material. With increasing con-

fining pressure, the thickness of the damaged zone decreases and the gouge-wall rock-interface becomes smoother and sharper (cf. Fig. A3.5a, Fig. A3.5b2, Fig. A3.5c1). This agrees with our macroscopic observation that the number of polished surfaces increased with increasing confinement.

Strain accumulation in the wall rock of both facies' types is indicated by pore collapse of the clay matrix shown by compacted clay minerals that align parallel to bedding and around larger clasts. We also found stretched organic matter and collapsed framboidal pyrite (Fig. 3.11b2 and 5, Fig. A3.5f, Fig. A3.5g1). With increasing confining pressure ($p_c > 5$ MPa), we observe enhanced alignment and compaction of clay platelets in the matrix as well as collapsed fossils in the shaly facies (Fig. A3.5g2). Sand layers in sandy facies wall rock show occasionally trans- or intergranular cracks opened sub-parallel to the maximum stress direction. Furthermore, clay particles in the interparticle pore space of grain-supported areas show no signs of compaction (random particle orientation) in comparison to matrix-supported domains.

3.4 Discussion

Triaxial deformation on saw-cut samples from the shaly and sandy facies of Opalinus Clay performed at confining pressures between 5 and 35 MPa reveal a combination of elastic and inelastic deformation. Strain is partitioned between fault slip and bulk rock deformation. With increasing confining pressure, bulk deformation increases at the expense of localized fault slip. At 5 MPa pressure, all samples show brittle deformation with small stress drops initiating fault slip and subsequent shearing at almost constant shear stress. With increasing confining pressure, stress-strain curves show non-linear strain hardening without dynamic localization upon fault reactivation. Shear strength at fault reactivation increases with increasing confining pressure, whereas the friction coefficient decreases. Friction coefficients at fault reactivation of the sandy facies are slightly higher (μ = 0.57 – 0.49) compared to the shaly facies (μ = 0.62 – 0.43). SHS tests reveal negligible strengthening and negative or close to zero healing rates. After relaxation, stress drops upon reloading become less sharp with increasing confining pressure. At all conditions, gouge is produced and gouge layer thickness increases with confining pressure. Microstructural observations suggest a complex combination of deformation mechanisms operating concurrently. Cataclasis and brittle creep involving fragmentation and rotation of quartz, feldspar and calcite, frictional granular flow of clastic and phyllosilicate minerals grains is dominant assisted by intracrystalline plasticity of phyllosilicates. With increasing confining pressure, we observe a shift in strain partitioning from dominantly localized fault slip towards ductile deformation of the wall rock with reduced slip along the saw-cut. This is corroborated by microstructural observations in conjunction with the recorded mechanical and acoustic data. In the following, we summarize and combine the obtained experimental results to explain the observed change in the deformation

behavior of faulted OPA from the sandy and shaly facies with increasing confining pressure. The results are compared to previous laboratory studies and implications for the mechanical behavior and mode of reactivation of faults in clay-rich host rocks will be discussed. Finally, deformation mechanisms during stress relaxation leading to frictional strengthening are examined to evaluate long-term stability of faults in OPA.

3.4.1 Fault Slip Behavior

3.4.1.1 Deformation Mechanisms and Behavior

For the samples deformed at 5 MPa confining pressure, we observe a rapid increase in bedding-perpendicular P-wave velocity at the beginning of axial loading (Fig. 3.8a, b). This indicates increasing contact area of surface asperities, resulting in better fault coupling as well as the closure of cracks and pores in the rock matrix. Compaction of bedding-parallel aligned pores has also been reported from experiments performed on intact shaly and sandy facies samples loaded perpendicular to bedding (Popp and Salzer 2007; Siegesmund et al. 2014). With further loading, the saw-cut fault starts slipping once the shear strength of the contact asperities is reached, resulting in a small stress drop. At 5 MPa confining pressure, yield stress of the bulk matrix σ_y is almost equal to the stress at reactivation σ_f. At the onset of fault slip, the slope of P-wave velocity perpendicular to bedding vs. time decreases. In sandy facies samples, the onset of fault slip is accompanied by acoustic emission activity, localizing on and near the saw-cut surface area (Fig. 3.8b, Fig. A3.3). Both observations suggest damage initiation and fragmentation of asperity contacts at the fault surface by microcracking of rigid minerals (dominating in the sandy facies) and grain rotation. In accordance with Popp and Salzer (2007) and Siegesmund et al. (2014), bedding-parallel P-wave velocity of the matrix is almost constant and increases at a much lower rate than perpendicular to it.

The concurrent increase of stress and vertical P-wave velocity at a relatively high rate indicates ongoing compaction of pore space, grain reorganization and particle rotation, presumably parallel to P-shear orientation. For both facies, the onset of brittle creep beyond yield stress is associated with strain hardening (accompanied by a second stress drop for the shaly facies sample). Matrix deformation and fault slip is accompanied by the formation of boundary and R_1-shear planes, which may contribute to the observed hardening (Haines et al. 2013). With continuing fault slip, the vertical P-wave velocity is almost constant and increases at a low, steady rate, suggesting a nearly stable microstructural configuration of the gouge. The increase in vertical P-wave velocity is likely due to gouge compaction by porosity reduction and grain fragmentation.

Axial matrix strain accounts for about 3 and 5% of the total deformation of the sandy facies and shaly facies samples, respectively. In turn, this indicates fault slip is strongly localized. This is consistent with our microstructural observations showing the formation of P- and Riedel shear

planes (Fig. 11). The relatively high friction coefficients ($\mu \approx 0.85$, cf., Fig. 3.2e, f) and the development of incohesive and granular gouge (Fig. 3.9) indicate the dominance of dilatant cataclastic deformation mechanisms involving transgranular microcracking, abrasion and grain rotation of mineral grains as well as frictional sliding of phyllosilicates orienting parallel to shear planes. The observed friction coefficients are similar to commonly observed values (Byerlee 1978). Similarly, high friction coefficients (peak and residual) in the range of $\mu = 0.85$ were also reported for the shaly facies by Wild and Amann (2018) at mean effective pressures $p_c < 5$ MPa as well as for the sandy facies by Zhang and Laurich (2019) at $p_c < 25$ MPa. Also, interlayer bond strength of basal (001) planes of clay minerals increases with decreasing water content and may enhance brittle wear and abrasion (e.g., Moore and Lockner 2004; Morrow et al. 2017).

Similar to the experiments performed at 5 MPa confinement, all samples deformed at 20 and 35 MPa confining pressure show a strong initial increase in bedding-perpendicular P-wave velocity due to elastic compaction. Hardening beyond yield stress is associated with further but smaller velocity increase related to progressive closure of the saw-cut fault and compaction of bedding parallel aligned pores (Fig. 3.8c-f). P-wave velocity parallel to the bedding plane remains relatively constant for the shaly facies. On the other hand, bedding-parallel P-wave velocity starts decreasing more significantly above yield stress in the sandy facies (Fig. 3.8d, f). Fortin et al. (2006) attributed the P-wave velocity reduction in experimentally deformed sandstones to the crushing of clastic mineral grains that dominate pore collapse and compaction. Due to the higher quartz and feldspar content of the sandy facies, damage in the bulk seems to be dominantly accommodated by microcracking, compared to the shaly facies, where pore collapse seems to dominate. This is consistent with the triaxial deformation tests on OPA performed by Popp and Salzer (2007) and Siegesmund et al. (2014), which show a higher loading-induced decrease of bedding parallel P-wave velocities for sandy compared to shaly facies. Note, that strain gauges on the upper and lower saw-cut blocks show bulk compaction in accordance with increasing axial velocity, whereas bedding-parallel P-wave velocities suggest local dilation by microcrack formation.

As no stress drop is observed at fault reactivation, we suspect developed shear fabrics to be immature and not pervasive. This may be explained by the continuing deformation of the bulk matrix at fault reactivation, resulting in low fault displacement that inhibits localized shear fabric development in the gouge but may also indicate a change of deformation mechanism towards an increasing contribution of viscous processes. The latter assumption is supported by the decrease of total acoustic emission activity (Fig. 3.8) in the sandy facies with increasing confining pressure as well as the generally decreasing friction coefficient of both facies (Fig. 3.2e, f). With increasing confining pressure, the fault contact area of the two saw-cut surfaces increases. Dilatant microfracturing of asperities is increasingly suppressed during fault slip assisting fault creep and the development of ductile shear zones as more space is needed for strain accommodation. This agrees with the findings of Moore and Lockner (2004) who suggested that clay gouge friction may

decrease with increasing confining pressure due to the progressive alignment of weak (001) basal planes with shear planes. Shear-induced particle rotation close to the saw-cut surface may also enhance gouge layer thickness as particles are incorporated into the shear zone. This may result in the development of boundary shear planes and eventually the formation of a sharp contact with the wall rock (Fig. 3.11, see Fig. A3.5). Cataclastic (grain fragmentation) and granular (grain rotation) flow with particle sliding along anastomosing µm-thin shear zones of aligned clay particles control deformation. This agrees with slickenside surfaces (Fig. 3.10d) that developed adjacent to gouge and wall rock in samples deformed at confining pressures >5 MPa.

Another factor potentially contributing to the reduction of friction coefficient with increasing confining pressure is the residual water content remaining in the samples after drying at 50 °C (see chapter 3.2). Friction of clay minerals is strongly influenced by adsorbed water (e.g., Ikari et al. 2007, 2009). Given the fixed residual water content of the sandy (≈0.4 wt%) and shaly (≈1.0 wt%) facies, the degree of saturation depends on porosity, which closes progressively with increasing confining pressure and strain. Therefore, the degree of saturation of the samples is potentially increasing with increasing confining pressure. As a result, the reduction in friction due to clay mineral alignment and changing deformation mechanisms may be further enhanced by water-aided surface lubrication of clay minerals. Furthermore, with decreasing porosity water can fill the available pore space, which can alter the effective stress state (e.g., Saffer and Marone 2003; Ikari et al. 2007; Morrow et al. 2017).

We observe continuing strain hardening and non-linear increase of vertical P-wave velocity with progressive slip. At elevated pressures, more strain is accumulated in the bulk matrix, leading to compaction. For the shaly facies samples, we estimate 28 and 41% of total deformation being accommodated in the bulk at 20 and 35 MPa respectively. For sandy facies samples, the bulk strain is 18 and 34% at 20 and 35 MPa, respectively. In addition, hardening may result from shear-enhanced compaction involving comminution and cataclasis. Strain hardening has been associated with an increasing gouge layer thickness (Morrow et al. 2017).

Interestingly, for the sandy facies deformed at a confining pressure of 20 MPa (Fig. 3.8d), a stress drop was observed after ≈4000 s (corresponding to a total axial strain of ≈3.5%), after which the bulk strain gauges show dilatancy. Differential stress and vertical P-wave velocity continue to increase, as observed for samples deformed at 5 MPa. We posit that with shear and compaction the gouge strengthens causing abrupt localized failure, once the strength is exceeded (Baud et al. 2006). Likely, at p_c = 35 MPa, the pressure was sufficiently high to suppress the dilatant behavior of the matrix, which is in line with the minor increase of axial velocity (Fig. 3.8f). Dilatancy of the bulk is therefore an important mechanism, affecting the partitioning of the fault and matrix deformation. Due to the higher content of clastic minerals in the sandy facies, dilatant microcracking is more active in the sandy facies, whereas matrix compaction and pore collapse are more active in the clay-rich shaly facies.

Microstructure analyses of deformed samples show microfracturing, abrasion and grain rotation of clastic minerals, intracrystalline plasticity of phyllosilicates including bending, kinking and boudinage as well as frictional sliding of clay and non-clay mineral grains all contribute to sample deformation and strain localization on the saw-cut surface. The relative contribution of each mechanism to deformation depends on the mineralogic composition as well as on the applied confining pressure. Our observations suggest that grain crushing, frictional sliding and rigid body grain rotation along slip surfaces are dominant at low confining pressure in all samples. At elevated pressures strain is accommodated by cataclastic flow in the sandy facies and by granular flow in the shaly facies. Shear zone formation controlled by the frictional sliding of phyllosilicates leads to connected shear networks. Increasing contribution of cataclasis, number of undulating shear networks and gouge layer thickness indicates continuous delocalization of strain within the developed gouge with increasing confining pressure. Therefore, the fault architecture of OPA changes with increasing confining pressure and/or decreasing overconsolidation. At 5 MPa confinement, a thin, central slip surface develops. This is in contrast to a thick, viscous shear zone produced at elevated pressures, where slip is accommodated on boundary shears at the interface between gouge and wall rock and along distributed shear planes within the gouge (cf., Fagereng and Sibson 2010). The obtained mechanical and acoustic data as well as the developed microstructures indicate a transition from brittle towards ductile deformation of OPA with increasing confining pressure at the applied conditions.

Our experimental observations show similarity to grain scale deformation mechanisms identified in the "Main Fault" at the Mont Terri URL (Laurich et al. 2014, 2017, 2018), in particular grain size reduction by cataclasis and abrasion, frictional granular flow as well as bending of phyllosilicates. However, due to the short time scale of our experiments performed on dried sample material, other processes observed under natural conditions such as pressure solution/mineral precipitation and mineral formation (Laurich et al. 2014) are not captured. Microfabrics developed in the shaly facies samples deformed at confining pressures $>$5 MPa show great similarity to the main structural elements of the "Main Fault" exposed in Mont Terri URL (cf., Laurich et al. 2014, 2017, 2018; Jaeggi et al. 2017b). There, the fault gouge displays sigmoidal P-foliation (S-C fabric) and an anastomosing network of µm-thick shear zones most in Y and R_1 orientation, which is bordered by sharp Y-shears forming slickenside surfaces. Comparing the in-situ gouge fabric at Mont Terri URL, formed by faulting of a slightly overconsolidated protolith (max. burial $\approx$1350 m) at an overburden of $\approx$1000 m (Nussbaum et al. 2011, 2017), with the experimentally developed microfabrics, we infer ductile, aseismic deformation behavior of the "Main Fault", in agreement with field studies (Laurich et al. 2017, 2018; Hopp et al. 2022).

Interestingly, XRD analysis of sheared gouge material of the sandy facies shows a clear enrichment of the clay mineral fraction in comparison to the bulk material, suggesting a stronger incorporation of clay into the gouge material compared to the more competent sand-rich layers.

These observations may have important implications for the clay smear potential (e.g., Vrolijk et al. 2016) and the sealing efficiency of fractures in the OPA sandy facies. In contrast, gouge produced in the shaly facies has a similar mineralogic composition compared to the starting material. This has also been reported for natural gouge from the "Main Fault" and the surrounding shaly facies host rock at the Mont Terri URL (Laurich et al. 2017; Wenning et al. 2021).

3.4.1.2 Fault Strength and Strain Localization

OPA shares deformation features of both weak rock and stiff soil (NAGRA 2002). As such, petrophysical (e.g., porosity, density) and mechanical properties (e.g., strength, compressibility and stiffness) depend on the maximum burial depth and diagenesis experienced during geological history. When a sedimentary layer is subjected to unloading after burial compaction, e.g., by geological uplift, it remains over-consolidated due to residual plastic volumetric strain. The over-consolidation ratio (OCR), expressed as the ratio of effective preconsolidation pressure to present effective vertical stress (Azizi 1999), may be used to characterize the burial history of sediment and predict its deformation behavior (Paterson and Wong 2005) when chemical cementation and horizontal tectonic compression are negligible (e.g., Ingram and Urai 1999). In the following, we discuss the obtained results in the framework of critical state theory (e.g., Cam-Clay-Model; Schofield and Wroth 1968; Roscoe and Burland 1968) and analyze volumetric strain changes in the mean effective stress ($p = (\sigma_1 + 2p_c)/3$) and differential stress ($\sigma_d = \sigma_1 - p_c$) space in an effort to explain the observed mode of fault reactivation and strain partitioning of the tested saw-cut samples.

In critical state models, the yielding of a porous material follows an approximately elliptically shaped, "capped" surface in the p-σ_d space, which is limited by prior normal consolidation (e.g., Schofield and Wroth 1968; Wood 1990). The yield surface expands with increasing normal consolidation or decreasing porosity, whereas elastic deformation is restricted to overconsolidated materials (Azizi 1999). It is divided by the critical state line that separates dilatant, brittle deformation including strain softening and shear localization (Hvorslev line) from compacting, ductile deformation involving strain hardening and shear-enhanced compaction (Roscoe line). With progressive shearing beyond yielding, the load path will terminate in both cases when the critical state is reached, hence when shear deformation occurs at constant volume, effective differential or mean stress, irrespective of the loading history. Describing the deformation and failure mode depending on effective stress and porosity, critical state, cap models were also applied in characterizing the constitutive behavior of several porous rocks such as sandstone, limestone, tuff and porous basalt (e.g., Scott and Nielsen 1991a, b; Wong et al. 1997; Cuss et al. 2003; Loaiza et al. 2012; Rutter and Glover 2012; Wong and Baud 2012; Nicolas et al. 2016). Failure of siliciclastic, porous rocks across the brittle-ductile transition is primarily determined by pressure-sensitive cataclastic defor-

mation mechanisms (cf., Rutter and Hadizadeh, 1991).

For simplicity, we assume identical initial porosity of the tested samples of the shaly ($\varphi_{shalyfacies}$ = 15.7±1.3vol%) and the sandy facies ($\varphi_{sandyfacies}$ = 11.1±1.1vol%). Furthermore, we assume that the volumetric strain measured by the strain gauges (average of SGV1/2, SGH1/2 in Fig. A3.1a) records a change of total porosity ($d\varphi = ((V_{sample} \times \varphi) - \varepsilon_{vol} \times V_{sample})/V_{sample}$). Following Azizi (1999), we calculated the evolution of the specific volume via the expression $\nu = 1 + ((\varphi - d\varphi)/(1 - (\varphi - d\varphi)))$ to represent porosity changes associated with the stress path in the p-σ_d-ν space (Fig. 3.12). We further neglect any potential pore pressure changes since the samples were dried before testing and exposed to drained boundary conditions during hydrostatic and axial deformation. Figures 3.12a, b show hydrostatic loading curves (solid line) of the shaly and sandy facies derived from volumetric strain measurements of the specimens deformed triaxially at a confining pressure of 35 MPa. Hydrostatic pre-compaction may represent normal consolidation (Azizi 1999) and resulted in higher volume reduction in the shaly compared to the sandy facies. During a hold phase of ≈18 h duration at 50 MPa confining pressure, we observe creep compaction of the shaly facies and subsequent permanent specific volume reduction after unloading for both facies. Hydrostatic unloading curves (dashed line in Fig. 3.12) were interpolated from the final volumetric deformation obtained for each sample after reducing the confining pressure to 20 and 5 MPa, respectively. Due to the higher content of strong mineral phases (e.g., quartz, carbonates, feldspar) and lower porosity, the sandy facies generally displays higher elastic stiffness and strength parameters compared to the shaly facies, as has also been shown in previous experimental studies on OPA (cf., Popp and Salzer 2007; Gräsle and Plischke 2010, 2011; Siegesmund et al. 2014; Wild and Amann 2018; Favero et al. 2018; Zhang and Laurich 2019; Crisci et al. 2021; Schuster et al. 2021). As confining pressures were reduced for subsequent testing, samples become overconsolidated. During subsequent loading, the elastic strain component of a specific stress path depends on OCR, limited by the yield point, forming a so-called elastic wall for different stress paths (Azizi 1999). In our experiments, the elastic wall (blue area in Fig. 3.12) is bounded by the unloading curve in the p–ν space and the yield stress of the bulk matrix. In this framework, it is assumed that the elastic wall is limited by maximum normal consolidation (Azizi 1999), which is why we extrapolated the upper limit of the wall to the p–ν condition before unloading.

The differential stress paths of the tests as well as the determined yield stress and stress at fault reactivation are displayed schematically in p-σ_d-ν space (Fig. 3.12). Elastic deformation is limited by a capped yield surface. For the specimens deformed at 5 MPa and OCR = 10, the stress at fault slip (indicated by black dots in Fig. 3.12) coincides with the yield stress and the upper limit of elastic matrix deformation. The release of stored elastic strain energy upon failure resulted in a stress drop (e.g., Byerlee 1970; Dieterich 1972) via stable slow slip (c.f., chapter 3.3.1.2). With ongoing axial shortening, deformation is first accommodated by a combination of fault slip and

matrix compaction until fault slip and dilatancy dominate (Fig. 3.12; blue stress path). An increase in differential stress after the onset of dilation was also observed in triaxial tests performed on full cylinder samples of OPA from both facies (e.g., Naumann et al. 2007; Amann et al. 2012; Wild and Amann 2018; Zhang and Laurich 2019; Winhausen et al. 2022), where the dilation threshold of the matrix was in the range of ≈80 – 90% of peak stress. These studies also showed that dilatancy is suppressed with increasing confining pressure indicating a transition of failure mode from brittle to ductile.

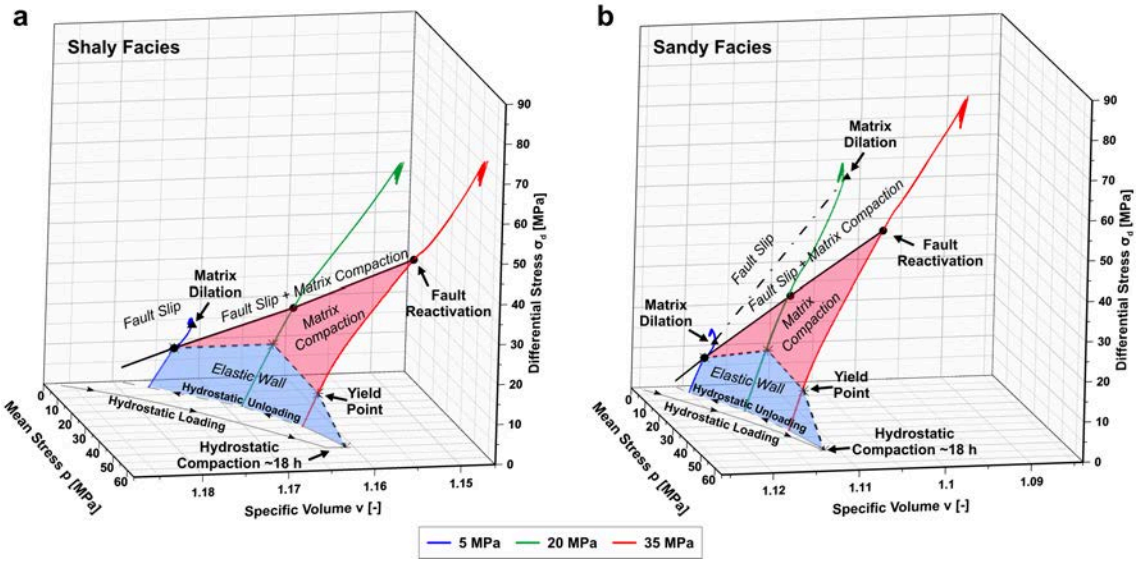

Figure 3.12: Stress paths of the shaly (**a**) and sandy (**b**) facies of Opalinus Clay deformed at p_c = 5 (blue), 20 (green) and 35 MPa (red) projected in the three-dimensional space of mean stress – differential stress – specific volume. The use of the hydrostatic unloading curve in conjunction with determined yield point of the bulk, fault reactivation and matrix dilation stress allowed mapping of the observed deformation modes. Stress at onset of fault slip is indicated by black dots. Matrix dilation is indicated by black triangles.

For all samples deformed at confining pressures >5 MPa, the bulk matrix yields before fault slip starts, resulting in strain-hardening matrix compaction. The stress paths (red and green paths, Fig. 3.12) approximately follow the Roscoe surface (red area Fig. 3.12). After the onset of fault slip, deformation occurs by a combination of fault slip and matrix compaction. All tested samples showed strain hardening and did not reach a critical state. This is also reflected in the gouge microstructures that evolve continuously without reaching a steady state (c.f., Haines et al. 2013; Morrow et al. 2017).

Stress at the onset of fault slip σ_f, increases linearly with increasing mean stress (Fig. 3.12). We use σ_f to fit a linear Mohr–Coulomb (MC) failure envelope and determine the friction coefficient at fault reactivation μ_f. In p-σ_d space, stress at fault reactivation may be expressed as

$\sigma_f = a + M \times p$, where a is the intercept with the σ_d axis and M is the slope. Both parameters are transformed to the Mohr–Coulomb parameters friction angle (ϕ) and cohesion (c) using the expressions: $\phi = tan^{-1}\mu = sin^{-1}((3 \times M)/(6 + M))$ and $c = (a \times tan\phi)/M$ (Azizi 1999). Least square regression yields M_{shaly} = 0.85 and M_{sandy} = 1.01 (Table 3.6) corresponding to ϕ = 22° and 26°, respectively. The resulting friction angles ϕ correspond well to the angle of the saw-cut with the loading direction, θ (e.g., Jaeger 1960; Sibson 1985). From $\theta = 45 - \phi/2$ (Jaeger et al. 2007), we infer θ_{shaly} = 34° and θ_{sandy} = 32°. The corresponding friction coefficients are μ_f = 0.4 and 0.48, respectively (Table 3.6), in good agreement with experimentally determined sliding friction coefficients for the shaly facies of μ = 0.36 obtained by Orellana et al. (2019) on dried artificial gouge of OPA. For the sandy facies, Ferrari et al. (2020) report friction coefficients at peak strength of μ = 0.64 – 0.73 performed at $p_c \leq 1$ MPa and Orellana et al. (2020) report of μ = 0.38 at a normal stress of ≈8 MPa, both under wet conditions. The slightly higher friction coefficient of the sandy facies compared to the shaly facies maybe is related to the higher quartz content and reduced clay content of the sandy facies.

Table 3.6: Frictional parameters of the shaly and sandy facies of Opalinus Clay determined at fault reactivation using a linear Mohr-Coulomb failure criterion.

Opalinus Clay	Fault reactivation				
	M (-)	α (MPa)	ϕ (°)	μ_f (-)	c (MPa)
Shaly Facies	0.85±0.02	3.5±0.7	22±1	0.4±0.01	1.7±0.4
Sandy Facies	1.01±0.01	1.4±0.2	26±<1	0.48±<0.01	0.6±0.1

ϕ friction angle, μ_f friction coefficient at fault reactivation, c cohesion

Our experimental results demonstrate the gradual transition from brittle to ductile deformation with increasing confining pressure for OPA. Brittle, highly localized fault slip is generally present as long as matrix yield strength is similar or larger than fault strength. Once fault strength exceeds matrix yield strength, semi-brittle deformation behavior is initiated with increasing delocalization of strain, which is progressively partitioned into the wall rock. This was also observed in deformation experiments on faulted Berea sandstone (Scott and Nielsen 1991a, b) and Carrara marble (Meyer et al. 2019; Aubry et al. 2020). Meyer et al. (2019) described the influence of bulk yield stress σ_y, fault strength σ_f and matrix failure/flow stress σ_{matrix} on strain partitioning of Carrara Marble. The authors found that the relative contribution of fault slip is proportional to the stress ratio $(\sigma_f - \sigma_y)/(\sigma_{matrix} - \sigma_y)$. Therefore, the pressure at which the frictional strength of the fault exceeds bulk strength defines the brittle-ductile transition, as suggested by Byerlee (1968), giving the pressure limit for strain partitioning beyond which the fault should remain permanently locked and all strain is accommodated by diffusive matrix deformation.

To determine the pressure at the transition to ductile deformation, we compare the frictional

strength of the saw-cut faults from this study with peak strength data of cylindrical samples obtained in triaxial deformation tests from several studies performed on unsaturated OPA from the shaly (water content <6.3 wt%) and the sandy facies (water content <4.5 wt%) deformed parallel and perpendicular to bedding orientation (Fig. 3.13). The data for shaly OPA are measured by Nüesch (1991), Rummel and Weber (1999), Rummel et al. (1999) and Gräsle and Plischke (2010). Data for sandy OPA are adopted from Siegesmund et al. (2014), Zhang and Laurich (2019) and Schuster et al. (2021).

The peak strength envelope for all samples in the range of applied confining pressures may be described by nonlinear failure criteria (e.g., Nüesch 1991; Naumann et al. 2007; Amann et al. 2012; Wild and Amann 2018). Assuming that the investigated range of strain rates, temperatures and water contents has no significant influence on peak strength at failure for dried samples (Schuster et al. 2021), we applied least square regression to fit the data to the empirically derived Hoek–Brown (HB) failure criterion for intact rock properties: $\sigma_1 = p_c + \sigma_{ci}(m_i(p_c/\sigma_{ci}) + 1)^{0.5}$, which relates σ_1 at peak to confining pressure p_c, uniaxial compressive strength (UCS) σ_{ci} and a material-specific constant m_i (Hoek and Brown 2019). Obtained m_i for shaly facies samples (Fig. 3.13a) corresponds well to previous work reporting $m_i = 7\pm2$ for siltstones (Hoek 2007). Also, σ_{ci} agrees with UCS of unsaturated shaly facies OPA (σ_{ci} = 20 – 25 MPa, NAGRA 2002) and/or OPA with low porosity (σ_{ci} = 31 – 34 MPa, Jahns 2013). For the sandy facies' samples (Fig. 3.13b), m_i is larger compared to the shaly facies with m_i values close to those reported for sandstones (m_i= 17±4; Hoek 2007).

Stress data at the onset of fault slip, σ_f, were fit with a linear MC envelope, $\sigma_f + p_c = \sigma_1 = np_c + \sigma_{ci}$, where the slope n is related to μ_f by the equation $\mu_f = (n-1)/(2\sqrt{n})$ (Zoback 2007). Due to the limited data available, we assume the validity of a linear MC criterion for fault reactivation, hence constant μ_f with increasing confining pressure, and extrapolate the intersection of the fault reactivation and matrix failure envelope. We obtain a confining pressure of about p_c = 165 MPa and p_c = 186 MPa at the intersection for the shaly and sandy facies of OPA, respectively (Fig. 3.13a). Shaly facies samples become ductile at lower pressures compared to sandy facies samples in agreement with the observed difference in strength. This is likely due to the high clay content of the shaly facies.

Finally, we use the obtained HB-failure envelope to extrapolate σ_{matrix} for OPA and calculate the relative slip contribution, where both fault slip and matrix compaction contribute to total deformation. Following Meyer et al. (2019), we find that slip partitioning is in good agreement with the stress ratio $(\sigma_f - \sigma_y)/(\sigma_{matrix} - \sigma_y)$ (Fig. 3.14). As also observed by Meyer et al. (2019), we find increasing shear zone thickness with increasing confining pressure.

For OPA, our results show that brittle fault slip is expected to be promoted at high OCRs. In laboratory experiments a transition from brittle to ductile deformation behavior of weakly cemented clays, clay-rich shales as well as for OPA was found with increasing effective confining pressure,

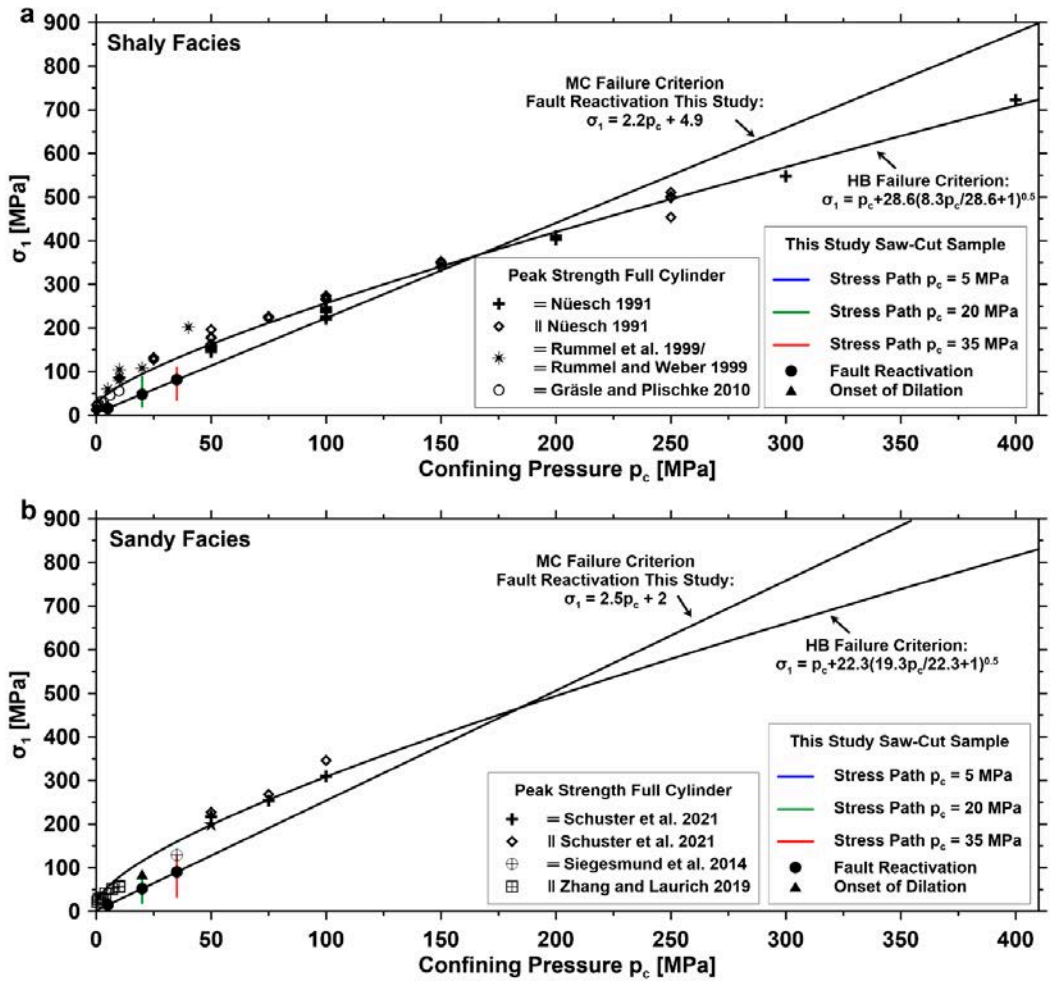

Figure 3.13: Peak strength as a function of confining pressure for the shaly (**a**) and sandy facies of Opalinus Clay deformed parallel (||) and perpendicular (=) to bedding orientation. Results of the shaly facies reported from Nüesch (1991) were obtained from samples with a water content of 1.8wt% deformed at room temperature and strain rates of $1.3 \times 10^{-7} - 8.4 \times 10^{-5}$ s^{-1}. Data selected from Rummel et al. (1999) and Rummel and Weber (1999) was limited to samples with a water content of <2.1wt% that were deformed at room temperature and strain rates of 10^{-6} s^{-1}. Shaly facies samples denoted as dry (water content <6.3wt%) by Gräsle and Plischke (2010) were also deformed at room temperature and strain rates of 10^{-6} s^{-1}. Results of the sandy facies (**b**) reported from Zhang and Laurich (2019) were obtained using samples with a water content <3.9wt% that were deformed at room temperature and a strain rate of 7×10^{-7} s^{-1}. Siegesmund et al. (2014) performed true triaxial experiments with $\sigma_2 = \sigma_3$ at room temperature and a load rate of 0.2 MPa/min on presumably unsaturated cubic samples of the sandy facies. Experimental results from Schuster et al. (2021) were obtained at temperatures of 100 °C and strain rates of 5 x 10^{-4} s^{-1} using dried samples from the sandy facies with a residual water content of ≈0.4wt%. Peak strengths of the shaly and sandy facies were fit to a non-linear Hoek-Brown (HB) failure criterion. Furthermore, the stress at fault reactivation obtained from this study was fit to a linear Mohr-Coulomb (MC) failure criterion. The intersection of both criterions for peak strength and fault reactivation marks the transition to ductile deformation, i.e. the confining pressure at which a pre-existing fault should remain locked.

i.e. decreasing OCR towards normal consolidation (OCR = 1) (e.g., Nüesch 1991; Gutierrez et al. 1996; Nygård et al. 2006). Furthermore, increasing strength of OPA with increasing OCR and decreasing porosity was shown experimentally in triaxial and uniaxial deformation tests, performed on samples originating from different sites with varying burial and present depths (Jahns 2010, 2013; Favero et al. 2016; Ferrari et al. 2018; Crisci et al. 2019). Based on oedometer tests and basin modelling, the maximum effective burial stress of OPA at the Mont Terri site was estimated to be 17±5 MPa, which results in an OCR of ≈3 – 5 (NAGRA 2002; Mazurek et al. 2006). In our experimental design, we performed hydrostatic pre-conditioning up to a confining pressure of 50 MPa, aimed to minimize micro-fissures potentially introduced by preparation artefacts and sample drying. Subsequent testing at confining pressures of p_c = 5, 20 and 35 MPa resulted in OCRs of 10, 2.5 and 1.4, respectively. We conclude that the mode of fault reactivation depends on sedimentary burial, geological uplift and erosion.

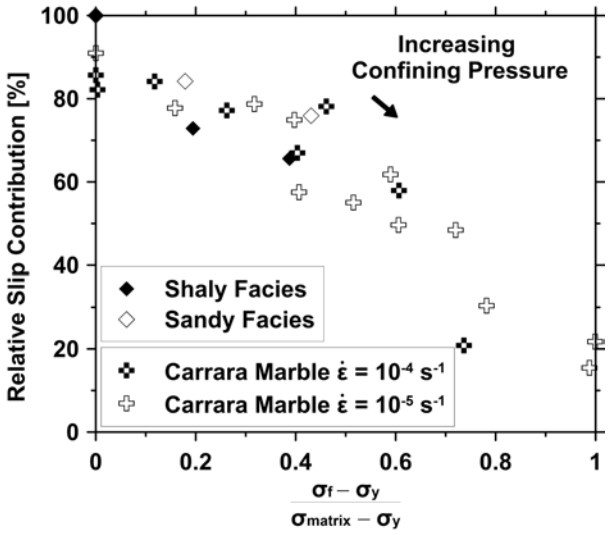

Figure 3.14: Fault slip contribution to total axial shortening of the shaly and sandy facies of Opalinus Clay as a function of the ratio $(\sigma_f - \sigma_y)/(\sigma_{matrix} - \sigma_y)$ after Meyer et al. (2019). Furthermore, we compare the obtained data of Opalinus Clay with results from Meyer et al. 2019, who performed similar experiments with Carrara Marble at confining pressures p_c = 10 – 80 MPa and strain rates $\dot{\varepsilon}$ between 10^{-5} – 10^{-4} s^{-1}.

The presented experiments were performed under dry conditions. However, fault zones in nature are barely dry and the frictional strength of clay minerals and of OPA highly depends on the degree of water saturation (e.g., Moore and Lockner 2004; Behnsen and Faulkner 2012; Morrow et al. 2017; Orellana et al. 2019). Therefore, a lower friction coefficient for the same given yield and failure envelope would increase the confining pressure where $\sigma_f < \sigma_y$, favoring brittle, highly localized fault reactivation as well as the pressure at the brittle-ductile transition where $\sigma_f > \sigma_{matrix}$ (Byerlee 1968). For saturated gouge, reactivation would probably result in a slow stable slip as shown by Orellana et al. (2018a). However, decameter, field-scale fault injection

experiments of the "Main Fault" at the Mont Terri URL revealed complex slip behavior (Guglielmi et al. 2020).

3.4.2 Stress Relaxation and Frictional Healing

For all samples, SHS tests were started at an axial piston displacement of ≈6 mm, i.e. an axial strain of about 6%. Total fault slip at the start of the SHS tests was different, as resolved fault slip decreased with confining pressure (Fig. 3.14). In general, SHS tests show minor frictional strengthening (Fig. 3.6c, d) and confining pressure-dependent fault slip (Fig. 3.7). Frictional strengthening rate in our study agrees with previous experiments performed on artificial gouge and intact samples of OPA (Orellana et al. 2018b, 2019). Generally, frictional healing arises from several time- and/or slip-dependent processes at asperity contacts and was shown to be influenced by mineral composition, temperature, pressure, presence and chemistry of pore fluids, sliding velocity, porosity, shear fabric, grainsize distribution and shape of grains (Beeler et al. 1994; Dieterich and Kilgore 1994; Hickman and Evans 1995; Karner et al. 1997; Marone 1998; Bos and Spiers 2002; Yasuhara et al. 2005; Niemeijer and Spiers 2006; Niemeijer et al. 2008; Renard et al. 2012; Carpenter et al. 2016). Following these studies, frictional strengthening of granular gouge (e.g., pure quartz or calcite mineral grains) may result from increasing compaction and fault closure by pore collapse, growth of grain contact area and increase of asperity contact strength. Pore space may be reduced by cataclasis, intercrystalline plasticity of phyllosilicates, frictional intergranular sliding and rotation (e.g., Schutjens 1991; Wong et al. 1997; Nakatani 1998; Rutter and Wanten 2000), or by time- and temperature-dependent creep accommodated by pressure solution (e.g., Bos and Spiers 2000), stress corrosion (e.g., Heap et al. 2009a, b), or dislocation activity (e.g., Renner et al. 2002).

For each hold period in the SHS runs, the piston was fixed and axial stress was allowed to relax (Fig. 3.4, Fig. 3.5). We observe time-dependent deformation of OPA accommodated by fault slip and matrix deformation that may involve a mixture of the presented mechanisms being active along the saw-cut and/or in the matrix (depending on confining pressure). Based on our microstructural observations, we found no evidence for solution-precipitation driven compaction and contact strengthening, such as grain indentation, solution seams or mineral overgrowths, nor indicators for significant dislocation motion. Therefore, we infer that time-dependent creep during relaxation is mainly due to brittle/frictional mechanisms such as grain crushing, pore collapse and grain rearrangement caused by intercrystalline plasticity of phyllosilicates, intergranular particle sliding and microcracking.

In an ideal stress relaxation experiment using an infinite stiff loading frame, stored elastic strain energy in the specimen is dissipated through permanent deformation resulting in the decay of stress as a function of time (Guiu and Pratt 1964; Schmid 1976; Rutter and Mainprice 1978; Rutter et

al. 1978). At any time during relaxation, the resulting permanent strain rate is proportional to the stress relaxation rate and depends on the rheological properties of the tested material. However, due to the compliance of the testing machine (k_m), there is an additional portion of elastic strain energy release during stress relaxation that has to be dissipated by permanent deformation in the specimen during the hold period. Therefore, during relaxation the strain rate of the specimen ($\dot{\varepsilon}_s$) is related to the stress rate ($\frac{d\sigma}{dt}$) via the expression: $\dot{\varepsilon}_s = -(k_m l_m + k_s)\frac{d\sigma}{dt}$, where k_s is the specimen compliance and l_m relates machine compliance to sample strain (Guiu and Pratt 1964).

With an emphasis on sample relaxation of 6000 s, we further characterize the different deformation behavior and the underlying acting deformation mechanisms and analyze the stress dependence of the stress relaxation rates. To determine the stress rates, stress data were first divided into 12-time intervals (1 – 2.5, 2.5 – 5, 5 – 10, 10 – 25, 25 – 50, 50 – 100, 100 – 250, 250 – 500, 500 – 1000, 1000 – 2500, 2500 – 5000, 5000 – 6000 s). Subsequently, stress rates were determined by linear fitting for the respective time intervals. Time-dependent creep may be described either by a power-law in the form of $\dot{\varepsilon}_{creep} = A(\sigma_d)^n$ or an exponential form $\dot{\varepsilon}_{creep} = Ce^{\beta\sigma d}$ commonly used to relate creep strain rate ($\dot{\varepsilon}_{creep}$) to applied differential stress (σ_d) (e.g., Lockner 1993; Heap et al. 2009a, b; Geng et al. 2018), where the stress exponent n or the exponential law gradient β is indicative of a characteristic deformation mechanism. As shown by Schmid (1976) and Rutter et al. (1978), the stress rate in relaxation experiments can be converted into a strain rate if the machine and specimen stiffness are known. Since we could not accurately determine the relevant elastic parameters prior to the performed SHS tests, we keep the stress rate as it can be used equivalently as a proxy for the strain rate and should show identical stress dependence (Rutter et al. 1978; Rutter and Mainprice 1978).

In Fig. 3.15 we plot the determined stress rates to the respective differential stress during relaxation in semilogarithmic scale. Least square fitting was applied for all determined stress rates to obtain n and β of the presented creep laws (Table 3.7). Obtained stress exponents range from n = 92 to 76 for the shaly facies and from n = 180 to 80 for the sandy facies and decrease with increasing applied confining pressure. The same applies to β showing higher values at low confining pressure ranging between β = 4.9 – 1.2 for the shaly and β = 5.9 – 0.9 for the sandy facies. The resulting stress exponents are significantly higher compared to the characteristic stress exponents ($n < 5$) for pressure solution (Rutter and Mainprice 1978; Schutjens 1991; Zhang and Spiers 2005; Zhang et al. 2010; Geng et al. 2018) or stress exponents inferred for dislocation creep in calcite or quartz (Hirth and Tullis 1992; Renner et al. 2002). Stress exponents with $n > 10$ were used to describe the brittle creep of different sandstones with n = 20 – 70 (Rutter and Mainprice 1978; Heap et al. 2009a, b), Tavel limestone with n = 40 – 66 (Nicolas et al. 2017), Westerly granite n = 59 – 64 (Lockner 1993) and Tournemire shale with n = 27 – 63 (Geng et al. 2018, 2021). These studies interpret determined stress exponents to be indicative of stress- and temperature-dependent, sub-critical crack growth by stress corrosion (Atkinson 1984) as govern-

ing deformation mechanism. Renner et al. (2000b) determined stress exponents of $n = 45 - 110$ for shaly facies OPA specimens deformed perpendicular to bedding in creep and relaxation tests at 35 MPa confining pressure, which was also interpreted as sub-critical crack growth as the main acting deformation mechanism. Microstructural analysis indicates that stress relaxation occurs by several micromechanisms, which may act in parallel. The high-stress sensitivity in combination with microstructures may indicate dominating brittle/frictional processes such as microcracking, pore collapse, grain rotation, intergranular slip with a contribution of intercrystalline plasticity of phyllosilicates.

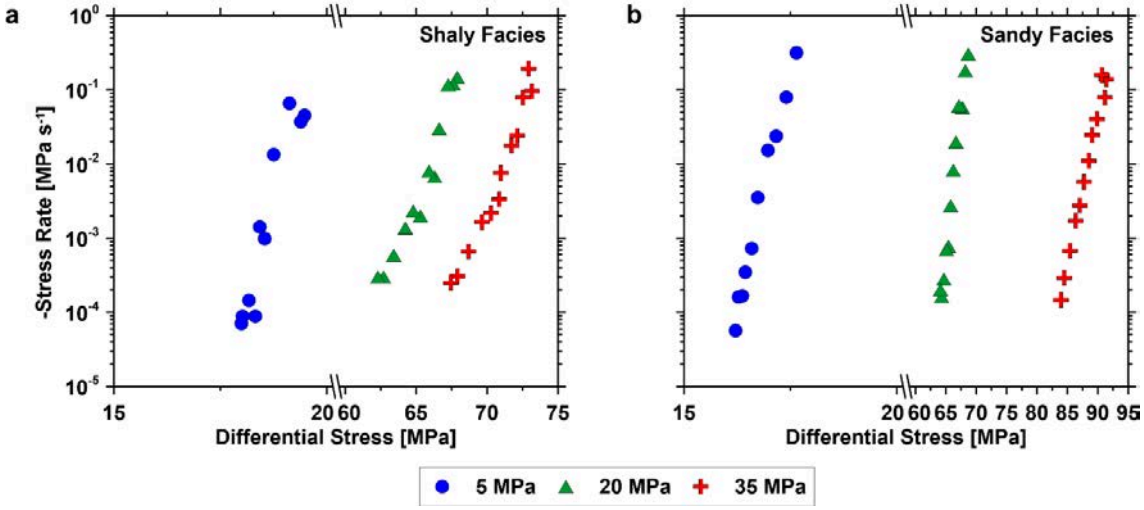

Figure 3.15: Stress relaxation rate of the shaly (**a**) and sandy (**b**) facies of Opalinus Clay from SHS test at a hold period of 6000 s. Stress rate and stress data are fitted to a power-law model to obtain the slope given by the stress exponent n. Note the different and broken scales. Error bars lie within the symbol size.

As described earlier, we observe continuing dilation of the shaly facies sample deformed at 5 MPa confining pressure and the sandy facies samples deformed at 5 and 20 MPa confining pressure. This suggests that the combined elastic strain of sample and machine is released by shear displacement along the saw-cut and/or gouge compaction. On the other hand, the shaly facies samples deformed at 20 and 35 MPa confining pressure and the sandy facies sample deformed at 35 MPa confining pressure show a change of axial and volumetric strain from dilation to compaction within $<$1000 s. This suggests stress relaxation occurred by a combination of fault slip and matrix shortening. Therefore, we suspect that deformation in the early stage of relaxation ($<$100 s) is dominated by slip along the saw-cut, which presumably decreases with increasing hold time. To investigate whether the stress sensitivity changes as soon as the dominating influence of slip decreases, we have determined n and β values as described before also for hold times $>$100 s (Table 3.7 marked by *). We find a significant reduction of n and β for the shaly facies samples deformed at 20 and 35 MPa confining pressure, supporting our previous assumption that strain partitioning

changes during a relaxation for both samples from slip to matrix compaction. On the other hand, determined gradients stay relatively constant for the remaining samples, suggesting no change in contributing deformation mechanism.

In general, our results confirm the contention from previous studies on clay-rich gouge that phyllosilicates reduce contact strengthening. Instead, clay-rich gouges may remain weak displaying stable, aseismic creep (Niemeijer et al. 2008; Tesei et al. 2012; Giorgetti et al. 2015; Carpenter et al. 2016; Ruggieri et al. 2021). However, upon reloading we find higher frictional weakening in the sandy facies compared to the shaly facies with increasing confinement. Clay-rich gouges and bulk rocks are expected to display a broad spectrum of deformation behavior related to composition and fluid content (Niemeijer and Spiers 2006; Niemeijer et al. 2010; Tesei et al. 2012; Giorgetti et al. 2015; Carpenter et al. 2016). For example, the higher phyllosilicate content of the shaly facies samples may limit compaction at confining pressure $>$5 MPa, as the intensity of shear foliation fabrics is higher compared to the sandy facies samples, allowing rapid saturation of asperity contact areas (Bos and Spiers 2000; Saffer and Marone 2003; Niemeijer and Spiers 2006; Niemeijer et al. 2008; Tesei et al. 2012; Giorgetti et al. 2015; Carpenter et al. 2016). Upon reload strain localizes in the interconnected shear surfaces developed in the shaly facies resulting in the observed stable reactivation with low frictional weakening (Niemeijer and Spiers 2006). Sandy facies samples display greater gouge heterogeneity and fraction of competent mineral clasts (e.g., quartz, carbonates) compared to the shaly facies possibly promoting frictional weakening and dilation by grain rearrangement after re-loading (cf., Fagereng and Sibson 2010). Kohli and Zoback (2013) found that a critical phyllosilicate content of less than $\approx$30wt% is required for unstable frictional behavior of shale gouge. XRD-analysis of the produced gouge material of the sandy facies (Table 3.5) revealed much greater clay content, suggesting stable behavior. However, the heterogeneity of the sandy facies (Schuster et al. 2021) causes variations in the composition of the gouge. This may result in unstable slip patches. Finally, the amount of calcite in natural and artificial fault gouge was found to increase strength recovery (Tesei et al. 2012; Giorgetti et al. 2015; Carpenter et al. 2016; Ruggieri et al. 2021) related to increased pressure solution processes at shallow crustal conditions even at room temperature. For a fault system in OPA, this may imply higher frictional strength recovery for shear zones crossing the carbonate-rich sandy facies of OPA composed of up to 40wt% calcite (Pearson et al. 2003).

Table 3.7: Experimental conditions at the beginning of the 6000 s hold period with the regression analysis for power and exponential law that relate stress rate and differential stress during relaxation. The gradients n and β were determined over the full relaxation period of 6000 s (see text for details). Gradients marked with a * were determined at hold times between 100 – 6000 s.

Opalinus Clay	p_c (MPa)	σ_d^H (MPa)	n	Power Law Fit R^2	β	Exponential Law Fit R^2
Sandy Facies	5	17.7	100±4	0.986	5.9±0.3	0.984
			104±16*	0.937*	6.3±0.9*	0.937*
Sandy Facies	20	68.9	117±5	0.980	1.8±0.1	0.979
			116±13*	0.939*	1.8±0.2*	0.941*
Sandy Facies	35	91.5	80±3	0.988	0.9±0.0	0.988
			80±2*	0.997*	0.9±0.0*	0.998*
Shaly Facies	5	19.5	92±11	0.898	4.9±0.6	0.895
			92±30*	0.697*	5.1±1.7*	0.699*
Shaly Facies	20	68.0	77±6	0.938	1.2±0.1	0.942
			56±6*	0.957*	0.8±0.1*	0.958*
Shaly Facies	35	73.4	80±6	0.955	1.1±0.1	0.958
			55±3*	0.989*	0.9±0.1*	0.962*

p_c confining pressure, σ_d^H initial differential stress at the start of SHS test, R^2 correlation coefficient

3.5 Conclusion

Fault reactivation, strain partitioning and frictional healing properties of saw-cut samples of OPA from the shaly and sandy facies were investigated in triaxial deformation tests. After hydrostatic pre-consolidation of 18 h at 50 MPa, constant strain rate experiments were performed at confining pressures of 5, 20 and 35 MPa at dry conditions. With increasing confinement, we observe a transition from highly localized, brittle to distributed, semi-brittle deformation behavior. At the lowest pressure, the fault slip of both facies is initiated by a small stress drop, with the subsequent strain being primarily accommodated by fault slip (>95%). This behavior changes as pressure increases: deformation reveals non-linear strain hardening and is increasingly partitioned from stable frictional sliding towards distributed bulk deformation. The upper-pressure limit for brittle localization and the onset of strain partitioning was identified at the stress at which fault reactivation strength exceeds matrix yield stress. Shear stress at reactivation increased with increasing confining pressure. Consequently, the slip contribution to total deformation decreased with increasing confinement as yield stress and fault strength gradually diverge.

The transition in deformation behavior with confining pressure is accompanied by an increas-

ing gouge layer thickness. Microstructural observation reveals that brittle fragmentation with frictional granular sliding and grain rotation dominate deformation at low confinement. With increasing confining pressure, we observe the formation of shear zones characterized by a higher contribution of cataclastic (sandy facies) and granular (shaly facies) flow, combined with the development of anastomosing shear plane networks, delocalizing strain within the gouge layer. AE activity during fault reactivation experiments decreased with increasing confining pressure and was only detected in sandy facies samples. Furthermore, P-wave velocity changes were more drastic in the sandy facies and became more pronounced with increasing confinement, indicating microcrack opening parallel to the stress axis and matrix compaction and pore collapse perpendicular to it.

The friction coefficient determined at fault reactivation is slightly lower for the shaly ($\mu \approx 0.4$) compared to the sandy facies ($\mu \approx 0.48$) and suggests relatively weak faults. Compared to the initial sample composition, XRD analysis of post-deformation fault gouge shows no changes in the shaly facies, but a significant depletion of quartz and enrichment of clay minerals in the sandy facies' samples, explaining the minor difference in frictional strength. Furthermore, the fractionation of clay minerals in the gouge implies increased sealing capacity of fault systems in the sandy facies. Slide-hold- slide tests (60 – 6000 s) performed after ≈6 mm axial shortening reveal negative or negligible frictional strengthening of both facies indicating stable creep and long-term weakness at the applied conditions. However, sandy facies samples showed rapid frictional weakening after reload, which is why dynamic reactivation cannot be ruled out for faults in this facies type.

Our results demonstrate that the mode of fault reactivation in OPA highly depends on the sedimentary history and present stress field. Brittle fault reactivation may be favored at high overconsolidation ratios and at shallow depth increasing the risk for creating permeable flow paths and seismicity.

Acknowledgments

The authors acknowledge the financial support for the iCross project by the Federal Ministry of Education and Research (project number 02NUK053D), the Helmholtz Association (project number SO-093) and the GFZ German Research Centre for Geosciences Potsdam. Furthermore, Michael Naumann is highly appreciated for his technical support during the experiments. We thank Stefan Gehrmann for sample preparation as well as Vladimir Roddatis and Anja Schreiber for assistance at the SEM. Finally, we would like to thank the editor and the two anonymous reviewers, who helped to improve the quality of this manuscript with their constructive comments and suggestions.

Appendix

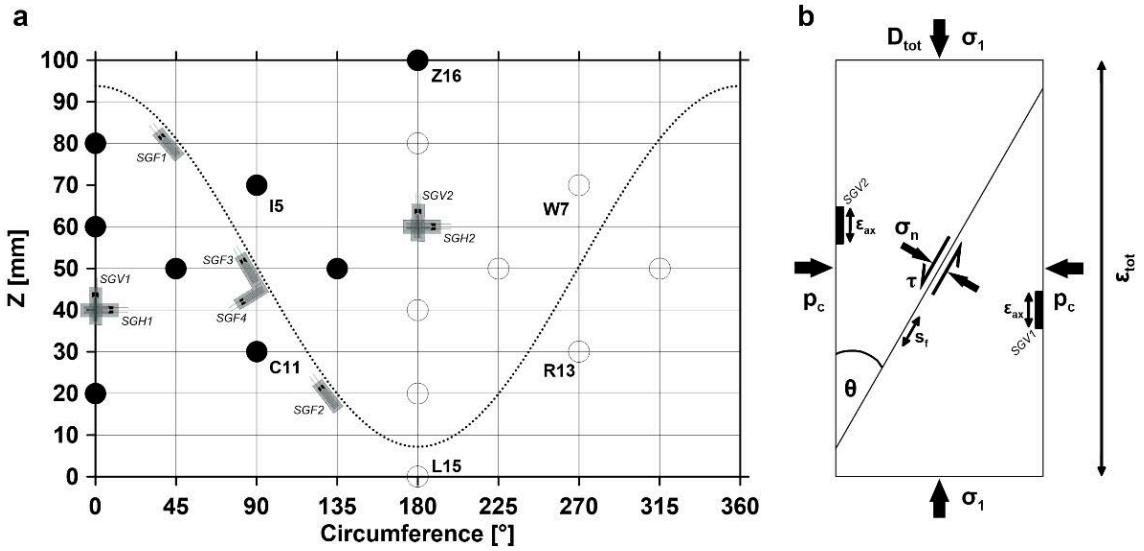

Figure A3.1: Sensor map with the position of piezoelectric P-wave transducers (bold circle: transmitter; open circle: receiver) and strain gauges projected on the sample surface (**a**). Schematic cross section of sample including a saw-cut inclined at θ = 30°, showing acting stresses and strain partitioning of total axial strain (ε_{tot}) in fault displacement (s_f) and matrix strain of the bulk sample (ε_{ax}) measured by strain gauges.

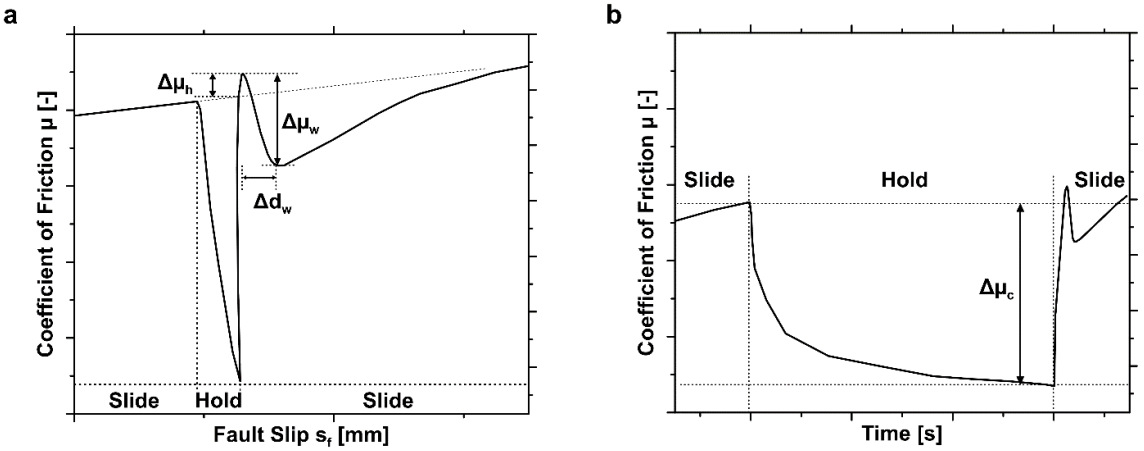

Figure A3.2: Schematic representation of a SHS test with parameter definition, showing the coefficient of friction as a function of fault slip s_f (**a**). **b** shows the temporal evolution of the friction coefficient during a hold period. During each hold period the coefficient of friction decreases due to sample creep ($\Delta\mu_c$). Upon subsequent reloading, the coefficient of friction increases again until it reaches a peak value at which slip resumes. $\Delta\mu_w$ is frictional weakening associated with a stress drop over a slip weakening distance (d_w). Frictional strengthening $\Delta\mu_h$ is determined from the linear interpolation of the hardening trend before the respective hold period.

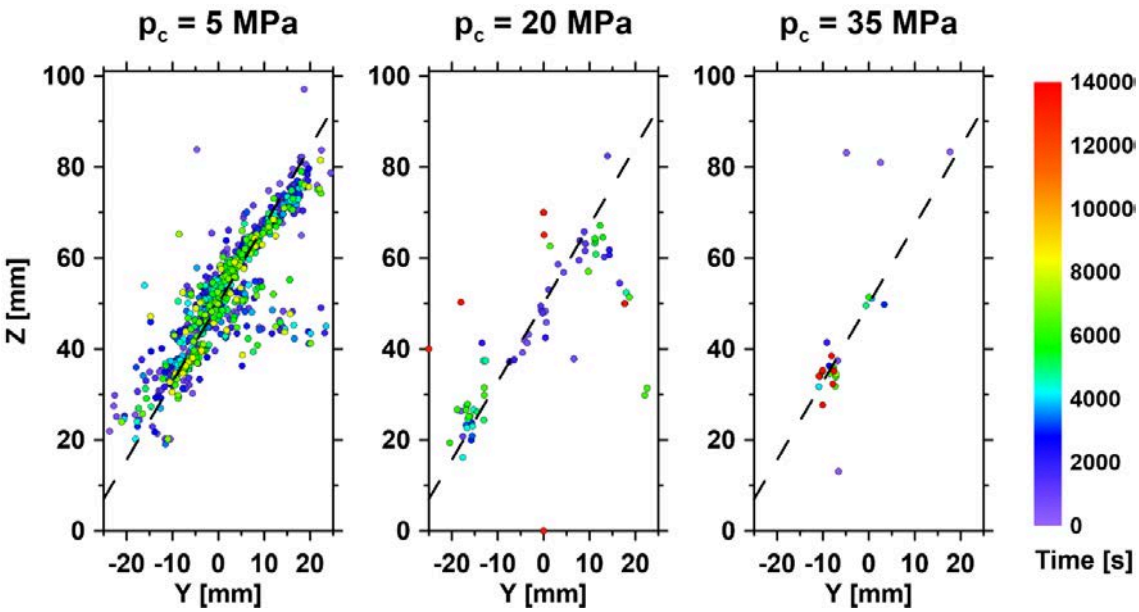

Figure A3.3: Hypocentre projection of acoustic emission (AE) events recorded during the deformation of the sandy facies of Opalinus Clay at confining pressures between 5 and 35 MPa. The colour code of the dots indicates the temporal occurrence of single events during each experiment. The dashed line represents the locaction of the saw-cut surface.

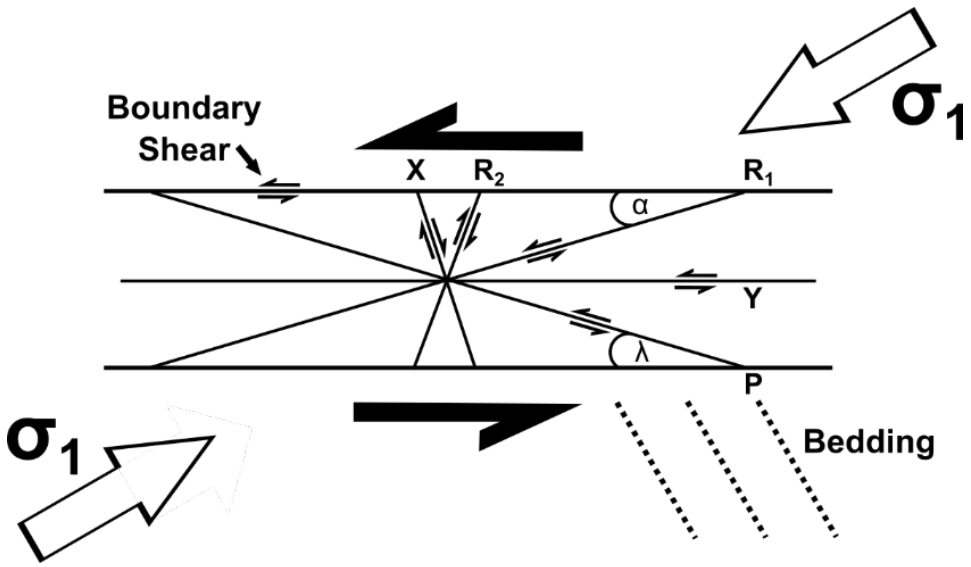

Figure A3.4: Scheme of structural fabric elements developed in deformed gouge after the terminology of Logan et al. (1979). Orientation of principal axial stress (σ_1) and bedding planes as present in our experimental setup.

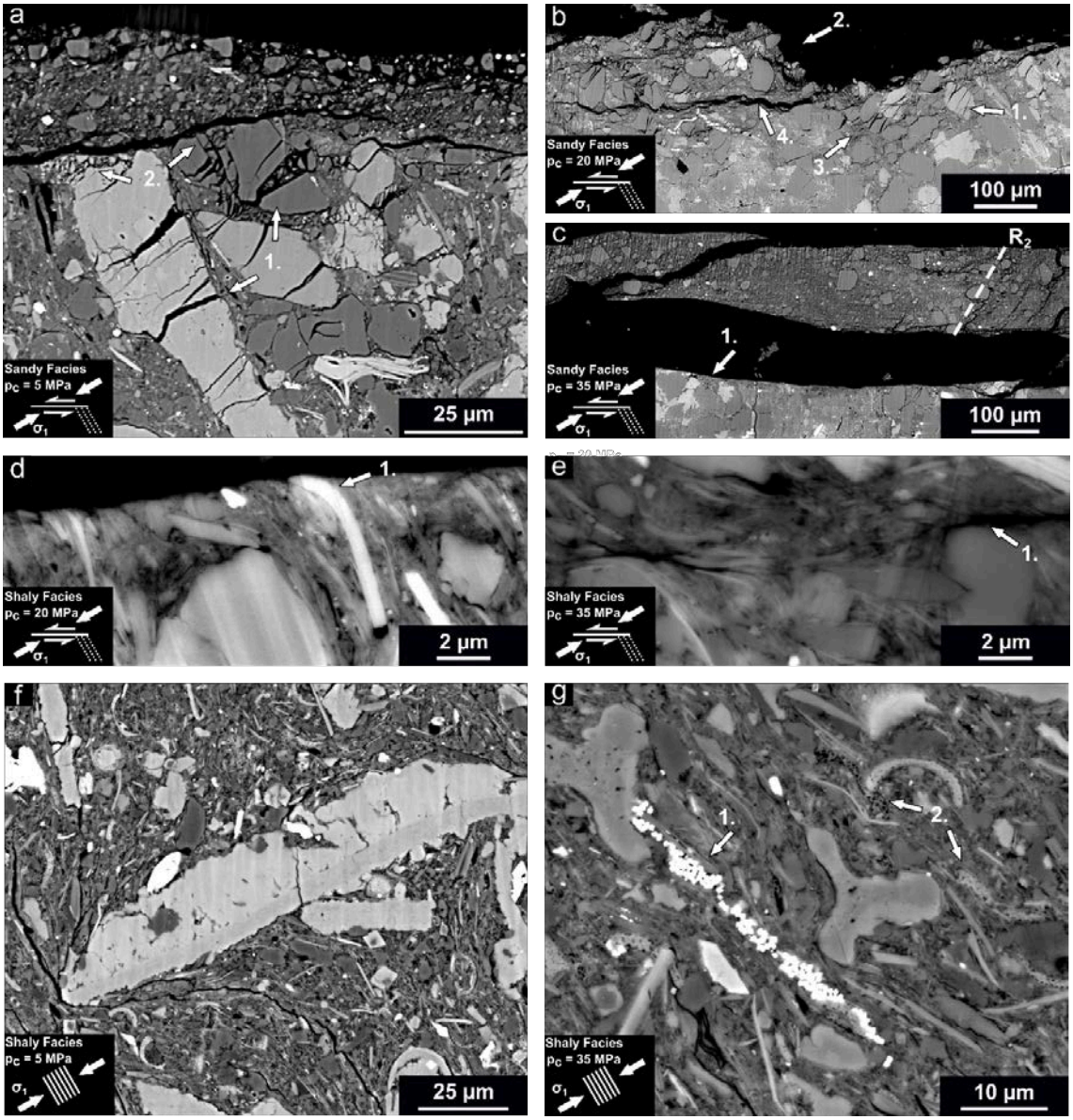

Figure A3.5: Overview and details of microstructures developed at the gouge-wall rock interface of the sandy (**a**, **b**, **c**) and shaly (**d**, **e**) facies of Opalinus Clay. In the sandy facies, this boundary is characterized by a rough topography and several fractured clastic grains (**a**, **b**), whereas the interface in the shaly facies displays a smooth surface with bent and aligned phyllosilicate minerals resulting in a sharp contact (**d**, **e**). Strain accommodated by bulk deformation in the shaly facies (**f**, **g**) is indicated by pore collapse, alignment of clay particles parallel to bedding. At elevated confining pressure (**g**) we also observe stretched pyrite (**1.**) and broken fossils (**2.**) that stay intact at p_c = 5 MPa. Bedding plane orientation of the wall rock as well as shear and loading direction are indicated in the black boxes at the bottom left of each picture.

4 Fracture Transmissivity in Prospective Host Rocks for Enhanced Geothermal Systems (EGS)

Summary

We experimentally determined the hydraulic properties of fractures within various rock types, focusing on a variety of Variscan rocks. Flow-through experiments were performed on slate, graywacke, quartzite, granite, natural fault gouge, and claystone samples containing an artificial fracture with a given roughness. For slate samples, the hydraulic transmissivity of the fractures was measured at confining pressures, p_c, at up to 50 MPa, temperatures, T, between 25 and 100 °C, and differential stress, σ, acting perpendicular to the fracture surface of up to 45 MPa. Fracture transmissivity decreases non-linearly and irreversibly by about an order of magnitude with increasing confining pressure and differential stress, with a slightly stronger influence of p_c than of σ. Increasing temperature reduces fracture transmissivity only at high confining pressures when the fracture aperture is already low. An increase in the fracture surface roughness by about three times yields an initial fracture transmissivity of almost one order of magnitude higher. Fractures with similar surface roughness display the highest initial transmissivity within slate, graywacke, quartzite and granite samples, whereas the transmissivity in claystone and granitic gouge material is up to several orders of magnitude lower. The reduction in transmissivity with increasing stress at room temperature varies with composition and uniaxial strength, where the reduction is lowest for rocks with a high fraction of strong minerals and associated high brittleness and strength. Microstructural investigations suggest that the reduction is induced by the compaction of the matrix and crushing of strong asperities. Our results suggest that for a given surface roughness, the fracture transmissivity of slate as an example of a target reservoir for unconventional EGS, is comparable to that of other hard rocks, e.g., granite, whereas highly altered and/or clay-bearing rocks display poor potential for extracting geothermal energy from discrete fractures.

List of Symbols

ρ	Bulk density
ρ_g	Grain density
φ	Sample Porosity (using Helium pycnometry)
k_{matrix}	Matrix permeability
σ_{UCS}	Uniaxial compressive strength
σ_{TCS}	Triaxial compressive strength
E	Static Young's modulus
p_c	Confining pressure
p_p	Fluid pressure
T	Temperature
σ	Axial deviatoric stress
S_q	Fracture surface roughness (root mean square)
k	Fracture permeability
t	Fracture thickness/ hydraulic aperture
Q	Volumetric flow rate
η	Dynamic viscosity
$2a$	Distance between up- and downstream borehole
r_0	Radius of up- and downstream borehole
Δp_p	Differential pore pressure within the fracture
Δx	Distance within the fracture over which is Δp_p measured
B	Geometry factor
B_{compo}	Brittleness based on composition
w_{xx}	Mineral weighting factor
f_{xx}	Mineral fraction

4.1 Introduction

Extracting geothermal energy from underground is of major interest in the transition from energy recovered from conventional resources such as coal or oil towards renewable energies (Vogler et al. 2016). Geothermal energy is expected to have a great potential to meet future energy demands. However, exploitation is highly dependent on the presence of accessible hot fluids within the reservoir formation to ensure sufficient energy extraction. In contrast to hydrothermal geothermal systems, where steam or hot water is extracted from the subsurface, hot (>150 °C) and deep (>3 km), but low permeable, reservoir rocks represent the largest geothermal energy resources (Lu 2018; Beauchamps et al. 2019; Roche et al. 2019; Favier et al. 2021). To facilitate the extraction of geothermal energy from tight reservoirs, a network of highly conductive fractures is required that serves as heat exchanger (Gringarten et al. 1975; Brogi et al. 2021; Liotta et al. 2021) in Enhanced Geothermal Systems (EGS). An EGS typically relies on two wells, an injection and a production well, which are connected by a network of open (conductive to fluid flow) fractures. In order to create such a fracture network, artificial fractures are often generated by hydraulic fracturing (HF). These are believed to be connected to pre-existing natural fractures in the reservoir (Li et al. 2015). The efficiency and sustainability of an EGS are critically dependent on sufficient water flow through the fracture network and on the conductive properties of the separate fractures (Vogler et al. 2016). This prerequisite, in addition to a relatively high geothermal gradient, is necessary to successfully run an EGS over several years (Milsch et al. 2008; Voltolini and Ajo-Franklin 2020).

Fluid flow within rough natural fractures is a complex process, influenced by many parameters, for example thermodynamic boundary conditions, surface roughness and chemical processes, such as mineral precipitation (Crandall et al. 2017). In addition, the bedding and cleavage orientation of anisotropic rocks such as shale or slate can have a strong effect on the development and permeability of fractures (Leung and Zimmerman 2012; Carey et al. 2015; Stober and Bucher 2015). The surface roughness of natural and artificially created fractures has a strong impact on the (hydraulic) aperture (Gutierrez et al. 2000; Liu 2005; Cho et al. 2013; Crandall et al. 2017). Fracture transmissivity can rapidly decrease with increasing confining pressure (p_c) (Cho et al. 2013; Crandall et al. 2017) and increasing effective stress, σ, oriented perpendicular to the fracture surface (e.g., Rutter and Mecklenburgh 2018). Increasing temperature, T, may (completely) seal fractures in sediments by thermal expansion (Gutierrez et al. 2000). Fracture sealing may be also induced by mineral precipitation processes, depending on fluid and rock composition (Milsch et al. 2008; Crandall et al. 2017; Blöcher et al. 2019). Injecting fluid into a fluid-bearing fracture with a different composition may lead to dissolution-precipitation reactions due to local changes in the chemical equilibrium, which typically results in a decrease in fracture transmissivity (Gutierrez et al. 2000; Milsch et al. 2008; Cheng and Milsch 2020b; Cheng et al. 2021). The transmissivity may

be also reduced by the clogging of flow channels due to the migration of fine particles, e.g., clay (Carey et al. 2015; Zhang et al. 2015; Vogler et al. 2016; Walsh et al. 2016) or by the production of a fine-grained gouge layer resulting from shear displacement (Rutter and Mecklenburgh 2018). On the other hand, fracture transmissivity may be enhanced with low effective normal stress acting on the fracture due to shear-induced dilatancy, resulting in self-propping of the fracture surfaces (Watanabe et al. 2011; Cho et al. 2013; Vogler et al. 2016; Crandall et al. 2017; Blöcher et al. 2019). The transmissivity of the propped fractures may be influenced by proppant embedment (e.g., Zhang et al. 2015).

Many existing EGS are located in granitic rocks, which often exhibit a relatively large amount of natural, highly permeable, open fractures and have a high potential for successfully creating fracture networks with stimulation techniques (Schill et al. 2017; Vidal and Genter 2018). However, metamorphic rocks may also be considered as potential host rocks for EGS. Within the European initiative 'Multidisciplinary and multi-context demonstration of Enhanced Geothermal Systems Exploration and Exploitation Techniques and potentials (MEET)', the suitability of Variscan rocks, such as granites (Vidal and Genter 2018), quartzites (Vanbrabant et al. 2020), slates and graywacke (Leiss et al. 2011a, b, 2021) were investigated to assess their potential for extracting geothermal energy. In this study, we focused on the influence of confining pressure, stress, temperature, and surface roughness on the fracture transmissivity of Wissenbach slate, which is the expected target rock for a planned EGS in Göttingen, Germany, dedicated to heating the University Campus (Leiss et al. 2021). Since the productivity of fractured rocks may be influenced by their composition, as well as their metamorphic and alteration grade, we additionally performed flow-through experiments at elevated stress on fractured graywacke, quartzite, fresh and altered (gouge) granite, and claystone, where the latter may be regarded as an end-member rock type of highly altered formations. This may help to assess the potential of different geological settings for future EGS.

4.2 Materials and Methods

4.2.1 Sample Material

Most of the experiments were performed on slates derived from the Middle Devonian (Eifelian age) Wissenbach Slate (WBS) Formation, one of the intended reservoir target horizons for the planned EGS in Göttingen. Because only a few existing wells in the Göttingen area penetrate the Paleozoic rock units below the Permian and Mesozoic sedimentary cover (Leiss et al. 2011a, 2021), rock samples were taken from an analogue site in the Western Harz Mountains. Samples were prepared from cores collected at a depth of 1134 – 1210 m from the scientific well 'Hahnenklee', which was drilled in the northwestern part of the Harz mountains in the early 1980's

(Brinckmann and Brüning 1986; Schubert 1996; Gerling et al. 1999; Littke et al. 2011; Sáez et al. 2011). On macroscopic scale, WBS appears as black, homogeneous, argillaceous rock with sporadically distributed pyrite aggregates (<0.25 mm). The very few carbonate layers that occur are aligned parallel to the visible and characteristic cleavage, which is rarely interrupted by carbonate-filled veins (<0.5 mm). An X-Ray diffraction (XRD) analysis revealed that this metamorphic rock is mainly composed of quartz (Qtz), calcite (Ca), dolomite (Dol), muscovite (Ms), illite (Ill), chlorite (Chl), and feldspar (Fsp) with minor amounts of apatite (Ap), pyrite (Py), and organic matter (Om). The bulk composition was categorized into three main groups consisting of mechanically weak (Phyl = phyllosilicates), intermediate strong (Cb = carbonates), and strong (QFSO = Qtz + Fsp + Sulfides + Oxides) minerals (Table 4.1) and plotted in a ternary diagram (Fig. 4.1).

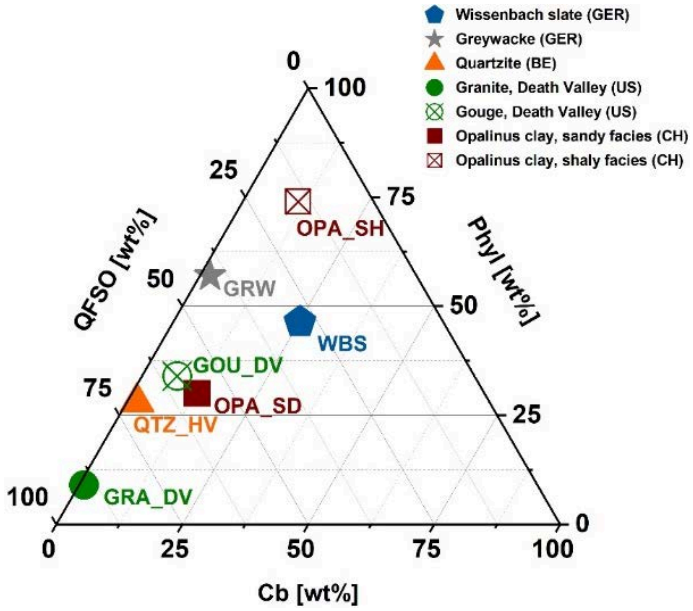

Figure 4.1: Ternary plot displaying mineral composition of investigated samples. Composition is separated into mechanically strong (QFSO = Qtz + Fsp + Sulfides + Oxides), intermediate strong (Cb = Carbonates), and weak (Phyl = Phyllosilicates) fractions. Mineral data given in wt%, WBS = Wissenbach slate, GRW = Graywacke, QTZ_HV = Quartzite Havelange, GRA_DV = Granite Death Valley, GOU_DV = Gouge Death Valley, OPA_SD = Opalinus Clay, sandy facies, OPA_SH = Opalinus Clay, shaly facies.

Optical and electron microscopy revealed a complex (expressed by a large range of mineral types and grain sizes), fine-grained microstructure of the starting material (Fig. 4.2a, b), with quartz, feldspar, chlorite and carbonates making up the largest mineral grains (<50 µm) that are dispersed in the phyllosilicate-rich matrix. Cleavage planes are characterized by phyllosilicates whose longest axes are oriented subparallel to each other. The bulk density of dried (110 °C for >48 h) WBS is in the range of around 2.8 g/cm^3 with a respective porosity measured with

He-pycnometry (Micrometrics, AccuPyc 1340) of $\varphi \approx 2$vol% (including micro pores). Matrix permeability, k_{matrix}, is less than 10^{-19} m^2, which is the detection limit of the gas permeameter used at TU Darmstadt (K. Bär, personal communication).

Another potential unit that has sufficient thickness for developing an EGS at the Göttingen site are Lower Carboniferous (Kulm facies) graywacke-successions (Leiss et al. 2021). Graywacke (GRW) samples also originate from an analogue site in the Western Harz Mountains and were taken at a depth of 843 m from the well 'Wulpke-2' that was drilled in the 1980's (Brinkmann and Brüning 1986). This grey to light-green marine psammite shows angular detrital quartz and feldspar grains (<200 µm) embedded in a fine-grained matrix made up of chlorite, feldspar and mica (Fig. 4.2c, d). The samples were taken from a relatively homogeneous part without any obvious grading. Larger, planar aligned biotite grains (<400 µm) indicate the macroscopically visible bedding orientation. The main mineral components determined by the XRD analysis show dominantly quartz, feldspar and micas with minor amounts of carbonates. Porosity and bulk density of dried samples are 0.7vol% and 2.67 g/cm^3, respectively.

A further demonstration site studied in the frame of the MEET-project is the Havelange deep borehole in Belgium (Wallonia). Here, Variscan quartzite formations are being considered for the development of potential EGS. Therefore, we also studied the fracture transmissivity of quartzite samples (QTZ_HV) obtained from a depth of z = 4732 m of the Havelange well, drilled in the Dinant Synclinorium in the early 1980's (Vanbrabant et al. 2020). The grey to light-green samples are characterized by a granoblastic fabric of fine-grained (<150 µm) quartz with illite and sparsely appearing dolomite (Fig. 4.2e, f). The Lower Devonian (Pragian) samples contain roughly 77wt% quartz and 20wt% clays and micas with minor amounts of dolomite. The porosity of the used samples was lowest off all the tested materials and ranges around $\varphi \approx 0.2$vol%.

To capture the influence of alteration on fracture transmissivity, tests were performed on fresh (GRA_DV), altered and sheared granite gouge (GOU_DV) samples recovered from an exposure located in the Noble Hills area in the southern part of the Death Valley (US) as an easily accessible analogue material to Variscan granites (Klee et al. 2021a, b). The light-reddish to pinkish, equigranular Noble Hill granite (Fig. 4.2g, h) is mainly composed of medium to coarse grained (≈3 mm) plagioclase (35wt%), quartz (30wt%), K-feldspar (30wt%) and biotite (10wt%) (Klee et al. 2021a) with an initial porosity of 1.3vol%. On the other hand, the light-yellowish to orange gouge (Fig. 4.2i, j), which was highly altered due to multiple shearing events and weathering processes, is characterized by granite clasts (≈5 mm) and brecciated quartz veins (≈1 cm) embedded in a carbonate- and clay-rich matrix (Klee et al. 2021b). In contrast to the granite, the gouge displays a high porosity of 12.6vol%.

In addition, we performed measurements on claystone samples to shed light on the influence of consolidation and metamorphic grades on fracture transmissivity in clay-rich formations, which may result from alteration processes in hard rocks. Claystone material was recovered from the Opalinus Clay Formation (OPA), whose mechanical properties have been well-studied in the context of nuclear waste disposal (e.g., Amann et al. 2017; Bossart et al. 2017a; Schuster et al. 2021). Compared to WBS, these rocks exhibited a much lower burial depth and temperature (Nussbaum et al. 2017). We investigated samples from the sandy (OPA_SD) (Fig. 4.2k, l) and shaly facies (OPA_SH) (Fig. 4.2m, n), both collected from the Underground Research Laboratory (URL) 'Mont Terri' (Switzerland, St. Ursanne), gratefully provided by the Swiss Federal Office of Topography–swisstopo. The fine-grained OPA_SD is mainly composed of Qtz (48wt%), carbonates (20wt%), and Fsp (9wt%), but contains a distinctly lower amount of weak sample constituents (30wt%), such as clay and mica, compared to WBS samples (Fig. 4.1). Note that these values may vary by about 10wt% because of the compositional heterogeneity of this facies (e.g., Schuster et al. 2021). The matrix permeability of OPA_SD is in the same range compared to WBS ($k_{matrix\_OPA\_SD}$ = 10^{-19} – 10^{-21} m^{-2}) (Yu et al. 2017), whereas the porosity of OPA_SD ($\varphi_{\_OPS_SD}$ = 11.8vol%) is significantly higher. In comparison to the sandy facies of OPA, the shaly facies contain less quartz (9wt%) and more clay minerals (74wt%). The main constituents of OPA_SH are clay minerals, quartz, carbonates, feldspar, pyrite, and organic matter. The permeability of OPA_SH is similar to that of OPA_SD ($k_{matrix\_OPA_SH}$ = 10^{-19} – 10^{-21} m^{-2}, Yu et al. 2017), but with a slightly higher porosity of 13.8vol%.

4.2.2 Methods

Flow-through experiments were performed on cm scale specimens at various p_c, T, σ-conditions using a modified MuSPIS (multiple sample production and injection simulator, Milsch et al. 2008) apparatus for long-term petrophysical investigations. The sample assembly consists of two separate cylindrical objects with a thickness of t^* = 10 mm (Fig. 4.3a, b), which were isolated by rubber (neoprene) jackets from the confining medium (hydraulic oil) inside the pressure vessel.

The confining pressure is controlled by a syringe pump (Isco 65D, max. p_c = 138 MPa). The maximum temperature is T = 200 °C, using a resistance-heating element (Thermocoax) mounted on a cylindrical stainless-steel tube placed inside the pressure vessel. To measure the transmissivity of the surface between the two disks, a continuous fluid flow at a pre-defined constant fluid pressure can be generated using two syringe pumps (Isco 100DM), which are connected to the surface via boreholes (up- and downstream boreholes in Fig. 4.3a). The maximum pore (fluid) pressure is p_p = 70 MPa at flowrates of $Q = 2.5 \times 10^{-2} – 1 \times 10^{-6}$ l/min. The fluid pressure is measured separately

Table 4.1: Petrophysical and mechanical properties.

Formation	Sample ID	Depth (m)	ρ (g/cm^3)	ρ_g (g/cm^3)	φ (vol%)	Phyl (wt%)	Cb (wt%)	QFSO (wt%)	S_{q_ini} (mm)	S_{q_def} (mm)	Mechanical Properties	Experimental Conditions	Fluid Medium
WBS		1134–1210	2.76	2.82	2.0	46	26	28	0.006 (low)		Perpendicular: σ_{UCS} = 219±2 MPa E = 27.4±0.3 GPa	UCS	-
											Parallel: σ_{UCS} = 124±1 MPa E = 31.4±0.3 GPa	UCS	-
									0.019 (high)		Perpendicular: σ_{TCS} = 498±20 MPa E = 69±14 GPa	Triaxial: p_c = 50 MPa T = 100°C $\dot{\varepsilon} = 5 \times 10^{-4}$ s^{-1}	-
	WBS_T									0.019		Hydrostatic: p_c = 5 MPa p_p = 1 MPa T = 25 – 100 °C	H_2O
	WBS_{pc}									0.020		Hydrostatic: p_c = 2 – 25 MPa p_p = 1 MPa T = 25 °C	H_2O
	$WBS_{pc\_\sigma\_T}$									0.021		Triaxial: p_c = 5 – 50 MPa p_p = 1 MPa σ = 0 – 45 MPa T = 25 – 90 °C	H_2O
	$WBS_{\sigma AR}$									0.020		Triaxial: p_c = 14 MPa p_p = 10 MPa σ = 0 – 45 MPa T = 25 °C	Ar
	$WBS_{pc\_lowrough}$									0.006		Triaxial: p_c = 1 – 5 MPa p_p = 0.5 – 1 MPa T = 25 °C	H_2O

GRW	843	2.67	2.69	0.7	57	2	41	0.016	σ_{UCS} = 185±2 MPa E = 35.2±0.3 GPa	UCS	-	
GRW_σ								0.016		Triaxial: p_c = 5 MPa p_p = 1 MPa σ = 0 – 45 MPa T = 25 °C	H_2O	
QTZ_HV	4732	2.69	2.7	0.2	20	3	77	0.014	σ_{UCS} = 175±2 MPa E = 35.6±0.4 GPa	UCS	-	
QTZ_HV_σ								0.014		Triaxial: p_c = 5 MPa p_p = 1 MPa σ = 0 – 45 MPa T = 25 °C	H_2O	
GRA_DV	OC	2.63	2.66	1.3	9	1	90	0.019	σ_{UCS} = 160±2 MPa E = 31.7±0.3 GPa	UCS	-	
GRA_DV_σ								0.019		Triaxial: p_c = 5 MPa p_p = 1 MPa σ = 0 – 45 MPa T = 25 °C	H_2O	
GOU_DV	OC	2.24	2.56	12.6	34	7	59	0.247	σ_{UCS} = 4.5±0.7 MPa E = 0.7±0.3 GPa	UCS	-	
GOU_DV_σ								0.175		Triaxial: p_c = 14 MPa p_p = 10 MPa σ = 0 – 20 MPa T = 25 °C	Ar	

OPA_SD		MT_URL	2.38	2.7	11.8	30	13	57	0.012		σ_{UCS} = 49.6±0.5 MPa E = 5.3±0.1 GPa	UCS	-
	OPA_SD_{σ}									0.012		Triaxial: p_c = 14 MPa p_p = 10 MPa σ = 0 – 45 MPa T = 25 °C	Ar
OPA_SH		MT_URL	2.39	2.77	13.8	74	11	15	0.016		σ_{UCS} = 34.9±0.3 MPa E = 1.8±0.1 GPa	UCS	-
	OPA_SH_{σ}									0.015		Triaxial: p_c = 14 MPa p_p = 10 MPa σ = 0 – 30 MPa T = 25 °C	Ar

WBS = Wissenbach slate, GRW = Graywacke, QTZ_HV = Quartzite Havelange, GRA_DV = Granite Death Valley, GOU_DV = Gouge Death Valley, OPA_SD = Opalinus Clay sandy facies, OPA_SH = Opalinus Clay shaly facies, MT_URL = 'Mont Terri' Underground research laboratory, OC = outcrop, σ_{TCS} = triaxial compressive strength, σ_{UCS} = uniaxial compressive strength, E = static Young's modulus, wt% = weight percent, ρ = bulk density, ρ_g = grain density, ϕ = porosity determined by Helium pycnometry, p_p = pore pressure, S_{q_ini} = initial fracture surface roughness, S_{q_def} = fracture surface roughness of the deformed sample (after testing), Phyl = phyllosilicates, Cb = carbonates, QFSO = quartz + feldspar + sulfides + oxides, p_c = confining pressure, T = temperature, σ = axial stress perpendicular to fracture surface, S_q = root mean square value of fracture surface roughness, H_2O = distilled water, Ar = Argon gas

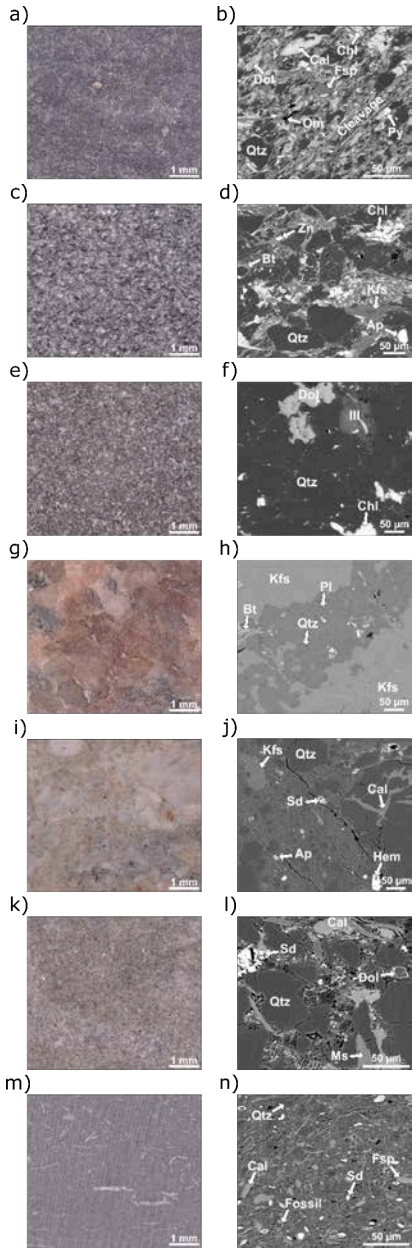

Figure 4.2: Optical micrographs (left column) and SEM-backscattered (BSE) images (right column) of investigated starting materials showing different composition and grain size (see text for details). (**a**, **b**) Wissenbach slate, (**c**, **d**) graywacke, (**e**, **f**) quartzite, (**g**, **h**) granite, (**I**, **j**) altered granitic gouge, (**k**, **l**) Opalinus Clay sandy facies, and (**m**, **n**) Opalinus Clay shaly facies. Note different scales. Dol = Dolomite, Cal = Calcite, Chl = Chlorite, Qtz = Quartz, Om = Organic Matter, Fsp = Feldspar, Py = Pyrite, Bt = Biotite, Zn = Zinc, Kfs = Kalifeldspar, Ap = Apatite, Ill = Illite, Pl = Plagioclase, Hem = Hematite, Sd = Siderite.

across two additional boreholes with an additional pressure transducer (Siemens Sitrans P DS III), which is capable of measuring differential pressures of $\Delta p_p = \pm$ 10 mbar (1000 Pa). This was

so that we could measure very low-pressure differences at low flow rates within the fracture. As our experiments were performed on low permeable rocks (matrix permeability $\approx 10^{-17}$ m^2), we assumed the contribution of fluid flow through the matrix to be negligible. Deviatoric stresses up to σ = 100 MPa perpendicular to the interface can be applied using an axial piston driven by another syringe pump (Isco 65D). The axial load is measured using an internally mounted load cell (200 kN). The displacement of the axial piston is measured by Linear Variable Differential Transformers (LVDT) with an uncertainty of ± 1 µm, allowing to correlate fracture transmissivity with changing fracture aperture and sample deformation induced by variations in axial stress, confining pressure, and temperature.

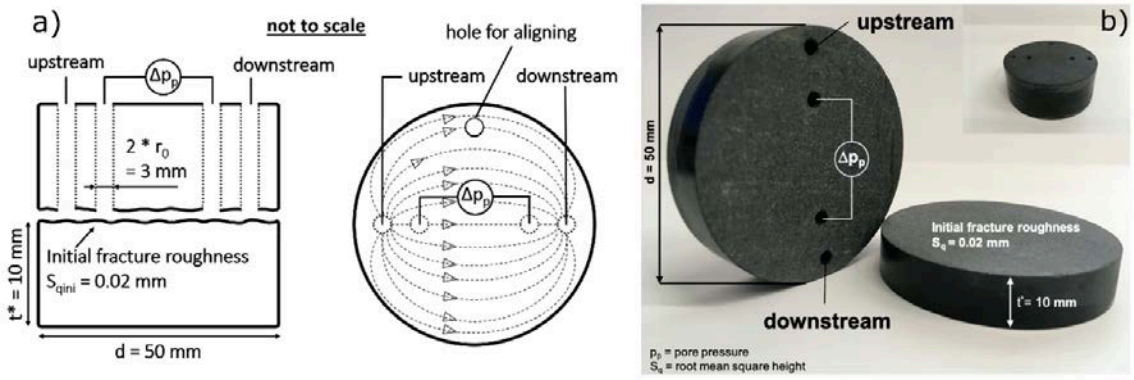

Figure 4.3: Schematic experimental setup of performed flow through experiments (**a**) and an example of a Wissenbach slate sample (**b**). Flow direction (dashed lines) is upstream borehole to downstream borehole. Differential pore pressure, δp_p, for the determination of fracture transmissivity is measured using a highly accurate pressure transducer by utilizing two additional boreholes. d = diameter, t^* = thickness.

For anisotropic rocks, the disks were prepared with the cylinder axis oriented perpendicular to bedding. The surface roughness of the artificial fracture, represented by the interface of the two sample disks, was controlled by grinding the flat saw-cut surfaces using SiC-grains of a defined diameter (Kl60 $\approx$ 260 µm). The resulting initial fracture surface roughness, S_q (root mean square value), prior to testing was S_{qini} = 0.016 $\pm$ 0.003 mm, except for the granitic gouge that revealed a considerably higher initial roughness of S_{qini} = 0.247 mm (Table 4.1), which was measured with a surface scanner (white light profilometer, Keyence VR3200, accuracy $\approx$ 3 µm). Since we also tested the influence of roughness on fracture transmissivity, an additional sample of Wissenbach slate was roughened with K600 SiC-grains (diameter $\approx$ 9 µm) resulting in lower S_{qini} of 0.006 mm.

Experiments on Wissenbach slate, Havelange quartzite, graywacke and the fresh Noble Hill granite from the Death Valley were performed using distilled water at a constant fluid pressure of p_p = 1 MPa (downstream borehole in Fig. 4.3) as fluid flowing through the artificial fracture. Samples prepared from Opalinus Clay, and the gouge material from the Death Valley were tested

using Argon gas to avoid sample disintegration during fluid flow. For comparison, one additional test on slate was also performed with Argon. Due to the high compressibility of the Argon gas, these experiments were performed at elevated p_p = 10 MPa to reduce the apparent permeability enhancement through the Klinkenberg effect (e.g., McKernan et al. 2017). The effective confining pressure $p_{eff} = p_c - p_p$ was kept constant (4 MPa) throughout most experiments so as to compare results gained with either distilled water or Argon gas. In a few cases, p_{eff} could not be held constant, for example, during tests with step-wise increasing confining pressure. Here, p_p was kept below p_c to avoid a 'blow-up' of the fracture.

Fracture transmissivity was calculated by assuming the fluid flow pattern within the fracture to be comparable to the flow of electric current through a resistive solid within an insulating medium (dashed lines in Fig. 4.3a). Assuming that the up- and downstream borehole form the dipole of a magnetic field and comparing Ohm's law with Darcy's law for steady fluid flow to characterize the transmissivity of thin cracks in various rocks, Ohm's law may be rewritten as (Rutter and Mecklenburgh 2018; Ji et al. 2022):

$$k^*t = \frac{Q * \eta * \ln\left(\frac{2a}{r_0} - 1\right)}{\Delta p_p * B * \pi} \tag{4.1}$$

where the term k^*t is the transmissivity of the fracture, with k and t representing fracture permeability and fracture thickness, respectively. Q is the volumetric flow rate, η is the (temperature-dependent) dynamic viscosity of the fluid, $2a$ is the distance between up- and downstream borehole with radius r_0, Δp_p is the pressure difference within the fracture, and B (=0.75 for our geometry) is a geometry factor accounting for the aspect ratio of the fracture (Rutter and Mecklenburgh 2018). Here, we assumed single-phase fluid flow within the fracture, which is certainly a simplification compared to multi-phase fluid flow that may occur in natural fractures and the surrounding matrix (Crandall et al. 2017).

A detailed microstructural analysis of the starting and the post-experimental samples was performed on mechanically as well as broad ion-beam polished, carbon-coated thin sections using a scanning electron microscope (SEM FEI Quanta 3D dual beam). SEM sections were prepared perpendicularly to the fracture surface. Broad ion-beam (BIB JEOL IB-19520CCP) polishing was used for the gouge and OPA samples to avoid preparation-induced damage of clay minerals. Due to its fragile character, the gouge was additionally solidified using epoxy resin prior to broad ion beam-milling.

In addition, we performed uniaxial compression (UCS) tests to determine the basic mechanical properties such as the uniaxial compressive strength (σ_{UCS}) and tangent Young's Modulus (E) of each sample material. The tests were performed according to the suggested ISRM method (Bieniawski and Bernede 1979) using cylindrical specimens with a length-to-diameter ratio of 2:1.

Results from UCS tests (Table 4.1) indicate that despite the high content of weak mineral phases, the strength and stiffness of WBS are comparable to granite, quartzite and graywacke samples that contain significantly more strong minerals. Furthermore, triaxial compressive strength (σ_{TCS}) and static secant Young's modulus of WBS were determined in constant strain rate tests of $\dot{\varepsilon} = 5 \times 10^{-4}$ s^{-1} at simulated reservoir conditions with a confining pressure of p_c = 50 MPa and temperature of T = 100 °C using a Paterson-type deformation apparatus (Paterson 1970).

4.3 Results

In total, we performed five flow-through experiments on Wissenbach slate to investigate the evolution of fracture transmissivity with changing confining pressure, differential stress oriented perpendicular to the fracture interface, temperature, and surface roughness. In addition, six tests under room temperature, constant confining pressure and stresses up to 45 MPa were conducted on the other rock types to evaluate the influence of composition on fracture transmissivity. The experimental duration for most of the experiments was between one and two weeks. Fracture transmissivity was determined after reaching steady-state flow conditions at the different thermodynamic boundary conditions.

Previously performed triaxial tests reveal σ_{TCS} = 498 $\pm$ 20 MPa and E = 69 $\pm$ 14 GPa (Table 4.1) that are comparable to the mechanical data of Westerly granite, Panzhihua gabbro or Novaculite (Rybacki et al. 2015) obtained at the same conditions.

4.3.1 Effect of Thermodynamic Boundary Conditions

Fracture fluid flow experiments at elevated p_c, T and σ -conditions were performed on Wissenbach slate samples with an average initial fracture surface roughness of S_q = 0.019 mm.

The influence of temperature on fracture transmissivity was evaluated at a confining pressure of p_c = 5 MPa and pore pressure of p_p = 1 MPa in the range of T = 20 – 100 °C (Table 4.2).

Except for a moderate decrease from T = 20 °C to T = 40 °C, fracture transmissivity does not change significantly at up to 100 °C (Fig. 4.4), showing that the fracture transmissivity of Wissenbach slate is insensitive to changes in temperature at a low confining pressure.

Table 4.2: Fracture transmissivity in Wissenbach slate at elevated temperatures (p_c = 5 MPa, σ = 0 MPa).

T (°C)	p_p (MPa)	k^*t (m^3)
25	1	1.33×10^{-14}
40	1	1.02×10^{-14}
60	1	1.02×10^{-14}
80	1	1.07×10^{-14}
100	1	9.40×10^{-15}

T = temperature, p_p = pore pressure, k^*t = fracture transmissivity

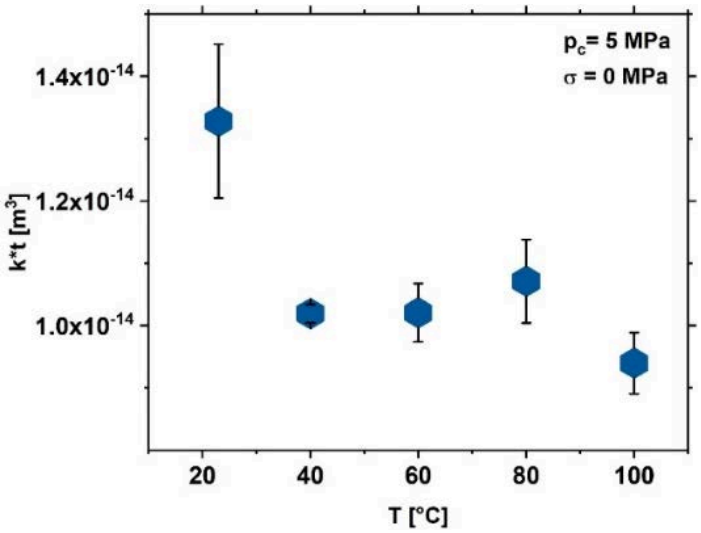

Figure 4.4: Effect of temperature, T, on fracture transmissivity, k^*t, in Wissenbach slate. Fracture transmissivity decreases only slightly from T = 20 °C towards T = 40 °C and remains almost constant with increasing temperature up to 100 °C. Experimental conditions are indicated.

Hydrostatic tests with confining pressures ranging from p_c = 2 – 25 MPa and p_p = 1 MPa were performed at a constant temperature of T = 25 °C (Table 4.3).

Fracture transmissivity decreased non-linearly by about one order of magnitude from ≈1.5 × 10^{-14} m^3 to 1.7 × 10^{-15} m^3 with increasing confining pressures, approaching almost constant values at high p_c (Fig. 4.5a).

Table 4.3: Fracture transmissivity in Wissenbach slate at elevated confining pressures (σ = 0 MPa, T = 25 °C).

p_c (MPa)	p_p (MPa)	k^*t (m^3)
2	1	1.46×10^{-14}
5	1	1.26×10^{-14}
10	1	3.01×10^{-15}
15	1	2.27×10^{-15}
20	1	1.24×10^{-15}
25	1	1.71×10^{-15}

p_c = confining pressure, pp = pore pressure, k^*t = fracture transmissivity

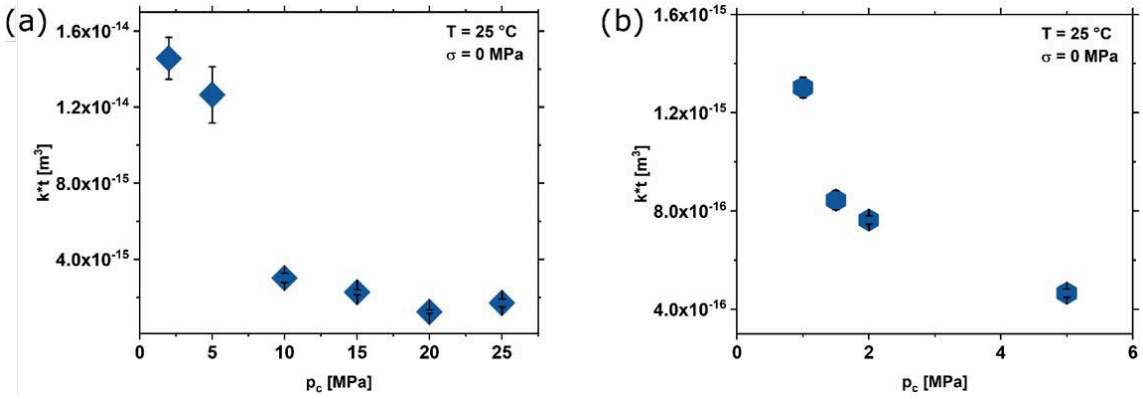

Figure 4.5: Effect of confining pressure, p_c, on fracture transmissivity, k^*t, in Wissenbach slate with high (S_q = 0.0196 mm) (**a**) and low (S_q = 0.006 mm) initial roughness (**b**). Fracture transmissivity is decreasing with increasing confining pressure. At relatively low p_c (≤5 MPa), fracture transmissivity is up to one order of magnitude lower for the sample with low initial roughness.

Experiments performed at p_c = 5 MPa, p_p = 1 MPa and T = 25 °C reveal a similar decrease in fracture transmissivity with increasing axial differential stress of σ = 0 – 45 MPa, but with a roughly 2-fold higher transmissivity than measured at similar p_c values (Table 4.4, Fig. 4.6a).

Interestingly, upon unloading, the fracture transmissivity did not recover and remained considerably lower than the initial transmissivity. For comparison, we performed a second test on the WBS slate using Argon gas as fluid medium at p_c = 14 MPa, p_p = 10 MPa, i.e., a similar effective pressure of $p_{c\_eff} = p_c - p_p = 4$ MPa, assuming that Terzaghi's principle (von Terzaghi 1923) is valid. For this sample, the initial transmissivity was found to be distinctly lower than of the sample with water as the fluid medium (Table 4.5, small symbols in Fig. 4.6a), but approaching similar values at high σ (≥40 MPa) and showing similar residual transmissivity upon unloading.

Table 4.4: Fracture transmissivity in Wissenbach slate at elevated differential stress (p_c = 5 MPa, T = 25 °C) using water as flow medium.

p_c (MPa)	p_p (MPa)	k^*t (m^3)
0.5	1	1.47×10^{-14}
5	1	1.01×10^{-14}
10	1	6.30×10^{-15}
15	1	4.83×10^{-15}
20	1	3.62×10^{-15}
25	1	2.67×10^{-15}
30	1	2.12×10^{-15}
35	1	1.51×10^{-15}
40	1	1.22×10^{-15}
45	1	8.87×10^{-16}
40	1	9.11×10^{-16}
35	1	9.22×10^{-16}
30	1	1.01×10^{-15}
25	1	1.04×10^{-15}
20	1	1.16×10^{-15}
15	1	1.29×10^{-15}
10	1	1.44×10^{-15}
5	1	1.63×10^{-15}
0.5	1	2.03×10^{-15}

σ = differential stress, p_p = pore pressure, k^*t = fracture transmissivity

For the sample tested with water, after the axial loading (phase I) and unloading (phase II) steps, we subsequently increased p_c from 5 to 50 MPa (phase III), resulting in a fracture transmissivity slightly lower than that measured at σ = 45 MPa (Table 4.6, Fig. 4.7), confirming the stronger influence of p_c on transmissivity reduction than of σ as described above.

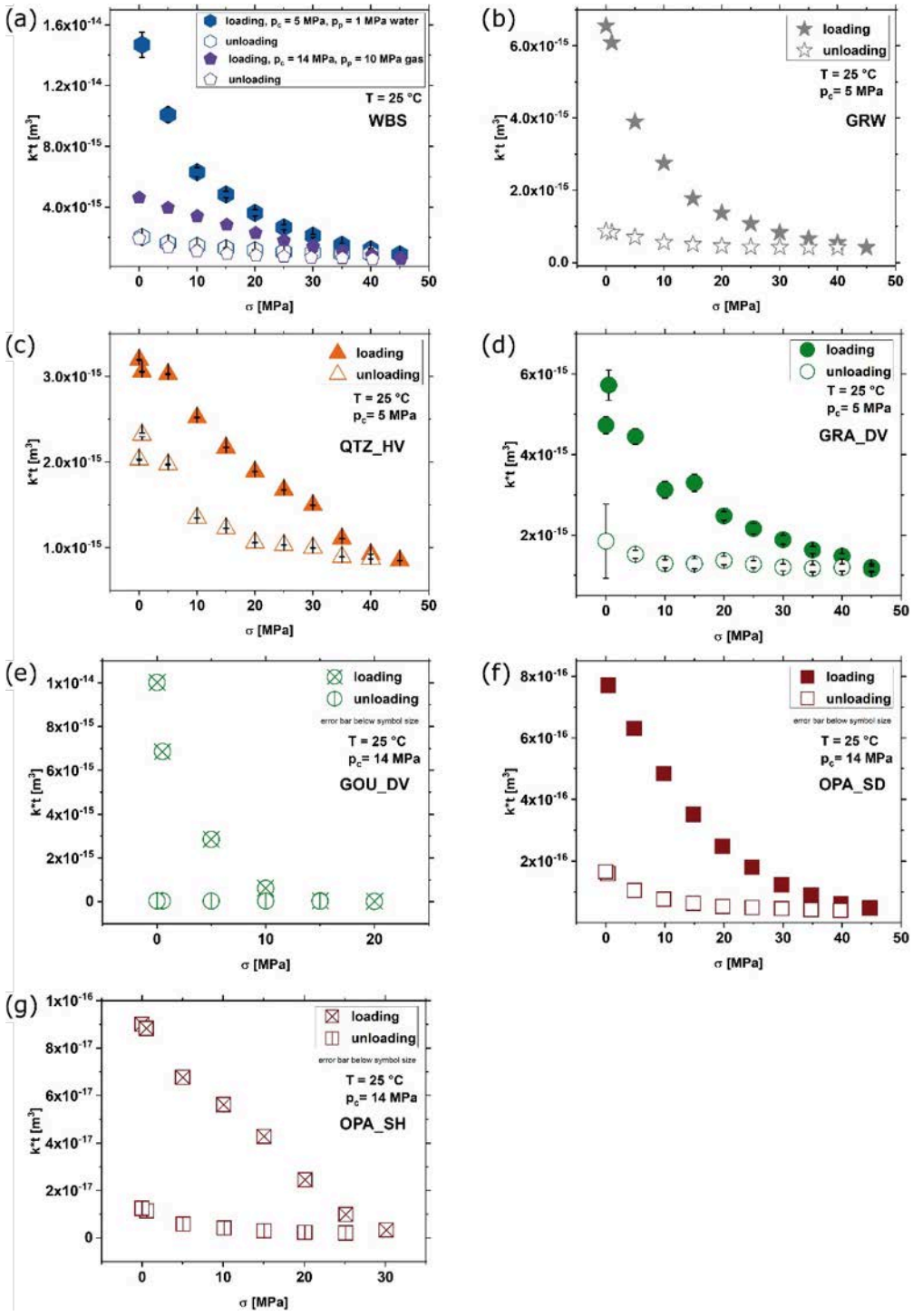

Figure 4.6: Effect of differential stress, σ, on fracture transmissivity, k^*t, in Wissenbach slate (**a**), Graywacke (**b**), Quartzite-Havelange (**c**), Granite-Death Valley (**d**), Gouge-Death Valley (**e**), Opalinus Clay sandy facies (**f**), and Opalinus Clay shaly facies (**g**). Experiments conducted at p_c = 14 MPa were performed using Argon gas as flow medium (gouge, OPA), all other with distilled water. The effective pressure ($p_c - p_p$) is 4 MPa in all cases. Experimental conditions are indicated. Note different scales.

Table 4.5: Fracture transmissivity in Wissenbach slate at elevated differential stress (p_c = 14 MPa, T = 25 °C) using Argon gas as flow medium.

σ (MPa)	p_p (MPa)	k^*t (m^3)
0	10	4.62×10^{-15}
5	10	3.95×10^{-15}
10	10	3.4×10^{-15}
15	10	2.83×10^{-15}
20	10	2.3×10^{-15}
25	10	1.8×10^{-15}
30	10	1.41×10^{-15}
35	10	1.08×10^{-15}
40	10	8.4×10^{-16}
45	10	6.58×10^{-16}
40	10	5.82×10^{-16}
35	10	6.41×10^{-16}
30	10	6.84×10^{-16}
25	10	7.44×10^{-16}
20	10	8.25×10^{-16}
15	10	9.3×10^{-16}
10	10	1.1×10^{-15}
5	10	1.37×10^{-15}
0	10	1.93×10^{-15}

σ = differential stress, p_p = pore pressure, k^*t = fracture transmissivity

Table 4.6: Fracture transmissivity in Wissenbach slate at elevated differential stress, confining pressures and temperatures.

Step	σ (MPa)	p_c (MPa)	T (°C)	p_p (MPa)	k^*t (m^3)
I	0.5	5	25	1	1.47×10^{-14}
	45	5	25	1	8.87×10^{-16}
II	0.5	5	25	1	2.03×10^{-15}
III	0	50	25	1	5.39×10^{-16}
IV	30	50	25	1	2.44×10^{-16}
V	30	50	90	1	1.88×10^{-17}

σ = differential stress, p_c = confining pressure, T = temperature, p_p = pore pressure, k^*t = fracture transmissivity

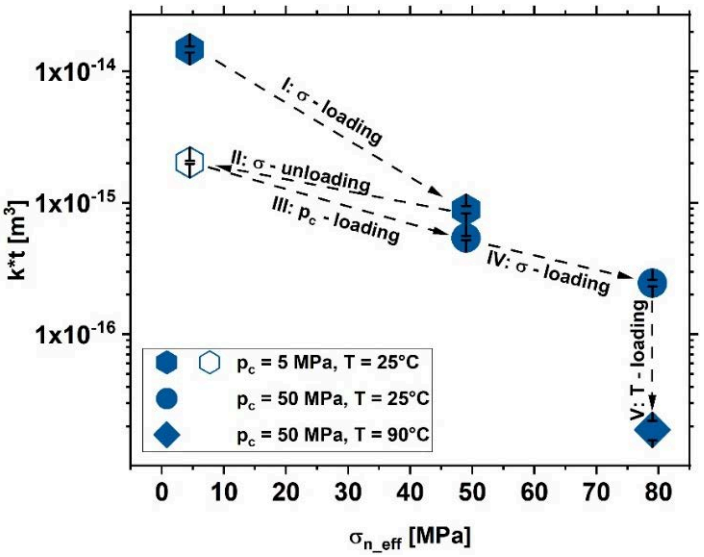

Figure 4.7: Combined effect of differential stress, σ, confining pressure, p_c, and temperature, T, on fracture transmissivity, k^*t, plotted versus effective normal stress, σ_{n_eff}, acting on the fracture surface in Wissenbach slate. Fracture transmissivity decreases along σ-loading path (I) and recovers only partly during unloading (II). Increasing p_c (III), σ (IV) and T (V) further decreases fracture transmissivity.

Note that for comparison we plotted the transmissivity data which are presented in Fig. 4.7 as a function of the effective normal stress $\sigma_{n_eff} = \sigma + p_c - p_p$, acting normal to the fracture surface. In phase IV, axial stress was increased again to σ = 30 MPa at a constant p_c of 50 MPa (σ_{n_eff} = 79 MPa), which yields a further transmissivity reduction, again with a lower gradient than observed in phase III (Fig. 4.7). Finally, we increased temperature from 25 to 90 °C at constant σ and p_c (phase V), which induced a strong transmissivity reduction of almost one order of magnitude.

4.3.2 Effect of Fracture Surface Roughness

The influence of reduced fracture surface roughness on the change of fracture transmissivity with increasing confining pressure of up to 5 MPa was measured on the Wissenbach slate at T = 25 °C (Table 4.7).

The initial fracture surface roughness of this sample was $S_{q_i ni_l ow}$ = 0.006 mm, which is roughly three times smaller than the surface roughness of previously examined samples ($S_{q_i ni}$ = 0.019 mm). Comparable to the rough surface, fracture transmissivity decreases non-linearly with increasing confining pressure (Fig. 4.5b), but at a similar p_c the transmissivity values are about one order of magnitude lower (Table 4.3). At higher confining pressures (p_c >5 MPa), we were not able to resolve transmissivity due to technical issues (below measurable range).

Table 4.7: Low-roughness-fracture transmissivity in Wissenbach slate at elevated confining pressures (σ = 0 MPa, T = 25 °C).

p_c (MPa)	p_p (MPa)	k^*t (m^3)
1	0.5	1.30×10^{-15}
1.5	0.5	8.44×10^{-16}
2	0.5	7.63×10^{-16}
5	1	4.65×10^{-16}

p_c = confining pressure, p_p = pore pressure, k^*t = fracture transmissivity

4.3.3 Effect of Sample Composition

To determine the impact of composition on fracture transmissivity, we performed flow-through experiments at T = 25 °C, with an effective pressure of p_{c_eff} = 4 MPa, and by increasing differential stress up to 45 MPa. Tests were conducted at p_c = 5 MPa, p_p= 1 MPa using water as fluid medium for samples WBS, GRW, QTZ_HV and GRA_DV. For the clay-rich samples GOU_DV, OPA_SD and OPA_SH, we used Argon at p_c =14 MPa and p_p = 10 MPa to avoid disintegration and swelling of the samples. As observed for WBS (Fig. 4.6a), in all other rocks, fracture transmissivity decreased non-linearly with increasing σ and demonstrated limited recovery upon unloading (Fig. 4.6, Table 4.8).

The initial transmissivity of the graywacke sample (Fig. 4.6b) is comparable to that of Havelange quartzite (Fig. 4.6c) and Noble Hill granite (Fig. 4.6d). However, the fracture transmissivity of the graywacke decreases at a higher rate upon differential loading, whereas the transmissivity of quartzite and granite decreases almost at the same point. The permanent reduction in transmissivity after unloading is lowest for the quartzite followed by the granite. On the other hand, the graywacke shows a reduction in transmissivity almost threefold that of the quartzite. Compared to WBS, the quartzite and granite were less sensitive to increasing stress, while the graywacke demonstrated a comparable sensitivity (Fig. 4.6). The Death Valley gouge shows a very strong transmissivity reduction already at low stress and almost no recovery after unloading (Fig. 4.6e), which is likely related to the relatively high preparation-related initial roughness, almost an order of magnitude higher than of the other rocks. For Opalinus Clay, transmissivity within the sandy facies (Fig. 4.6f) is about one order of magnitude higher than for the shaly facies (Fig. 4.6g). Interestingly, the non-linearity of transmissivity with increasing stress is least pronounced for OPA_SH. Note that the maximum stress on OPA_SH and GOU_DV samples was less than for the other rocks to avoid potential major creep deformation of these weak rocks.

For comparison, all data are shown in Fig. 4.8 in a semi-logarithmic scale, revealing that hard rocks such as granite and quartzite display transmissivity of several orders of magnitude higher at high σ and less irreversible damage than relatively weak OPA and gouge. Moreover, slate and

Table 4.8: Fracture transmissivity of Graywacke (GRW), Quartzite-Havelange (QTZ_HV), Granite Death-Valley (GRA_DV), Gouge-Death Valley (GOU_DV), Opalinus Clay sandy facies (OPA_SD), Opalinus Clay shaly facies (OPA_SH) at elevated differential stress and T = 25 °C.

Formation	Fluid	σ (MPa)	p_c (MPa)	p_p (MPa)	k^*t (m^3)
GRW	H2O	0	5	1	6.55×10^{-15}
		1			6.08×10^{-15}
		5			3.89×10^{-15}
		10			2.75×10^{-15}
		15			1.77×10^{-15}
		20			1.37×10^{-15}
		25			1.07×10^{-16}
		30			8.26×10^{-16}
		35			6.55×10^{-16}
		40			5.44×10^{-16}
		45			4.12×10^{-16}
		40			4.14×10^{-16}
		35			4.19×10^{-16}
		30			4.20×10^{-16}
		25			4.26×10^{-16}
		20			4.56×10^{-16}
		15			5.02×10^{-16}
		10			5.53×10^{-16}
		5			7.00×10^{-16}
		1			8.26×10^{-16}
		0			8.68×10^{-16}
QTZ_HV	H2O	0	5	1	3.20×10^{-15}
		0.5			3.06×10^{-15}
		5			3.03×10^{-15}
		10			2.52×10^{-15}
		15			2.17×10^{-15}
		20			1.89×10^{-15}
		25			1.67×10^{-15}
		30			1.50×10^{-15}
		35			1.11×10^{-15}
		40			9.22×10^{-16}
		45			8.50×10^{-16}
		40			8.68×10^{-16}

		35			8.90×10^{-16}
		30			9.98×10^{-16}
		25			1.03×10^{-15}
		20			1.06×10^{-15}
		15			1.23×10^{-15}
		10			1.35×10^{-15}
		5			1.97×10^{-15}
		0.5			2.32×10^{-15}
		0			2.03×10^{-15}
GRA_DV	H2O	0	5	1	4.73×10^{-15}
		0.5			5.72×10^{-15}
		5			4.44×10^{-15}
		10			3.13×10^{-15}
		15			3.30×10^{-15}
		20			2.48×10^{-15}
		25			2.16×10^{-15}
		30			1.88×10^{-15}
		35			1.63×10^{-15}
		40			1.47×10^{-15}
		45			1.16×10^{-15}
		40			1.20×10^{-15}
		35			1.17×10^{-15}
		30			1.20×10^{-15}
		25			1.27×10^{-15}
		20			1.37×10^{-15}
		15			1.28×10^{-15}
		10			1.29×10^{-15}
		5			1.52×10^{-15}
		0			1.84×10^{-15}
GOU_DV	Argon	0	14	10	1.00×10^{-14}
		0.5			6.86×10^{-15}
		5			2.85×10^{-15}
		10			6.17×10^{-16}
		15			4.69×10^{-17}
		20			2.14×10^{-17}
		15			2.84×10^{-17}
		10			3.02×10^{-17}

		5			3.22×10^{-17}
		0.5			3.81×10^{-17}
		0			3.86×10^{-17}
OPA_SD	Argon	0.5	14	10	7.71×10^{-16}
		5			6.30×10^{-16}
		10			4.83×10^{-16}
		15			3.51×10^{-16}
		20			2.48×10^{-16}
		25			1.79×10^{-16}
		30			1.23×10^{-16}
		35			8.95×10^{-17}
		40			6.05×10^{-17}
		45			4.78×10^{-17}
		40			3.91×10^{-17}
		35			4.22×10^{-17}
		30			4.52×10^{-17}
		25			4.88×10^{-17}
		20			5.20×10^{-17}
		15			6.23×10^{-17}
		10			7.58×10^{-17}
		5			1.04×10^{-16}
		0.5			1.59×10^{-16}
		0			1.65×10^{-16}
OPA_SH	Argon	0	14	10	8.99×10^{-17}
		0.5			8.82×10^{-17}
		5			6.76×10^{-17}
		10			5.61×10^{-17}
		15			4.27×10^{-17}
		20			2.44×10^{-17}
		25			9.86×10^{-18}
		30			1.85×10^{-18}
		25			2.06×10^{-18}
		20			2.30×10^{-18}
		15			2.98×10^{-18}
		10			4.20×10^{-18}
		5			5.81×10^{-18}
		0.5			1.13×10^{-17}

	0	1.24×10^{-17}

p_c = confining pressure, σ = differential stress, p_p = pore pressure, k^*t = fracture transmissivity

graywacke transmissivity is also relatively high (in the same range as of granite and quartzite transmissivity) at high σ but shows much less reversibility upon unloading. Note, however, that the initial roughness of the gouge sample is higher than of the other tested rocks, which may obscure the systematics to some extent.

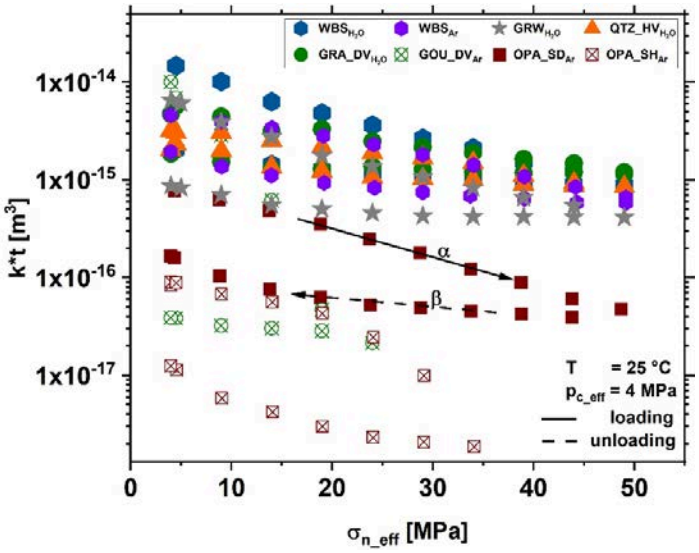

Figure 4.8: Comparison of the influence of effective normal stress, σ_{n_eff}, acting on the fracture surface on fracture transmissivity, k^*t. Data are the same as shown in Fig. 4.6, but plotted in semi-logarithmic scale. α and β indicate the linear slopes for fitting of the loading and unloading path to an exponential relationship (c.f., Equation (2)). Note that for unloading the slope is deviating from linearity at low stress.

4.4 Microstructures

After each experiment, the topography of the fracture surface of each sample was measured again with a white light profilometer in order to quantify changes due the applied experimental procedures. Thin sections of the tested specimens were then prepared for a subsequent SEM analysis.

In order to compare the surface topographies before and after the experiments, we show surface height distribution of the lower sample half (without injection/production holes, see Fig. 4.3a) of each sample in Figs. A4.1 and A4.2. In comparison to the initial surface, the height distribution of WBS samples (Fig. A4.1) measured after testing at increasing p_c, σ or T became slightly wider but remained more or less unaffected. This is also reflected by the determined surface roughness measurements, which are relatively similar to the initial roughness values (Table 4.1). The same applies to the other samples, showing slight widening of height distributions after deformation

(Fig. A4.2). However, height distributions of the quartzite and granite samples show the least changes (Fig. A4.2b, c), indicating no obvious change in the topography after loading. On the other hand, the distribution and fracture roughness of the gouge (Fig. A4.2d, Table 4.1) display the highest grade of asperity degradation, although the maximum applied stress did not exceed 20 MPa. Independent of the facies, the surface of fractures within the Opalinus Clay (Fig. A4.2e, f) exhibit a moderate alteration due to axial loading.

SEM micrographs of the Wissenbach slate and of the other rocks prepared perpendicular to the fracture surface are shown in Figs. 4.9 and 4.10, respectively.

For WBS, in comparison to the intact initial rough artificial fracture surface (Fig. 4.9a), the matrix close to the surface of samples after testing is severely damaged (Fig. 4.9b–e). Samples being step-wisely exposed to increasing temperature locally displayed a slightly flattened fracture surface profile (Fig. 4.9b, white arrow). Sporadically, quartz, carbonate and dolomite grains are fractured, potentially induced by local stress concentration. On the other hand, small intergranular fractures (<5 μm opening; black arrow in Fig. 4.9b) oriented subparallel to the macroscopic artificial fracture can be frequently observed, which may be partially induced by unloading and/or cooling and follows a cleavage orientation. Deformation microstructures of the sample deformed at varying confining pressure of up to 25 MPa are similar compared to the previously described sample. However, the density of intergranular, cleavage-parallel fractures is higher in comparison (Fig. 4.9c). Damage of the sample subjected to combined pressure, axial stress, and temperature variations was highest when a large number of intra- and transgranular cracks in calcite, dolomite and quartz mineral grains (white arrow in Fig. 4.9d) were detected. In addition, this sample shows several bent, kinked and delaminated micas (black arrows in Fig. 4.9d, e), indicative for crystal plasticity. Furthermore, we observed boudinage micas suggesting shear motion at grain boundary surfaces (white arrows in Fig. 4.9e). For all samples, the maximum damage zone is limited to <150 μm below the fracture surface profile line. As expected, the surface of the sample with a low initial roughness was considerably smoother compared to the other samples (Fig. 4.9f). Except for the subparallel fractures with a small aperture, damage of the surface by the applied pressure was hardly visible, likely because of the relatively low applied confinement.

The damage near the fracture surface of the other rocks after stress stepping varies with composition. The graywacke sample shows some spalling microfractures in quartz and feldspar grains close to the fracture interface (white and black arrow in Fig. 4.10a). Rarely, minor intergranular fractures (aperture <5 μm) propagate into the rock. The damage zone is limited to <150 μm.

In the Havelange quartzite, microfractures in quartz are confined to single grains. The intragranular cracks form near the surface and lead to the spalling of grain fragments, indicative of small grain contact areas during differential loading (white arrow in Fig. 4.10b). Despite the high number of fractures, the grain shape still remains relatively intact, resulting in a recognizable topography of asperities on the fracture surface. The damage zone below the fracture surface does not exceed

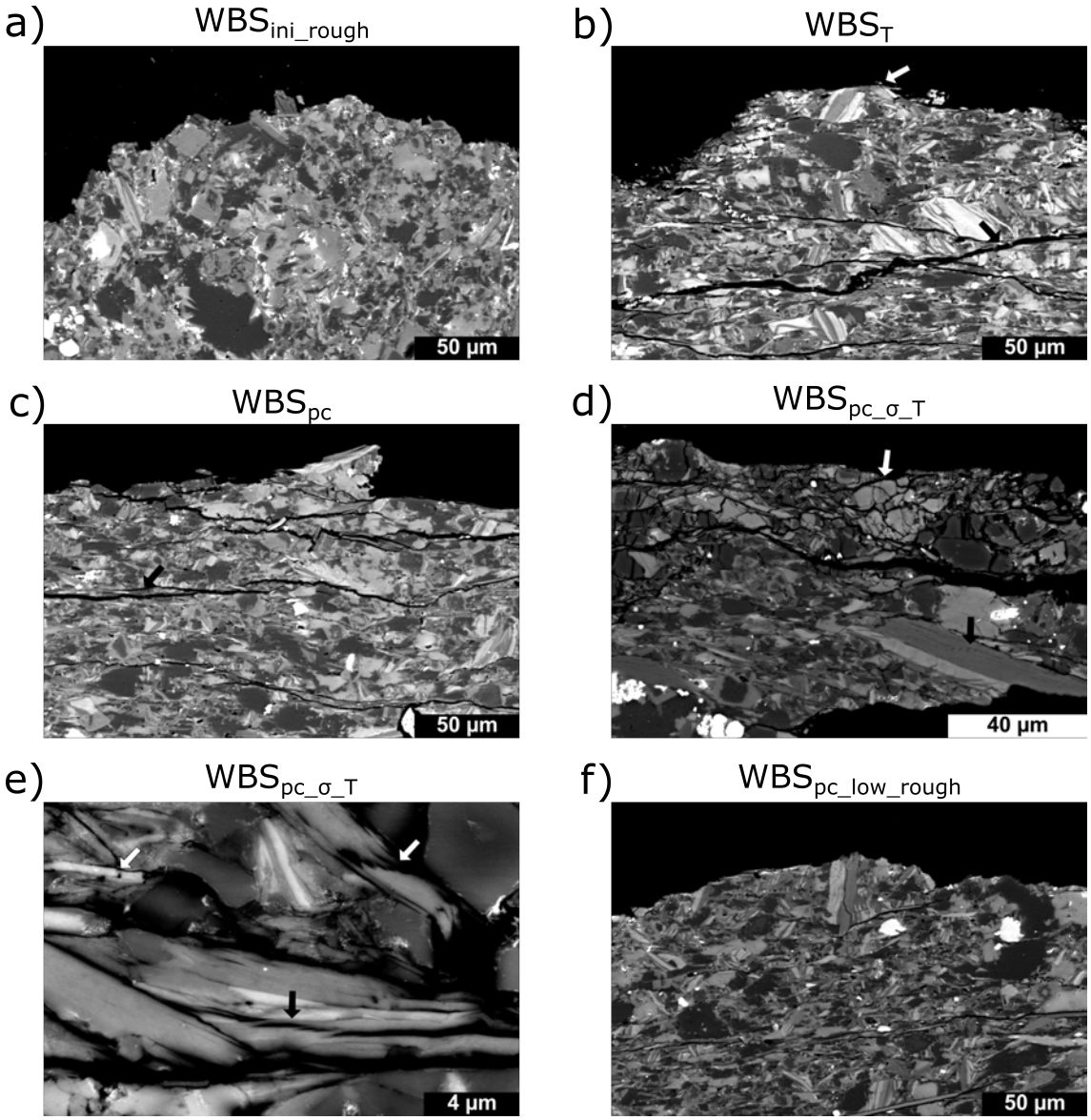

Figure 4.9: Scanning electron microscope-back scattered electron (SEM-BSE) photographs of sections prepared from Wissenbach slate (WBS) samples. All thin sections have been prepared perpendicular to the artificially prepared macro fracture located at the top of each image. Panel (**a**) shows the initial (ini_rough) fracture prior to testing. Subscripts 'T', 'pc', and 'pc_σ_T' refer to tests performed at increasing temperature (**b**), confining pressures (**c**), a combination of pressure, stress, and temperature (**d**, **e**). Panel (**f**) shows the post-experimental profile of the sample with initial low roughness. Arrows indicate microfracturing and intracrystalline plasticity (see text for details). Note the different scales.

150 µm and is limited to the first layer of grains below the fracture boundary. The Noble Hill granite also exhibited spalling in quartz and feldspar grains at the contact to the fracture surface (white arrow in Fig. 4.10c). In addition, we observed several intra- and trans-granular fractures opening

sub-parallel to the loading direction (black arrow in Fig. 4.10c) as well as the refracturing of previously healed, pre-existing fractures. Compared to the quartzite, the damage zone in the granite

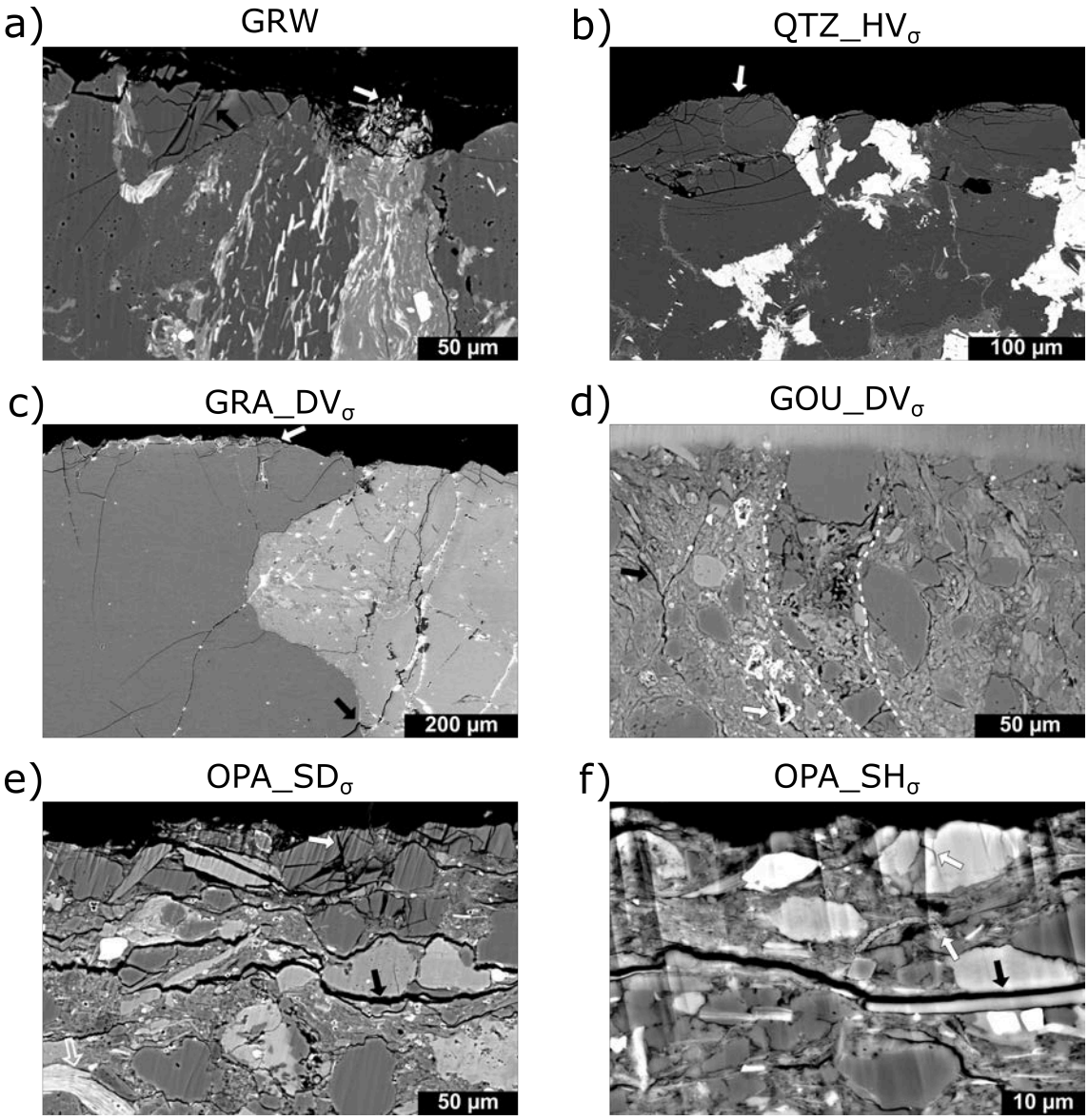

Figure 4.10: Scanning electron microscope-back scattered electron (SEM-BSE) photographs of sections prepared from samples of various formations after applying differential stress normal to the fracture surface. All thin sections have been prepared perpendicular to the artificially prepared macro fracture (located at the top of each figure). (**a**) Graywacke (GRW), (**b**) quartzite recovered from the Havelange borehole (QTZ_HV), (**c**) granite recovered from the Death Valley (GRA_DV), (**d**) gouge like material recovered from the Death Valley (GOU_DV), (**e**) Opalinus Clay material recovered from the sandy facies (OPA_SD), (**f**) Opalinus Clay recovered from the shaly facies (OPA_SH). Arrows indicate testing-induced damage (see text for details). Note different scales.

sample was found to be significantly larger. Single fractures extend up to 700 µm below the sur-

face. Due to the high alteration and tectonic overprint (Klee et al. 2021b), deformation structures that were generated by our experimental procedure were difficult to identify in the gouge from the Death Valley. Besides the cataclastic fabric and alteration of minerals (e.g., siderite, white arrow Fig. 4.10d), we identified deformation features such as strongly bent phyllosilicates, the collapse of pore space and altered mineral grains (area between dashed white lines in Fig. 4.10d). Clastic mineral grains (quartz, carbonates, feldspars) and mineral fragments show rare evidence of experimentally induced fractures. We observed several intergranular fractures that potentially opened during unloading (black arrow in Fig. 4.10d). Note that the milling artifacts at the fracture surface are caused by the partly remaining resin, which was applied after testing to avoid preparation-induced damage. Opalinus Clay of the sandy (Fig. 4.10e) and shaly (Fig. 4.10f) facies typically displayed matrix deformation by the bending of phyllosilicates (open arrow in Fig. 4.10e) and small fractures opening sub-parallel to the fracture surface (black arrows in Fig. 4.10e, f). Clastic mineral grains in the sandy facies display several transgranular microfractures (white arrow in Fig. 4.10e). On the other hand, the shaly facies show a significantly lower amount of fractured mineral grains compared to the sandy facies. Furthermore, these are limited to calcite grains and fossil shells, whereas quartz grains remained unfractured (white arrows in Fig. 4.10f). In both facies, the 'card house' structure of the clay matrix observed in the undeformed material collapsed with clay minerals being reoriented, with their longest axis parallel to the fracture surface and perpendicular to the maximum principal stress direction. The damage zone extends up to 150 µm below the surface in the sandy facies and up to 300 µm in the shaly facies.

4.5 Discussion

Our set of flow-through experiments demonstrated that at given fracture surface roughness increasing confining pressure, differential stress, and temperature at elevated pressure reduces the fracture transmissivity of slates (Figs. 4.4–4.7). Furthermore, the initial transmissivity reduced considerably for smooth surfaces compared to rough surfaces (Fig. 4.5). A strong influence of sample composition and associated mechanical properties on transmissivity is also evident (Figs. 4.6 and 4.8). These effects will be discussed in the following paragraphs.

4.5.1 Influence of Thermodynamic Boundary Conditions (T, p_c, σ) on Fracture Transmissivity of Wissenbach Slate

Temperature has a strong effect on the interaction between the fluid transported through the fracture and the adjacent host rock (Yasuhara et al. 2011; Li et al. 2014; Lima et al. 2019; Cheng et al. 2020b). The rate of dissolution of asperities is often enhanced at high temperatures and can reduce the mean fracture aperture due to mineral precipitation (Yasuhara and Elsworth 2008; Yasuhara et

al. 2011; Kamali-Asl et al. 2018; Lima et al. 2019). For WBS flushed with water, Cheng et al. (2021) observed a slight (few %), time-dependent fracture permeability decline in long-term flow-through tests at p_c = 10 MPa, σ = 0 MPa and elevated temperatures up to 90 °C due to pressure solution and free face dissolution. However, using saline fluids, the authors measured an increase in permeability with increasing T, probably related to enhanced dissolution kinetics. In our tests with distilled water, we observed that at p_c = 5 MPa and σ = 0 MPa the fracture transmissivity of WBS was hardly affected by temperature between 25 and 100 °C (Fig. 4.4), except a small decrease (≈23%) between 25 and 40 °C. This confirms that temperature sensitive processes, like chemical dissolution-precipitation processes or stress corrosion at areas of high stress concentration were not very effective within the relatively short time span of our experiments. In contrast, transmissivity dropped considerably more (≈93%) at p_c = 50 MPa and σ = 30 MPa in response to a temperature increase from 25 to 90 °C (Fig. 4.7). This observation suggests that thermal dilation is more effective at high effective normal stress since the mean fracture aperture is lower than at low p_c, σ conditions (e.g., Lima et al. 2019; Rutqvist et al. 2015). However, performing experiments over a longer time range may be necessary to reliably record chemical processes such as diffusion and mineral precipitation as reported by Cheng et al. (2021). These authors performed similar flow-through experiments on samples prepared from the same slate material emphasizing the effect of fluid-rock interactions on the time-dependent transmissivity of fractures.

Concerning the influence of pressure and stress on transmissivity, we observed that the transmissivity is slightly (about two times) higher at enhanced p_c compared to a similar enhancement of σ alone, although the effective stress acting normal to the interface is the same (e.g., Fig. 4.7). The difference may be explained by the increasing strength of the matrix adjacent to the fracture and the suppression of tensile fracturing with increasing pressure, whereas with increasing stress but constant (low) confining pressure the strength of the aggregate is lower than at high p_c. In both cases, the observed reduction in fracture transmissivity with increasing p_c or σ (Figs. 4.5 and 4.6) is likely induced by indentation and damage of fracture surface asperities (Figs. 4.9 and 4.10), resulting in a change of contact area and therefore mean aperture. A similar trend of decreasing fracture transmissivity induced by mechanical and/or pressure solution processes is reported for other rocks, e.g., shales, (tight) sandstones, granites, and granodiorite (Yasuhara et al. 2004; Yasuhara et al. 2011; Cho et al. 2013; Vogler et al. 2016; Rutter and Mecklenburgh 2017, 2018; Cao et al. 2019; Lima et al. 2019; Cheng and Milsch 2020a).

Interestingly, the transmissivity of WBS at low applied stress was distinctly lower for the sample tested with Argon at p_c = 14 MPa, p_p = 10 MPa than for the sample flushed with water at p_c = 5 MPa, p_p = 1 MPa, i.e., at the same effective pressure (Fig. 4.6a). The difference may be attributed to the experimental protocol, where in the case of Argon the initial 14 MPa confining pressure was applied before applying the fluid pressure. This may induce more initial damage of the surface compared to the test with water at only 5 MPa confining pressure (cf., Fig. 4.5a). In addition, it

is not well established that Terzaghi's principle of effective stresses, i.e., $p_{c\_eff} = p_c - \delta p_p$ with δ = 1, is valid here because at the microscale asperities are in contact, which reduces the Biot coefficient δ to a value <1. This effect may result in a higher effective pressure in the experiment conducted with Argon gas compared to that with water, which would reduce the transmissivity difference at low stress. On the long term, chemical effects may also contribute to the transmissivity evolution due to different chemical fluid-rock interaction rates for different types of fluids.

In Fig. 4.11, a comparison of our data with that measured by Rutter and Mecklenburgh (2018) on Westerly granite, Pennant sandstone and Bowland shale is presented, revealing that the influence of effective pressure on transmissivity disappears at high p_{c_eff}. The transmissivity of WBS appears to be comparable to that of Pennant sandstone, whereas the transmissivity of our granite appears to be considerably lower than that of Westerly granite. Bowland shale exhibits the lowest transmissivity values, which are even lower than our clay-rich samples. The difference may be attributed to the initial roughness of the samples used by Rutter and Mecklenburgh (2018), which was unfortunately not provided by the authors.

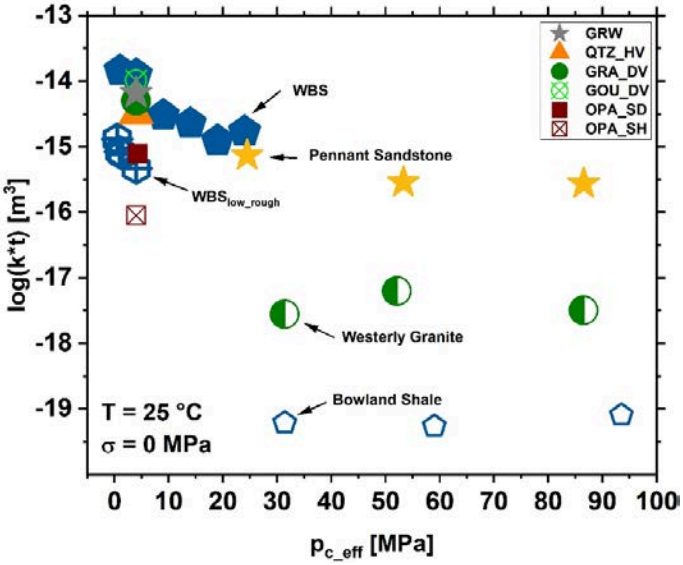

Figure 4.11: Effect of effective confining pressure, $p_{c\_eff} = p_c - p_p$, on fracture transmissivity, k^*t, in Wissenbach slate (WBS) in comparison with other formations as reported by Rutter and Mecklenburgh (2018). Data of the other formations investigated here (at σ = 0 MPa, c.f., Fig. 4.6) are shown in addition.

The non-linear transmissivity reduction with increasing pressure and/or stress (Figs. 4.5, 4.6 and 4.8) may be explained by the initial elastic deformation of the asperities that is gradually replaced by irreversible damage due to high stress concentrations. Since the effective contact area also increases with load (e.g., Bowden and Tabor 1964), deformation or the breaking of further asperities or grains in the vicinity of the fracture surface become increasingly hampered and additional deformation is increasingly promoted by matrix deformation. As a consequence,

the fluid flow pattern likely changes towards a higher tortuosity of the flow path and probably towards more localized flow through channels at high pressures, as also observed for other rocks (e.g., Cheng and Milsch 2020a). A number of theoretical attempts were made to relate fracture transmissivity to surface roughness and the applied normal stress (e.g., Gangi 1978; Witherspoon et al. 1980; Walsh 1981; Tsang and Witherspoon 1983; Zimmerman et al. 1992; Huo and Benson 2015). From that and from empirical correlations based on experiments, the change in fracture permeability with stress was described by a hyperbolic relationship (Barton et al. 1985), power law (Gale 1982), or an exponential law (Gutierrez et al. 2000; Huo and Benson 2015). Here, we used an exponential law of the following form:

$$k^*t = c * e^{x*\sigma_{n\_eff}} \tag{4.2}$$

where c is a constant and x is the slope in a plot of $\ln(k^*t)$ vs. σ_{n_eff}, with $x = \alpha$ for the loading path and $x = \beta$ for the unloading path (c.f., Fig. 4.8). For WBS, β is about 3 times smaller than α (Table 4.9), showing that irreversible damage changes the stress-sensitivity of transmissivity considerably.

Table 4.9: Influence of host rock composition on fracture transmissivity.

Sample	α	β	B_{compo}
WBS	-0.061±0.002	-0.018±0.002	0.32
WBSAr	-0.044±0.001	-0.025±0.002	0.32
GRW	-0.061±0.003	-0.019±0.003	0.41
QTZ_HV	-0.030±0.001	-0.022±0.003	0.71
GRA_DV	-0.032±0.001	-0.008±0.002	0.90
GOU_DV	-0.319±0.023	-0.026±0.003	0.61
OPA_SD	-0.065±0.001	-0.030±0.005	0.61
OPA_SH	-0.110±0.014	-0.064±0.008	0.16

α = slope of loading branch, β = slope of the unloading branch, B_{compo} = brittleness index based on sample composition. WBS = Wissenbach slate, WBS_{Ar} = Wissenbach slate tested with Argon, GRW = Graywacke, QTZ_HV = Quartzite Havelange, GRA_DV = Granite Death Valley, GOU_DV = Gouge Death Valley, OPA_SD = Opalinus Clay sandy facies, OPA_SH = Opalinus Clay shaly facies

4.5.2 Sample Composition and Mechanical Properties

To better quantify the influence of composition and mechanical properties on fracture transmissivity, we applied the exponential law on the transmissivity–stress data of all other rocks, yielding values in the range of -0.03 and -0.32 for α, and -0.008 and -0.064 for β (Table 4.9).

Lowest (absolute) α-values were fitted for granite and quartzite samples, whereas absolute α-

values of the graywacke and slate are about twice as high and comparable to the sandy facies of OPA. Lowest (absolute) β-values were found in the granite and graywacke. In order to relate these values to composition, we superimposed them in ternary diagrams (Fig. 4.12).

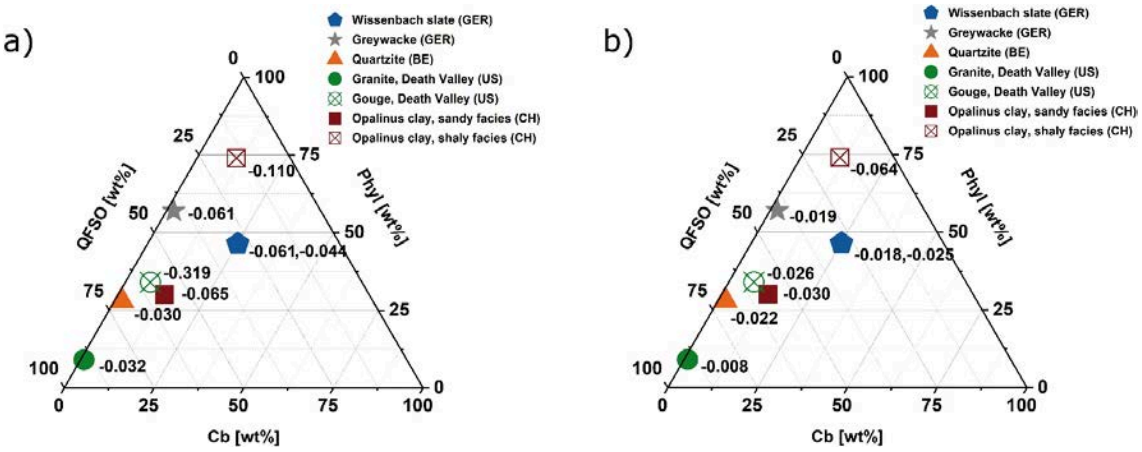

Figure 4.12: Influence of sample composition on the (effective) stress-sensitivity of fracture transmissivity indicated by superimposed α-values for the loading path (**a**) and by β-values for the unloading path (**b**). The (absolute) sensitivity generally decreases for a high fraction of strong (QFSO) minerals and low amount of weak (Phyl) constituents.

Low (absolute) α-values, indicative of a weak reduction in transmissivity at elevated stress appear to be correlated with a high fraction of strong components (QFSO) and a low amount of weak constituents (Phyl), whereas carbonates appear to have no influence (Fig. 4.12a). For the unloading sensitivity β, which is high for strong fracture transmissivity recovery, we observed a trend of enhanced unloading recovery with an increasing quantity of weak minerals and decreasing amount of QFSO (Fig. 4.12b). Note that other parameters, which likely influence α and β, for example, porosity and cementation, are not captured in the diagrams.

In addition, we compared the σ-sensitivity of transmissivity for the different rock types with their brittleness defined by composition. Here, we used the empirical brittleness definition suggested by Rybacki et al. (2016):

$$B_{compo} = \frac{w_{QFSO} * f_{QFSO}}{w_{QFSO} * f_{QFSO} + w_{Cb} * f_{Cb} + w_{Phyl} * f_{Phyl}} \tag{4.3}$$

where f_{xx} is the fraction of minerals xx given in wt% and w_{QFSO}, w_{Cb}, and w_{Phyl} are the weighting factors ranging from 0 to 1. We set $w_{QFSO} = w_{Phyl} = 1$ and $w_{Cb} = 0.5$ as suggested by Rybacki et al. (2016). Calculated brittleness values are given in Table 4.9, ranging from 0.16 to 0.90. Based on the simplified assumption that in the absence of strong (QFSO) minerals the mechanical behavior is dominantly ductile, B values can vary between 0 and 1, indicating ductile and brittle deformation behavior, respectively. For rocks with high brittleness, the effect of increasing pressure or axial

stress on fracture transmissivity is expected to be lower than for those with low B values. With the exception of the gouge, absolute values of α decrease with increasing B_{compo} (Fig. 4.13a) in line

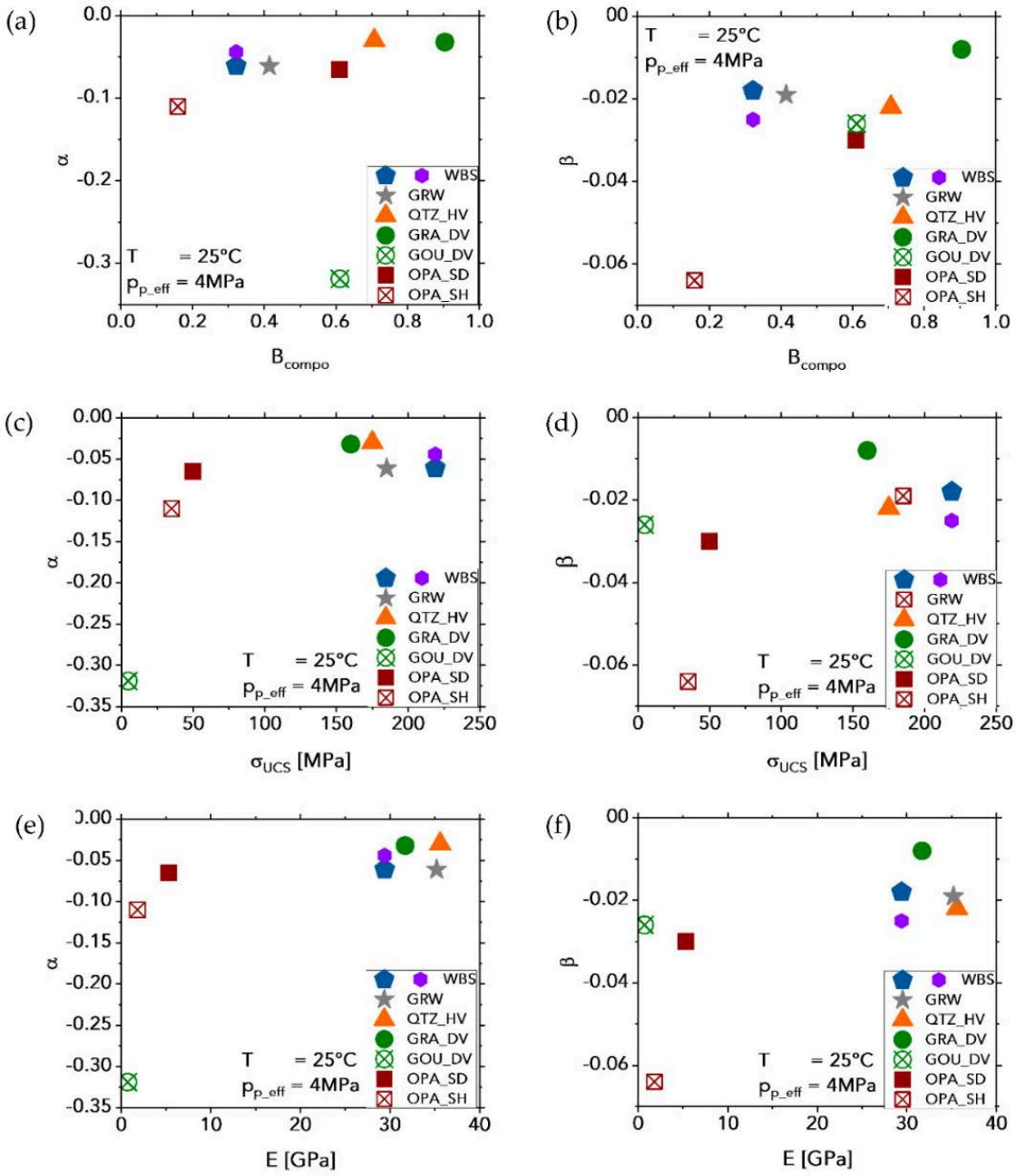

Figure 4.13: Influence of brittleness based on composition, B_{compo}, uniaxial compressive strength, σ_{UCS}, and static Young's modulus, E, on the (effective) stress-sensitivity of fracture transmissivity, α, for the loading path (**a**, **c**, **e**) and for the unloading path β (**b**, **d**, **f**), respectively. The (absolute) sensitivity decreases with increasing brittleness, strength, and elastic stiffness.

with the common assumption that the deformation of brittle rocks is less stress-sensitive than that

of ductile rocks. The low α value of the gauge-like material recovered from the Death Valley is most likely due induced by the high initial roughness and a high porosity of about 13 vol% (Table 4.1). Similarly, the (absolute) unloading sensitivity β seems to slightly decrease with increasing brittleness (Fig. 4.13b), which may be explained by the crushing of strong and brittle minerals at the fracture surface at elevated stresses, where the produced fines prevent the recovery of fracture transmissivity during unloading.

Another parameter that likely explains the stress-sensitivity of the fracture transmissivity of the different investigated rocks are their mechanical properties. The measured unconfined uniaxial strength, σ_{UCS}, and the static Young's moduli, E, vary over wide range and appear to be linearly correlated (Table 4.1, Fig. A4.3), as has been observed frequently (e.g., Rybacki et al. 2015; Herrmann et al. 2018). Compared to composition-based brittleness, both (absolute) α and β values decrease with increasing σ_{UCS} and E (c.f., Fig. 4.13c–f, respectively), revealing that rocks with a high strength and/or elastic stiffness are less sensitivity to stress-induced damage of the fracture surface and associated transmissivity reduction.

4.5.3 Implications for EGS in Different Host Rocks

An assessment of the performance and sustainability of fractured rock systems for EGS requires knowledge of the response of fractures to the acting effective stress, temperature, and fluid flow. The effective normal stress on fractures changes during and after hydraulic stimulation of reservoirs. As may be expected, our results of flow-through experiments on various rock types (i.e., slate, quartzite, graywacke, granite, claystone, and gouge material) demonstrate that the key parameters that determine the stress resistance of fracture transmissivity are fracture surface roughness and the mechanical properties of the respective rock material. Fractures with similar surface roughness display the highest transmissivity in slate, quartzite, graywacke, and fresh granite, all of which contain a high amount of strong minerals and display high brittleness, high strength, and high elastic stiffness. On the other hand, in weak and porous rocks such as claystone and gouge material, transmissivity is reduced by several orders of magnitude by deformation of the soft matrix and limited crushing of contact asperities. Therefore, highly altered, clay-bearing formations are not favorable candidates for EGS. For hard rocks, grain size may also play a role if fracture propagation is predominantly intergranular. For example, the grain size of slate and graywacke is much smaller than that of quartzite and granite (Fig. 4.2), so that at the microscale the real contact area of fine-grained rocks is higher, which reduces the stress acting on contact asperities, thereby maintaining a higher transmissivity.

Our results also imply that beside fracture surface roughness and composition, the degree of consolidation and metamorphic grade affects the potential of reservoir rocks for EGS. For example, the shaly facies of Opalinus Clay, graywacke and slate are relatively rich in phyllosilicates

(Fig. 4.1), but the latter two experienced a higher degree of metamorphosis with a strong cementation of grains, resulting in a much higher strength and elastic stiffness (Fig. A4.3). Accordingly, fractures in slates are much more resistant against stress-induced fracture closure than in OPA (Fig. 4.8). We also noticed that (for slate samples) an increase in the fracture surface roughness (S_q) by about three times yields a fracture transmissivity of almost one order of magnitude higher at a low effective pressure (<5 MPa), which vanishes at high pressure (up to 25 MPa in our experiments), possibly due to the fact that the mechanical strength of slate at the microscale is not sufficient to resist high effective stresses. During hydraulic stimulation in EGS, tensile fractures are created that may connect to a preexisting fracture network. The surface roughness of these fractures is likely higher than the roughness of the artificially prepared surfaces in our study. For example, we measured a significantly larger (up to 20×) and more heterogeneously distributed roughness of tensile fractures created in WBS by Brazilian Disk (BD) experiments in divider, short transverse, and arrester configuration following the ISRM suggested method (Ulusay 2015). However, even fractures with high initial roughness, e.g., created during hydraulic fracturing, may show a strong transmissivity decline at high stress conditions as long as they are not self-propped by shearing or artificially kept open by the addition of proppants (e.g., Durham and Bonner 1994). For the latter, high stress may crush the proppants and embed them into the matrix, which leads again to a transmissivity reduction (e.g., Reinicke et al. 2010).

Other parameters, which were not investigated in this study, may also affect the efficiency and sustainability of an EGS in different formations, for example self-propping due to a shear deformation event or fine production and clogging of flow path by ongoing deformation. Additionally, chemical effects due to long-term fluid–rock interactions or scaling may change the fracture transmissivity, depending on fluid and rock composition and thermodynamic boundary conditions.

4.6 Conclusion

Fracture transmissivity decreases asymptotically with increasing confining pressure and stress due to the damage caused to surface asperities and the matrix deformation of weak rocks, which is largely irreversible. A lower initial roughness also reduces transmissivity, while a temperature increase only significantly reduces the transmissivity by thermal dilation if the fracture aperture is already low. As may be expected, the fracture transmissivity of hard brittle rocks with a high fraction of strong minerals is less sensitive to stress-induced fracture closure and exhibits less irreversible damage. However, since the transmissivity of slates is much higher than of claystone, as well as the transmissivity of granite compared to a highly altered and sheared granitic gouge, the grade of consolidation, metamorphosis, and alteration of rocks is also important for fluid flow within discrete fractures under in situ conditions. Our results suggest that Variscan metamorphic rocks such as slate, graywacke and quartzite can be considered as host rocks for unconventional

Enhanced Geothermal systems, with resistance to fracture transmissivity against thermodynamic boundary conditions that is as good as that of granite or quartzite for similar initial fracture roughness.

Acknowledgments

We thank Michael Naumann for the construction of the modified MuSPIS apparatus and for their assistance with the uniaxial and triaxial deformation as well as fracture transmissivity experiments, Stefan Gehrmann for sample and thin section preparation, Anja Schreiber for carbon coating of SEM samples, Bianca Wagner and Bernd Leiss from the University of Göttingen for XRD results and providing Wissenbach slate and graywacke samples, Yves Vanbrabant from Institut Royal des Sciences Naturelles de Belgique for providing Havelange quartzite samples, Ghislain Trullenque and Johanne Klee from Institut Polytechnique LaSalle Beauvais for providing granite and gouge samples, and Kristian Bär and Aysegül Turan from the Technical University of Darmstadt for providing some mechanical and petrophysical data.

Appendix

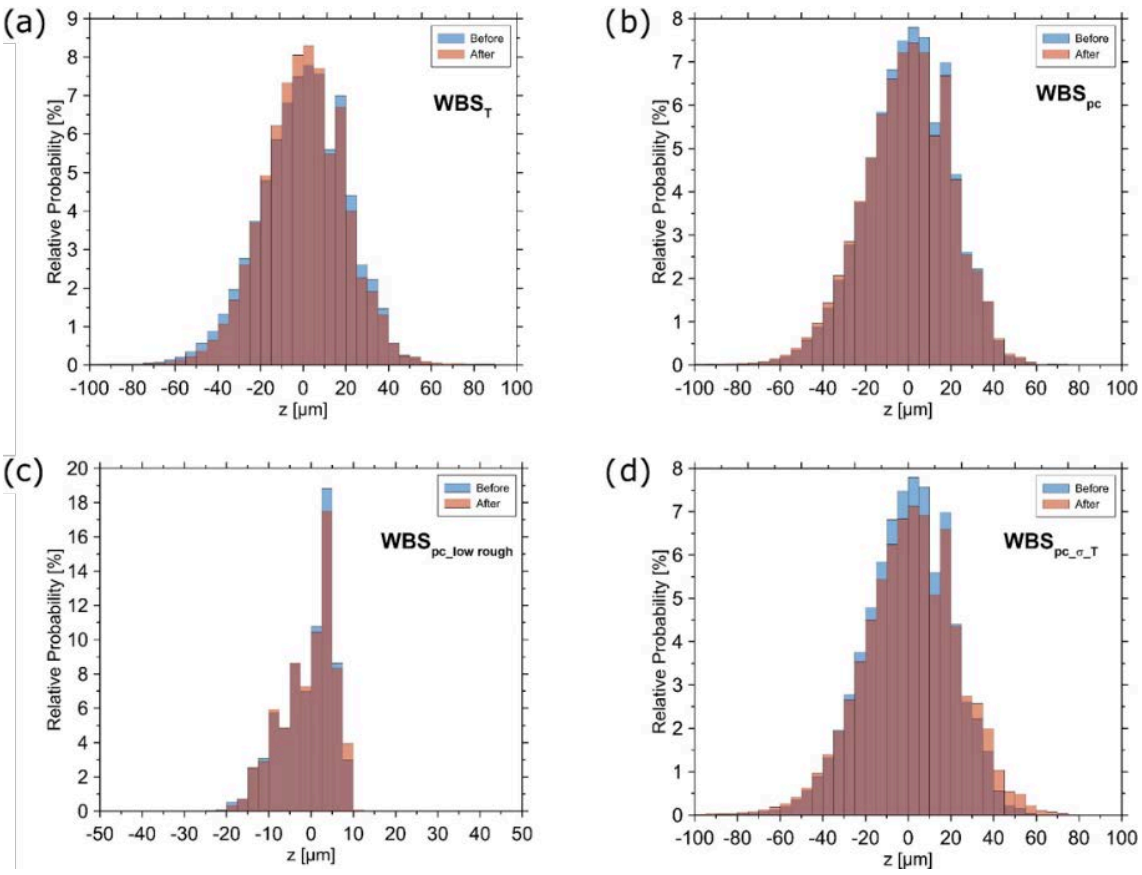

Figure A4.1: Fracture surface height distribution before and after experiments for Wissenbach slate tested at different temperatures (**a**), confining pressures (**b**, **c**), and a combination of different pressures, stresses and temperatures (**d**). Initial sample roughness was S_q = 0.019 mm in (**a**, **b**, **d**) and S_q = 0.006 mm in (**c**).

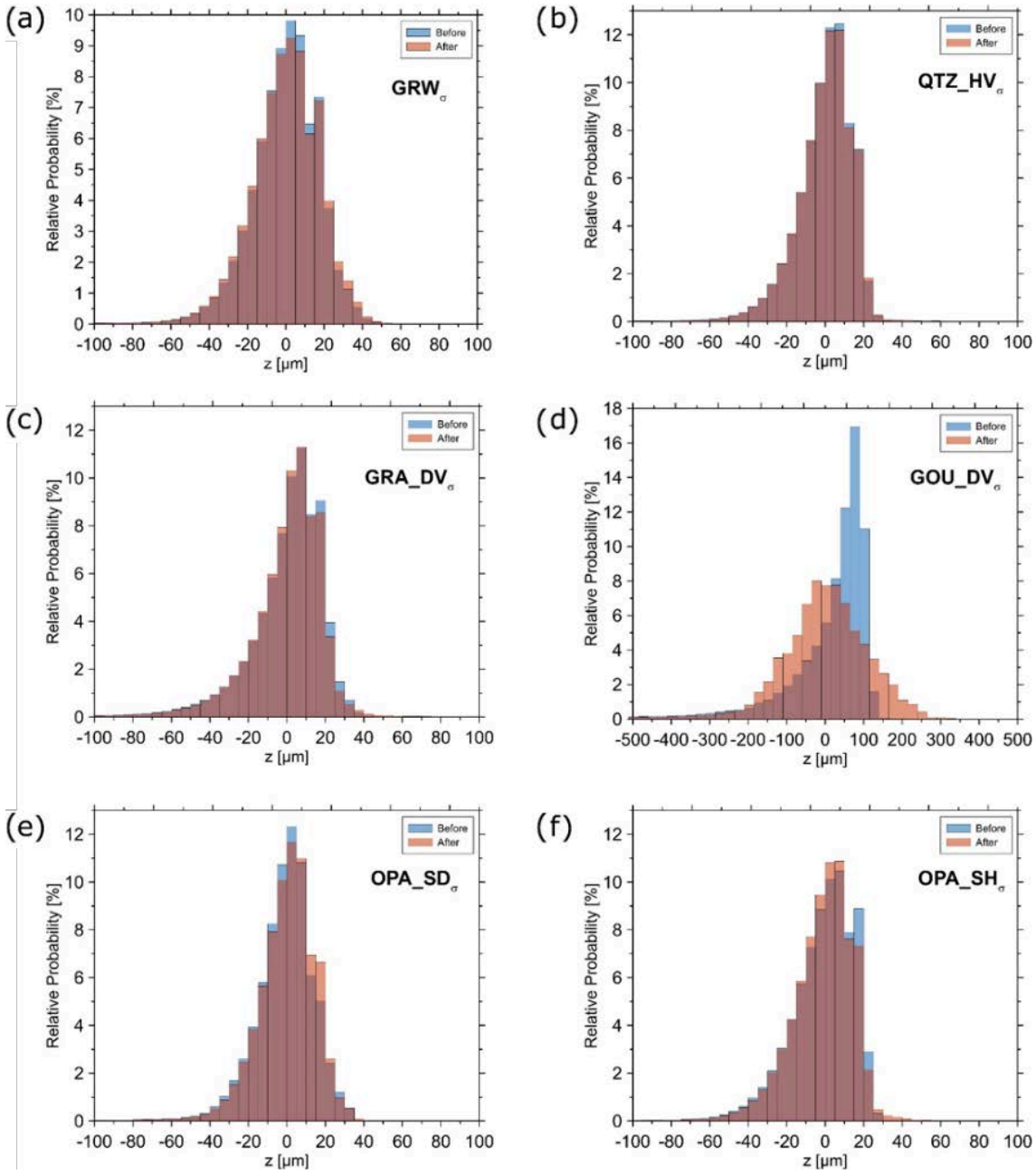

Figure A4.2: Fracture surface height distribution before and after testing at elevated stresses for graywacke (**a**), quartzite (**b**), fresh granite (**c**), altered granitic gouge (**d**), Opalinus Clay sandy facies (**e**), and Opalinus Clay shaly facies (**f**).

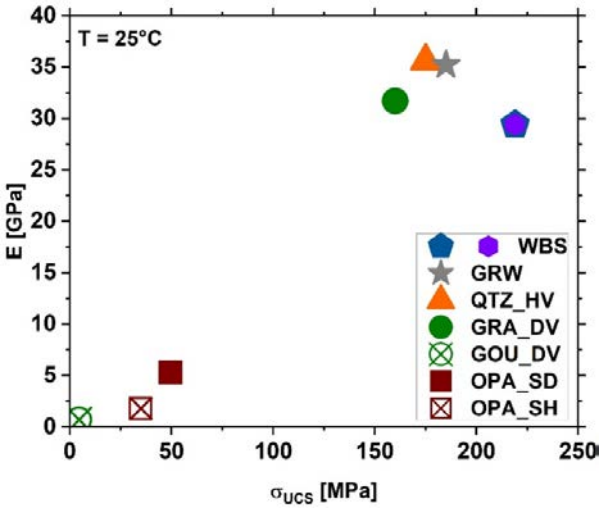

Figure A4.3: Static Young's modulus E vs. uniaxial compressive strength σ_{UCS} of all tested rock types.

5 General Summary and Conclusions

Clays are considered suitable rocks for the deep-geological storage of nuclear waste due to their low permeability, high sorption capacity and their potential for self-sealing of fractures (e.g., Delage et al. 2010; Sellin and Leubin 2013). However, their sealing performance is affected by compositional heterogeneities and the presence of natural and/or artificially induced faults and fractures. Against this background, this thesis focused on the mechanical characterization of Opalinus Clay (OPA), a clay formation considered as a potential host rock for the storage of nuclear waste in Switzerland and Germany (NAGRA 2002, 2019; Hoth et al. 2007; BFE 2018; BGE 2020).

Several lithostratigraphic sub-units were identified in the formation (e.g., Hostettler et al. 2017; Lauper et al. 2018, 2021), of which the two with the greatest thickness comprise the shaly and sandy facies that were investigated in the current study. Simplified, both facies types can be distinguished by their mineral composition, with the clay mineral and quartz content varying the most (e.g., Pearson et al. 2003; Peters et al. 2011). The influence of composition of both facies was investigated in several studies, highlighting that the quartz-rich sandy facies is characterized by a higher shear strength (e.g., Siegesmund et al. 2014; Crisci 2019; Zhang and Laurich 2019), lower compressibility and swelling capacity (e.g., Minardi et al. 2016; Crisci 2019), higher matrix permeability (e.g., Philipp et al. 2017), lower adsorption of radionuclides (e.g., Hennig et al. 2020) as well as a lower cation exchange capacity (e.g., Kneuker et al. 2020) compared to the clay-rich shaly facies. Furthermore, brittle deformation may be favored in the sandy facies due to the higher quartz content, increasing the probability for the creation of fluid migration pathways if damage is introduced to the host rock during tunnel excavation or long-term evolution of the potential repository.

Considering the aforementioned characteristics of the sandy facies, illustrates that a detailed characterization of the mechanical deformation behavior of this facies and the underlying deformation mechanisms is needed to evaluate the extent to which the integrity of OPA as a natural barrier is compromised by compositional heterogeneity. In an effort to improve the general characterization of how composition, thermodynamic boundary conditions, and pre-existing structural discontinuities affect the mechanical behavior and sealing properties of Opalinus Clay (OPA), a series of triaxial deformation experiments was conducted and presented in this thesis. The obtained results may contribute to a better understanding of the mechanical processes leading to damage or failure during underground excavation and potentially improve modeling approaches, which are necessary to predict the short and long-term evolution of a deep geological nuclear waste repository. The results presented aim to address the questions formulated in Chapter 1.2.

In Chapter 3, we performed a series of 42 constant strain rate deformation experiments using a Paterson-type apparatus to understand the micromechanical and physical processes that lead to damage and failure in the sandy facies of OPA and how these are affected by changing thermodynamic boundary conditions and rock fabric. The experiments were performed at dry conditions using samples cored at 0°, 45° and 90° to the bedding orientation. For each orientation, we tested the influence of confining pressures (50 – 100 MPa), temperature (25 – 200 °C) and strain rate (1 $\times$ 10^{-3} – 5 $\times$ 10^{-6} s^{-1}) on the deformation behavior. The influence of water content was investigated at fixed confining pressure (50 MPa) and temperature (100 °C) at strain rates of 5 $\times$ 10^{-4} and 5 $\times$ 10^{-6} s^{-1}, using re-saturated samples. Optical and scanning electron microscopy was used to investigate the developed deformation structures and underlying microphysical processes. At the applied conditions, the sandy facies displays brittle to semi-brittle deformation behavior, whereas strain localizes by the development of narrow shear zones. Deformation was dominantly governed by cataclastic flow comprising microcracking and particle rotation by rigid mineral clasts as well as granular flow including frictional particle sliding by clay- and non-clay minerals. In addition, crystalline plasticity, indicated by bent and kinked phyllosilicates, was found to be active during deformation, but of subordinate importance for the deformation behavior. The analyzed microstructures indicate predominantly dilatant, brittle deformation of the sandy facies under the applied conditions, which is also reflected by the obtained mechanical data. With increasing confining pressure, dried samples showed a strong increase in shear strength and decreasing brittleness, while no clear effect of confining pressure on Young's modulus was observed. In addition, with increasing degree of water saturation peak strength and Young's modulus decreased. On the other hand, strength, Young's modulus and brittleness showed a minor sensitivity to variations in temperature and strain rate. Mechanical properties of the sandy facies were found to depend on bedding orientation. Samples deformed at 0° to bedding direction show highest, 45° oriented samples displayed lowest strength, whereas strength anisotropy is smaller compared to anisotropy of elastic properties. Young's modulus was highest for the 0° specimens, which can be attributed to the axially aligned quartz-rich layers forming a load-bearing framework. In contrast, Young's modulus decreased continuously in 45° and 90° oriented samples as strain is increasingly accumulated within the more compliant clay-rich matrix. Finally, we observed a strong influence of compositional heterogeneity on the mechanical behavior, with low porous samples or samples with a high amount of interconnected quartz-rich layers displayed higher strength and increased brittle failure behavior.

Shown by the micro-mechanical analysis as well as the low effect of temperature and strain rate variations on mechanical parameters, the obtained results indicate that the sandy facies of OPA fails predominantly by brittle deformation mechanisms despite the high confining pressure. Due to its low permeability, the sandy facies exhibits significant hydro-mechanical coupling, as demonstrated by the strong effect of water saturation on strength and stiffness. This implies that

temperature and strain rate variations could have a stronger effect on saturated specimens, as thermal pressurization and rapid strain rates create excessive pore pressure at undrained conditions (e.g., Masri et al. 2014; Giger et al. 2018), which would reduce the effective mean stress, resulting in lower strength. Although it has been demonstrated that the sandy facies is characterized by some advantageous properties that may be desirable for tunneling, such as higher strength and stiffness compared to the shaly facies, brittle mechanisms produce several dilatant microcracks in non-clay minerals due to deformation. On the other hand, the microstructure of the deformed samples in this study showed grain size reduction and reworking of fractured grains in the clay-rich matrix with increasing shear strain, indicating efficient gouge compaction and a potential resealing of the developed shear zone. However, the validity of this hypothesis needs to be demonstrated in future studies. Our findings are of particular interest for future modeling approaches in order to predict the construction-related damage and long-term evolution of a future repository.

Pre-existing natural fractures or faults will alter the mechanical properties and deformability of OPA, which has an effect on the extent of induced damage due to tunneling activity. Furthermore, stress re-distribution during excavation may lead to the reactivation of tectonic faults increasing the risk for potential seismic hazard and the creation of fluid migration pathways. Therefore, we intended in Chapter 3 to analyze the mechanical behavior of OPA containing pre-existing structural discontinuities in the laboratory. Triaxial deformation experiments were performed using the sandy and shaly facies to identify the impact of mineral composition and confining pressure on fault reactivation. To create an artificial fault, cylindrical samples of both facies were dried and cut in half at an angle of 30° to the cylinder axis, followed by subsequent roughening of the obtained fault surfaces. The samples were equipped with several strain gauges along the saw-cut plane as well as on the upper and lower sample block to measure strain partitioning during reactivation and strain distribution along the fault. Prior to axial deformation, the samples were hydrostatically pre-compacted at 50 MPa followed by unloading to the respective target confining pressure of 5, 20 and 35 MPa. Subsequently, we applied a constant strain rate of 1×10^{-5} s^{-1} and deformed the samples at room temperature to a total axial shortening of 6 –7 mm, followed by slide-hold-slide (SHS) tests. The latter were performed to investigate the frictional healing properties of both facies. The experimental results show a gradual transition from brittle, highly localized at 5 MPa confining pressure, where fault reactivation is initiated by a stress drop to semi-brittle deformation behavior at a confinement of 20 and 35 MPa that is characterized by non-linear strain hardening and decreasing strain localization. Brittle, localized deformation is limited to the confining pressure at which fault strength exceeds the yield strength of the matrix, which determines the onset of strain partitioning in fault slip and matrix deformation. Shear strength at the onset of fault slip was found to increase with increasing confining pressure resulting in decreasing slip contribution with confinement. Determined friction coefficient at fault reactivation is only slightly higher for the sandy ($\mu \approx 0.48$) compared to the shaly facies ($\mu \approx 0.4$). SHS tests revealed negative or neg-

ligible frictional strengthening for both facies. Scanning electron microscopy of developed gouge indicated a mixture of cataclasis, granular flow and intercrystalline plasticity of phyllosilicates as predominant deformation mechanism. However, the relative contribution of each process depends on applied pressure and facies type resulting in different gouge appearance. At 5 MPa confinement, central slip surfaces develop, covered by pulverized wear particles that were produced by frictional sliding, grain crushing and rotation. With increasing confinement, cataclastic flow dominates in the sandy facies, whereas granular flow was primarily acting in the shaly facies. Both processes lead to the production of viscous shear zones dominated by anastomosing slip surfaces and slickensides covering the gouge surface and wall rock. A positive relation between gouge thickness and confining pressure was found. X-ray diffraction analysis of the developed gouge in the sandy facies showed a significant reduction of quartz and increase of clay mineral content compared to the initial bulk composition, whereas the composition of gouge in the shaly facies remained unchanged.

The presented results suggest that disturbed samples of both facies deform relatively similar. Dilatant, brittle fault reactivation, including stress drops may be favored at high consolidation ratios, at shallow depths and low mean stress, increasing the risk for seismic hazard and the creation of fluid pathways. Accordingly, the damage caused by shear reactivation of pre-existing faults or induced fractures due to underground excavation potentially changes with increasing distance from the tunnel as the acting mean stress increases. In addition, shear strength of faults in the sandy facies is slightly higher compared to the shaly facies, decreasing the risk of reactivation in the sandy facies due to stress changes. An increased risk of creating fluid flow paths at low confining pressure was also confirmed by the developed microstructures, especially in the sandy facies where non-clay minerals were strongly fractured in the gouge. From the negative frictional strengthening, determined in the SHS tests, it can be inferred that faults in the shaly and sandy facies, once developed, deform by stable creep at the applied conditions and remain weak in the long term. However, for the sandy facies we observe higher frictional weakening upon reloading compared to the shaly facies' samples. This observation is consistent with previous studies on mature, natural fault zones and laboratory experiments that identified the stabilizing effect of clay minerals on the nucleation and propagation of earthquakes (e.g., Scholz 1998; Giorgetti et al. 2015; Carpenter et al. 2016; Collettini et al. 2019). In our experiments, the higher phyllosilicate content of the shaly facies gouge potentially reduces contact strengthening due to the development of an anastomosing shear network. With increasing confining pressure and/or decreasing overconsolidation ratio, the high intensity of developed shear foliation leads to a rapid saturation of asperity contacts during the relaxation phase and a strong strain localization in the interconnected shear surfaces upon reload. On the other hand, the cataclastic fabric and higher proportion of rigid clasts in the sandy facies gouge results in higher frictional weakening after re-loading due to dilatation of the compacted gouge. Therefore, low frictional strengthening of shaly facies fault gouge

could be explained by the limited cataclastic processes and the dominance of frictional sliding of phyllosilicates along foliated networks of interconnected anastomosing shear zones as observed in mature clay-rich fault gouge (e.g., Imber et al. 2008; Collettini et al. 2009a, b). Comparing the structural elements that developed in the shaly facies samples deformed at confining pressures >5 MPa with the microfabric of the "Main Fault" at the Mont Terri URL (Laurich et al. 2014, 2017, 2018) we find good comparability. For the "Main Fault", this implies strain accommodation by ductile aseismic creep that prevents seismic rupture nucleation, and thus long-term weakness promoted by the phyllosilicate-rich gouge. However, structural heterogeneities, e.g., caused by mineralogical variations as observed in the sandy facies, may cause stress concentration in strong (quartz-rich) patches, whereas surrounding weak (phyllosilicate-rich) patches accommodate strain by creep (e.g., Fagereng and Sibson 2010). This process may increase the potential of seismic slip once the shear strength of the strong patches is reached (Imber et al. 2008; Collettini et al. 2019). Nevertheless, we observe shear-induced compositional fractionation in the gouge of the sandy facies. This suggests that the accumulation of phyllosilicates in the gouge possibly leads to a weakening of faults in this facies and to an increased self-sealing potential. Further studies are needed to identify if the sandy and carbonate-rich sandy facies have the potential to act as strong, velocity weakening patches in a fault system crossing the OPA formation.

In addition, we revealed the important role of matrix yield stress on strain partitioning between localized fault slip and distributed deformation. Therefore, strain partitioning and brittle reactivation in OPA depend on the sedimentary history including burial depth and uplift as well as the present stress field and gouge composition. This study demonstrates the need for site-specific characterization of mechanical parameters, including the geologic history of the intended host rock. The observed change in strain partitioning between fault slip and matrix compaction may help in future models to estimate the risk of shear reactivation and the damaged volume induced by stress changes.

After identifying the different deformation mechanisms contributing to shear motion in artificial faults in the shaly and sandy facies at laboratory scale, we intended to test experimentally to what extend the sealing capacity of fractures in both facies is due to the difference in composition. To this end, we conducted a series of flow-through experiments in Chapter 4 using samples of the sandy and shaly facies of OPA as well as slate, graywacke, quartzite, natural fault gouge, and granite. Prepared samples were containing a roughened, artificial fracture, allowing to investigate the sustainability of fracture transmissivity as a function of normal stress, mineralogy and diagenesis. At room temperature, samples of different composition and comparable initial roughness were subjected to a constant confining and pore pressure of either 5 and 1 MPa or 14 and 10 MPa, depending on whether fracture transmissivity was measured with distilled water or Argon gas. Despite the comparable preparation, initial fracture transmissivity was highest in brittle, hard rocks (high unconfined compressive strength and Young's modulus) e.g., slate, graywacke,

quartzite, and granite. In addition, the initial transmissivity of the sandy facies sample was one order of magnitude higher than in the shaly facies. Subsequently, samples were loaded stepwise by applying a differential stress of up to 45 MPa acting perpendicular to the fracture plane. With increasing normal stress, fracture transmissivity decreased non-linearly in all samples, which was described by an exponential law. Again, it was found that the fracture transmissivity of brittle, strong rocks is less sensitive to stress changes compared to OPA and natural gouge samples, while the transmissivity of the sandy facies sample was consistently less sensitive to stress than that of the shaly facies.

A general positive relation was found between the sensitivity of transmissivity changes due to differential loading and the content of mechanically weak phyllosilicates. With a focus on OPA, microstructural observation of deformed samples using electron microscopy supports this assumption. Several transgranular microfractures in quartz, feldspar and carbonate mineral grains could be found in the sandy facies, whereas we observed a significantly lower number of fractured grains in the shaly facies. On the other hand, pore collapse and reorientation of clay particles perpendicular to the major principle stress axis was more pronounced in the shaly facies after deformation. Therefore, the lower phyllosilicate content of the sandy facies decreases the sealing capacity due to the higher asperity strength and the creation of fractures at rigid mineral grain contacts, creating potential new flow pathways. However, although having a higher phyllosilicate content, the fracture transmissivity of slate samples is less stress sensitive than the transmissivity of sandy facies OPA. We can conclude that other influences such as porosity, cementation, consolidation, type of phyllosilicate and degree of metamorphism have to be considered in order to evaluate mechanical and hydraulic properties of phyllosilicate-rich rocks. Evaluating the sustainability of fracture transmissivity due to stress changes as a function of mineral composition in the laboratory may support the validation of models that aim to predict the sealing integrity of the excavation damage zone (e.g., Alcolea et al. 2016; Marschall et al. 2017). Furthermore, experiments such as those performed in this study at defined boundary conditions can improve the characterization of the mechanisms that lead to the reduction of fracture transmissivity with increasing distance from the tunnel and to self-sealing as it was observed at Mont Terri (e.g., Bossart et al. 2002, 2004).

Finally, we combined the observations and conclusions from Chapters 3 and 4 and tested the hydraulic persistence of fractures in the shaly and sandy facies against shear motion. For this purpose, samples from both facies were prepared perpendicular to bedding according to Chapter 3.2 with a 30° inclined roughened saw-cut plane. Obtained samples were dried at 50 °C as it was done for the other OPA samples tested in this thesis. As described in Chapter 4.2, two boreholes were drilled on the upper and lower sample block, allowing the continuous flow of Argon gas along the saw-cut from the outer boreholes, while the inner boreholes were monitoring the differential pore pressure gradient (Fig. 5.1c). Experiments were performed in the in the MuSPIS apparatus described in Chapter 4.2.2. To study the change of fracture transmissivity with shear strain, we

applied the same confining pressure of 14 MPa and pore pressure of 10 MPa as in the experiments presented in Chapter 4.2.2 that were performed on disk shaped samples (Fig. 5.1a, b). We used a constant strain rate of $\approx 5 \times 10^{-6}$ s^{-1} to axially load the saw-cut samples, resulting in an increase of normal (σ_n) and shear stress (τ). After a total axial displacement of 1 mm, the samples were unloaded while changes in fracture transmissivity were measured in continuously.

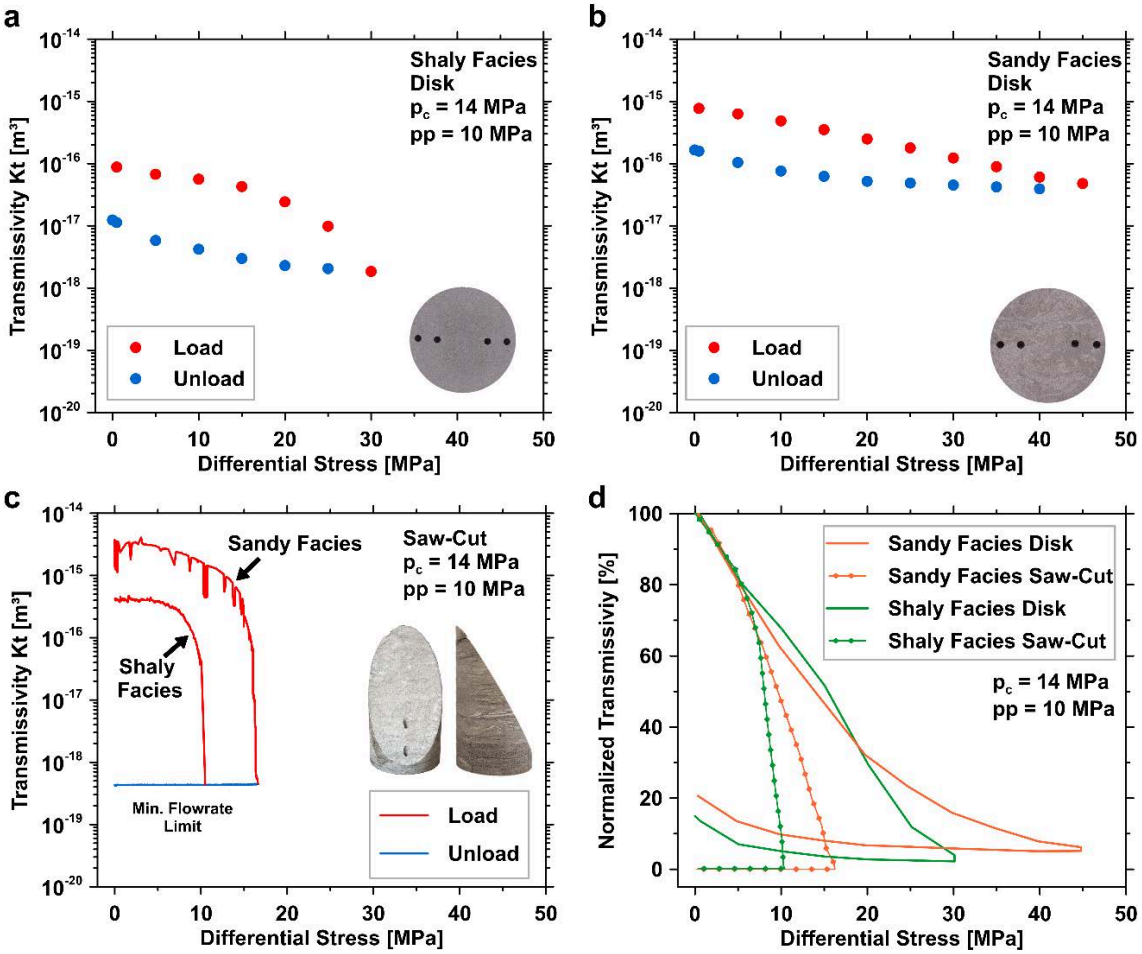

Figure 5.1: The influence of normal stress on the fracture transmissivity in the shaly (**a**) and sandy (**b**) facies of Opalinus Clay as presented in Chapter 4. The fracture transmissivity reduces dramatically as a consequence of shear displacement in both facies (**c**) and at a higher rate compared to the experiments performed on disk-shaped samples, where no shear deformation was applied (**d**).

In Fig. 5.1c we show the preliminary results of the described shear experiments. Comparable to the experiments in Chapter 4.3.3 (Fig. 4.6; Fig. 5.1a, b), the initial transmissivity of the sandy facies is about one order of magnitude larger compared to the shaly facies. With increasing differential stress, transmissivity of the saw-cut samples decreases at a similar rate compared to the disk-shaped samples (Fig. 5.1d). However, at a differential stress between 7 and 9 MPa, the

fault planes in the saw-cut samples are reactivated, resulting in a strong decrease of transmissivity. After an axial displacement of $\approx$ 200 µm, the fracture transmissivity is reduced by almost 4 orders of magnitude and remains unchanged with further shear displacement. Although we applied the minimum flow rate of the pore pressure pumps, the upper limit of the differential pressure transducer and thus the limit of the measurable transmissivity in our setup, using constant head method, was reached (c.f., Chapter 4.3). After unloading, no differential pressure below the detection limit could be measured, which indicates that the fracture surface was irreversibly sealed. Our results are in good agreement to the experimental data obtained by Fang et al. (2017), who also observed a drastic fracture permeability reduction upon shear displacement using distilled water as flow medium. Interestingly, we find similar strong reduction in our tested samples even though our samples were dried and tested in the absence of water (reduced influence of swelling clay minerals). Although the sandy facies has a higher initial fracture transmissivity compared to the shaly facies, our results show that the sandy facies is an efficient barrier despite the comparatively higher proportion of rigid minerals (e.g., quartz). As suggested in Chapter 2, wear products of rigid minerals are presumably reworked in the gouge that is becoming enriched in clay minerals as it was observed in Chapter 3. Both processes seem to counteract fracture dilation, resulting in the closure of fracture apertures. The results of this study provide first order estimates, that the sandy facies has the potential to effectively seal fractures due to stress changes and/or shear deformation. Nevertheless, our results also demonstrate that the self-sealing capacity of clay-rich facies types is higher than that of quartz-rich ones that was also shown recently by Zhang and Talandier (2022) for OPA and Callovo-Oxfordian clay. In addition, due to the higher shear strength of the sandy facies compared to the shaly, more stress is required to achieve a reduction in transmissivity of the same magnitude. To reduce the fracture transmissivity, for example by 80% of the initial value in our experiments, a differential stress of $\approx$ 9.5 MPa ($\tau \approx$ 4.1 MPa; $\sigma_n \approx$ 16.4 MPa) is required for the shaly facies, whereas $\approx$ 13.5 MPa ($\tau \approx$ 5.8 MPa; $\sigma_n \approx$ 17.4 MPa) is needed in the sandy facies for the same relative reduction of transmissivity (Fig. 5.1d). The same applies for the disk-shaped samples, where a differential stress of $\approx$ 22.8 MPa ($\sigma_n \approx$ 36.8 MPa) and $\approx$ 27 MPa ($\sigma_n \approx$ 41 MPa) is needed for the shaly and sandy facies, respectively to reduce the initial fracture transmissivity at the tested conditions by 80%. As a consequence, fractures in the sandy facies remain more permeable than in the shaly facies at a given stress. The lower mechanical sealing capacity of the sandy facies needs to be considered in future repository designs in order to guarantee the sealing integrity of a future repository in OPA. Therefore, this work highlights the need to identify compositional heterogeneities and characterize their influence on mechanical and hydraulic parameters. However, as our experiments were performed at dry conditions using Argon gas, beneficial effects on the sealing behavior such as swelling are therefore excluded, presumably enhancing the self-sealing capacity (e.g., Zhang and Talandier 2022).

6 Implications and Outlook

This experimental study aimed at improving the understanding of how compositional heterogeneity and pre-existing tectonic structures affect the mechanical and hydraulic behavior of Opalinus Clay (OPA) at different thermodynamic boundary conditions. A detailed characterization and description of the key processes and influences has been presented, however some issues remain to be addressed in future research.

Triaxial deformation experiments performed on dried samples of the sandy facies of OPA showed little dependence on temperature and strain rate at the relatively high pressure conditions applied (Chapter 2). Although the chosen boundary conditions may not be directly transferable to a future repository, the conducted experiments allowed the extension and comparison to the existing data set of the shaly facies obtained by Nüesch (1991). The results show that brittle mechanism dominate the short-term deformation behavior of both facies up to elevated pressure (<200 MPa) and temperature (<200 °C) conditions. However, since several construction plans for future repository sites envisage a maximum emplacement depth of <1000 m (e.g., NAGRA 2002; StandAG 2017), and saturated host rock conditions can be expected, further deformation experiments at the relevant confining pressures, using re-saturated samples (e.g., Amann and Vogelhuber 2015; Wild et al. 2017; Favero et al. 2018; Giger et al. 2018) are necessary to characterize the hydro-mechanical deformation behavior of sandy facies OPA and provide effective strength parameters that are necessary for tunneling activity and construction designs. Since saturation plays a crucial role on the strength of OPA, effective strength parameters need to be further characterized as a function of the saturation degree and bedding orientation. In addition, the effect of temperature on the deformation behavior of saturated samples needs to be further investigated, while future experimental setups will require accurate measurement of effective stress states as thermally induced pore pressure generation needs to be considered at undrained conditions. Conducting triaxial deformation experiments in conjunction with permeability (Zhang 2016) and ultrasonic velocity measurements (Popp and Salzer 2007; Siegesmund et al. 2014) as standard in the laboratory would further provide valuable information on the damage initiation and evolution of OPA. Experiments should be conducted with different sample orientations and at varying confining pressure to account for damage that is related to the formation of an excavation damage zone. Not subject of the presented work, but of importance for the lifetime performance of the host rock, is the characterization of the creep behavior of OPA and the identification of the underlying deformation mechanisms. Especially in combination with the variation of temperature, the role of viscoplastic processes such as dislocation glide or stress corrosion on the deformation behavior needs to be identified and would allow to predict the long-term evolution of the geological barrier.

Strength and stiffness properties of OPA were identified to depend on mineral composition, with the sandy facies being more rigid than the shaly facies. Furthermore, we found that cm-scale heterogeneities have a strong influence on the mechanical properties of the sandy facies. Samples with a high amount of sandy, quartz-rich layers and low porosity displayed higher shear strength and stiffness. In order to fully quantify the influence of composition on the mechanical properties of OPA (e.g., Kaufhold et al. 2013), it is necessary to develop models that account for mineralogic composition, as proposed in Chapter 2.4.4 using effective medium theories (e.g., Mavko et al. 2009). In addition, analytical solutions and empirical correlations may be combined as suggested by Crisci et al. (2021). Models need to be calibrated, benchmarked and justified with large, uniformly conducted experimental series. These models can potentially be extended to larger scale, as information on composition are available at the drill core-scale using calibrated computed tomography scans (e.g., Keller and Giger 2019) or at repository scale by seismic tomography (e.g., Esefelder et al. 2021) or mini-seismic methods (Schuster et al. 2017) enabling to map mechanical properties of OPA at the site scale.

At the Mont Terri Underground Research Laboratory (URL), it has been observed that fractures develop as a result of tunneling by shear failure along bedding planes or by reactivation of pre-existing tectonic faults, as well as by extensional brittle failure, forming a damage zone around the excavation (e.g., Bossart et al. 2002, 2004; Yong et al. 2010; Thöny 2014; Kupferschmied et al. 2015). Therefore, the mechanical and sealing behavior of fractured OPA was studied in dependence of shear displacement and normal stress. We found decreasing brittle localization with increasing confining pressure for the reactivation of pre-existing fractures (Chapter 3), suggesting that shear movement along fractures becomes more localized and potentially dilatant in the vicinity of the tunnel wall. Therefore, it is necessary to further investigate the sealing behavior of OPA at lower confining pressures as applied in this thesis also using re-saturated samples. In addition, OPA of the sandy (Chapter 2) and shaly facies (e.g., Wild and Amann 2018) exhibits anisotropic stiffness properties. Performing deformation and flow-through experiments with fractures oriented at angles to the bedding other than those presented here would make a valuable contribution to characterizing the mechanical behavior and sealing properties of the damaged host rock. Although experiments on artificial fractures and faults in the laboratory offer the possibility to analyze specific processes at constrained boundary conditions, they are strongly simplified and can only represent nature to a limited extent. Performing in-situ experiments to study the hydromechanical behavior as well as the rupture mechanisms and leakage potential of natural fault zones and fractures (e.g., Guglielmi et al. 2017, 2020, 2021; Amann et al. 2018; Hopp et al. 2022) are therefore necessary to understand large scale processes. In addition, field studies and microstructural analysis of natural fractures in OPA (e.g., Laurich et al. 2014, 2017, 2018; Clauer et al. 2017, 2022) provide information on dissolution/precipitation processes and paleo-fluid flow that help to understand and predict long-term flow mechanisms that cannot be captured in the lab-

oratory.

The obtained results from the performed slide-hold-slide tests (Chapter 3) suggest that fault zones in OPA remain stable in the long term. However, after relaxation phases, we observe frictional weakening in the sandy and shaly facies during reloading that is potentially related to shear-enhanced dilation. Experiments in the field and in the laboratory show that fault zones in OPA may act as preferential fluid pathways once reactivated (Guglielmi et al. 2017; Orellana et al. 2019). Fluid injection experiments on the Main Fault at the Mont Terri URL revealed that leakage can occur when injection pressures come close to the normal stress acting on the low-permeable fault (Guglielmi et al. 2017, 2020, 2021) in agreement with reactivation experiments in the laboratory (Rutter and Hackston 2017). In addition, Cuss et al. (2011, 2015) showed that gas flow in clay-rich synthetic faults follows along discrete, dilatant pathways. These studies indicate that reactivation in low-permeable faults cannot be adequately described by using a Mohr-Coulomb failure criterion in combination with a simple effective stress law (e.g., Passelègue et al. 2018; Guglielmi et al. 2020). Further laboratory injection and reactivation experiments as performed in this thesis are needed in order to better characterize the hydromechanical properties and rupture mechanisms of low-permeable artificial faults. Field-scale injection experiments in natural fault zones (with and without reactivation) using tracers in combination with observation wells to monitor strain and pore pressure development (e.g., Guglielmi et al. 2014) and selective core probing of the reactivated and/or flowed through volume could help to understand the architecture of fault zones in OPA e.g., the characteristics of the damage zone and the presence of scaly clay and its influence on fluid flow (Caine et al. 1996; Faulkner et al. 2010; Jeanne et al. 2014; Guglielmi et al. 2021). This could help identify the flow mechanisms acting, since in the case of OPA it is still unclear whether the fault gouge in the Main Fault acts as permeable conduit (e.g., Orellana et al. 2022).

With regard to the sealing capacity of sandy facies OPA tested under dry conditions, we have identified that the initial transmissivity of fractures in the sandy facies is about one order of magnitude higher compared to the shaly facies. Furthermore, higher normal and shear stress is required to achieve transmissivity reduction in the sandy facies. Compositional models, such as those proposed above, could be used to quantify and constrain the critical clay content in the sandy facies of OPA at which self-sealing is no longer assured (e.g., Bourg 2015). Another important aspect that can be studied in the apparatus used in Chapter 4 is to clarify the effect of temperature on fracture transmissivity and to analyze how the swelling potential of OPA changes in the short and long term due to temperature changes by mineral transformations e.g., illitization (Cuadros and Linares 1996; Hansen et al. 2011; Sauer et al. 2020) or thermal dilation (e.g., Delage 2013; Zhang et al. 2017; Yu et al. 2018). Finally, the degree of induration was found to influence the mechanical behavior of OPA (e.g., Jahns et al. 2013; Crisci et al. 2019). Accordingly, the influence of induration and burial diagenesis on the self-sealing potential in terms of cementation bonds and clay

mineral swelling needs to be investigated in more detail, highlighting the need for site-specific material characterization. For this purpose, triaxial deformation and flow-through experiments as conducted in this thesis could be performed using samples of OPA from different depth and locations, e.g., in Switzerland and Germany.

References

Abou-Chakra Guéry, A., Cormery, F., Shao, J. F., & Kondo, D. (2008). A micromechanical model of elastoplastic and damage behavior of a cohesive geomaterial. *International Journal of Solids and Structures*, 45(5), 1406-1429. doi:https://doi.org/10.1016/j.ijsolstr.2007.09.025

Al-Bazali, T., Zhang, J., Chenevert, M. E., & Sharma, M. M. (2008). Experimental and numerical study on the impact of strain rate on failure characteristics of shales. *Journal of Petroleum Science and Engineering*, 60(3), 194-204. doi:https://doi.org/10.1016/j.petrol.2007.09.001

Alcolea, A., Kuhlmann, U., Marschall, P., Lisjak, A., Grasselli, G., Mahabadi, O., . . . Shao, H. (2016). A pragmatic approach to abstract the excavation damaged zone around tunnels of a geological radioactive waste repository: application to the HG-A experiment in Mont Terri. *Geological Society, London, Special Publications*, 443, SP443.448. doi:10.1144/SP443.8

Amann, F., Button, E. A., Evans, K. F., Gischig, V. S., & Blumel, M. (2011). Experimental Study of the Brittle Behavior of Clay shale in Rapid Unconfined Compression. *Rock Mechanics and Rock Engineering*, 44(4), 415-430. doi:10.1007/s00603-011-0156-3

Amann, F., Gonidec, Y. L., Senis, M., Gschwind, S., Wassermann, J., Nussbaum, C., & Sarout, J. (2018). Analysis of acoustic emissions recorded during a mine-by experiment in an underground research laboratory in clay shales. *International Journal of Rock Mechanics and Mining Sciences*, 106, 51-59. doi:https://doi.org/10.1016/j.ijrmms.2018.04.021

Amann, F., Kaiser, P., & Button, E. A. (2012). Experimental Study of Brittle Behavior of Clay Shale in Rapid Triaxial Compression. *Rock Mechanics and Rock Engineering*, 45(1), 21-33. doi:10.1007/s00603-011-0195-9

Amann, F., & Vogelhuber, M. (2015). Assessment of geomechanical properties of intact opalinus clay. Unpublished expert report *ENSI* 33/461, p 69.

Amann, F., Wild, K. M., Loew, S., Yong, S., Thoeny, R., & Frank, E. (2017). Geomechanical behaviour of Opalinus Clay at multiple scales: results from Mont Terri rock laboratory (Switzerland). *Swiss Journal of Geosciences*, 110(1), 151-171. doi:10.1007/s00015-016-0245-0

ANDRA (2005). *Evaluation of the feasibility of a geological repository in an argillaceous formation: Dossier 2005 Argile Synthesis*. Report Series. Châtenay-Malabry: Agence nationale pour la gestion des dechets radioactifs (ANDRA).

Atkinson, B. K. (1984). Subcritical crack growth in geological materials. *Journal of Geophysical Research: Solid Earth*, 89(B6), 4077-4114. doi:10.1029/JB089iB06p04077

Aubry, J., Passelègue, F. X., Escartín, J., Gasc, J., Deldicque, D., & Schubnel, A. (2020). Fault Stability Across the Seismogenic Zone. *Journal of Geophysical Research: Solid Earth*, 125(8), e2020JB019670. doi:https://doi.org/10.1029/2020JB019670

Azizi, F. (1999). *Applied analyses in geotechnics*. Boca Raton, FL: CRC Press.

Bala, P., Samantaray, B. K., & Srivastava, S. K. (2000). Dehydration transformation in Ca-montmorillonite. *Bulletin of Materials Science*, 23(1), 61-67. doi:10.1007/BF02708614

Barbour, A. J. (2015). Pore pressure sensitivities to dynamic strains: Observations in active tectonic regions. *Journal of Geophysical Research: Solid Earth*, 120(8), 5863-5883. doi:https://doi.org/10.1002/2015JB012201

Barton, N., Bandis, S., & Bakhtar, K. (1985). Strength, deformation and conductivity coupling of rock joints. *International Journal of Rock Mechanics and Mining Sciences & Geomechanics Abstracts*, 22(3), 121-140. doi:https://doi.org/10.1016/0148-9062(85)93227-9

Baud, P., Vajdova, V., & Wong, T.-F. (2006). Shear-enhanced compaction and strain localization: Inelastic deformation and constitutive modeling of four porous sandstones. *Journal of Geophysical Research: Solid Earth*, 111(B12). doi:https://doi.org/10.1029/2005JB004101

Beauchamps, G., Ledésert, B., Hébert, R., Navelot, V., & Favier, A. (2019). The characterisation of an exhumed high-temperature paleo-geothermal system on Terre-de-Haut Island (the Les Saintes archipelago, Guadeloupe) in terms of clay minerals and petrophysics. *Geothermal Energy*, 7(1), 6. doi:10.1186/s40517-019-0122-y

Becker, J. K. (2012). HA Experiment: Laboratory analyses-mineralogy and petrophysical properties on core material from the BVA boreholes. *Mont Terri Technical Note*, TN 2012-38, 17.

Beeler, N. M., Tullis, T. E., & Weeks, J. D. (1994). The roles of time and displacement in the evolution effect in rock friction. *Geophysical Research Letters*, 21(18), 1987-1990. doi:https://doi.org/10.1029/94GL01599

Behnsen, J., & Faulkner, D. R. (2012). The effect of mineralogy and effective normal stress on frictional strength of sheet silicates. *Journal of Structural Geology*, 42, 49-61. doi:10.1016/j.jsg.2012.06.015

Belmokhtar, M., Delage, P., Ghabezloo, S., & Conil, N. (2018). Drained Triaxial Tests in Low-Permeability Shales: Application to the Callovo-Oxfordian Claystone. *Rock Mechanics and Rock Engineering*, 51(7), 1979-1993. doi:10.1007/s00603-018-1442-0

BFE (2018). Sachplan geologische Tiefenlager Bericht über die Ergebnisse der Vernehmlassung zu Etappe 2 «Auswertungsbericht». Eidgenössisches Departement für Umwelt, Verkehr, Energie und Kommunikation UVEK, Bundesamt für Energie (BFE) Abteilung Recht, Wasserkraft und Entsorgung: Bern, Switzerland.

BFE (2021). Sachplan geologische Tiefenlager. Available at: https://www.bfe.admin.ch/bfe/de/home/versorgung/kernenergie/radioaktive-abfaelle/sachplan-geologische-tiefenlager.html, Eidgenössisches Departement für Umwelt, Verkehr, Energie und Kommunikation UVEK, Bundesamt für Energie (BFE) Abteilung Recht, Wasserkraft und Entsorgung: Bern, Switzerland.

BGE (2020). Zwischenbericht Teilgebiete gemäß § 13 StandAG. Bundesgesellschaft für Endlagerung mbH (BGE): Peine, Germany, 28.09.2020.

Bieniawski, Z. T., & Bernede, M. J. (1979). Suggested methods for determining the uniaxial compressive strength and deformability of rock materials: Part 1. Suggested method for determining deformability of rock materials in uniaxial compression. *International Journal of Rock Mechanics and Mining Sciences & Geomechanics Abstracts*, 16(2), 138-140. doi:https://doi.org/10.1016/0148-9062(79)91451-7

Bishop, A. W., & Henkel., D. J. (1962). The measurement of soil properties in the triaxial test. (2 ed.): Edward Arnold, London.

Bjørlykke, K., & Høeg, K. (1997). Effects of burial diagenesis on stresses, compaction and fluid flow in sedimentary basins. *Marine and Petroleum Geology*, 14(3), 267-276. doi:https://doi.org/10.1016/S0264-8172(96)00051-7

Blackwell, D., Frone, Z., & Richards, M. (2013). The future of geothermal energy: The shale gas analogy significant electrical EGS resource areas in the US. *Transactions - Geothermal Resources Council*, 37, 117-122.

Blöcher, G., Kluge, C., Milsch, H., Cacace, M., Jacquey, A. B., & Schmittbuhl, J. (2019). Permeability of matrix-fracture systems under mechanical loading – constraints from laboratory experiments and 3-D numerical modelling. *Adv. Geosci.*, 49, 95-104. doi:10.5194/adgeo-49-95-2019

Bock, H., Blümling, P., & Konietzky, H. (2006). Study of the micro-mechanical behaviour of the Opalinus Clay: an example of co-operation across the ground engineering disciplines. *Bulletin of Engineering Geology and the Environment*, 65(2), 195-207. doi:10.1007/s10064-005-0019-9

Bock, H., Dehandschutter, B., Martin, C. D., Mazurek, M., De Haller, A., Skoczylas, F., & Davy, C. (2010). Self-Sealing of Fractures in Argillaceous Formations in the Context of Geological Disposal of Radioactive Waste – Review and Synthesis, OECD 2010, NEA No. 6184.

Bonnelye, A., Schubnel, A., David, C., Henry, P., Guglielmi, Y., Gout, C., . . . Dick, P. (2017a). Strength anisotropy of shales deformed under uppermost crustal conditions. *Journal of Geophysical Research: Solid Earth*, 122(1), 110-129. doi:10.1002/2016jb013040

Bonnelye, A., Schubnel, A., David, C., Henry, P., Guglielmi, Y., Gout, C., . . . Dick, P. (2017b). Elastic wave velocity evolution of shales deformed under uppermost crustal conditions. *Journal of Geophysical Research: Solid Earth*, 122(1), 130-141. doi:10.1002/2016jb013540

Boosari, S., Aybar, U., & O. Eshkalak, M. (2015). Carbon Dioxide Storage and Sequestration in Unconventional Shale Reservoirs. *Journal of Geoscience and Environment Protection*, 3(1), 7-15. .

Bos, B., & Spiers, C. J. (2000). Effect of phyllosilicates on fluid-assisted healing of gouge-bearing faults. *Earth and Planetary Science Letters*, 184(1), 199-210. doi:https://doi.org/10.1016/S0012-821X(00)00304-6

Bos, B., & Spiers, C. J. (2002). Fluid-assisted Healing Processes in Gouge-bearing Faults: Insights from Experiments on a Rock Analogue System. *Pure and Applied Geophysics*, 159(11), 2537-2566. doi:10.1007/s00024-002-8747-2

Bossart, P., Bernier, F., Birkholzer, J., Bruggeman, C., Connolly, P., Dewonck, S., . . . Wieczorek, K. (2017a). Mont Terri rock laboratory, 20 years of research: introduction, site characteristics and overview of experiments. *Swiss Journal of Geosciences*, 110(1), 3-22. doi:10.1007/s00015-016-0236-1

Bossart, P., Jaeggi, D., & Nussbaum, C. (2017b). Experiments on thermo-hydro-mechanical behaviour of Opalinus Clay at Mont Terri rock laboratory, Switzerland. *Journal of Rock Mechanics and Geotechnical Engineering*, 9(3), 502-510. doi:https://doi.org/10.1016/j.jrmge.2016.11.014

Bossart, P., Meier, P. M., Moeri, A., Trick, T., & Mayor, J.-C. (2002). Geological and hydraulic characterisation of the excavation disturbed zone in the Opalinus Clay of the Mont Terri Rock Laboratory. *Engineering Geology*, 66(1), 19-38. doi:https://doi.org/10.1016/S0013-7952(01)00140-5

Bossart, P., & Milnes, A. G. (2017). Mont Terri Rock Laboratory, 20 Years of Research. *Swiss Journal of Geosciences* (110), 1-411. doi:10.1007/978-3-319-70458-6

Bossart, P., & Thury, M. (2008). Mont Terri Rock Laboratory - Project Programme 1996 to 2007 and Results (Vol. 3): Swiss Geological Survey, Wabern, Switzerland.

Bossart, P., Trick, T., Meier, P. M., & Mayor, J.-C. (2004). Structural and hydrogeological characterisation of the excavation-disturbed zone in the Opalinus Clay (Mont Terri Project, Switzerland). *Applied Clay Science*, 26(1), 429-448. doi:https://doi.org/10.1016/j.clay.2003.12.018

Bouazza, A., Van Impe, W. F., & Haegeman, W. (1996). Some mechanical properties of reconstituted Boom clay. *Geotechnical & Geological Engineering*, 14(4), 341-352. doi:10.1007/BF00421948

Bourg, I. C. (2015). Sealing Shales versus Brittle Shales: A Sharp Threshold in the Material Properties and Energy Technology Uses of Fine-Grained Sedimentary Rocks. *Environmental Science & Technology Letters*, 2(10), 255-259. doi:10.1021/acs.estlett.5b00233

Bowden, F. P., & Tabor, D. (1964). *The Friction and Lubrication of Solids*, Clarendon Press: Oxford, UK, 1964; Volume 2, No. 2.

Brace, W. F., & Martin, R. J. (1968). A test of the law of effective stress for crystalline rocks of low porosity. *International Journal of Rock Mechanics and Mining Sciences & Geomechanics Abstracts*, 5(5), 415-426. doi:https://doi.org/10.1016/0148-9062(68)90045-4

Bracke, G., Fischer-Appelt, K., & Baltes, B. (2013). Preliminary Safety Analysis of the Gorleben Site: Overview -13298, in *Proceedings of the WM2013 Conference*, February 24 – 28, 2013, Phoenix, Arizona USA.

Brinckmann, J., & Brüning, U. E. (1986). Das Bundesbohrprogramm im West-Harz, Paläogeographische Ergebnisse (The Federal Drilling Program in the Western Harz Mountains: Paleogeographic Results and Five Additional Contributions to the Geology of the Western Harz Mountains). *Geologisches Jahrbuch Reihe D: Hanover*, Germany, 1986; Band D.

Brogi, A., Alçiçek, M. C., Liotta, D., Capezzuoli, E., Zucchi, M., & Matera, P. F. (2021). Step-over fault zones controlling geothermal fluid-flow and travertine formation (Denizli Basin, Turkey). *Geothermics*, 89, 101941. doi:https://doi.org/10.1016/j.geothermics.2020.101941

Bruno, G., Decarreau, A., Proust, D., & Lajudie, A. (1992). Clay mineral transformations in static hydrothermal conditions within a simulated engineered barrier for nuclear waste disposal. *Applied Clay Science*, 7(1), 169-178. doi:https://doi.org/10.1016/0169-1317(92)90037-N

Bullock, R. J., De Paola, N., & Holdsworth, R. E. (2015). An experimental investigation into the role of phyllosilicate content on earthquake propagation during seismic slip

in carbonate faults. *Journal of Geophysical Research: Solid Earth*, 120(5), 3187-3207. doi:https://doi.org/10.1002/2015JB011914

Busch, A., Alles, S., Gensterblum, Y., Prinz, D., Dewhurst, D. N., Raven, M. D., . . . Krooss, B. M. (2008). Carbon dioxide storage potential of shales. *International Journal of Greenhouse Gas Control*, 2(3), 297-308. doi:https://doi.org/10.1016/j.ijggc.2008.03.003

Byerlee, J. D. (1968). Brittle-ductile transition in rocks. *Journal of Geophysical Research* (1896-1977), 73(14), 4741-4750. doi:https://doi.org/10.1029/JB073i014p04741

Byerlee, J. D. (1970). The mechanics of stick-slip. *Tectonophysics*, 9(5), 475-486. doi:https://doi.org/10.1016/0040-1951(70)90059-4

Byerlee, J. D. (1978). Friction of rocks. *Pure and Applied Geophysics*, 116(4), 615-626. doi:10.1007/BF00876528

Caine, J. S., Evans, J. P., & Forster, C. B. (1996). Fault zone architecture and permeability structure. *Geology*, 24(11), 1025-1028. doi:10.1130/0091-7613(1996)024<1025:Fzaaps>2.3.Co;2

Cao, N., Lei, G., Dong, P., Li, H., Wu, Z., & Li, Y. (2019). Stress-Dependent Permeability of Fractures in Tight Reservoirs. *Energies*, 12(1), 117.

Carey, J. W., Lei, Z., Rougier, E., Mori, H., & Viswanathan, H. (2015). Fracture-permeability behavior of shale. *Journal of Unconventional Oil and Gas Resources*, 11, 27-43. doi:https://doi.org/10.1016/j.juogr.2015.04.003

Carpenter, B. M., Ikari, M. J., & Marone, C. (2016). Laboratory observations of time-dependent frictional strengthening and stress relaxation in natural and synthetic fault gouges. *Journal of Geophysical Research: Solid Earth*, 121(2), 1183-1201. doi:https://doi.org/10.1002/2015JB012136

Cheng, C., Herrmann, J., Wagner, B., Leiss, B., Stammeier, J. A., Rybacki, E., & Milsch, H. (2021). Long-Term Evolution of Fracture Permeability in Slate: An Experimental Study with Implications for Enhanced Geothermal Systems (EGS). *Geosciences*, 11(11), 443.

Cheng, C., & Milsch, H. (2020a). Evolution of Fracture Aperture in Quartz Sandstone under Hydrothermal Conditions: Mechanical and Chemical Effects. *Minerals*, 10(8), 657.

Cheng, C., & Milsch, H. (2020b). Permeability Variations in Illite-Bearing Sandstone: Effects of Temperature and NaCl Fluid Salinity. *Journal of Geophysical Research: Solid Earth*, 125(9), e2020JB020122. doi:https://doi.org/10.1029/2020JB020122

Chester, F. M., Rowe, C., Ujiie, K., Kirkpatrick, J., Regalla, C., Remitti, F., . . . Toczko, S. (2013). Structure and composition of the plate-boundary slip zone for the 2011 Tohoku-Oki earthquake. *Science*, 342(6163), 1208-1211. doi:10.1126/science.1243719

Chiarelli, A.-S., Ledesert, B., Sibai, M., Karami, M., & Hoteit, N. (2000). Influence of mineralogy and moisture content on plasticity and induced anisotropic damage of a claystone; application to nuclear waste disposals. *Bulletin de la Société Géologique de France*, 171(6), 621-627. doi:10.2113/171.6.621

Cho, Y., Apaydin, O. G. G., & Ozkan, E. (2013). Pressure-Dependent Natural-Fracture Permeability in Shale and Its Effect on Shale-Gas Well Production. *SPE Reservoir Evaluation & Engineering*, 16(02), 216-228. doi:10.2118/159801-pa

Chong, K. P., & Boresi, A. P. (1990). Strain rate dependent mechanical properties of new albany reference shale. *International Journal of Rock Mechanics and Mining Sciences & Geomechanics Abstracts*, 27(3), 199-205. doi:https://doi.org/10.1016/0148-9062(90)94328-Q

Chong, K. P., Hoyt, P. M., Smith, J. W., & Paulsen, B. Y. (1980). Effects of strain rate on oil shale fracturing. *International Journal of Rock Mechanics and Mining Sciences & Geomechanics Abstracts*, 17(1), 35-43. doi:https://doi.org/10.1016/0148-9062(80)90004-2

Clauer, N., Techer, I., & Nussbaum, C. (2022). Elemental and isotopic tracing of mineral infillings from various microstructures of a fault system into fine-grained sediments: which interacting fluids? *International Journal of Earth Sciences*, 111(4), 1107-1127. doi:10.1007/s00531-021-02143-4

Clauer, N., Techer, I., Nussbaum, C., & Laurich, B. (2017). Geochemical signature of paleofluids in microstructures from Main Fault in the Opalinus Clay of the Mont Terri rock laboratory, Switzerland. *Swiss Journal of Geosciences*, 110(1), 105-128. doi:10.1007/s00015-016-0253-0

Collettini, C., Niemeijer, A., Viti, C., & Marone, C. (2009a). Fault zone fabric and fault weakness. *Nature*, 462(7275), 907-910. doi:10.1038/nature08585

Collettini, C., Tesei, T., Scuderi, M. M., Carpenter, B. M., & Viti, C. (2019). Beyond Byerlee friction, weak faults and implications for slip behavior. *Earth and Planetary Science Letters*, 519, 245-263. doi:https://doi.org/10.1016/j.epsl.2019.05.011

Collettini, C., Viti, C., Smith, S. A. F., & Holdsworth, R. E. (2009b). Development of interconnected talc networks and weakening of continental low-angle normal faults. *Geology*, 37(6), 567-570. doi:10.1130/G25645A.1

Corkum, A. G., & Martin, C. D. (2007). The mechanical behaviour of weak mudstone (Opalinus Clay) at low stresses. *International Journal of Rock Mechanics and Mining Sciences*, 44(2), 196-209. doi:https://doi.org/10.1016/j.ijrmms.2006.06.004

Crandall, D., Moore, J., Gill, M., & Stadelman, M. (2017). CT scanning and flow measurements of shale fractures after multiple shearing events. *International Journal of Rock Mechanics and Mining Sciences*, 100, 177-187. doi:https://doi.org/10.1016/j.ijrmms.2017.10.016

Crawford, B. R., Faulkner, D. R., & Rutter, E. H. (2008). Strength, porosity, and permeability development during hydrostatic and shear loading of synthetic quartz-clay fault gouge. *Journal of Geophysical Research: Solid Earth*, 113(B3). doi:10.1029/2006jb004634

Crisci, E. (2019). Hydro-mechanical response of Opalinus Clay shale: dependency on composition and burial depth. EPFL, Retrieved from https://infoscience.epfl.ch/record/271680/files/EPFL_TH7421.pdf

Crisci, E., Ferrari, A., Giger, S. B., & Laloui, L. (2019). Hydro-mechanical behaviour of shallow Opalinus Clay shale. *Engineering Geology*, 251, 214-227. doi:10.1016/j.enggeo.2019.01.016

Crisci, E., Ferrari, A., Giger, S. B., & Laloui, L. (2021). Effect of the mineralogical composition on the elastoplastic hydromechanical response of Opalinus Clay shale. *International Journal of Rock Mechanics and Mining Sciences*, 143, 104747. doi:https://doi.org/10.1016/j.ijrmms.2021.104747

Crisci, E., Ferrari, A., & Laloui, L. (2022). Discussion on "Experimental Deformation of Opalinus Clay at Elevated Temperature and Pressure Conditions: Mechanical Properties and the Influence of Rock Fabric" of Schuster, V., Rybacki, E., Bonnelye, A., Herrmann, J., Schleicher, A.M., Dresen, G. *Rock Mechanics and Rock Engineering*, 55(1), 463-465. doi:10.1007/s00603-021-02654-1

Cuadros, J., & Linares, J. (1996). Experimental kinetic study of the smectite-to-illite transformation. *Geochimica Et Cosmochimica Acta*, 60(3), 439-453. doi:https://doi.org/10.1016/0016-7037(95)00407-6

Cuss, R. J., Harrington, J. F., Noy, D. J., Sathar, S., & Norris, S. (2015). An experimental study of the flow of gas along synthetic faults of varying orientation to the stress field: Implications for performance assessment of radioactive waste disposal. *Journal of Geophysical Research: Solid Earth*, 120(5), 3932-3945. doi:https://doi.org/10.1002/2014JB011333

Cuss, R. J., Milodowski, A., & Harrington, J. F. (2011). Fracture transmissivity as a function of normal and shear stress: First results in Opalinus Clay. *Physics and Chemistry of the Earth*, Parts A/B/C, 36(17), 1960-1971. doi:https://doi.org/10.1016/j.pce.2011.07.080

Cuss, R. J., Rutter, E. H., & Holloway, R. F. (2003). The application of critical state soil mechanics to the mechanical behaviour of porous sandstones. *International Journal of Rock Mechanics and Mining Sciences*, 40(6), 847-862. doi:https://doi.org/10.1016/S1365-1609(03)00053-4

Delage, P. (2013). On the thermal impact on the excavation damaged zone around deep radioactive waste disposal. *Journal of Rock Mechanics and Geotechnical Engineering*, 5(3), 179-190. doi:https://doi.org/10.1016/j.jrmge.2013.04.002

Delage, P., Cui, Y. J., & Tang, A.-M. (2010). Clays in radioactive waste disposal. *Journal of Rock Mechanics and Geotechnical Engineering*, 2, 111-123. doi:10.3724/SP.J.1235.2010.00111

den Hartog, S. A. M., Niemeijer, A. R., & Spiers, C. J. (2012a). New constraints on megathrust slip stability under subduction zone P–T conditions. *Earth and Planetary Science Letters*, 353-354, 240-252. doi:https://doi.org/10.1016/j.epsl.2012.08.022

den Hartog, S. A. M., Peach, C. J., de Winter, D. A. M., Spiers, C. J., & Shimamoto, T. (2012b). Frictional properties of megathrust fault gouges at low sliding velocities: New data on effects of normal stress and temperature. *Journal of Structural Geology*, 38, 156-171. doi:https://doi.org/10.1016/j.jsg.2011.12.001

Desbois, G., Höhne, N., Urai, J. L., Bésuelle, P., & Viggiani, G. (2017). Deformation in cemented mudrock (Callovo–Oxfordian Clay) by microcracking, granular flow and phyllosilicate plasticity: insights from triaxial deformation, broad ion beam polishing and scanning electron microscopy. *Solid Earth*, 8(2), 291-305. doi:10.5194/se-8-291-2017

Desbois, G., Klaver, J., Urai, J. L., Amann, F., & Schmatz, J. (2018). PS Experiment: Microstructural evolution of experimentally deformed, overconsolidated mudrock (shaly Opalinus Clay) based on BIB-SEM investigations. *Mont Terri Technical Note*, TN 2017-91, 53.

Dieterich, J. H. (1972). Time-dependent friction in rocks. *Journal of Geophysical Research* (1896-1977), 77(20), 3690-3697. doi:https://doi.org/10.1029/JB077i020p03690

Dieterich, J. H., & Kilgore, B. D. (1994). Direct observation of frictional contacts: New insights for state-dependent properties. *Pure and Applied Geophysics*, 143(1), 283-302. doi:10.1007/BF00874332

Döbelin, N., & Kleeberg, R. (2015). Profex: a graphical user interface for the Rietveld refinement program BGMN. *Journal of Applied Crystallography*, 48(5), 1573-1580. doi:doi:10.1107/S1600576715014685

Duda, M., & Renner, J. (2012). The weakening effect of water on the brittle failure strength of sandstone. *Geophysical Journal International*, 192(3), 1091-1108. doi:10.1093/gji/ggs090

Durham, W. B., & Bonner, B. P. (1994). Self-propping and fluid flow in slightly offset joints at high effective pressures. *Journal of Geophysical Research: Solid Earth*, 99(B5), 9391-9399. doi:https://doi.org/10.1029/94JB00242

EC (2019). COMMUNICATION FROM THE COMMISSION TO THE EUROPEAN PARLIAMENT, THE EUROPEAN COUNCIL, THE COUNCIL, THE EUROPEAN ECONOMIC AND SOCIAL COMMITTEE AND THE COMMITTEE OF THE REGIONS. COM/2019/640 final, Document 52019DC0640, European Commission (EC), Secretariat-General: Brussels, Belgium.

EC (2022). COMMISSION DELEGATED REGULATION (EU) of 9.3.2022 amending Delegated Regulation (EU) 2021/2139 as regards economic activities in certain energy sectors and Delegated Regulation (EU) 2021/2178 as regards specific public disclosures for those economic activities. Delegated regulation, Document C(2022)631, European Commission (EC), Directorate-General for Financial Stability, Financial Services and Capital Markets Union: Brussels, Belgium.

EP (2020). REGULATION (EU) 2020/852 OF THE EUROPEAN PARLIAMENT AND OF THE COUNCIL of 18 June 2020 on the establishment of a framework to facilitate sustainable investment, and amending Regulation (EU) 2019/2088: Strasbourg, France.

Esefelder, R., Wawerzinek, B., Lüth, S., Giese, R., & Krawczyk, C. M. (2021). Seismic anisotropy of Opalinus Clay: tomographic investigations using the infrastructure of an underground rock laboratory (URL). *Swiss Journal of Geosciences*, 114(1), 21. doi:10.1186/s00015-021-00398-2

Eurostat (2022). Shedding light on energy in the EU - 2022 interactive edition European Union. doi:10.2785/640865

Evans, B., & Kohlstedt, D. L. (1995). Rheology of Rocks. *Rock Physics & Phase Relations: A handbook of Physical Constants*, 148-165. AGU Reference Shelf, Washington.

Ewing R., C., & Macfarlane, A. (2002). Yucca Mountain. *Science*, 296(5568), 659-660. doi:10.1126/science.1071886

Ewy, R. T., & Stankovich, R. J. (2000). Pore Pressure Change Due to Shale-Fluid Interactions: Measurements Under Simulated Wellbore Conditions. In: Proceedings of the 4th North American Rock Mechanics Symposium, Seattle, WA, 31 July–3 August, 2000. Rotterdam: Balkema; 2000:147–54.

Fagereng, Å., & Sibson, R. H. (2010). Mélange rheology and seismic style. *Geology*, 38(8), 751-754. doi:10.1130/G30868.1

Fang, Y., Elsworth, D., Wang, C., Ishibashi, T., & Fitts, J. P. (2017). Frictional stability-permeability relationships for fractures in shales. *Journal of Geophysical Research: Solid Earth*, 122(3), 1760-1776. doi:10.1002/2016jb013435

Faulkner, D. R., Jackson, C. A. L., Lunn, R. J., Schlische, R. W., Shipton, Z. K., Wibberley, C. A. J., & Withjack, M. O. (2010). A review of recent developments concerning the structure, mechanics and fluid flow properties of fault zones. *Journal of Structural Geology*, 32(11), 1557-1575. doi:https://doi.org/10.1016/j.jsg.2010.06.009

Faulkner, D. R., Lewis, A. C., & Rutter, E. H. (2003). On the internal structure and mechanics of large strike-slip fault zones: field observations of the Carboneras fault in southeastern Spain. *Tectonophysics*, 367(3), 235-251. doi:https://doi.org/10.1016/S0040-1951(03)00134-3

Faulkner, D. R., Mitchell, T. M., Behnsen, J., Hirose, T., & Shimamoto, T. (2011). Stuck in the mud? Earthquake nucleation and propagation through accretionary forearcs. *Geophysical Research Letters*, 38(18). doi:https://doi.org/10.1029/2011GL048552

Favero, V., Ferrari, A., & Laloui, L. (2016). On the hydro-mechanical behaviour of remoulded and natural Opalinus Clay shale. *Engineering Geology*, 208, 128-135. doi:https://doi.org/10.1016/j.enggeo.2016.04.030

Favero, V., Ferrari, A., & Laloui, L. (2018). Anisotropic Behaviour of Opalinus Clay Through Consolidated and Drained Triaxial Testing in Saturated Conditions. *Rock Mechanics and Rock Engineering*, 51(5), 1305-1319. doi:10.1007/s00603-017-1398-5

Favier, A., Lardeaux, J. M., Corsini, M., Verati, C., Navelot, V., Géraud, Y., . . . Voitus, E. (2021). Characterization of an exhumed high-temperature hydrothermal system and its application for deep geothermal exploration: An example from Terre-de-Haut Island (Guadeloupe archipelago, Lesser Antilles volcanic arc). *Journal of Volcanology and Geothermal Research*, 418, 107256. doi:https://doi.org/10.1016/j.jvolgeores.2021.107256

Ferrari, A., Crisci, A., & Laloui, L. (2018). Geotechnical Experimental Characterization of Opalinus Clay Cores from the Borehole Lausen (Vol. Nagra Arbeitsbericht NAB 17-27): Nagra, Wettingen, Switzerland.

Ferrari, A., Favero, V., & Laloui, L. (2016). One-dimensional compression and consolidation of shales. *International Journal of Rock Mechanics and Mining Sciences*, 88, 286-300. doi:10.1016/j.ijrmms.2016.07.030

Ferrari, A., Rosone, M., Ziccarelli, M., & Giger, S. B. (2020). The shear strength of Opalinus Clay shale in the remoulded state. *Geomechanics for Energy and the Environment*, 21, 100142. doi:https://doi.org/10.1016/j.gete.2019.100142

Fischer, G. J., & Paterson, M. S. (1989). Dilatancy during rock deformation at high temperatures and pressures. *Journal of Geophysical Research: Solid Earth*, 94(B12), 17607-17617. doi:https://doi.org/10.1029/JB094iB12p17607

Fisher, Q. J., & Knipe, R. J. (2001). The permeability of faults within siliciclastic petroleum reservoirs of the North Sea and Norwegian Continental Shelf. *Marine and Petroleum Geology*, 18(10), 1063-1081. doi:https://doi.org/10.1016/S0264-8172(01)00042-3

Folk, R. L. (1980). Petrology of sedimentary rocks. Hemphill Publishing Company Austin Texas.

Font, Y., Kao, H., Lallemand, S., Liu, C.-S., & Chiao, L.-Y. (2004). Hypocentre determination offshore of eastern Taiwan using the Maximum Intersection method. *Geophysical Journal International*, 158(2), 655-675. doi:10.1111/j.1365-246X.2004.02317.x

Fortin, J., Stanchits, S., Dresen, G., & Guéguen, Y. (2006). Acoustic emission and velocities associated with the formation of compaction bands in sandstone. *Journal of Geophysical Research: Solid Earth*, 111. doi:https://doi.org/10.1029/2005JB003854

Gale, J. E. (1982). The effects of fracture type induced versus natural on the stress-fracture closure-fracture permeability relationships. In *Proceedings of the 23rd U.S. Symposium on Rock Mechanics*, University of California, Berkeley, CA, USA, 25–27 August 1982, 290–298.

Gangi, A. F. (1978). Variation of whole and fractured porous rock permeability with confining pressure. *International Journal of Rock Mechanics and Mining Sciences & Geomechanics Abstracts*, 15(5), 249-257. doi:https://doi.org/10.1016/0148-9062(78)90957-9

Geng, Z., Bonnelye, A., Chen, M., Jin, Y., Dick, P., David, C., . . . Schubnel, A. (2018). Time and Temperature Dependent Creep in Tournemire Shale. *Journal of Geophysical Research: Solid Earth*, 123(11), 9658-9675. doi:https://doi.org/10.1029/2018JB016169

Geng, Z., Bonnelye, A., David, C., Dick, P., Wang, Y., & Schubnel, A. (2021). Pressure Solution Compaction During Creep Deformation of Tournemire Shale: Implications for Temporal Sealing in Shales. *Journal of Geophysical Research: Solid Earth*, 126(3), e2020JB021370. doi:https://doi.org/10.1029/2020JB021370

Gens, A., Vaunat, J., Garitte, B., & Wileveau, Y. (2007). In situ behaviour of a stiff layered clay subject to thermal loading: observations and interpretation. *Geotechnique*, 57(2), 207-228. doi:10.1680/geot.2007.57.2.207

Gerling, P., Kockel, F., & Krull, P. (1999). The HC Potential of Pre-Westphalian sediments in the North German Basin—A Synthesis. *DGMKResearch Report 43*; 1999. Available online: https://www.osti.gov/etdeweb/biblio/695510 (accessed on 29.04.2022)

Ghabezloo, S., & Sulem, J. (2009). Stress dependent thermal pressurization of a fluid-saturated rock. *Rock Mechanics and Rock Engineering*, 42(1), 1-24. doi:10.1007/s00603-008-0165-z

Giger, S. B., Ewy, R. T., Favero, V., Stankovic, R., & Keller, L. M. (2018). Consolidated-undrained triaxial testing of Opalinus Clay: Results and method validation. *Geomechanics for Energy and the Environment*, 14, 16-28. doi:10.1016/j.gete.2018.01.003

Giorgetti, C., Carpenter, B. M., & Collettini, C. (2015). Frictional behavior of talc-calcite mixtures. *Journal of Geophysical Research: Solid Earth*, 120(9), 6614-6633. doi:https://doi.org/10.1002/2015JB011970

Goebel, T. H. W., Becker, T. W., Sammis, C. G., Dresen, G., & Schorlemmer, D. (2014). Off-fault damage and acoustic emission distributions during the evolution of structurally complex faults over series of stick-slip events. *Geophysical Journal International*, 197(3), 1705-1718. doi:10.1093/gji/ggu074

Gräsle, W., & Plischke, I. (2010). LT Experiment: Mechanical Behaviour of Opalinus Clay, Final Report from Phase 6 - 14. *Mont Terri Technical Report* 2009-07.

Gräsle, W., & Plischke, I. (2011). LT-A Experiment: Mechanical Behavior of Opalinus Clay, Data report from Phase 15. *Mont Terri Technical Note*, TN 2010-86.

Gringarten, A. C., Witherspoon, P. A., & Ohnishi, Y. (1975). Theory of heat extraction from fractured hot dry rock. *Journal of Geophysical Research* (1896-1977), 80(8), 1120-1124. doi:https://doi.org/10.1029/JB080i008p01120

Guglielmi, Y., Birkholzer, J., Rutqvist, J., Jeanne, P., & Nussbaum, C. (2017). Can Fault Leakage Occur Before or Without Reactivation? Results from an in Situ Fault Reactivation Experiment at Mont Terri. *Energy Procedia*, 114, 3167-3174. doi:https://doi.org/10.1016/j.egypro.2017.03.1445

Guglielmi, Y., Cappa, F., Lançon, H., Janowczyk, J. B., Rutqvist, J., Tsang, C. F., & Wang, J. S. Y. (2014). ISRM Suggested Method for Step-Rate Injection Method for Fracture In-Situ Properties (SIMFIP): Using a 3-Components Borehole Deformation Sensor. *Rock Mechanics and Rock Engineering*, 47(1), 303-311. doi:10.1007/s00603-013-0517-1

Guglielmi, Y., Nussbaum, C., Cappa, F., De Barros, L., Rutqvist, J., & Birkholzer, J. (2021). Field-scale fault reactivation experiments by fluid injection highlight aseismic leakage in caprock analogs: Implications for CO2 sequestration. *International Journal of Greenhouse Gas Control*, 111, 103471. doi:https://doi.org/10.1016/j.ijggc.2021.103471

Guglielmi, Y., Nussbaum, C., Jeanne, P., Rutqvist, J., Cappa, F., & Birkholzer, J. (2020). Complexity of Fault Rupture and Fluid Leakage in Shale: Insights From a Controlled Fault Activation Experiment. *Journal of Geophysical Research: Solid Earth*, 125(2), e2019JB017781. doi:https://doi.org/10.1029/2019JB017781

Guiu, F., & Pratt, P. L. (1964). Stress Relaxation and the Plastic Deformation of Solids. *physica status solidi* (b), 6(1), 111-120. doi:https://doi.org/10.1002/pssb.19640060108

Gutierrez, M., Øino, L. E., & Nygård, R. (2000). Stress-dependent permeability of a de-mineralised fracture in shale. *Marine and Petroleum Geology*, 17(8), 895-907. doi:https://doi.org/10.1016/S0264-8172(00)00027-1

Gutierrez, M., Vik, G., & Berre, T. (1996). Shale Strength As Function of Stress History And Diagenesis. Paper presented at the ISRM International Symposium - EUROCK 96, Torino, Italy (1996), 69-76.

Haines, S. H., Kaproth, B., Marone, C., Saffer, D., & van der Pluijm, B. (2013). Shear zones in clay-rich fault gouge: A laboratory study of fabric development and evolution. *Journal of Structural Geology*, 51, 206-225. doi:https://doi.org/10.1016/j.jsg.2013.01.002

Hansen, F. D., & Leigh, C. D. (2011). *Salt Disposal of Heat-Generating Nuclear Waste*. SAND2011-0161. Albuquerque, NM: Sandia National Laboratories.

Hartmann, E., Geckeis, H., Rabung, T., Lützenkirchen, J., & Fanghänel, T. (2008). Sorption of radionuclides onto natural clay rocks. *Radiochimica Acta*, 96(9-11), 699-707. doi:doi:10.1524/ract.2008.1556

Head, K. H., & Epps, R. J. (2014). *Manual of Soil Laboratory Testing, Volume 3: Effective Stress Tests*. (Third Edition ed.): Whittles Publishing.

Heap, M. J., Baud, P., & Meredith, P. G. (2009a). Influence of temperature on brittle creep in sandstones. *Geophysical Research Letters*, 36(19). doi:https://doi.org/10.1029/2009GL039373

Heap, M. J., Baud, P., Meredith, P. G., Bell, A. F., & Main, I. G. (2009b). Time-dependent brittle creep in Darley Dale sandstone. *Journal of Geophysical Research: Solid Earth*, 114. doi:https://doi.org/10.1029/2008JB006212

Hennig, T., Stockmann, M., & Kühn, M. (2020). Simulation of diffusive uranium transport and sorption processes in the Opalinus Clay. *Applied Geochemistry*, 123, 104777. doi:https://doi.org/10.1016/j.apgeochem.2020.104777

Herrmann, J., Rybacki, E., Sone, H., & Dresen, G. (2018). Deformation Experiments on Bowland and Posidonia Shale—Part I: Strength and Young's Modulus at Ambient and In Situ pc–T Conditions. *Rock Mechanics and Rock Engineering*, 51(12), 3645-3666. doi:10.1007/s00603-018-1572-4

Hickman, S. H., & Evans, B. (1995). Kinetics of pressure solution at halite-silica interfaces and intergranular clay films. *Journal of Geophysical Research*, 100, 13,113-113,132. doi:10.1029/95JB00911

Hirth, G., & Tullis, J. (1992). Dislocation creep regimes in quartz aggregates. *Journal of Structural Geology*, 14(2), 145-159. doi:https://doi.org/10.1016/0191-8141(92)90053-Y

Hoek, E. (2007). Practical Rock Engineering: RocScience. Available from the publisher at http://www. rocscience. com/hoek/PracticalRockEngineering. asp.

Hoek, E., & Brown, E. T. (2019). The Hoek–Brown failure criterion and GSI – 2018 edition. *Journal of Rock Mechanics and Geotechnical Engineering*, 11(3), 445-463. doi:https://doi.org/10.1016/j.jrmge.2018.08.001

Holt, R. M., Fjaer, E., Nes, O. M., & Alassi, H. T. (2011). A shaly look at brittleness. 45th *US Rock Mechanics/Geomechanics Symposium*, ARMA 11-366, San Francisco, CA, USA, June 26–29 (2011).

Hopp, C., Guglielmi, Y., Rinaldi, A. P., Soom, F., Wenning, Q., Cook, P., . . . Zappone, A. (2022). The Effect of Fault Architecture on Slip Behavior in Shale Revealed by Distributed Fiber Optic Strain Sensing. *Journal of Geophysical Research: Solid Earth*, 127(1), e2021JB022432. doi:https://doi.org/10.1029/2021JB022432

Hornby, B. E., Schwartz, L. M., & Hudson, J. A. (1994). Anisotropic effective-medium modeling of the elastic properties of shales. *Geophysics*, 59(10), 1570-1583. doi:10.1190/1.1443546

Hostettler, B., Reisdorf, A. G., Jaeggi, D., Deplazes, G., Bläsi, H., Morard, A., . . . Menkveld-Gfeller, U. (2017). Litho- and biostratigraphy of the Opalinus Clay and bounding formations in the Mont Terri rock laboratory (Switzerland). *Swiss Journal of Geosciences*, 110(1), 23-37. doi:10.1007/s00015-016-0250-3

Hoth, P., Wirth, H., Reinhold, K., Bräuer, V., Krull, P., & Feldrappe, H. (2007). *Endlagerung radioaktiver Abfälle in tiefen geologischen Formationen Deutschlands. Untersuchung und Bewertung von Tongesteinsformationen*. Berlin / Hannover: Bundesanstalt für Geowissenschaften und Rohstoffe (BGR).

Hou, Z., Gutierrez, M., Ma, S., Almrabat, A., & Yang, C. (2019). Mechanical Behavior of Shale at Different Strain Rates. *Rock Mechanics and Rock Engineering*, 52(10), 3531-3544. doi:10.1007/s00603-019-01807-7

Houben, M. E., Desbois, G., & Urai, J. L. (2013). Pore morphology and distribution in the Shaly facies of Opalinus Clay (Mont Terri, Switzerland): Insights from representative 2D BIB–SEM investigations on mm to nm scale. *Applied Clay Science*, 71, 82-97. doi:https://doi.org/10.1016/j.clay.2012.11.006

Houben, M. E., Desbois, G., & Urai, J. L. (2014). A comparative study of representative 2D microstructures in Shaly and Sandy facies of Opalinus Clay (Mont Terri, Switzerland) inferred form BIB-SEM and MIP methods. *Marine and Petroleum Geology*, 49, 143-161. doi:10.1016/j.marpetgeo.2013.10.009

Hu, D. W., Zhang, F., & Shao, J. F. (2014). Experimental study of poromechanical behavior of saturated claystone under triaxial compression. *Acta Geotechnica*, 9(2), 207-214. doi:10.1007/s11440-013-0259-y

Huo, D., & Benson, S. M. (2015). An Experimental Investigation of Stress-Dependent Permeability and Permeability Hysteresis Behavior in Rock Fractures. *Fluid Dynamics in Complex Fractured-Porous Systems*, 99-114.

Ibanez, W. D., & Kronenberg, A. K. (1993). Experimental Deformation of Shale - Mechanical-Properties and Microstructural Indicators of Mechanisms. *International Journal of Rock Mechanics and Mining Sciences & Geomechanics Abstracts*, 30(7), 723-734. doi:Doi 10.1016/0148-9062(93)90014-5

Ikari, M. J., Saffer, D. M., & Marone, C. (2007). Effect of hydration state on the frictional properties of montmorillonite-based fault gouge. *Journal of Geophysical Research: Solid Earth*, 112(B6). doi:10.1029/2006jb004748

Ikari, M. J., Saffer, D. M., & Marone, C. (2009). Frictional and hydrologic properties of clay-rich fault gouge. *Journal of Geophysical Research: Solid Earth*, 114(B5). doi:10.1029/2008jb006089

Ilgen, A. G., Heath, J. E., Akkutlu, I. Y., Bryndzia, L. T., Cole, D. R., Kharaka, Y. K., . . . Suarez-Rivera, R. (2017). Shales at all scales: Exploring coupled processes in mudrocks. *Earth-Science Reviews*, 166, 132-152. doi:https://doi.org/10.1016/j.earscirev.2016.12.013

Imber, J., Holdsworth, R. E., Smith, S. A. F., Jefferies, S. P., & Collettini, C. (2008). Frictional-viscous flow, seismicity and the geology of weak faults: a review and future directions. In C.

A. J. Wibberley, W. Kurz, J. Imber, R. E. Holdsworth, & C. Collettini (Eds.), *The Internal Structure of Fault Zones: Implications for Mechanical and Fluid-Flow Properties* (Vol. 299, pp. 0). doi:10.1144/SP299.10

Ingram, G. M., & Urai, J. L. (1999). Top-seal leakage through faults and fractures: the role of mudrock properties. *Geological Society, London, Special Publications*, 158, 125 - 135.

Islam, M. A., & Skalle, P. (2013). An Experimental Investigation of Shale Mechanical Properties Through Drained and Undrained Test Mechanisms. *Rock Mechanics and Rock Engineering*, 46(6), 1391-1413. doi:10.1007/s00603-013-0377-8

Jaeger, J. C. (1960). Shear Failure of Anistropic Rocks. *Geological Magazine*, 97(1), 65-72. doi:10.1017/S0016756800061100

Jaeger, J. C., Cook, N. G. W., & Zimmerman, R. W. (2007). *Fundamentals of rock mechanics* (4th ed.). Malden, Mass. ; Oxford: Blackwell.

Jaeggi, D., Bossart, P., & Nussbaum, C. (2017a). The Rock Mechanical Behavior of Opalinus Clay – 20 Years of Experience in the Mont Terri Rock Laboratory. *Advances in Laboratory Testing and Modelling of Soils and Shales*, 351-356.

Jaeggi, D., Bossart, P., & Wymann, L. (2014). Kompilation der lithologischen Variabilität und Eigenschaften des Opalinus-Ton im Felslabor Mont Terri. Swisstopo, Wabern, Switzerland.

Jaeggi, D., Laurich, B., Nussbaum, C., Schuster, K., & Connolly, P. (2017b). Tectonic structure of the "Main Fault" in the Opalinus Clay, Mont Terri rock laboratory (Switzerland). *Swiss Journal of Geosciences*, 110(1), 67-84. doi:10.1007/s00015-016-0243-2

Jahns, E. (2007). Rock mechanics Analysis (RA) Experiment: Rock strength of Opalinus Clay Subject to Time of Storage. *Mont Terri Technical Note* TN 2007-30.

Jahns, E. (2010). RA Experiment: Opalinus Clay rock characterization. *Mont Terri Technical Note* 2008-55 rev.

Jahns, E. (2013). Geomechanical laboratory tests on Opalinus Clay cores from the borehole Schlattingen SLA-1 (Vol. Nagra Arbeitsbericht NAB 13-18): Nagra, Wettingen, Switzerland.

Jeanne, P., Guglielmi, Y., Cappa, F., Rinaldi, A. P., & Rutqvist, J. (2014). The effects of lateral property variations on fault-zone reactivation by fluid pressurization: Application to CO2 pressurization effects within major and undetected fault zones. *Journal of Structural Geology*, 62, 97-108. doi:https://doi.org/10.1016/j.jsg.2014.01.017

Ji, Y., Hofmann, H., Rutter, E. H., Xiao, F., & Yang, L. (2022). Revisiting the Evaluation of Hydraulic Transmissivity of Elliptical Rock Fractures in Triaxial Shear-Flow Experiments. *Rock Mechanics and Rock Engineering*. doi:10.1007/s00603-022-02797-9

Jobmann, M., Bebiolka, A., Burlaka, V., Herold, P., Jahn, S., Lommerzheim, A., . . . Ziefle, G. (2017). Safety assessment methodology for a German high-level waste repository in clay formations. *Journal of Rock Mechanics and Geotechnical Engineering*, 9(5), 856-876. doi:https://doi.org/10.1016/j.jrmge.2017.05.007

Kamali-Asl, A., Ghazanfari, E., Perdrial, N., & Bredice, N. (2018). Experimental study of fracture response in granite specimens subjected to hydrothermal conditions relevant for enhanced geothermal systems. *Geothermics*, 72, 205-224. doi:https://doi.org/10.1016/j.geothermics.2017.11.014

Karner, S. L., Marone, C., & Evans, B. (1997). Laboratory study of fault healing and lithification in simulated fault gouge under hydrothermal conditions. *Tectonophysics*, 277(1), 41-55. doi:https://doi.org/10.1016/S0040-1951(97)00077-2

Kaufhold, A., Grasle, W., Plischke, I., Dohrmann, R., & Siegesmund, S. (2013). Influence of carbonate content and micro fabrics on the failure strength of the sandy facies of the Opalinus Clay from Mont Terri (Underground Rock Laboratory). *Engineering Geology*, 156, 111-118. doi:10.1016/j.enggeo.2013.01.014

Kaufhold, A., Halisch, M., Zacher, G., & Kaufhold, S. (2016). X-ray computed tomography investigation of structures in Opalinus Clay from large-scale to small-scale after mechanical testing. *Solid Earth*, 7(4), 1171-1183. doi:10.5194/se-7-1171-2016

Keller, L. M., & Giger, S. B. (2019). Petrophysical Properties of Opalinus Clay Drill Cores Determined from Med-XCT Images. *Geotechnical and Geological Engineering*, 37(4), 3507-3522. doi:10.1007/s10706-019-00815-2

Keller, L. M., & Holzer, L. (2018). Image-Based Upscaling of Permeability in Opalinus Clay. *Journal of Geophysical Research: Solid Earth*, 123(1), 285-295. doi:10.1002/2017jb014717

Keller, L. M., Holzer, L., Schuetz, P., & Gasser, P. (2013a). Pore space relevant for gas permeability in Opalinus clay: Statistical analysis of homogeneity, percolation, and representative volume element. *Journal of Geophysical Research: Solid Earth*, 118(6), 2799-2812. doi:10.1002/jgrb.50228

Keller, L. M., Holzer, L., Wepf, R., & Gasser, P. (2011). 3D geometry and topology of pore pathways in Opalinus clay: Implications for mass transport. *Applied Clay Science*, 52(1-2), 85-95. doi:10.1016/j.clay.2011.02.003

Keller, L. M., Schuetz, P., Erni, R., Rossell, M. D., Lucas, F., Gasser, P., & Holzer, L. (2013b). Characterization of multi-scale microstructural features in Opalinus Clay. *Microporous and Mesoporous Materials*, 170, 83-94. doi:10.1016/j.micromeso.2012.11.029

Kim, J.-S., Kwon, S.-K., Sanchez, M., & Cho, G.-C. (2011). Geological storage of high level nuclear waste. *KSCE Journal of Civil Engineering*, 15(4), 721-737. doi:10.1007/s12205-011-0012-8

Klee, J., Chabani, A., Ledésert, B. A., Potel, S., Hébert, R. L., & Trullenque, G. (2021a). Fluid-Rock Interactions in a Paleo-Geothermal Reservoir (Noble Hills Granite, California, USA). Part 2: The Influence of Fracturing on Granite Alteration Processes and Fluid Circulation at Low to Moderate Regional Strain. *Geosciences*, 11(11), 433.

Klee, J., Potel, S., Ledésert, B. A., Hébert, R. L., Chabani, A., Barrier, P., & Trullenque, G. (2021b). Fluid-Rock Interactions in a Paleo-Geothermal Reservoir (Noble Hills Granite, California, USA). Part 1: Granite Pervasive Alteration Processes away from Fracture Zones. *Geosciences*, 11(8), 325.

Klinkenberg, M., Kaufhold, S., Dohrmann, R., & Siegesmund, S. (2009). Influence of carbonate microfabrics on the failure strength of claystones. *Engineering Geology*, 107(1), 42-54. doi:https://doi.org/10.1016/j.enggeo.2009.04.001

Kneuker, T., & Furche, M. (2021). Capturing the structural and compositional variability of Opalinus Clay: constraints from multidisciplinary investigations of Mont Terri drill cores (Switzerland). *Environmental Earth Sciences*, 80(11), 421. doi:10.1007/s12665-021-09708-1

Kneuker, T., Hammer, J., & Dohrmann, R. (2020). PE Experiment: Microstructural and mineralogical-geochemical investigations on selected core samples from prospection boreholes BPE-1, BPE-2 and BPE-3. *Mont Terri Technical Note*, TN 2018-12, 86.

Kohli, A. H., & Zoback, M. D. (2013). Frictional properties of shale reservoir rocks. *Journal of Geophysical Research: Solid Earth*, 118(9), 5109-5125. doi:10.1002/jgrb.50346

Kranz, R. L., Harris, W. J., & Carter, N. L. (1982). Static fatigue of granite at 200°C. *Geophysical Research Letters*, 9(1), 1-4. doi:10.1029/GL009i001p00001

Kronenberg, A. K., Kirby, S. H., & Pinkston, J. (1990). Basal slip and mechanical anisotropy of biotite. *Journal of Geophysical Research: Solid Earth*, 95(B12), 19257-19278. doi:10.1029/JB095iB12p19257

Kubo, T., & Katayama, I. (2015). Effect of temperature on the frictional behavior of smectite and illite. *Journal of Mineralogical and Petrological Sciences*, 110(6), 293-299. doi:10.2465/jmps.150421

Kupferschmied, N., Wild, K. M., Amann, F., Nussbaum, C., Jaeggi, D., & Badertscher, N. (2015). Time-dependent fracture formation around a borehole in a clay shale. *International Journal of Rock Mechanics and Mining Sciences*, 77, 105-114. doi:https://doi.org/10.1016/j.ijrmms.2015.03.027

Kwiatek, G., Goebel, T. H. W., & Dresen, G. (2014). Seismic moment tensor and b value variations over successive seismic cycles in laboratory stick-slip experiments. *Geophysical Research Letters*, 41(16), 5838-5846. doi:https://doi.org/10.1002/2014GL060159

Kwon, O., & Kronenberg, A. K. (1994). Deformation of Wilcox shale: Undrained strengths and effects of strain rate. Paper presented at the 1st North American Rock Mechanics Symposium, NARMS 1994.

Laloui, L., Salager, S., & Rizzi, M. (2013). Retention behaviour of natural clayey materials at different temperatures. *Acta Geotechnica*, 8(5), 537-546. doi:10.1007/s11440-013-0255-2

Lauper, B., Jaeggi, D., Deplazes, G., & Foubert, A. (2018). Multi-proxy facies analysis of the Opalinus Clay and depositional implications (Mont Terri rock laboratory, Switzerland). *Swiss Journal of Geosciences*, 111(3), 383-398. doi:10.1007/s00015-018-0303-x

Lauper, B., Zimmerli, G. N., Jaeggi, D., Deplazes, G., Wohlwend, S., Rempfer, J., & Foubert, A. (2021). Quantification of Lithological Heterogeneity Within Opalinus Clay: Toward a Uniform Subfacies Classification Scheme Using a Novel Automated Core Image Recognition Tool. *Frontiers in Earth Science*, 9(313). doi:10.3389/feart.2021.645596

Laurich, B., Urai, J. L., Desbois, G., Vollmer, C., & Nussbaum, C. (2014). Microstructural evolution of an incipient fault zone in Opalinus Clay: Insights from an optical and electron microscopic study of ion-beam polished samples from the Main Fault in the Mt-Terri Underground Research Laboratory. *Journal of Structural Geology*, 67, 107-128. doi:https://doi.org/10.1016/j.jsg.2014.07.014

Laurich, B., Urai, J. L., & Nussbaum, C. (2017). Microstructures and deformation mechanisms in Opalinus Clay: insights from scaly clay from the Main Fault in the Mont Terri Rock Laboratory (CH). *Solid Earth*, 8(1), 27-44. doi:10.5194/se-8-27-2017

Laurich, B., Urai, J. L., Vollmer, C., & Nussbaum, C. (2018). Deformation mechanisms and evolution of the microstructure of gouge in the Main Fault in Opalinus Clay in the Mont Terri rock laboratory (CH). *Solid Earth*, 9(1), 1-24. doi:10.5194/se-9-1-2018

Lee, J. O., Kang, I. M., & Cho, W. J. (2010). Smectite alteration and its influence on the barrier properties of smectite clay for a repository. *Applied Clay Science*, 47(1), 99-104. doi:https://doi.org/10.1016/j.clay.2008.10.007

Leiss, B., Tanner, D., Vollbrecht, A., & Wemmer, K. (2011a). *Neue Untersuchungen zur Geologie der Leinetalgrabenstruktur*. Universitätsverlag Göttingen: Göttingen, Germany.

Leiss, B., Tanner, D., Vollbrecht, A., & Wemmer, K. (2011b). Tiefengeothermisches Potential in der Region Göttingen—Geologische Rahmenbedingungen. In *Neue Untersuchungen zur Geologie der Leinetalgrabenstruktur*, Leiss, B., Tanner, D., Vollbrecht, A., Arp, G., Eds.. Universitätsverlag Göttingen: Göttingen, Germany, 2011, 163–170. https://doi.org/10.17875/gup2011-226

Leiss, B., Wagner, B., Heinrichs, T., Romanov, D., Tanner, D. C., Vollbrecht, A., & Wemmer, K. (2021). Integrating deep, medium and shallow geothermal energy into district heating and cooling system as an energy transition approach for the Göttingen University Campus. Proceedings of the World Geothermal Congress 2021, Reykjavik, Iceland, 24–27 October 2021, 1–9.

Leung, C. T. O., & Zimmerman, R. W. (2012). Estimating the Hydraulic Conductivity of Two-Dimensional Fracture Networks Using Network Geometric Properties. *Transport in Porous Media*, 93(3), 777-797. doi:10.1007/s11242-012-9982-3

Li, F.-b., Sheng, J.-c., Zhan, M.-l., Xu, L.-m., Wu, Q., & Jia, C.-l. (2014). Evolution of limestone fracture permeability under coupled thermal, hydrological, mechanical, and chemical conditions. *Journal of Hydrodynamics*, 26(2), 234-241. doi:10.1016/S1001-6058(14)60026-3

Li, Q., Xing, H., Liu, J., & Liu, X. (2015). A review on hydraulic fracturing of unconventional reservoir. *Petroleum*, 1(1), 8-15. doi:https://doi.org/10.1016/j.petlm.2015.03.008

Lima, M. G., Vogler, D., Querci, L., Madonna, C., Hattendorf, B., Saar, M. O., & Kong, X.-Z. (2019). Thermally driven fracture aperture variation in naturally fractured granites. *Geothermal Energy*, 7(1), 23. doi:10.1186/s40517-019-0140-9

Liotta, D., Brogi, A., Ruggieri, G., & Zucchi, M. (2021). Fossil vs. Active Geothermal Systems: A Field and Laboratory Method to Disclose the Relationships between Geothermal Fluid Flow and Geological Structures at Depth. *Energies*, 14(4), 933.

Lisjak, A., Garitte, B., Grasselli, G., Müller, H. R., & Vietor, T. (2015). The excavation of a circular tunnel in a bedded argillaceous rock (Opalinus Clay): Short-term rock mass response and FDEM numerical analysis. *Tunnelling and Underground Space Technology*, 45, 227-248. doi:https://doi.org/10.1016/j.tust.2014.09.014

Littke, R., Krooss, B., Uffmann, A. K., Schulz, H.-M., & Horsfield, B. (2011). Unconventional Gas Resources in the Paleozoic of Central Europe. *Oil Gas Sci. Technol. – Rev. IFP Energies nouvelles*, 66(6), 953-977. Retrieved from https://doi.org/10.2516/ogst/2010033

Liu, E. (2005). Effects of fracture aperture and roughness on hydraulic and mechanical properties of rocks: implication of seismic characterization of fractured reservoirs. *Journal of Geophysics and Engineering*, 2(1), 38-47. doi:10.1088/1742-2132/2/1/006

Liu, H., Guo, W., Liu, D., Zhou, S., & Deng, J. (2018). Authigenic embrittlement of marine shale in the process of diagenesis. *Natural Gas Industry B*, 5(6), 575-582. doi:https://doi.org/10.1016/j.ngib.2018.11.005

Liu, Z., Shao, J., Xie, S., Conil, N., & Talandier, J. (2019). Mechanical Behavior of Claystone in Lateral Decompression Test and Thermal Effect. *Rock Mechanics and Rock Engineering*, 52(2), 321-334. doi:10.1007/s00603-018-1573-3

Loaiza, S., Fortin, J., Schubnel, A., Gueguen, Y., Vinciguerra, S., & Moreira, M. (2012). Mechanical behavior and localized failure modes in a porous basalt from the Azores. *Geophysical Research Letters*, 39(19). doi:https://doi.org/10.1029/2012GL053218

Lockner, D. (1993). Room temperature creep in saturated granite. *Journal of Geophysical Research: Solid Earth*, 98(B1), 475-487. doi:https://doi.org/10.1029/92JB01828

Logan, J. M., Freiedman, M., Higgs, N., Dengo, C., & Shimamoto, T. (1979). Experimental studies of simulated gouge and their application to studies of natural fault zones. *Proceedings of Conference VIII on Analysis of Actual Fault Zones in Bedrock*. US Geological Survey, Open File Report, 79-1239.

Logan, J. M., & Rauenzahn, K. A. (1987). Frictional dependence of gouge mixtures of quartz and montmorillonite on velocity, composition and fabric. *Tectonophysics*, 144, 87-108.

Loucks, R. G., Reed, R. M., Ruppel, S. C., & Hammes, U. (2012). Spectrum of pore types and networks in mudrocks and a descriptive classification for matrix-related mudrock pores. *Aapg Bulletin*, 96(6), 1071-1098. doi:10.1306/08171111061

Lu, S.-M. (2018). A global review of enhanced geothermal system (EGS). *Renewable and Sustainable Energy Reviews*, 81, 2902-2921. doi:https://doi.org/10.1016/j.rser.2017.06.097

Lupini, J. F., Skinner, A. E., & Vaughan, P. R. (1981). The drained residual strength of cohesive soils. *Geotechnique*, 31(2), 181-213. doi:10.1680/geot.1981.31.2.181

Madsen, F. T. (1998). Clay mineralogical investigations related to nuclear waste disposal. *Clay Minerals*, 33(1), 109-129. doi:10.1180/000985598545318

Mahanta, B., Tripathy, A., Vishal, V., Singh, T. N., & Ranjith, P. G. (2017). Effects of strain rate on fracture toughness and energy release rate of gas shales. *Engineering Geology*, 218, 39-49. doi:https://doi.org/10.1016/j.enggeo.2016.12.008

Mares, V. M., & Kronenberg, A. K. (1993). Experimental deformation of muscovite. *Journal of Structural Geology*, 15(9), 1061-1075. doi:https://doi.org/10.1016/0191-8141(93)90156-5

Marone, C. (1998). Laboratory-derived friction laws and their application to seismic faulting. *Annual Review of Earth and Planetary Sciences*, 26(1), 643-696. doi:10.1146/annurev.earth.26.1.643

Marschall, P., Giger, S., De La Vassière, R., Shao, H., Leung, H., Nussbaum, C., . . . Alcolea, A. (2017). Hydro-mechanical evolution of the EDZ as transport path for radionuclides and gas: insights from the Mont Terri rock laboratory (Switzerland). *Swiss Journal of Geosciences*, 110(1), 173-194. doi:10.1007/s00015-016-0246-z

Marschall, P., Horseman, S., & Gimmi, T. (2005). Characterisation of Gas Transport Properties of the Opalinus Clay, a Potential Host Rock Formation for Radioactive Waste Disposal. *Oil & Gas Science and Technology - Rev. IFP*, 60(1), 121-139. Retrieved from https://doi.org/10.2516/ogst:2005008

Masri, M., Sibai, M., Shao, J. F., & Mainguy, M. (2014). Experimental investigation of the effect of temperature on the mechanical behavior of Tournemire shale. *International Journal of Rock Mechanics and Mining Sciences*, 70, 185-191. doi:10.1016/j.ijrmms.2014.05.007

Mavko, G., Mukerji, T., & Dvorkin, J. (2009). *The Rock Physics Handbook: Tools for Seismic Analysis of Porous Media* (2 ed.). Cambridge: Cambridge University Press.

Mazurek, M., Alt-Epping, P., Bath, A., Gimmi, T., Niklaus Waber, H., Buschaert, S., . . . Wouters, L. (2011). Natural tracer profiles across argillaceous formations. *Applied Geochemistry*, 26(7), 1035-1064. doi:https://doi.org/10.1016/j.apgeochem.2011.03.124

Mazurek, M., Hurford, A. J., & Leu, W. (2006). Unravelling the multi-stage burial history of the Swiss Molasse Basin: integration of apatite fission track, vitrinite reflectance and biomarker isomerisation analysis. *Basin Research*, 18(1), 27-50. doi:10.1111/j.1365-2117.2006.00286.x

Mazzoldi, A., Rinaldi, A. P., Borgia, A., & Rutqvist, J. (2012). Induced seismicity within geological carbon sequestration projects: Maximum earthquake magnitude and leakage potential from undetected faults. *International Journal of Greenhouse Gas Control*, 10, 434-442. doi:https://doi.org/10.1016/j.ijggc.2012.07.012

McCartin, T., Tadesse, R., Li, J., Umeki, H., Bilbao y Leon, S., & Palos, G. (2020). *Management and Disposal of High-Level Radioactive Waste: Global Progress and Solutions*. NEA No. 7532. Nuclear Energy Agency Organisation for Economic Co-operation and Development (NEA/OECD).

McGlade, C., Speirs, J., & Sorrell, S. (2013). Unconventional gas – A review of regional and global resource estimates. *Energy*, 55, 571-584. doi:https://doi.org/10.1016/j.energy.2013.01.048

McKernan, R., Mecklenburgh, J., Rutter, E., & Taylor, K. (2017). Microstructural controls on the pressure-dependent permeability of Whitby mudstone. *Geological Society, London, Special Publications*, 454(1), 39. doi:10.1144/SP454.15

Menaceur, H., Delage, P., Tang, A. M., & Conil, N. (2016). On the Thermo-Hydro-Mechanical Behaviour of a Sheared Callovo-Oxfordian Claystone Sample with Respect to the EDZ Behaviour. *Rock Mechanics and Rock Engineering*, 49(5), 1875-1888. doi:10.1007/s00603-015-0897-5

Meyer, G. G., Brantut, N., Mitchell, T. M., & Meredith, P. G. (2019). Fault reactivation and strain partitioning across the brittle-ductile transition. *Geology*, 47(12), 1127-1130. doi:10.1130/G46516.1

Mikhail, R. S., & Guindy, N. M. (1971). Rates of low-temperature dehydration of montmorillonite and illite. *Journal of Applied Chemistry and Biotechnology*, 21(4), 113-116. doi:10.1002/jctb.5020210407

Milliken, K. (2014). A Compositional Classification For Grain Assemblages In Fine-Grained Sediments and Sedimentary Rocks. *Journal of Sedimentary Research*, 84(12), 1185-1199. doi:10.2110/jsr.2014.92

Milsch, H. H., Spangenberg, E., Kulenkampff, J., & Meyhöfer, S. (2008). A new Apparatus for Long-term Petrophysical Investigations on Geothermal Reservoir Rocks at Simulated In-situ Conditions. *Transport in Porous Media*, 74(1), 73-85. doi:10.1007/s11242-007-9186-4

Minardi, A., Crisci, E., Ferrari, A., & Laloui, L. (2016). Anisotropic volumetric behaviour of Opalinus clay shale upon suction variation. *Géotechnique Letters*, 6(2), 144-148. doi:10.1680/jgele.16.00023

Minardi, A., Giger, S. B., Ewy, R. T., Stankovic, R., Stenebråten, J., Soldal, M., . . . Laloui, L. (2020). Benchmark study of undrained triaxial testing of Opalinus Clay shale: Results and implications for robust testing. *Geomechanics for Energy and the Environment*, 100210. doi:https://doi.org/10.1016/j.gete.2020.100210

Minon, S., Salager, S., & Laloui, L. (2010). WS-H Experiment: Identification tests and rheological analysis of Opalinus Clay: Shaley facies, Sandy facies and Wet Spot material. *Mont Terri Technical Note*, TN 2010-61, 45.

Mohajerani, M., Delage, P., Sulem, J., Monfared, M., Tang, A. M., & Gatmiri, B. (2012). A laboratory investigation of thermally induced pore pressures in the Callovo-Oxfordian

claystone. *International Journal of Rock Mechanics and Mining Sciences*, 52, 112-121. doi:https://doi.org/10.1016/j.ijrmms.2012.02.012

Monfared, M., Delage, P., Sulem, J., Mohajerani, M., Tang, A. M., & De Laure, E. (2011a). A new hollow cylinder triaxial cell to study the behavior of geo-materials with low permeability. *International Journal of Rock Mechanics and Mining Sciences*, 48(4), 637-649. doi:https://doi.org/10.1016/j.ijrmms.2011.02.017

Monfared, M., Sulem, J., Delage, P., & Mohajerani, M. (2011b). A Laboratory Investigation on Thermal Properties of the Opalinus Claystone. *Rock Mechanics and Rock Engineering*, 44(6), 735. doi:10.1007/s00603-011-0171-4

Moore, D. E., & Lockner, D. A. (2004). Crystallographic controls on the frictional behavior of dry and water-saturated sheet structure minerals. *Journal of Geophysical Research: Solid Earth*, 109(B3). doi:10.1029/2003jb002582

Morley, C. K., von Hagke, C., Hansberry, R. L., Collins, A. S., Kanitpanyacharoen, W., & King, R. (2017). Review of major shale-dominated detachment and thrust characteristics in the diagenetic zone: Part I, meso- and macro-scopic scale. *Earth-Science Reviews*, 173, 168-228. doi:https://doi.org/10.1016/j.earscirev.2017.07.019

Morrow, C. A., Moore, D. E., & Lockner, D. A. (2017). Frictional strength of wet and dry montmorillonite. *Journal of Geophysical Research: Solid Earth*, 122(5), 3392-3409. doi:https://doi.org/10.1002/2016JB013658

Müller, P., & Jaeggi, D. (2012). SO (Sedimentology of the Opalinus Clay), Sedimentary structure in the sandy facies of the Opalinus Clay at Mont Terri rock laboratory. *Mont Terri Technical Note*, TN 2012-45, 34.

NAGRA (2002). Projekt Opalinuston - Synthese der geowissenschaftlichen Untersuchungsergebnisse (Vol. NTB 02-03): Nagra, Wettingen, Switzerland.

NAGRA (2019). Sachplan geologische Tiefenlager Etappe 3 Vorschläge zur Konkretisierung der Oberflächeninfrastruktur der geologischen Tiefenlager. Teil 2: Standortspezifische Vorschläge (Vol. NAB 19-08): Nagra, Wettingen, Switzerland.

Nakatani, M. (1998). A new mechanism of slip weakening and strength recovery of friction associated with the mechanical consolidation of gouge. *Journal of Geophysical Research: Solid Earth*, 103(B11), 27239-27256. doi:https://doi.org/10.1029/98JB02639

Naumann, M., Hunsche, U., & Schulze, O. (2007). Experimental investigations on anisotropy in dilatancy, failure and creep of Opalinus Clay. *Physics and Chemistry of the Earth*, Parts A/B/C, 32(8), 889-895. doi:https://doi.org/10.1016/j.pce.2005.04.006

Neuzil, C. E. (1994). How permeable are clays and shales? *Water Resources Research*, 30(2), 145-150. doi:https://doi.org/10.1029/93WR02930

Niandou, H., Shao, J. F., Henry, J. P., & Fourmaintraux, D. (1997). Laboratory investigation of the behaviour of Tournemire shale. *International Journal of Rock Mechanics and Mining Sciences*, 34(1), 3-16. doi:Doi 10.1016/S0148-9062(96)00053-8

Nicolas, A., Fortin, J., Regnet, J. B., Dimanov, A., & Guéguen, Y. (2016). Brittle and semi-brittle behaviours of a carbonate rock: influence of water and temperature. *Geophysical Journal International*, 206(1), 438-456. doi:10.1093/gji/ggw154

Nicolas, A., Fortin, J., Regnet, J. B., Verberne, B. A., Plümper, O., Dimanov, A., . . . Guéguen, Y. (2017). Brittle and semibrittle creep of Tavel limestone deformed at room temperature. *Journal of Geophysical Research: Solid Earth*, 122(6), 4436-4459. doi:https://doi.org/10.1002/2016JB013557

Niemeijer, A., Marone, C., & Elsworth, D. (2008). Healing of simulated fault gouges aided by pressure solution: Results from rock analogue experiments. Journal *of Geophysical Research: Solid Earth*, 113(B4). doi:https://doi.org/10.1029/2007JB005376

Niemeijer, A., Marone, C., & Elsworth, D. (2010). Fabric induced weakness of tectonic faults. *Geophysical Research Letters*, 37(3). doi:https://doi.org/10.1029/2009GL041689

Niemeijer, A., & Spiers, C. J. (2006). Velocity dependence of strength and healing behaviour in simulated phyllosilicate-bearing fault gouge. *Tectonophysics*, 427(1), 231-253. doi:https://doi.org/10.1016/j.tecto.2006.03.048

Nüesch, R. (1991). Das mechanische Verhalten von Opalinuston. Diss., Switzerland: ETH Zurich, 9349.

Nussbaum, C., Bossart, P., Amann, F., & Aubourg, C. (2011). Analysis of tectonic structures and excavation induced fractures in the Opalinus Clay, Mont Terri underground rock laboratory (Switzerland). *Swiss Journal of Geosciences*, 104(2), 187. doi:10.1007/s00015-011-0070-4

Nussbaum, C., Kloppenburg, A., Caër, T., & Bossart, P. (2017). Tectonic evolution around the Mont Terri rock laboratory, northwestern Swiss Jura: constraints from kinematic forward modelling. *Swiss Journal of Geosciences*, 110(1), 39-66. doi:10.1007/s00015-016-0248-x

Nygård, R., Gutierrez, M., Bratli, R. K., & Høeg, K. (2006). Brittle–ductile transition, shear failure and leakage in shales and mudrocks. *Marine and Petroleum Geology*, 23(2), 201-212. doi:https://doi.org/10.1016/j.marpetgeo.2005.10.001

Nygård, R., Gutierrez, M., Gautam, R., & Høeg, K. (2004). Compaction behavior of argillaceous sediments as function of diagenesis. *Marine and Petroleum Geology*, 21(3), 349-362. doi:https://doi.org/10.1016/j.marpetgeo.2004.01.002

OECD/NEA (2008). Moving Forward with Geological Disposal of Radioactive Waste. A Collective Statement by the NEA Radioactive Waste Management Committee: OECD, Paris.

OECD/NEA (2020). Management and Disposal of High-Level Radioactive Waste: Global Progress and Solutions: OECD, Paris.

Ojovan, M. I., Lee, W. E., & Kalmykov, S. N. (2019). *An introduction to nuclear waste* immobilisation (3rd Ed.). Elsevier.

ONDRAF/NIRAS (2001). SAFIR2 - Safety Assessment and Feasibility Interim Report 2 (NIROND 2001-06 E). ONDRAF/NIRAS (Belgian agency for radioactive waste and enriched fissile materials): Brussels, Belgium.

Orellana, L. F., Giorgetti, C., & Violay, M. (2019). Contrasting Mechanical and Hydraulic Properties of Wet and Dry Fault Zones in a Proposed Shale-Hosted Nuclear Waste Repository. *Geophysical Research Letters*, 46(3), 1357-1366. doi:10.1029/2018gl080384

Orellana, L. F., Giorgetti, C., & Violay, M. (2020). Fault creep behavior and the frictional response of the Opalinus Clay formation. Paper presented at the AGU Fall Meeting Abstracts, MR007-0012.

Orellana, L. F., Nussbaum, C., Grafulha, L., Henry, P., & Violay, M. (2022). Physical characterization of fault rocks within the Opalinus Clay formation. *Scientific Reports*, 12(1), 4389. doi:10.1038/s41598-022-08236-7

Orellana, L. F., Scuderi, M. M., Collettini, C., & Violay, M. (2018a). Do scaly clays control seismicity on faulted shale rocks? *Earth and Planetary Science Letters*, 488, 59-67. doi:https://doi.org/10.1016/j.epsl.2018.01.027

Orellana, L. F., Scuderi, M. M., Collettini, C., & Violay, M. (2018b). Frictional Properties of Opalinus Clay: Implications for Nuclear Waste Storage. *Journal of Geophysical Research: Solid Earth*, 123(1), 157-175. doi:10.1002/2017jb014931

Ortiz, L., Volckaert, G., & Mallants, D. (2002). Gas generation and migration in Boom Clay, a potential host rock formation for nuclear waste storage. *Engineering Geology*, 64, 287-296.

Parisio, F., Samat, S., & Laloui, L. (2015). Constitutive analysis of shale: a coupled damage plasticity approach. *International Journal of Solids and Structures*, 75-76, 88-98. doi:https://doi.org/10.1016/j.ijsolstr.2015.08.003

Passelègue, F. X., Brantut, N., & Mitchell, T. M. (2018). Fault Reactivation by Fluid Injection: Controls From Stress State and Injection Rate. *Geophysical Research Letters*, 45(23), 12,837-812,846. doi:https://doi.org/10.1029/2018GL080470

Paterson, M. S. (1970). A high-pressure, high-temperature apparatus for rock deformation. *International Journal of Rock Mechanics and Mining Sciences & Geomechanics Abstracts*, 7(5), 517-526. doi:10.1016/0148-9062(70)90004-5

Paterson, M. S., & Wong, T.-F. (2005). *Experimental rock deformation-the brittle field*. Springer, Heidelberg, p 348.

Pearson, F. J., Arcos, D., Bath, D., Boisson, J. Y., Fernández, A. M., Gäbler, H.-E., . . . Waber, H. N. (2003). *Mont Terri project: geochemistry of water in the opalinus clay formation at the Mont Terri rock laboratory*. Reports of the Federal Office for Water and Geology (FOWG), Geology Series No. 5.

Peters, M., Mazurek, M., Jaeggi, D., & Müller, H. (2011). WS-H Experiment: Heterogeneities in the sandy facies of Opalinus Clay on a scale on millimetres to centimeters. *Mont Terri Technical Note*, TN 2010-76, 66.

Petley, D. N. (1999) Failure envelopes of mudrocks at high confining pressures. *Geological Society Special Publication*, 158, 61-71.

Philipp, T., Amann-Hildenbrand, A., Laurich, B., Desbois, G., Littke, R., & Urai, J. (2017). The effect of microstructural heterogeneity on pore size distribution and permeability in Opalinus Clay (Mont Terri, Switzerland): insights from an integrated study of laboratory fluid flow and pore morphology from BIB-SEM images. *Geological Society, London, Special Publications*, 454(1), 85-106.

Popp, T., & Salzer, K. (2007). Anisotropy of seismic and mechanical properties of Opalinus clay during triaxial deformation in a multi-anvil apparatus. *Physics and Chemistry of the Earth*, 32(8-14), 879-888. doi:10.1016/j.pce.2006.04.022

Posiva/Oy (2012). Safety Case for the Disposal of Spent Nuclear Fuel at Olkiluoto – Complementary Considerations Posiva Report 2012-11. Eurajoki: Posiva Oy.

Rassouli, F. S., & Zoback, M. D. (2018). Comparison of Short-Term and Long-Term Creep Experiments in Shales and Carbonates from Unconventional Gas Reservoirs. *Rock Mechanics and Rock Engineering*, 51(7), 1995-2014. doi:10.1007/s00603-018-1444-y

Reches, Z. e., & Lockner, D. A. (2010). Fault weakening and earthquake instability by powder lubrication. *Nature*, 467(7314), 452-455. doi:10.1038/nature09348

Reinicke, A., Rybacki, E., Stanchits, S., Huenges, E., & Dresen, G. (2010). Hydraulic fracturing stimulation techniques and formation damage mechanisms—Implications from laboratory testing of tight sandstone–proppant systems. *Geochemistry*, 70, 107-117. doi:https://doi.org/10.1016/j.chemer.2010.05.016

Reisdorf, A. G., Hostettler, B., Waltschew, A., Jaeggi, D., & Menkveld-Gfeller, U. (2014). SO (Sedimentology of the Opalinus Clay), Biostratigraphy of the Basal Part of the Opalinus-Ton at the Mont Terri rock laboratory, Switzerland. *Mont Terri Technical Report*, TR 2014-07, 29.

Renard, F., Beauprêtre, S., Voisin, C., Zigone, D., Candela, T., Dysthe, D. K., & Gratier, J.-P. (2012). Strength evolution of a reactive frictional interface is controlled by the dynamics of contacts and chemical effects. *Earth and Planetary Science Letters*, 341-344, 20-34. doi:https://doi.org/10.1016/j.epsl.2012.04.048

Renner, J., Evans, B., & Hirth, G. (2000a). On the rheologically critical melt fraction. *Earth and Planetary Science Letters*, 181(4), 585-594. doi:https://doi.org/10.1016/S0012-821X(00)00222-3

Renner, J., Evans, B., & Siddiqi, G. (2002). Dislocation creep of calcite. Journal of Geophysical Research: Solid Earth, 107(B12), ECV 6-1-ECV 6-16. doi:https://doi.org/10.1029/2001JB001680

Renner, J., Hettkamp, T., & Rummel, F. (2000b). Rock Mechanical Characterization of an Argillaceous Host Rock of a Potential Radioactive Waste Repository. *Rock Mechanics and Rock Engineering*, 33(3), 153-178. doi:10.1007/s006030070005

Rinaldi, A. P., & Urpi, L. (2020). Fault reactivation induced by tunneling activity in clay material: Hints from numerical modeling. *Tunnelling and Underground Space Technology*, 102, 103453. doi:https://doi.org/10.1016/j.tust.2020.103453

Roche, V., Bouchot, V., Beccaletto, L., Jolivet, L., Guillou-Frottier, L., Tuduri, J., . . . Tokay, B. (2019). Structural, lithological, and geodynamic controls on geothermal activity in the Menderes geothermal Province (Western Anatolia, Turkey). International *Journal of Earth Sciences*, 108(1), 301-328. doi:10.1007/s00531-018-1655-1

Roscoe, K. H., & Burland, J. (1968). On the Generalized Stress-Strain Behavior of Wet Clays. *Engineering plasticity* (ed. J. Heyman & F. A. Leckie), Cambridge University Press, London, England, 535-609.

Ross, Z. E., Meier, M.-A., & Hauksson, E. (2018). P Wave Arrival Picking and First-Motion Polarity Determination With Deep Learning. *Journal of Geophysical Research: Solid Earth*, 123(6), 5120-5129. doi:https://doi.org/10.1029/2017JB015251

Ruggieri, R., Scuderi, M. M., Trippetta, F., Tinti, E., Brignoli, M., Mantica, S., . . . Collettini, C. (2021). The role of shale content and pore-water saturation on frictional properties of simulated carbonate faults. *Tectonophysics*, 807, 228811. doi:https://doi.org/10.1016/j.tecto.2021.228811

Ruina, A. (1983). Slip instability and state variable friction laws. *Journal of Geophysical Research: Solid Earth*, 88(B12), 10359-10370. doi:https://doi.org/10.1029/JB088iB12p10359

Rummel, F., Hettkamp, T., & Weber, U. (1999). DM Experiment: Laboratory experiments for the determination of deformation mechanisms and a constitutive law for time dependent deformation behaviour of the Opalinus Clay. *Mont Terri Technical Note* TN 1999-35.

Rummel, F., & Weber, U. (1999). Sondierbohrung Benken: Felsmechanische Laboruntersuchung an Bohrkernen. Unpublished. Nagra interner Bericht. Nagra, Wettingen.

Rutqvist, J. (2015). Fractured rock stress-permeability relationships from in situ data and effects of temperature and chemical-mechanical couplings. *Geofluids*, 15(1-2), 48-66. doi:https://doi.org/10.1111/gfl.12089

Rutqvist, J., Rinaldi, A. P., Cappa, F., Jeanne, P., Mazzoldi, A., Urpi, L., . . . Vilarrasa, V. (2016). Fault activation and induced seismicity in geological carbon storage – Lessons learned from recent modeling studies. *Journal of Rock Mechanics and Geotechnical Engineering*, 8(6), 789-804. doi:https://doi.org/10.1016/j.jrmge.2016.09.001

Rutter, E., & Hackston, A. (2017). On the effective stress law for rock-on-rock frictional sliding, and fault slip triggered by means of fluid injection. *Philosophical Transactions of the Royal Society A: Mathematical, Physical and Engineering Sciences*, 375(2103), 20160001. doi:10.1098/rsta.2016.0001

Rutter, E., & Wanten, P. (2000). Experimental Study of the Compaction of Phyllosilicate-Bearing Sand at Elevated Temperature and with Controlled Pore Water Pressure. *Journal of Sedimentary Research*, 70. doi:10.1306/2DC40902-0E47-11D7-8643000102C1865D

Rutter, E. H., Atkinson, B. K., & Mainprice, D. H. (1978). On the use of the stress relaxation testing method in studies of the mechanical behaviour of geological materials. *Geophysical Journal International*, 55(1), 155-170. doi:10.1111/j.1365-246X.1978.tb04754.x

Rutter, E. H., & Glover, C. T. (2012). The deformation of porous sandstones; are Byerlee friction and the critical state line equivalent? *Journal of Structural Geology*, 44, 129-140. doi:https://doi.org/10.1016/j.jsg.2012.08.014

Rutter, E. H., & Hadizadeh, J. (1991). On the influence of porosity on the low-temperature brittle—ductile transition in siliciclastic rocks. *Journal of Structural Geology*, 13(5), 609-614. doi:https://doi.org/10.1016/0191-8141(91)90047-M

Rutter, E. H., Maddock, R. H., Hall, S. H., & White, S. H. (1986). Comparative microstructures of natural and experimentally produced clay-bearing fault gouges. *Pure and Applied Geophysics*, 124(1), 3-30. doi:10.1007/BF00875717

Rutter, E. H., & Mainprice, D. H. (1978). The effect of water on stress relaxation of faulted and unfaulted sandstone. *Pure and Applied Geophysics*, 116(4), 634-654. doi:10.1007/BF00876530

Rutter, E. H., & Mecklenburgh, J. (2017). Hydraulic conductivity of bedding-parallel cracks in shale as a function of shear and normal stress. *Geological Society, London, Special Publications*, 454(1), 67. doi:10.1144/SP454.9

Rutter, E. H., & Mecklenburgh, J. (2018). Influence of Normal and Shear Stress on the Hydraulic Transmissivity of Thin Cracks in a Tight Quartz Sandstone, a Granite, and a Shale. *Journal of Geophysical Research: Solid Earth*, 123(2), 1262-1285. doi:https://doi.org/10.1002/2017JB014858

Rybacki, E., Meier, T., & Dresen, G. (2016). What controls the mechanical properties of shale rocks? - Part II: Brittleness. *Journal of Petroleum Science and Engineering*, 144, 39-58. doi:10.1016/j.petrol.2016.02.022

Rybacki, E., Reinicke, A., Meier, T., Makasi, M., & Dresen, G. (2015). What controls the mechanical properties of shale rocks? – Part I: Strength and Young's modulus. *Journal of Petroleum Science and Engineering*, 135, 702-722. doi:https://doi.org/10.1016/j.petrol.2015.10.028

Sáez, R., Moreno, C., González, F., & Almodóvar, G. R. (2011). Black shales and massive sulfide deposits: causal or casual relationships? Insights from Rammelsberg, Tharsis, and Draa Sfar. *Mineralium Deposita*, 46(5), 585-614. doi:10.1007/s00126-010-0311-x

Saffer, D. M., & Marone, C. (2003). Comparison of smectite- and illite-rich gouge frictional properties: application to the updip limit of the seismogenic zone along subduction megathrusts. *Earth and Planetary Science Letters*, 215(1-2), 219-235. doi:10.1016/s0012-821x(03)00424-2

Salager, S., François, B., Nuth, M., & Laloui, L. (2013). Constitutive analysis of the mechanical anisotropy of Opalinus Clay. *Acta Geotechnica*, 8(2), 137-154. doi:10.1007/s11440-012-0187-2

Sammis, C. G., Lockner, D. A., & Reches, Z. e. (2011). The role of adsorbed water on the friction of a layer of submicron particles. *Pure and Applied Geophysics*, 168(12), 2325-2334. doi:10.1007/s00024-011-0324-0

Sauer, K., Caporuscio, F., Rock, M., Cheshire, M., & Jové-Colón, C. (2020). Hydrothermal Interaction of Wyoming Bentonite and Opalinus Clay. *Clays and Clay Minerals*, 68(2), 144-160. doi:10.1007/s42860-020-00068-8

Schill, E., Genter, A., Cuenot, N., & Kohl, T. (2017). Hydraulic performance history at the Soultz EGS reservoirs from stimulation and long-term circulation tests. *Geothermics*, 70, 110-124. doi:https://doi.org/10.1016/j.geothermics.2017.06.003

Schleicher, A. M., Boles, A., & van der Pluijm, B. A. (2015). Response of natural smectite to seismogenic heating and potential implications for the 2011 Tohoku earthquake in the Japan Trench. *Geology*, 43(9), 755-758. doi:10.1130/G36846.1

Schleicher, A. M., van der Pluijm, B. A., & Warr, L. N. (2010). Nanocoatings of clay and creep of the San Andreas fault at Parkfield, California. *Geology*, 38(7), 667-670. doi:10.1130/G31091.1

Schmid, S. M. (1976). Rheological evidence for changes in the deformation mechanism of Solenhofen limestone towards low stresses. *Tectonophysics*, 31(1), T21-T28. doi:https://doi.org/10.1016/0040-1951(76)90160-8

Schnetzer, F., Thissen, P., Giraudo, N., & Emmerich, K. (2016). Unraveling the Coupled Processes of (De)hydration and Structural Changes in Na+-Saturated Montmorillonite. *The Journal of Physical Chemistry* C, 120(28), 15282-15287. doi:10.1021/acs.jpcc.6b04986

Schnier, H., & Stührenberg, D. (2006). LT Experiment: Strength tests on cylindrical specimens, documentation and evaluation (phases 8 & 9). *Mont Terri Technical Note*, TN 2004-87, 124.

Schofield, A., & Wroth, C. (1968). *Critical State Soil Mechanics*. McGraw-Hill, London.

Scholz, C. H. (1998). Earthquakes and friction laws. *Nature*, 391(6662), 37-42. doi:10.1038/34097

Schubert, M. (1996). *Die dysaerobe Biofazies der Wissenbach Schiefer (Rheinisches Schiefergebirge, Harz, Devon)*. Institute der Georg-August-Universit: Göttingen, Germany.

Schuck, B., Desbois, G., & Urai, J. L. (2020). Grain-scale deformation mechanisms and evolution of porosity in experimentally deformed Boom Clay. *Journal of Structural Geology*, 130, 103894. doi:https://doi.org/10.1016/j.jsg.2019.103894

Schuster, K., Amann, F., Yong, S., Bossart, P., & Connolly, P. (2017). High-resolution miniseismic methods applied in the Mont Terri rock laboratory (Switzerland). *Swiss Journal of Geosciences*, 110(1), 213-231. doi:10.1007/s00015-016-0241-4

Schuster, V., Rybacki, E., Bonnelye, A., Herrmann, J., Schleicher, A. M., & Dresen, G. (2021). Experimental Deformation of Opalinus Clay at Elevated Temperature and Pressure Conditions: Mechanical Properties and the Influence of Rock Fabric. Rock *Mechanics and Rock Engineering*, 54(8), 4009-4039. doi:10.1007/s00603-021-02474-3

Schutjens, P. M. T. M. (1991). Experimental compaction of quartz sand at low effective stress and temperature conditions. *Journal of the Geological Society*, 148(3), 527-539. doi:10.1144/gsjgs.148.3.0527

Scott, T. E., & Nielsen, K. C. (1991a). The effects of porosity on fault reactivation in sandstones. *Journal of Geophysical Research*, 96, 2353-2362.

Scott, T. E., & Nielsen, K. C. (1991b). The effects of porosity on the brittle-ductile transition in sandstones. *Journal of Geophysical Research: Solid Earth*, 96(B1), 405-414. doi:https://doi.org/10.1029/90JB02069

Seiphoori, A., Whittle, A. J., Krakowiak, K. J., & Einstein, H. H. (2017). Insights into Diagenesis and Pore Structure of Opalinus Shale through Comparative Studies of Natural and Reconstituted Materials. *Clays and Clay Minerals*, 65(2), 135-153. doi:10.1346/Ccmn.2017.064055

Sellin, P., & Leupin, O. X. (2013). The Use of Clay as an Engineered Barrier in Radioactive-Waste Management a Review. *Clays and Clay Minerals*, 61(6), 477-498. doi:10.1346/CCMN.2013.0610601

Shackelford, C. D., & Moore, S. M. (2013). Fickian diffusion of radionuclides for engineered containment barriers: Diffusion coefficients, porosities, and complicating issues. *Engineering Geology*, 152(1), 133-147. doi:https://doi.org/10.1016/j.enggeo.2012.10.014

Sharma, P., Prakash, R., & Abedi, S. (2019). Effect of temperature on nano- and microscale creep properties of organic-rich shales. *Journal of Petroleum Science and Engineering*, 175, 375-388. doi:https://doi.org/10.1016/j.petrol.2018.12.039

Sibson, R. H. (1985). A note on fault reactivation. *Journal of Structural Geology*, 7(6), 751-754. doi:https://doi.org/10.1016/0191-8141(85)90150-6

Siegesmund, S., Popp, T., Kaufhold, A., Dohrmann, R., Grasle, W., Hinkes, R., & Schulte-Kortnack, D. (2014). Seismic and mechanical properties of Opalinus Clay: comparison between sandy and shaly facies from Mont Terri (Switzerland). *Environmental Earth Sciences*, 71(8), 3737-3749. doi:10.1007/s12665-013-2768-2

SKB/AB (2011). Site selection - siting of the final repository for spent nuclear fuel. Retrieved from Svensk Kärnbränslehantering (SKB AB): Solna, Sweden: https://www.osti.gov/etdeweb/servlets/purl/1027624

Soe, A. K. K., Osada, M., Takahashi, M., & Sasaki, T. (2009). Characterization of drying-induced deformation behaviour of Opalinus Clay and tuff in no-stress regime. *Environmental Geology*, 58(6), 1215-1225. doi:10.1007/s00254-008-1616-2

Sone, H., & Zoback, M. D. (2013). Mechanical properties of shale-gas reservoir rocks — Part 2: Ductile creep, brittle strength, and their relation to the elastic modulus. *Geophysics*, 78(5), D393-D402. doi:10.1190/geo2013-0051.1

Stanchits, S., Mayr, S., Shapiro, S., & Dresen, G. (2011). Fracturing of porous rock induced by fluid injection. *Tectonophysics*, 503(1), 129-145. doi:https://doi.org/10.1016/j.tecto.2010.09.022

StandAG (2017). Gesetz zur Suche und Auswahl eines Standortes für ein Endlager für hochradioaktive Abfälle (Standortauswahlgesetz - StandAG) vom 5. Mai 2017 (BGBl. I S. 1074), das zuletzt durch Artikel 247 der Verordnung vom 19.Juni 2020 (BGBl. I S. 1328) geändert worden ist.

Stober, I., & Bucher, K. (2015). Hydraulic conductivity of fractured upper crust: insights from hydraulic tests in boreholes and fluid-rock interaction in crystalline basement rocks. *Geofluids*, 15(1-2), 161-178. doi:https://doi.org/10.1111/gfl.12104

Swan, G., Cook, J., Bruce, S., & Meehan, R. (1989). Strain rate effects in Kimmeridge bay shale. *International Journal of Rock Mechanics and Mining Sciences & Geomechanics Abstracts*, 26(2), 135-149. doi:https://doi.org/10.1016/0148-9062(89)90002-8

Swift, P. N., & Bonano, E. J. (2016). Geological disposal of nuclear waste in tuff: Yucca Mountain (USA). *Elements*, 12(4), 263-268.

swisstopo (2022a). Geologische Strukturen. Available at: https://www.mont-terri.ch/de/geologie/geologische-strukturen.html, Mont Terri Project swisstopo

swisstopo (2022b). Stratigraphie und Fazies. Available at: https://www.mont-terri.ch/de/geologie/stratigraphie-und-fazies.html, Mont Terri Project swisstopo

Tembe, S., Lockner, D. A., & Wong, T.-F. (2010). Effect of clay content and mineralogy on frictional sliding behavior of simulated gouges: Binary and ternary mixtures of quartz, illite, and montmorillonite. *Journal of Geophysical Research: Solid Earth*, 115(B3). doi:10.1029/2009jb006383

Tesei, T., Collettini, C., Carpenter, B. M., Viti, C., & Marone, C. (2012). Frictional strength and healing behavior of phyllosilicate-rich faults. *Journal of Geophysical Research: Solid Earth*, 117(B9). doi:https://doi.org/10.1029/2012JB009204

Thöny, R. (2014). Geomechanical analysis of excavation-induced rock mass behavior of faulted opalinus clay at the Mont Terri underground rock laboratory (Switzerland). ETH-Zürich, Retrieved from http://hdl.handle.net/20.500.11850/154612

Thury, M. F., & Bossart, P. J. (1999). *Mont Terri Rock Laboratory: Results of the hydrogeological, geochemical and geotechnical experiments performed in 1996 and 1997*. Swiss National Hydrological and Geological Survey, Bern, Switzerland.

Tsang, C. F., Barnichon, J. D., Birkholzer, J., Li, X. L., Liu, H. H., & Sillen, X. (2012). Coupled thermo-hydro-mechanical processes in the near field of a high-level radioactive waste repository in clay formations. *International Journal of Rock Mechanics and Mining Sciences*, 49, 31-44. doi:https://doi.org/10.1016/j.ijrmms.2011.09.015

Tsang, C.-F., Bernier, F., & Davies, C. (2005). Geohydromechanical processes in the Excavation Damaged Zone in crystalline rock, rock salt, and indurated and plastic clays—in the context of radioactive waste disposal. *International Journal of Rock Mechanics and Mining Sciences*, 42(1), 109-125. doi:https://doi.org/10.1016/j.ijrmms.2004.08.003

Tsang, Y. W., & Witherspoon, P. A. (1983). The dependence of fracture mechanical and fluid flow properties on fracture roughness and sample size. *Journal of Geophysical Research: Solid Earth*, 88(B3), 2359-2366. doi:https://doi.org/10.1029/JB088iB03p02359

Ulusay, R. (2015). *The ISRM Suggested Methods for Rock Characterization, Testing and Monitoring 2007–2014*. Springer: Cham, Switzerland. https://doi.org/10.1007/978-3-319-07713-0

Urpi, L., Rinaldi, A. P., Rutqvist, J., & Wiemer, S. (2019). Fault Stability Perturbation by Thermal Pressurization and Stress Transfer Around a Deep Geological Repository in a Clay Formation. *Journal of Geophysical Research: Solid Earth*, 124(8), 8506-8518. doi:https://doi.org/10.1029/2019JB017694

Valès, F., Nguyen Minh, D., Gharbi, H., & Rejeb, A. (2004). Experimental study of the influence of the degree of saturation on physical and mechanical properties in Tournemire shale (France). *Applied Clay Science*, 26(1), 197-207.

Van Geet, M., Bastiaens, W., & Ortiz, L. (2008). Self-sealing capacity of argillaceous rocks: Review of laboratory results obtained from the SELFRAC project. *Physics and Chemistry of the Earth*, Parts A/B/C, 33, S396-S406. doi:https://doi.org/10.1016/j.pce.2008.10.063

Van Loon, L. R., Soler, J. M., Muller, W., & Bradbury, M. H. (2004). Anisotropic diffusion in layered argillaceous rocks: A case study with opalinus clay. *Environmental Science & Technology*, 38(21), 5721-5728. doi:10.1021/es049937g

Vanbrabant, Y., Stenmans, V., Burlet, C., Petitclerc, E., Meyvis, B., Stasi, G., . . . Goovaerts, T. (2020). Havelange deep borehole (Belgium): A study case for the evaluation of metasedimentary formations as potential geothermal reservoir—H2020 MEET project. In Proceedings of EGU General Assembly Conference 2020, online, 4–8 May 2020; p. 10943.

Vannucchi, P., Maltman, A., Bettelli, G., & Clennell, B. (2003). On the nature of scaly fabric and scaly clay. *Journal of Structural Geology*, 25(5), 673-688. doi:https://doi.org/10.1016/S0191-8141(02)00066-4

Vidal, J., & Genter, A. (2018). Overview of naturally permeable fractured reservoirs in the central and southern Upper Rhine Graben: Insights from geothermal wells. *Geothermics*, 74, 57-73. doi:https://doi.org/10.1016/j.geothermics.2018.02.003

Vöbel, T., Gräsle, W., & Plischke, I. (2014). LT-A Experiment: Strength and Deformation of Opalinus Clay: Data report from phase 19. *Mont Terri Technical Note*, TN 2014-06, 52.

Vogler, D., Amann, F., Bayer, P., & Elsworth, D. (2016). Permeability Evolution in Natural Fractures Subject to Cyclic Loading and Gouge Formation. *Rock Mechanics and Rock Engineering*, 49(9), 3463-3479. doi:10.1007/s00603-016-1022-0

Voltolini, M., & Ajo-Franklin, J. (2020). Evolution of propped fractures in shales: The microscale controlling factors as revealed by in situ X-Ray microtomography. *Journal of Petroleum Science and Engineering*, 188, 106861. doi:https://doi.org/10.1016/j.petrol.2019.106861

von Terzaghi, K. (1923).Die Berechnung der Durchlassigkeitzifer des Tones aus dem Verlauf der hydrodynamischen Spannungserscheinungen. *Sitzungsber. Akad. Wiss.(Wien). Math.-Naturwiss. Kl.*, 125-138.

Vrolijk, P. J., Urai, J. L., & Kettermann, M. (2016). Clay smear: Review of mechanisms and applications. *Journal of Structural Geology*, 86, 95-152. doi:https://doi.org/10.1016/j.jsg.2015.09.006

Walsh, J. B. (1981). Effect of pore pressure and confining pressure on fracture permeability. *International Journal of Rock Mechanics and Mining Sciences & Geomechanics Abstracts*, 18(5), 429-435. doi:https://doi.org/10.1016/0148-9062(81)90006-1

Walsh, S. D. C., Smith, M., Carroll, S. A., & Crandall, D. (2016). Non-invasive measurement of proppant pack deformation. *International Journal of Rock Mechanics and Mining Sciences*, 87, 39-47. doi:https://doi.org/10.1016/j.ijrmms.2016.05.005

Watanabe, N., Ishibashi, T., Ohsaki, Y., Tsuchiya, Y., Tamagawa, T., Hirano, N., . . . Tsuchiya, N. (2011). X-ray CT based numerical analysis of fracture flow for core samples under various confining pressures. *Engineering Geology*, 123(4), 338-346. doi:https://doi.org/10.1016/j.enggeo.2011.09.010

Wenk, H. R., Voltolini, M., Mazurek, M., Van Loon, L. R., & Vinsot, A. (2008). Preferred orientations and anisotropy in shales: Callovo-Oxfordian shale (France) and opalinus clay (Switzerland). *Clays and Clay Minerals*, 56(3), 285-306. doi:10.1346/Ccmn.2008.0560301

Wenning, Q. C., Madonna, C., Zappone, A., Grab, M., Rinaldi, A. P., Plötze, M., . . . Wiemer, S. (2021). Shale fault zone structure and stress dependent anisotropic permeability and seismic velocity properties (Opalinus Clay, Switzerland). *Journal of Structural Geology*, 144, 104273. doi:https://doi.org/10.1016/j.jsg.2020.104273

Wetzel, A., & Allia, V. (2003). Der Opalinuston in der Nordschweiz: Lithologie und Ablagerungsgeschichte. *Ecologae Geologicae Helvetiae*, 96, 451-469.

Wild, K. M. (2016). Evaluation of the hydro-mechanical properties and behavior of Opalinus Clay. ETH Zurich, Retrieved from http://hdl.handle.net/20.500.11850/128300

Wild, K. M., & Amann, F. (2018). Experimental study of the hydro-mechanical response of Opalinus Clay - Part 1: Pore pressure response and effective geomechanical properties under consideration of confinement and anisotropy. *Engineering Geology*, 237, 32-41. doi:10.1016/j.enggeo.2018.02.012

Wild, K. M., Barla, M., Turinetti, G., & Amann, F. (2017). A multi-stage triaxial testing procedure for low permeable geomaterials applied to Opalinus Clay. *Journal of Rock Mechanics and Geotechnical Engineering*, 9(3), 519-530. doi:https://doi.org/10.1016/j.jrmge.2017.04.003

Wild, K. M., Wymann, L. P., Zimmer, S., Thoeny, R., & Amann, F. (2015). Water Retention Characteristics and State-Dependent Mechanical and Petro-Physical Properties of a Clay Shale. *Rock Mechanics and Rock Engineering*, 48(2), 427-439. doi:10.1007/s00603-014-0565-1

Winhausen, L., Jalali, M., Amann, A., Khaledi, K., Hamdi, P., Urai, J., . . . Amann, F. (2020). A comparative study on methods for determining the hydraulic properties of a clay shale. *Geophysical Journal International*, 224. doi:10.1093/gji/ggaa532

Winhausen, L., Khaledi, K., Jalali, M., Urai, J. L., & Amann, F. (2022). Failure mode transition in Opalinus Clay: a hydro-mechanical and microstructural perspective. *Solid Earth*, 13(5), 901-915. doi:10.5194/se-13-901-2022

Witherspoon, P. A., Wang, J. S. Y., Iwai, K., & Gale, J. E. (1980). Validity of Cubic Law for fluid flow in a deformable rock fracture. *Water Resources Research*, 16(6), 1016-1024. doi:https://doi.org/10.1029/WR016i006p01016

Wong, T.-F., & Baud, P. (2012). The brittle-ductile transition in porous rock: A review. *Journal of Structural Geology*, 44, 25-53. doi:https://doi.org/10.1016/j.jsg.2012.07.010

Wong, T.-F., David, C., & Zhu, W. (1997). The transition from brittle faulting to cataclastic flow in porous sandstones: Mechanical deformation. *Journal of Geophysical Research: Solid Earth*, 102(B2), 3009-3025. doi:https://doi.org/10.1029/96JB03281

Wood, D. M. (1990). *Soil Behaviour and Critical State Soil Mechanics*. Cambridge: Cambridge University Press.

Yamaguchi, A., Sakaguchi, A., Sakamoto, T., Iijima, K., Kameda, J., Kimura, G., . . . Curewitz, D. (2011). Progressive illitization in fault gouge caused by seismic slip propagation along a megasplay fault in the Nankai Trough. *Geology*, 39(11), 995-998. doi:10.1130/g32038.1

Yasuhara, H., & Elsworth, D. (2008). Compaction of a Rock Fracture Moderated by Competing Roles of Stress Corrosion and Pressure Solution. *Pure and Applied Geophysics*, 165(7), 1289-1306. doi:10.1007/s00024-008-0356-2

Yasuhara, H., Elsworth, D., & Polak, A. (2004). Evolution of permeability in a natural fracture: Significant role of pressure solution. *Journal of Geophysical Research: Solid Earth*, 109(B3). doi:https://doi.org/10.1029/2003JB002663

Yasuhara, H., Kinoshita, N., Ohfuji, H., Lee, D. S., Nakashima, S., & Kishida, K. (2011). Temporal alteration of fracture permeability in granite under hydrothermal conditions and its interpretation by coupled chemo-mechanical model. *Applied Geochemistry*, 26(12), 2074-2088. doi:https://doi.org/10.1016/j.apgeochem.2011.07.005

Yasuhara, H., Marone, C., & Elsworth, D. (2005). Fault zone restrengthening and frictional healing: The role of pressure solution. *Journal of Geophysical Research: Solid Earth*, 110(B6). doi:https://doi.org/10.1029/2004JB003327

Yong, S., Kaiser, P. K., & Loew, S. (2010). Influence of tectonic shears on tunnel-induced fracturing. *International Journal of Rock Mechanics and Mining Sciences*, 47(6), 894-907. doi:https://doi.org/10.1016/j.ijrmms.2010.05.009

Yu, C., Matray, J.-M., Gonçalvès, J., Jaeggi, D., Gräsle, W., Wieczorek, K., . . . Sykes, E. (2017). Comparative study of methods to estimate hydraulic parameters in the hydraulically undisturbed Opalinus Clay (Switzerland). *Swiss Journal of Geosciences*, 110(1), 85-104. doi:10.1007/s00015-016-0257-9

Yu, H., Chen, W., Gong, Z., Ma, Y., Chen, G., & Li, X. (2018). Influence of temperature on the hydro-mechanical behavior of Boom Clay. *International Journal of Rock Mechanics and Mining Sciences*, 108, 189-197. doi:https://doi.org/10.1016/j.ijrmms.2018.04.023

Zappone, A., Rinaldi, A. P., Grab, M., Wenning, Q. C., Roques, C., Madonna, C., . . . Wiemer, S. (2021). Fault sealing and caprock integrity for CO2 storage: an in situ injection experiment. *Solid Earth*, 12(2), 319-343. doi:10.5194/se-12-319-2021

Zhang, C.-L. (2016). The stress–strain–permeability behaviour of clay rock during damage and recompaction. *Journal of Rock Mechanics and Geotechnical Engineering*, 8(1), 16-26. doi:https://doi.org/10.1016/j.jrmge.2015.10.001

Zhang, C.-L. (2017). Examination of effective stress in clay rock. *Journal of Rock Mechanics and Geotechnical Engineering*, 9(3), 479-489. doi:https://doi.org/10.1016/j.jrmge.2016.07.008

Zhang, C.-L., Conil, N., & Armand, G. (2017). Thermal effects on clay rocks for deep disposal of high-level radioactive waste. *Journal of Rock Mechanics and Geotechnical Engineering*, 9(3), 463-478. doi:https://doi.org/10.1016/j.jrmge.2016.08.006

Zhang, C.-L., & Laurich, B. (2019). Mechanical behavior of sandy facies of Opalinus Clay under different load conditions. *Journal of Rock Mechanics and Geotechnical Engineering*, 12(2), 223-241. doi:https://doi.org/10.1016/j.jrmge.2019.09.005

Zhang, C.-L., Rothfuchs, T., Su, K., & Hoteit, N. (2007). Experimental study of the thermo-hydro-mechanical behaviour of indurated clays. *Physics and Chemistry of the Earth*, Parts A/B/C, 32(8), 957-965. doi:https://doi.org/10.1016/j.pce.2006.04.038

Zhang, C.-L., & Talandier, J. (2022). Self-sealing of fractures in indurated claystones measured by water and gas flow. *Journal of Rock Mechanics and Geotechnical Engineering*. doi:https://doi.org/10.1016/j.jrmge.2022.01.014

Zhang, D. C., Ranjith, P. G., & Perera, M. S. A. (2016). The brittleness indices used in rock mechanics and their application in shale hydraulic fracturing: A review. *Journal of Petroleum Science and Engineering*, 143, 158-170. doi:10.1016/j.petrol.2016.02.011

Zhang, F., Xie, S. Y., Hu, D. W., Shao, J. F., & Gatmiri, B. (2012). Effect of water content and structural anisotropy on mechanical property of claystone. *Applied Clay Science*, 69, 79-86. doi:https://doi.org/10.1016/j.clay.2012.09.024

Zhang, J., Ouyang, L., Zhu, D., & Hill, A. D. (2015). Experimental and numerical studies of reduced fracture conductivity due to proppant embedment in the shale reservoir. *Journal of Petroleum Science and Engineering*, 130, 37-45. doi:https://doi.org/10.1016/j.petrol.2015.04.004

Zhang, X., & Spiers, C. J. (2005). Compaction of granular calcite by pressure solution at room temperature and effects of pore fluid chemistry. *International Journal of Rock Mechanics and Mining Sciences*, 42(7), 950-960. doi:https://doi.org/10.1016/j.ijrmms.2005.05.017

Zhang, X., Spiers, C. J., & Peach, C. J. (2010). Compaction creep of wet granular calcite by pressure solution at 28°C to 150°C. *Journal of Geophysical Research: Solid Earth*, 115(B9). doi:https://doi.org/10.1029/2008JB005853

Zheng, L., Rutqvist, J., Birkholzer, J. T., & Liu, H.-H. (2015). On the impact of temperatures up to 200°C in clay repositories with bentonite engineer barrier systems: A study with coupled thermal, hydrological, chemical, and mechanical modeling. *Engineering Geology*, 197, 278-295. doi:https://doi.org/10.1016/j.enggeo.2015.08.026

Zimmerman, R. W., Chen, D.-W., & Cook, N. G. W. (1992). The effect of contact area on the permeability of fractures. *Journal of Hydrology*, 139(1), 79-96. doi:https://doi.org/10.1016/0022-1694(92)90196-3

Zoback, M. D. (2007). *Reservoir Geomechanics*. Cambridge: Cambridge University Press.

Zoback, M. D., & Gorelick, S. M. (2012). Earthquake triggering and large-scale geologic storage of carbon dioxide. *Proceedings of the National Academy of Sciences*, 109(26), 10164. doi:10.1073/pnas.1202473109

Zoback, M. D., Kohli, A., Das, I., & McClure, M. (2012). *The Importance of Slow Slip on Faults During Hydraulic Fracturing Stimulation of Shale Gas Reservoirs*. Paper presented at the SPE Americas Unconventional Resources Conference. https://doi.org/10.2118/155476-MS